National Library of Canada
Acquisitions and Bibliographic Services Branch
395 Wellington Street
Ottawa, Ontario
K1A 0N4

Bibliothèque nationale du Canada
Direction des acquisitions et des services bibliographiques
395, rue Wellington
Ottawa (Ontario)
K1A 0N4

Your file Votre référence

Our file Notre référence

NOTICE

The quality of this microform is heavily dependent upon the quality of the original thesis submitted for microfilming. Every effort has been made to ensure the highest quality of reproduction possible.

If pages are missing, contact the university which granted the degree.

Some pages may have indistinct print especially if the original pages were typed with a poor typewriter ribbon or if the university sent us an inferior photocopy.

Reproduction in full or in part of this microform is governed by the Canadian Copyright Act, R.S.C. 1970, c. C-30, and subsequent amendments.

AVIS

La qualité de cette microforme dépend grandement de la qualité de la thèse soumise au microfilmage. Nous avons tout fait pour assurer une qualité supérieure de reproduction.

S'il manque des pages, veuillez communiquer avec l'université qui a conféré le grade.

La qualité d'impression de certaines pages peut laisser à désirer, surtout si les pages originales ont été dactylographiées à l'aide d'un ruban usé ou si l'université nous a fait parvenir une photocopie de qualité inférieure.

La reproduction, même partielle, de cette microforme est soumise à la Loi canadienne sur le droit d'auteur, SRC 1970, c. C-30, et ses amendements subséquents.

Canada

THEORY, DESIGN, CONSTRUCTION and CHARACTERIZATION of CONFOCAL SCANNING LASER MICROSCOPE CONFIGURATIONS

by
Tilemachos D. Doukoglou

Department of Electrical Engineering
and
Department of Biomedical Engineering

McGill University, Montréal, Québec, Canada

A thesis submitted to the Faculty of Graduate Studies and Research in partial fulfillment of the requirements for the degree of Doctor of Philosophy

ISBN 0-612-08095-1

Canada

To Olympia, Dimitri, Maria-Ephrosyne and George

και στους γονείς μου

Abstract

The objective of this study was the development of the imaging subsystem of an organ mapping system that would be able to acquire sufficient information for building a 3D cellular level map of a small organ. The imaging subsystem that is presented is a confocal scanning laser microscope arrangement that is versatile and offers a number of different imaging modes, with minimal modifications in the optical configuration, and no need for realignment of optical components.

The organ mapping system is a part of a larger project involving the building of a tele-operated microsurgical robot capable of operating on small organs, such as the eye. In this context a second imaging system prototype based again on a scanning laser microscope configuration is presented. The development of this second imaging system is for investigating possible integration of such a device into the surgical microrobot for high resolution image acquisition during operations. The main feature of this system is that the scanning is performed in spherical coordinates; making it suitable and advantageous for imaging organs that exhibit some form of spherical shape, such as the eye.

Before the two imaging systems are presented an overview of the theory governing the operation of confocal microscope arrangements is given, together with a simple model based on geometric optics with Gaussian beam weighting that describes the depth response of a confocal arrangement as a function of the detector size. Finally, a detailed analysis of the error due to refractive index mismatches, that can lead to significant dimensional miscalculations when volumetric imaging is performed with a confocal microscope, is also presented.

Résumé

L'objectif de cette étude a été la conception et le développement d'une système d'imagerie destiné à acquérir les données requises pour construire une carte tridimensionnelle de petits organes (avec une précision de l'ordre cellulaire). La conception de cet appareil est basée sur un système de microscopie confocale très versatile, offrant de multiples modes d'acquisition d'images et ne nécessitant presque aucune réorganisation de ses composantes physiques.

Cet appareil fait partie d' un projet plus important, à savoir, la construction d' un micro-robot "teleoperé" destiné à faire des opérations chirurgicales sur de petits organes, comme l'oeil. Un deuxième système d'imagerie, faisant également partie du micro-robot, est présenté dans cet ouvrage. Ce deuxième appareil est aussi un microscope confocal, dont le fonctionnement est basé sur un système de déplacement à coordonnées sphériques. Ce prototype a été développé afin d' étudier la possibilité d'intègrer ce système au micro-robot pour acquérir des images de haute fidélité durant les procédures chirurgicales. Le système est donc particulièrement adapté aux opérations sur les organes ayant une certaine symétrie radiale (l'oeil par exemple).

Avant la description détaillée de ces deux systèmes d'acquisition d'images , une section présente un aperçu d'importants principes thèoriques de la microscopie confocale. En plus, un modèle simple est présenté basé sur l'optique géométrique et des faisceaux Gaussiens décrivant la résolution en profondeur en fonction des dimensions du détecteur. Finalement, une analyse détaillé des erreurs dûes aux différences entre les coefficient de réfraction, qui peuvent causer des erreurs importantes dans les calculs des dimensions lorsque l'acquisition d'image volumétrique est faite avec un microscope confocal, est aussi présentée.

Περίληψη

Ο βασικός σκοπός της διατριβής αυτής είναι ο σχεδιασμός, η κατασκευή και ο χαρακτηρισμός ενός συστήματος μικροσκοπίας γιά τήν απόκτηση τριδιάστατων εικόνων βιολογικών ουσιών. Το μικροσκόπιο είναι μέρος ενός μεγαλύτερου συστήματος που έχει σαν σκοπό, την αυτοματικοποίηση της διαδικασίας απόκτησης μιάς τριδιάστατης ανατομικής χαρτογράφησης των κυττάρων ενός μικρού βιολογικού οργάνου.

Το σύστημα χαρτογράφησης είναι ένα από τα υποσυστήματα ενός μεγαλύτερου συστήματος ρομποτικής μικροχειρουργικής ικανό να εκτελεί (κάτω από καθοδήγηση εξαποστάσεως) μικροχειρουργικές επεμβάσεις σε μικρά βιολογικά όργανα όπως το μάτι. Μέ σκοπό την ολοκλήρωση αυτού του συστήματος έχει κατασκευαστεί και ένα δεύτερο πρότυπο μικροσκοπίου σάρωσης. Η πρωτοτυπία του δεύτερου αυτού συστήματος είναι ότι η σάρωση γίνεται σε σφαιρικές συντεταγμένες. Αυτός ο τύπος σάρωσης έχει σημαντικά πλεονεκτήματα για απόκτηση εικόνων από όργανα που παρουσιάζουν κάποια μορφή σφαιρικής συμμετρίας. Ένα τέτοιο όργανο είναι το μάτι. Ο απώτερος σκοπός μας είναι η ενσωμάτωση του συστήματος στο ρομπότ μικροχειρουγικής, γιά απόκτηση εικόνων υψηλής διακριτικότητας κατά την διάρκεια της χειρουργικής επέμβασης.

Πρίν παρουσιάσουμε λεπτομερειακά τα δύο αυτά συστήματα μικροσκοπίας σάρωσης, μια εμπεριστατωμένη ανάλυση της θεωρίας που διέπει την συνεστιακή μικροσκοπία σάρωσης με ακτίνες Laser συμπεριλαμβάνεται σαν μέρος αυτής της διατριβής. Η θεωρητική ανάλυση περιλαμβάνει και ένα καινούργιο μοντέλο της εξάρτησης της συνάρτησης μεταφοράς κατά μήκος του οπτικού άξονα ενός συνεστιακού μικροσκοπίου, από το μέγεθος του φωτοανιχνευτή. Η ανάλυση είναι βασισμένη στη θεωρία της γεωμετρικής οπτικής και αυτή της Gaussian δέσμης. Επίσης η ανάλυση του λάθους που υπεισέρχεται στον υπολογισμό των διαστάσεων, κατά την απόκτηση τριαδιάστατων εικονων, λόγω της ανομοιογένειας του συντελεστή διάθλασης, συμπεριλαμβάνεται στο θεωρητικό μέρος.

Acknowledgments

This work would not have been possible without the help of many people. I wish to express my gratitude to the following individuals:

My supervisor, Dr Ian W. Hunter, for his constant advice and support. The remarkable breadth and depth of his knowledge in so many different fields was and will be an inspiration to me. Working in his laboratory both at McGill and later at MIT was a privilege. Beyond his supervision I would also like to thank him for his patience.

Professor Robert E. Kearney for his encouragement and help, especially in the first stages of this project.

Colin Brenan for our endless arguments and counter arguments that helped enrich my understanding of optics.

Serge Lafontaine for his constant help and advice in an extremely wide range of problems.

Paul Charette for kindly listening to my suggestions in expanding his xvg program to allow visualization of the images acquired with the Confocal Laser Microscope.

Sylvain Martel and Ross Wagner for their comments, advice and for helping making the Department of Biomedical Engineering a pleasant place to work in. John and Peter Madden for their questions and the proof reading of parts of this manuscript.

Noemia Sebastio for the valuable advice that she provided regarding biological tissue preparation.

I am also indebted to NSERC, MRC, IRIS, and all other organizations that financially helped the above project.

Table of Contents

List of Figures

List of Tables

List of Plates

Abbreviations

2D	Two dimensional
3D	Three dimensional
A/D	Analog to digital converter
APD	Avalanche photo diode
CSLM	Confocal scanning laser microscope
CSM	Confocal scanning microscope
D/A	digital to analog converter
DPC	Differential Phase Contrast
FWHM	Full width half maximum
I/O	input output
IRF	Impulse response function
MSR	Microsurgical robot
NA	Numerical Aperture
NED	Noise equivalent displacement
OSF	Optical transfer function
PDRF	Planar depth response function
PSF	Point spread function
SNR	Signal-to-noise ratio
SCSLM	Spherical coordinates scanning laser microscope
SRF	Step response function

CHAPTER 1

Introduction

1.1 Preface

The work presented in this thesis represents an integral part of the ongoing development of a tele-operated micro-surgical robot (MSR-1) at the Biorobotics Laboratory of McGill University and recently the Massachusetts Institute of Technology [Hunter *et al.*, 1993]. Placing the current work within the context of the MSR-1 development, will help in understanding the purpose of designing, building and characterizing the scanning imaging configurations presented in subsequent chapters of this thesis.

This chapter begins with a brief description of the MSR-1, its associated subsystems and areas of research. A statement of the objectives of this thesis work is then followed by an overview of the related research areas that have been addressed.

1.2 The Micro-surgical Robot System (MSR-1)

The focus of this section in on a micro-surgical robot (referred to also as MSR-1) which is under development for use in micro-surgery of small organs. Although the MSR-1 can be used to perform micro-surgical procedures in a variety of organs, eye-surgery will be used as the example in the description that follows. In order to design a surgical robot, an understanding of the biological system or organ that is being operated on is required, as well as detailed information about the dynamic behavior of the human operator who forms part of the closed-loop system controlling the robot. This thesis work is concerned with the former. Figure 1.1 summarizes the different aspects of the micro-surgical robot system and shows that it can be divided into two parts: (a) the micro-surgical robot itself, and (b) the supporting subsystems. The information acquired from the different subsystems depicted

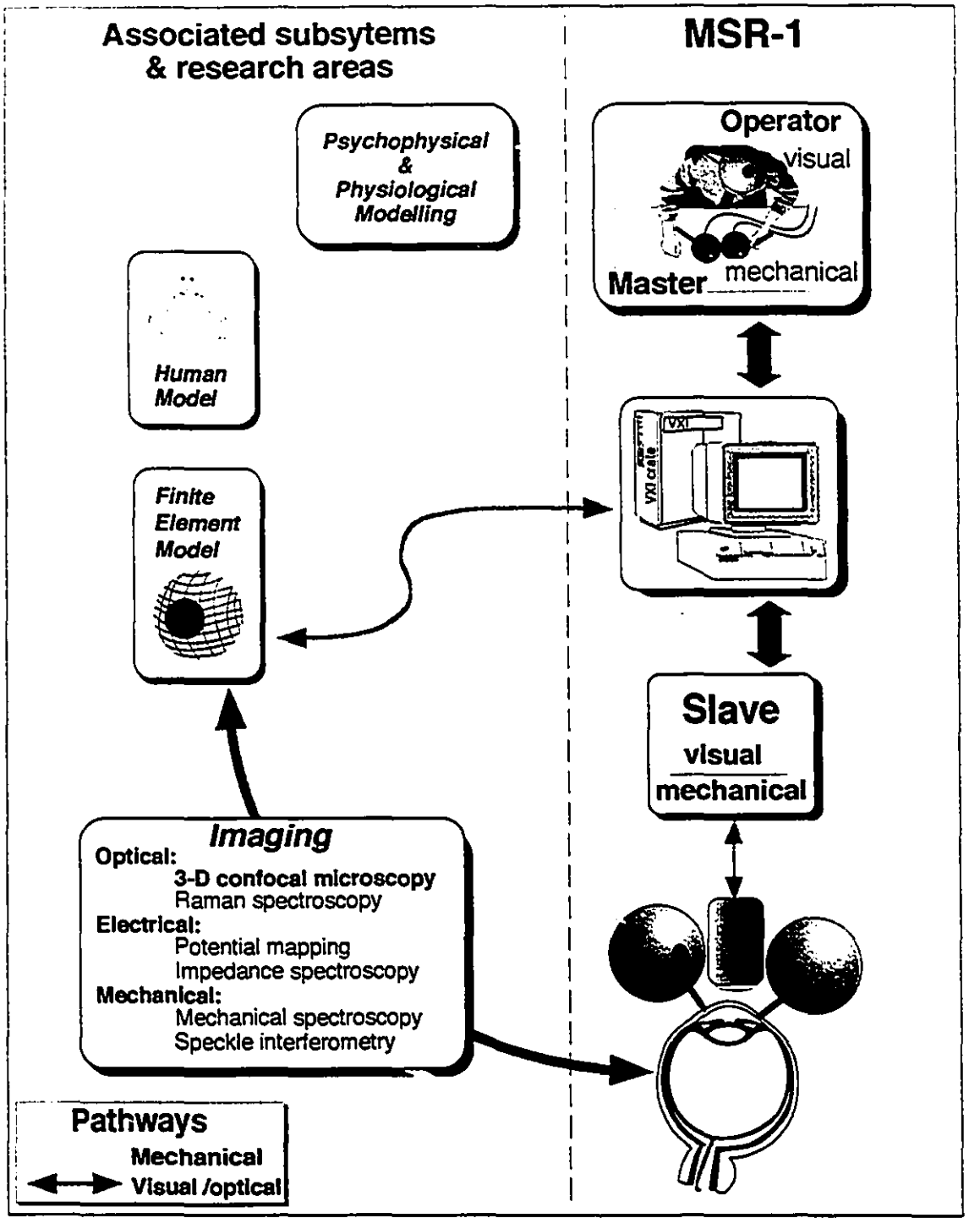

Figure 1.1 *Block diagram of the microsurgical robot system together with the associated subsystems and research areas.*

in the left side of Figure 1.1 are used not only in the design and construction of the robot but also during the actual operation and training sessions.

1.2.1 Global System Design

The MSR-1 is similar in concept to an earlier tele-operated micro-motion robot, MR-1, that was built for use as a scientific instrument [Hunter *et al.*, 1990; Hunter *et al.*, 1991]. MSR-1, like MR-1, contains a two-limbed force-reflecting master which controls a two-limbed slave micro-motion robot. Currently, only one limb of the master and slave is fully functional. For clarity in this section, the MSR-1 is presented as though the master and slave have both limbs operational. Bi-directional pathways relay visual and mechanical information between the master and slave as shown in Figure 1.2. The surgeon wears a helmet (audio-visual master) that is used to control the orientation of a stereoscopic camera system (visual slave) observing the surgery scene (organ under operation). Images from the stereoscopic camera system are relayed back to the helmet or an adjacent stereoscopic display where they are viewed by the surgeon.

In each hand the surgeon holds a pseudo-tool (shaped like a surgical scalpel) which projects from the left and right limbs of a force reflecting interface (mechanical master). Movements of the left and right pseudo-tools cause corresponding movements, scaled down 1 to 100 times, in the micro-surgical tools held by the left and right limbs of the micro-surgical robot (mechanical slave) that performs the surgery. Forces experienced by the left and right limbs of the slave micro-surgical robot are reflected back, after being scaled up, 1 to 100 times, to the surgeon via the tools. The master and slave subsystems (both visual and mechanical) communicate through a computer system which serves (among other things) to enhance and augment images, filter hand tremor, perform co-ordinate transformations and safety checks. The objective of the system is to enhance the accuracy and dexterity of the surgeon by creating mechanical and visual "telepresence".

1.2.2 The Slave Subsystem

The slave subsystem can be considered to consist of two distinct parts: the mechanical and the visual. A brief description of the two parts follows.

1.2.2a Mechanical Slave

Microsurgery is performed by a slave micro-motion robot that has two limbs (left and right) which hold the operating tools and have a one-to-one correspondence with the limbs of the

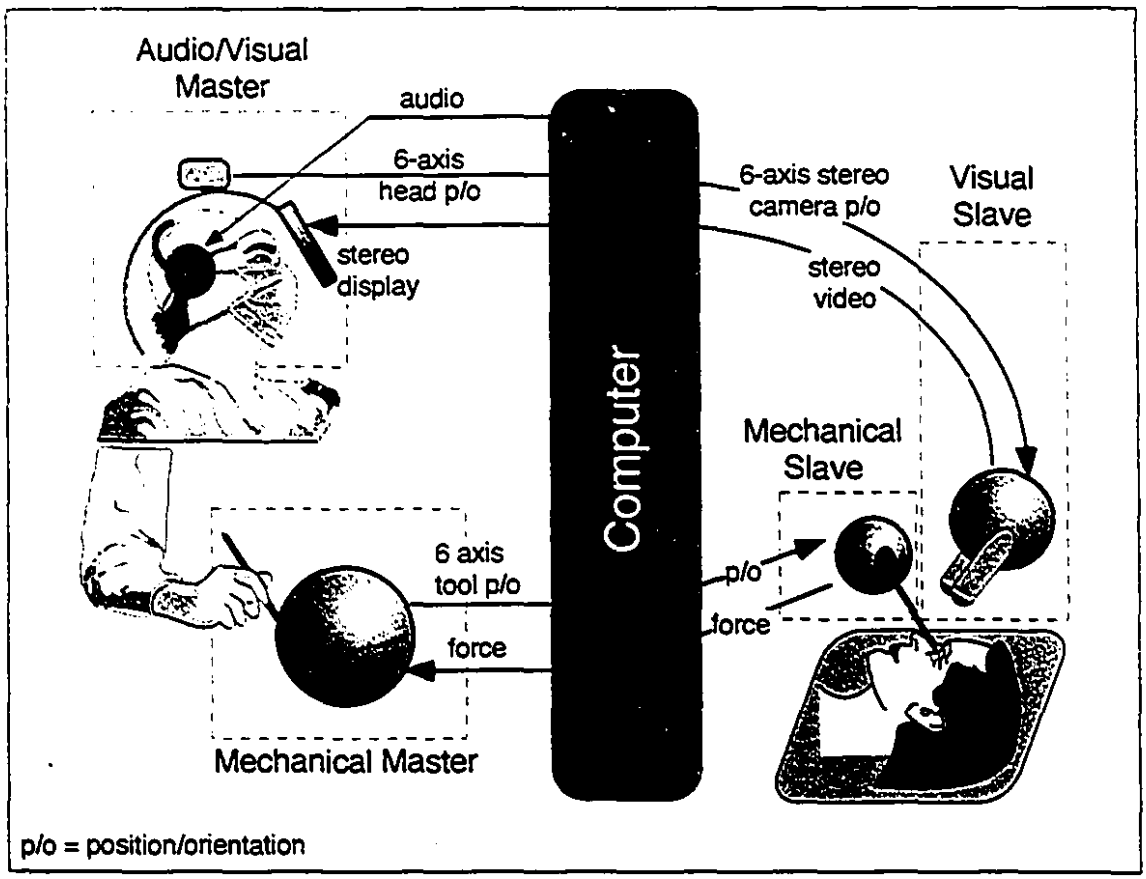

Figure 1.2 *Block diagram of the MSR-1's master and slave visual and mechanical systems.*

mechanical master. The computer subsystem controls the slave's mechanical subsystem using input commands from the master. Each limb of the slave has six direct-drive rotary electromagnetic actuators which are arranged in a redundant parallel configuration that provides a 5 degrees-of-freedom (dof) motion (three linear, two rotary). The parallel-drive design (as opposed to a series-drive configuration) was developed to meet the simultaneous requirements of both wide bandwidth (high speed) and high precision. Both the master and slave mechanical systems offer a displacement bandwidth exceeding that of the human hand (>10 Hz).

Each actuator is equipped with a sensitive position and force transducer which records the very small movements of the slave limbs together with the forces that are experienced by the limbs while in operation. The position and force transducers have low frequency noise levels of less than 1 μm RMS and 1 mN RMS, respectively. The five orthogonal position and force spatial components (three linear and two rotary) are amplified and then sent back through the position/orientation pathways to the master subsystem (see Figure 1.2). This permits the operator to feel not only the magnitude, but also the direction, of the micro-motion and resistance experienced by the slave during operation. In this way, the surgeon is able to feel via the left and right master pseudo-tools the forces experienced by the micro-tools held by the left and right limbs of the micro-surgical slave robot. Micro-cutting forces which are normally below the sensory threshold and hence not detected, may, after scaling, be felt for the first time. The slave micro-surgical robot can hold a variety of micro-tools (diamond knives, probes, etc.) and will eventually be able to select tools from a carousel of tools contained within the slave housing.

1.2.2b Visual Slave

The stereoscopic-imaging system, built for MSR-1, views the location of each slave limb with respect to each other, the organ (e.g. eye), and the surrounding tissue being approached. It consists of a computer-controlled, four rotary-axis parallel-drive stereoscopic camera mount ("head") which has approximately the same range of motion as the human head with respect to the shoulders. The stereoscopic-head is faster (>1000 deg/s) than the human head and can rotate in three planes: sagittal (up-down), transverse (left-right) and coronal (tilt). Two small color video cameras (Panasonic KS102), mounted in the head, provide stereoscopic images at 30 frames/s. A visible wavelength laser diode, (mounted also in the head) forms part of the servo-system which sets the correct vergence

angle for the two cameras. The vergence is controlled by the fourth rotary actuator. The cameras use large depth of field optics to avoid the necessity of a separate focus control.

For high resolution imaging, one of the slave limbs may be used together with an appropriate imaging subsystem to acquire images via 3D scanning. A number of techniques to image, via such scanning, some of the optical, chemical, electrical and mechanical properties of biological tissue (see Sections 1.4 below) are currently under development. Chapter 6 of this thesis presents two spherical-coordinate confocal scanning laser microscope prototypes. These prototypes were built to investigate the suitability of such imaging modalities as part of the MSR-1. Further miniaturization of these prototypes is also needed before they can be integrated as imaging tools of the MSR-1.

1.2.3 The Master Subsystem

The master subsystem also consists of a mechanical part, namely the pseudo-tools, and a visual part, which is a helmet-mounted stereoscopic display with an integral head-motion tracking system.

1.2.3a Mechanical Master

As with the slave subsystem, the master's mechanical system consists of two active limbs, each of which includes six direct-drive rotary electromagnetic actuators with six force and six displacement transducers integrated into the actuators. Position changes applied to the master's limb (pseudo-tools) are measured and sent to the computer system for processing (nonlinear filtering, boundary checking, etc.) before being transmitted to the slave. Forces experienced by the slave are reflected back via the computer to the master where they exert a force on the operator. Feedback of force is important in high precision tasks (Hannaford, Wood, McAffee & Zak, 1991), such as micro-surgery, as it can improve the operator's accuracy.

1.2.3b Audio-Visual Master

The six-axis position/orientation of the surgeon's head (helmet) (measured by an Ascension Technology Corp. Bird 6D sensor, model 6BI001) is used to control the slave stereoscopic camera head. Color stereoscopic images from the slave cameras are transmitted (either as analog RGB or digitally frame grabbed) back to the surgeon and displayed on either a helmet-mounted display or on a (1.8 m diagonal) high resolution video rear projection screen/lens (Draper, Diamond Black Matrix) viewed by frame sequential liquid crystal

shutter glasses (Stereograhics GDC-3) mounted on the helmet. The images may be displayed directly or merged into the virtual environment as described below (Section 1.3). The video projector (Electrohome model Marquee 8000) runs at 154 frames/s (77 1280*1024*3 color stereoscopic frames/s) and is considerably superior to the relatively low resolution color LCDs on the current helmet.

The left and right slave tools are represented and displayed in the virtual environment (see below) where they are observed by the surgeon via the helmet or screen. The positions of the slave tools can also be fed back to the surgeon via the surgical helmet's headphones as a stereo tone whose amplitude and/or frequency is a function of the forces experienced at the tool-tissue interface.

1.2.4 Computer system

MSR-1's computer requirements include the need for high speed 3D graphics for the virtual reality system, fast image processing, high floating-point performance for coordinate transforms, control algorithm evaluation and finite element computations, and finally (and frequently neglected), high-performance, low-latency, real-time throughput for control purposes. This latter requirement cannot be met by most commercial computers.

The master and slave computers are IBM RISC System/6000 workstations connected via a 220 Mbit/s optical fiber link (IBM #2860). The IBM RISC System/6000 computer was selected because of the real-time potential of its super-scalar CPU architecture which incorporates a software accessible nano-second clock (updated in 40 ns increments). Each computer is connected to a VXI bus crate (Hewlett Packard #E1401A) containing the i/o hardware. The IBM MicroChannel bus to VXI bus connection is made via the MXI protocol and hardware (National Instruments, #VXI-MC6000). The VXI bus was chosen because it is particularly well suited for the control of low-noise instrumentation. The VXI crates contain high resolution ADCs (Hewlett Packard, #E1413A, 64 channel, 100 kHz throughput, 18-bit precision plus 4 bit log sample by sample auto-ranging gain), DACs (Tasco, #TVXI/DAC16, 16 bit precision, 16 channel, 30 kHz/channel, auto-calibrating) and DIOs (Kinetics Systems, #V387, 128 channel digital i/o).

1.3 MSR-1 Operation

Associated with the MSR-1 is a virtual environment to allow surgeon training and rehearsal of surgical procedures. The virtual environment is designed to produce both a

realistic visual display of the organ/tissue being operated on, as well as effective mechanical feedback to simulate tissue properties during manipulation and cutting. The virtual environment for the eye incorporates a very detailed continuum model of the anatomy of the eye, its mechanics and optical properties, together with a less detailed geometric/mechanical model of the face and representations of the micro-tools. The continuum model of the eye is built using information gathered by some of the MSR-1 optical subsystems presented next. An extensive description of the MSR-1 virtual environment and its modes of operation (i.e. Manual mode control, Supervisory mode control. Tele-operation etc.) are beyond the scope of this thesis. More details can be found in [Hunter *et al.*, 1993] & [Hunter *et al.*, 1994].

1.4 MSR Imaging Subsystems

Development of the MSR-1 and the continuum model (used in the virtual environment) necessitates, among other things, detailed knowledge of the organ operated upon. Part of this thesis work (Chapters 4 & 5) presents a microscope prototype designed as the imaging subsystem of an organ mapping system to be used for gathering detailed anatomical knowledge (at the cellular level) of a small organ.

During operation anatomical as well as structural information regarding the organ undergoing operation should also be gathered and presented to the surgeon. A number of imaging techniques and systems are being developed for use in MSR-1, in order to acquire information about the optical, mechanical and chemical properties of the tissue being operated upon. Such information aids diagnosis and helps in the execution of the micro-surgical procedure. Chapter 6 of this thesis presents such a prototype of a scanning imaging system very well suited for imaging organs having a quasi-spherical shape (i.e. the eye). A miniaturized version of such a system could be used as the imaging micro-tool of the MSR-1. These MSR-1 related imaging modalities, (either already used or under development) are summarized next.

1.4.1 Imaging of Optical Properties (Confocal Laser Scanning Microscopy)

The optical transfer function of confocal optical systems is well suited to the collection of images encoding various tissue optical properties [Wilson & Sheppard, 1984]. The characteristics of this particular imaging modality allow thin optical slices of non-opaque objects to be acquired without mechanically sectioning the specimen, which can result in tissue distortion. This property is known as optical sectioning or microtomoscopy. High resolution, 3D volumetric images of small semi-transparent organs can be acquired using

3D confocal scanning laser microscopy and these can be used both to build a model of the geometry and topology of the organ and to serve as a basis for constructing the geometry for a FE model of the organ. In addition, these images can form part of an on-line 3D navigation and anatomical map for the particular organ under study. Chapters 4 and 5 present in more details the imaging part of such an organ mapping apparatus (under construction).

A variety of laser-based confocal microscopic imaging system prototypes for use in micro-robotic systems [Doukoglou, Hunter & Brenan, 1992][Doukoglou & Hunter, 1993] were built in the Biorobotics Laboratory of McGill University. These systems are able to image intensity, phase, as well as polarization characteristics of tissue [Hunter *et al.*, 1990]. Instead of holding a micro-tool, the MSR-1 mechanical slave can grasp a confocal optical module and scan with it over the tissue (such as cornea). A step in this direction is the system prototype presented in Chapter 6.

1.4.2 Imaging of Mechanical Properties

The mechanical properties of biological tissue vary over a wide range and may be used to distinguish and identify, when used in conjunction with other characteristics, tissue type. For example, a patch of collagen which has grown over the retina (causing blindness) is considerably stiffer than the underlying and delicate retinal membrane. An image in which each pixel codes tissue stiffness, for example, will readily demarcate the collagen patch, while a conventional optical intensity image will only faintly reveal the patch. Two techniques are being developed to image the mechanical properties of tissue.

1.4.2a Mechanical Spectroscopic Imaging

The MSR-1 slave microsurgical robot limbs have sufficient bandwidth to enable the dynamic stiffness of tissue to be measured from 0 to 100 Hz. The technique involves applying an appropriately tailored stochastic displacement perturbation [Hunter & Kearney, 1983] and recording the resulting force fluctuation. The mechanical spectrum (stiffness frequency response function) is then determined using system identification techniques [Kearney & Hunter, 1990]. Some parameter of this spectrum is chosen (e.g. tissue elastic stiffness) and its magnitude encoded as a pixel intensity (or color). This process is then repeated at a sufficient number of locations across the tissue to generate a mechanical image. The technique is rather time consuming if mechanical images containing many spatial samples must be obtained. Unlike ultrasonic imaging which records the spatial

distribution of the tissue's mechanical response to small high frequency perturbations (at a single frequency), this technique images relatively large deformation tissue mechanical characteristics at low frequencies. Indeed, a microscopic ultrasonic probe might be scanned in the same way to generate complementary mechanical images.

The mechanical data acquired by the slave micro-surgical robot may be used to construct realistic FE models of the tissue being perturbed. Indeed the creation of FE models of diseased tissue (e.g. cataracts) is a prerequisite to the development of clinically useful virtual environments.

1.4.2b Speckle Interferometric Imaging

Minute surface deformations of a material or biological specimen can be measured with an appropriate interferometric optical arrangement using the "speckle effect". Speckle is observed in the reflected or transmitted optical beam when an optically rough surface is illuminated by a coherent light source such as a laser [Jones & Wykes, 1989]. The surface strain across the entire surface of an organ under a known state of experimentally applied stress can be measured using this method, and from these data a distributed stress-strain constitutive law map can be built. The strain field imaging system which was developed [Charette *et al.*, 1992, 1993] using speckle interferometry is able to measure high resolution strain field images of tissue. By applying a known stress to tissue, the system may also be used to acquire data from which a finite element model (FEM) of the tissue mechanics may be determined. Such models are essential for achieving mechanical virtual reality in surgical simulators.

1.4.3 Imaging of Chemical Properties (Confocal Scanning Laser Raman Microscopy)

This technique is an extension of the laser confocal method mentioned above (see Section 1.4.1) and includes a sensitive Fourier-transform Raman spectrometer. High resolution, 3D volumetric chemical images of the specimen under observation are obtained with this technique. The information acquired can be used to build a very accurate 3D map of the chemical composition of the organ. One advantage of this technique, which can be a problem with traditional 3D confocal scanning laser microscopy, is that high contrast images of objects that exhibit weak phase and/or intensity contrast images can be acquired. This can, however, involve longer acquisition times for an image. The confocal Raman microscopic imaging system [Brenan, Hunter & Charette, 1992][Brenan & Hunter, 1994]

should be integrated in the MSR-1 so that it will be seen by the MSR-1 mechanical slave as another tool available in the tool carousel.

1.5 Human Model

The performance of a surgeon when controlling a micro-robot will depend on numerous variables including the sensory modalities used to convey information from the robot to the surgeon (i.e. vision, touch, proprioception, audition), the information content of the signals fed back (i.e. frequency content, gain, statistical properties), and the characteristics of the interface (e.g. mechanical properties) through which the surgeon controls the robot. In order to develop a model of the surgeon or human operator, an understanding of the sensory, actuating and computational components of the surgeon must be achieved (see Figure 1.1). This entails psychophysical studies of the human tactile and proprioceptive systems (i.e. the haptic system), mechanical experiments on the neuromuscular system, and in particular on the dynamics of the human hand and forearm, and studies of human operator tracking performance.

Information regarding the methods and results of the human operator modeling studies are beyond the scope of this introduction. More information regarding this related research area can be found in [Jones & Hunter, 1990, 1993].

1.6 Thesis Objectives

Having completed the description of the MSR-1 and its subsystems and related research areas, an brief overview of the objectives of this thesis work will be presented next.

During the development of the MSR-1, the need for detailed information regarding the organ or tissue being operated upon led to the idea of an organ mapping system. The information (to be gathered by the organ mapping apparatus) is essential for building a realistic model of the particular organ. The organ model is in turn utilized by the virtual reality engine of the MSR-1 for surgeon training and during surgical procedure rehearsal. The development of the imaging part of the organ mapping apparatus partially constitutes the objective of this thesis work.

More specifically the specific objectives of this thesis work are:

a) Development of the imaging subsystem of an 3D organ mapping system, that will be able to automate the process of acquiring complete and detailed anatomical and structural information from a small organ.

b) Building of a microscope prototype to investigate the possibility of non-Cartesian coordinate scanning, having as an ultimate goal the possible integration of such a system as an in-vivo imaging accessory of the MSR-1.

1.7 Organ Mapping System

A number of modalities were considered for the imaging subsystem of the organ mapping apparatus. These are briefly presented next and are i) Scanning Electron Microscopy, ii) X-ray Microtomography, iii) Magnetic Resonance Microscopy, iv) Acoustic Wave Microscopy and v) Confocal Scanning Laser Microscopy. Although all the modalities have their own merits the last one was chosen. By choosing confocal microscopy as the imaging system for the organ mapping apparatus, it was appropriate that the suitability of such a modality as an imaging tool for the MSR-1 should also be investigated. This later part is addressed in Chapter 5 of the thesis.

System Requirements

- 3D image acquisition capabilities.
- Sub-cellular resolution capabilities (for biological tissue this translates to micron and submicron resolutions).
- Acquired images in digital form, so that further processing is possible to extract the information of interest (i.e. cell orientation [Doukoglou *et al.*, 1992], tissue density, cell size, isolation of various structures via segmentation, etc.).
- Design that allows the incorporation of a cutting subsystem, if imaging of the whole organ without the need for sectioning is not possible.
- Minimally invasive specimen preparation requirements (preferably ex-vivo and in-vivo imaging capabilities) are also highly desirable.

1.7.1 Imaging Subsystem

Before confocal microscopy was selected as the imaging modality, a number of alternatives, that are used for 3D high resolution image acquisition of biological tissue, were considered. More specifically Scanning Electron Microscopy, X-ray microtomography, Magnetic Resonance Microscopy and Ultrasound/Acoustic microscopy imaging are other alternatives.

Scanning Electron Microscopy

Scanning Electron Microscopy (SEM) [Goldstein, *et al.*, 1992] offers the highest lateral spatial resolution from all the imaging modalities considered. For qualitative observations, the extremely large depth of field together with the shadow-relief effect of the secondary and backscattered electron contrast, makes SEM a very powerful imaging modality. Nevertheless, its depth resolution is inferior to that of confocal microscopy and quantitative measurements of its depth discrimination cannot be easily obtained. Consequently real volumetric 3D images cannot be acquired. SEM is also more invasive since it requires a conductive surface for image development and therefore makes examination of in vivo or ex-vivo biological tissue difficult (if not impossible). The fact that a vacuum chamber is also required makes SEM a more complicated instrument overall, in that it cannot be easily integrated with the sectioning subsystem of the organ mapping apparatus.

X-ray Microtomography

In X-ray microtomography in vitro and ex-vivo image acquisition with resolution in the tens of micrometers (~20 to ~200 μm) volume elements (voxels) has been achieved [Holdsworth *et al.*, 1993], [Morton *et al.*, 1990]. X-ray microtomography is very well suited for imaging bones and highly x-ray absorbing structures but it is not as effective in imaging soft-tissue. It is powerful in that it can provide both transverse sections (2D images) as well as 3-D images of the specimen. Nevertheless for in-vivo application caution should be taken due to maximum x-ray dosage requirements. X-ray microtomography is very well suited for volumetric imaging of highly x-ray absorbing tissue, with voxel size resolution in the order of tens of micrometers and in situations that x-ray dosage requirements do not pose a limit.

Magnetic Resonance Microscopy

Magnetic Resonance Microscopy (MRM) is an adaptation of the Magnetic Resonance Imaging, routinely used in hospitals, to work with smaller volumes and possibly higher density magnetic fields. MRM offers in vivo and ex-vivo imaging of soft tissue but its resolution is still low in the order of tens of micrometers (~10 to 100 μm) [Johnson *et al.*, 1992 & 1993]. MRM is a very powerful method in that it can provide 3D images of specimens without the need of mechanical scanning of any kind. It is also capable of high contrast imaging of soft tissue and since it is based on the use of high density (from ~1 to ~10 T) electromagnetic fields (that are not considered harmful), offers itself for in-vivo imaging. MRM nevertheless suffers from nonuniformity of voxel size (within the imaging

volume) and low signal-to-noise ratio when the resolution is decreased to the 10-25 μm range. MRM is capable of acquiring a volumetric image of a small organ without the need of mechanical sectioning if resolution in the order of tens of microns is adequate.

Acoustic Wave Imaging

Using very high frequency sound waves (2-10 MHz) both 2D and 3D images of biological tissue can be acquired [Quate *et al.*, 1979]. By increasing the excitation frequency to the GHz range the wavelength of the probe wave can become comparable to that of light (especially inside acoustically dense material like water). In the GHz range scanning acoustic microscopes (SAM) with micrometer resolution have been achieved (at 1.2 GHz the resolution is in the order of 1 μm) [Ermert & Harjes, 1992]. SAMs can also be used in a confocal configuration also providing depth discrimination. The initial properties of the depth response of confocal arrangements were actually studied in acoustic microscopes [Sheppard & Wilson, 1981]. At lower ultrasonic wave frequencies, acoustic microscopes can image through tissue (acquire volumetric images) to a depth better than that achieved by optical microscopes. At higher frequencies though, (where SAM resolution approached that of optical microscopes) they do not offer a significant advantage in terms of resolution, and depth discrimination. Recently optical laser sources and optical components (lenses, detectors etc.) have become cheaper and at submicron resolutions the complexity of the optical based microscope is reduced compared to that of an equivalent SAM.

Confocal Scanning Laser Microscopy

Light (and more specifically coherent light) is suitable for in-vivo and ex-vivo applications with minimal safety considerations. The probe beam power is the only parameter to be kept within safe limits (no maximum dosage requirements - like in the case of X-Ray Microtomography where X-Ray dosages are cumulative). Confocal scanning laser microscopy (CSLM) offers submicron resolution and depth discrimination that allows acquisition of 3D volumetric images [Wilson (ed.), 1989]. It is capable of producing high contrast images of soft biological tissue and has a multitude of imaging contrast modes. The confocal configuration can be used in conjunction with phase, intensity or spectroscopic configurations, thus allowing identification of different tissue properties (i.e. structure, chemical composition). In the beam or object scanning configurations (see Chapter 2 for more details) the output is already in digital form offering itself to the application of a number of powerful digital image processing techniques.

For the previously mentioned reasons confocal scanning laser microscopy was found to be the most appropriate modality as the imaging subsystem of the organ mapping system and for integration into the micro-surgical robot for in-vivo imaging.

In this thesis two separate confocal microscope arrangements will be presented: one that is designed specifically as the imaging subsystem of the organ mapping system and a second one that is suited for imaging of organs or parts of organs having quasi-spherical shape, such as the cornea. Both systems are parts of the larger system described above. Nevertheless, one is used for gathering information regarding the organ to be operated upon, while the other is a prototype to investigate the possible application of such a system while surgery is performed. It has to be clarified that although the first system can be immediately applied for organ mapping application, the second will need further improvements (in terms of speed of data acquisition and size) before it can be nicely integrated as the imaging system of the surgical microrobot.

1.7.2 Tissue Removing Subsystem

If either MRM, X-ray Microtomography, or 3D Ultrasound based imaging were used as the imaging modality for the organ mapping apparatus the whole organ would have been imaged without the need of tissue removal or sectioning. These modalities do not though offer the desirable submicron resolution. The other imaging modalities, namely SEM and CSLM offer the desirable resolution but in their case, imaging of a whole organ is not possible since the signal-to-noise ratio deteriorates significantly when imaging tissue layers deep below the organ's surface (a few hundred micrometers). This latter case requires mechanical sectioning of the tissue. A possible problem with tissue sectioning is the possibility of introducing structural distortion to the tissue. Therefore image acquisition should be performed prior to the sectioning operation or tissue removal operation. To satisfy the above considerations, an approach is developed where a layer of tissue is first imaged (in all 3 dimensions in a tile-like fashion) and then removed to expose the next tissue layer for further processing. The process is depicted in Figure 1.3 below.

The tissue removal subsystem is the second major part of the organ mapping apparatus. It should be responsible for removing the tissue layer already imaged by the imaging subsystem to allow further processing of the subsequent layer (refer to Figure 1.3 below). Possible alternatives for the tissue removal subsystem can be grouped in two types.

a) Mechanical cutting apparati and more specifically i) cryotomes, ii) microtomes or ii) high speed inertial cutting (machining) systems.

b) Laser based tissue cutting configurations (e.g. excimer laser ablation).

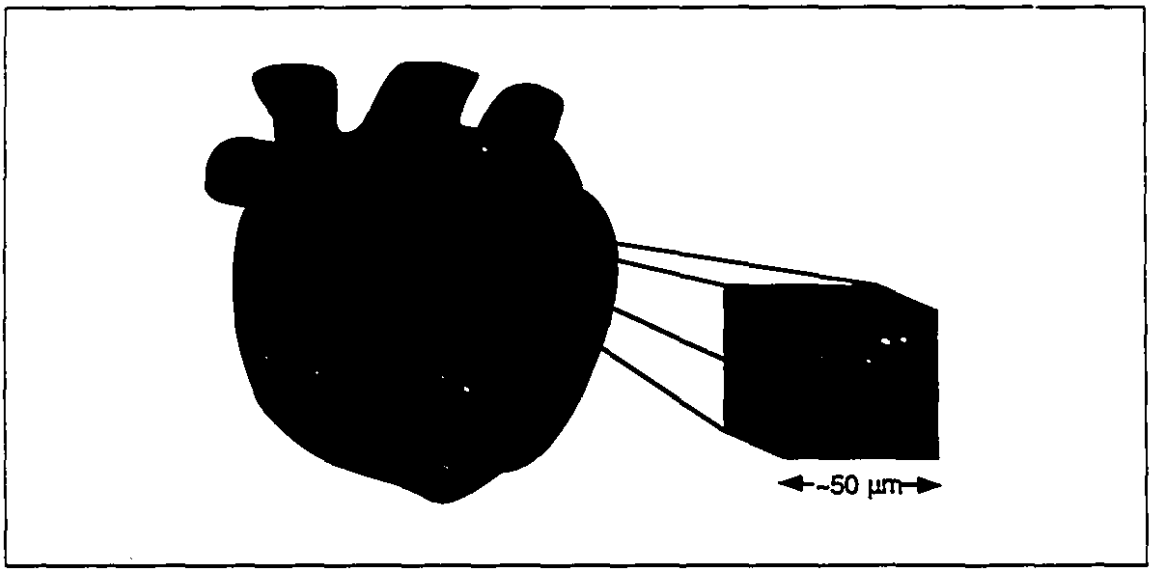

Figure 1.3 *The scanning strategy for the organ mapping system. Small 3D volumetric images are acquired using the imaging subsystem. The whole front side of the organ is scanned in a tile-like fashion. After all of the front surface is imaged a thin slice (equal to the depth of the acquired 3D images) of material is removed to expose the next layer down for further processing.*

Although the development of the machining subsystem is beyond the immediate scope of this thesis a number of considerations as well as preliminary investigations are presented in Appendix 4. It can be easily understood that the organ mapping process can produce an enormous amount of data. Note that not all acquired images are saved. Instead, for every small volumetric image, only a few parameters are saved (e.g. cell orientation, tissue density, type of tissue etc.) after the processing. Since the parameters of interest can vary for different organs, it is important that the construction of the organ mapping system be modular so that the tissue removal part can be integrated with different imaging modalities. In a second level of modularity the imaging subsystem should also be versatile enough to allow different contrast mechanisms (intensity, phase, spectroscopic, etc.) so that different tissue parameters can be investigated.

1.3 The Confocal Microscope as an MSR-1 Imaging Tool

The major advantages that make the CSLM suitable for the organ mapping apparatus, can also be utilized to perform in-vivo image acquisition during microsurgical procedures. The

requirements of such a system are different from the one built as part of the organ mapping apparatus. More specifically the system should be small and lightweight (possibly optical fiber based) so that its integration as an imaging tool for the MSR-1 is possible [Doukoglou & Hunter, 1994]. Beam or optics scanning (as opposed to object scanning) and real time image acquisition (25-30 images/s) are some other desirable characteristics.

The MSR-1 is designed with ocular microsurgical procedures as the target application. Ocular tissue imaging using a scanning optical arrangement can benefit from non-Cartesian scanning, and more specifically spherical coordinate scanning. In order to investigate non-rectilinear coordinate scanning, a system prototype, that performs scanning in spherical coordinates, was constructed. It is presented in detail in Chapter 6 of this thesis. Before such a system can be integrated into MSR-1 miniaturization is required. This entails the replacement of many bulk optics components with optical fiber based ones. A prototype that replaces some optical components and open air links with an optical fiber is also presented in Chapter 6. Future improvements of such a prototype should be the integration of the optics together with the scanning subsystem (as in [Dickensheets & Kino, 1994]) in a package similar in size with the other end-effector tools used by the MSR-1 Slave.

1.9 Thesis Outline

Chapter 1 is this introduction.

Chapter 2 is a review of the literature of the field of confocal microscopy as well as a brief historical overview of the major developments that have occurred in the field.

Chapter 3 presents a brief overview of the confocal scanning laser microscopy theory, and more specifically the theory that is necessary to understand the different configurations of the microscope prototype that is described in Chapter 4. Theoretical models describing how the various physical parameters (i.e. wavelength, numerical aperture) influence the performance of a confocal scanning laser microscope, can also be found in Chapter 3.

Chapter 4 is a description of the confocal scanning laser microscope (CSLM) that is constructed as the imaging system of an organ mapping apparatus. A description of its subsystems and its different modes of operation are presented in this chapter.

Chapter 5 includes details for a number of issues that concern proper operation of the CSLM presented in Chapter 4. In the same chapter the results of an extensive characterization performed on the CSLM subsystems are also presented.

Chapter 6 presents a spherical-coordinate scanning laser microscope system that was also constructed as part of this thesis work. This novel optical-fiber based spherical-coordinate scanning laser microscope prototype is intended for imaging of organs (or part of organs) having quasi-spherical shapes. The ultimate goal is the integration of such a system (in a miniature form) into the MSR-1 presented in Section 1.2 above.

Chapter 7 is an overview of the subjects presented in this thesis together with a summary of the original contributions. Future directions for continuation of this thesis work are also proposed.

Appendix 1 presents a brief overview of the graphical user interface software that was developed as part of the CSLM presented in Chapter 4.

Appendix 2 presents a byproduct of this thesis work consisting of a novel design for a 3D scanning direct drive system. Only one axis of a 3-axis arrangement was built. This single axis prototype is currently used to scan a mirror in a Fourier Raman spectrometer [Brenan and Hunter, 1994].

Appendix 3 consists of the code of two computer subroutines for evaluating the depth response of a CSLM using the scalar paraxial theory and the geometric optics (with Gaussian beam weighting) models presented in Chapter 3 of the thesis.

Appendix 4 presents a preliminary study investigating different tissue preservation and cutting (machining) techniques. The results can be used for the proper development of the cutting subsystem of the organ mapping apparatus.

1.10 References

Brenan, C.J.R. & Hunter, I.W. (1994), "Chemical imaging with a confocal scanning FT-Raman microscope", *Applied Optics*, **33**(31), pp. 7520-7528.

Dickensheets, D. & Kino, G.S. (1994), "A scanned optical fiber confocal microscope," in *Proceedings SPIE* **2184** Three-dimensional microscopy, pp. 39-47.

Doukoglou, T.D., Hunter, I.W., Brenan, C.J.H. (1992), "Confocal Scanning Laser Microscopy for Muscle Fiber Orientation Studies," *Proceedings of the Canadian Medical and Biological Engineering Conference*, **18**, pp. 106-107.

Doukoglou, T.D., Hunter, I.W. (1994), "Confocal imaging arrangement as accessories of a micro-surgical robot system," *Proceedings IRIS-Precarn IV Conf.*, pp. 174-175.

Ermert, H. & Harjes, H.-P. (eds) (1992), *Acoustical Imaging*, **19**, Plenum Press, New York.

Johnson, A.G., Hedlund, L.W., Cofer, G.P. & Suddarth, S.A. (1992), "Magnetic Resonance Microscopy in the Life Sciences," *Reviews of Magnetic Resonance in Medicine*, **4**, pp. 187-219.

Johnson, A.G., Benveniste, H., Black, R.D., Hedlund, L.W., Maronpot, R.R. & Smith, B.R. (1993), "Histology by magnetic resonance microscopy," *Magnetic Resonance Quarterly*, **9**(1), pp. 1-30.

Jones, L.A. & Hunter, I.W. (1990), "Influence of mechanical propertied of a manipulandum on human operator dynamics. 1.Elastic stiffness," *Biological Cybernetics*, **62**, pp. 299-307.

Jones, L.A. & Hunter, I.W. (1993), "Influence of mechanical propertied of a manipulandum on human operator dynamics. II. Viscosity," Biological *Cybernetics*, **69**, pp. 295-303.

Holdsworth, D.W., Drangova, M. & Fenster, A. (1993), "A high resolution XRII-based quantitative volume CT scanner," *Medical Physics*, **20**(2), pp. 449-562.

Hunter, I.W., Doukoglou, T.D., Lafontaine, S.R., Charette P.G., Jones, L.A., Sagar, M.A., Mallinson, G.D. & Hunter, P.J. (1993), "A Teleoperated Microsurgical Robot and Associated Virtual Environment for Eye Surgery," *PRESENCE*, **2**(4), pp. 265-280.

Hunter, I.W., Jones, L.A., Doukoglou, T.D., Lafontaine, S., Hunter P.J. & Sagar, M. (1994), "Ophthalmic microsurgical robot and surgical simulator," *Proceedings SPIE*, **2531**: Telemanipulator and Telepresence Technologies, pp. 184-190.

Hunter, I.W., Lafontaine, S., Nielsen, P.M.F., Hunter, P.J. & Hollerbach, J.M. (1990), "Manipulation and dynamic mechanical testing of microscopic objects using a tele-micro-robot system," *IEEE Control Systems Magazine*, **10**, pp. 3-9.

Hunter, I.W., Lafontaine, S., Doukoglou, T.D., Jones, L.A., Korenberg, M.J., Nielsen, P.M.F., Kirsch, R.F. & Kearney, R.E. (1991), "Micro-robotics and the study of muscle: special problems in control, system identification and modeling," *IFAC Symposium on Identification and System Parameter Estimation*, pp. 197-202.

Goldstein, J.I., Newbury, D.E., Echlin, P., Joy, D.C., Roming Jr., A.D., Lyman, C.E., Fiori, C. & Lifshin, E. (1992), *Scanning electron microscopy and X-ray microanalysis : a text for biologists, materials scientists, and geologists*, Plenum Press, New York.

Morton, E.J., Webb, S, Bateman, J.E., Clarke, L.J. & Shelton, C.G. (1990), "Three-dimensional x-ray microtomography for medical and biological applications," *Physics in Medicine and Biolology*, **35**, pp.805-820. (in Health Sciences-Journals)

Quate, C.F., Atalar, A. & Wickramasinghe, H.K. (1979), "Acoustic microscopy with mechanical scanning - A review," *Proceedings IEEE*, **67**, pp. 1092-1114.

Sheppard, C.J.R., & Wilson, T. (1981), "Effects of high angles of convergence in V(z) in the scanning acoustic microscope," *Applied Physics Letters*, **38** (11), pp. 858-859.

CHAPTER 2

Literature Review

2.1 Preface

In this chapter an overview of the work done today in the field of confocal microscopy is presented. A brief historical overview regarding the development of the confocal microscope is followed by an extensive literature review of the various forms of confocal microscopy configurations. Finally a list of the fields and applications that confocal microscopy has been applied to is included at the end of the chapter.

2.2 History

The principle behind confocal microscopy was first described by Lukosz [Lukoz, 1966] and states that the resolution of an imaging system can be increased at the expense of field of view. Even though the idea of confocal detection has been around since the last century [Masters, 1992], many researchers erroneously consider the microscope described in the patent by Minsky [Minsky, 1961] as the first confocal microscope. In Minsky's patent a condenser lens focused the microscope's light source onto the sample. The objective lens of the microscope was also focused on the same area of the sample. Since both condenser and objective lenses shared the same focal spot the microscope was termed confocal. In a recent paper Minsky recalls the development of his confocal microscope [Minsky, 1988]. Marvin Minsky had a great insight into the several advantages of the confocal arrangement and he pointed them out in his patent:

- Reduced blurring of image from light scattering;
- Increased effective resolution;
- Improved signal-to-noise ratio;
- Permits unusually clear examination of thick and light scattering objects;

- x-y scans that can be made over a wide area of the specimen;
- Inclusion of z- scans is possible;
- The magnification can be adjusted electronically;
- Especially well suited for making quantitative studies of the specimen;
- Essentially an infinite number of aperture planes are available for modulating the aperture with dark field stops, annuli phase plates, etc.;
- Complex contrast effects can be provided with comparatively simple equipment;
- Less complex objective lenses can be used, including those for long working distance, UV or infrared imaging, since they need to be corrected only for a single axial point;

Since the confocal arrangement limits the field of view (in exchange for improved resolution) the field of view has to be recovered by scanning. Minsky suggested a specimen scanning approach where the specimen was scanned in a raster-like fashion through a point of light. The reflected (or transmitted) light is then detected through an exit pinhole.

Minsky's invention did not earn much acclaim at the time. He continued research in different fields, and is currently known as the father of artificial intelligence. In the years following his patent, more confocal microscopes started appearing and it is still not clear whether they were influenced by Minsky's early work or they were developed independently.

Many of the first confocal scanning microscopes employed a Nipkow type disk [Egger & Petran, 1967] containing a large number of small holes (pinholes) arranged in Archimedian spiral patterns to selectively illuminate sample points and to detect light only from these points. Nipkow used such a disk as early as 1884 to convert two-dimensional (2D) images into a time varying electrical signal to be transmitted as a time-varying one-dimensional signal over a cable. On the spinning disk the pinholes were located in optically conjugate (symmetrical with respect to the disk's center) source/detector points, and their mutual dependence for image formation led to the naming of these first microscopes as Tandem Scanning Confocal Microscopes (TSCM). More recently, Kino and Xiao developed a spinning disk (they name it real time) confocal microscope that utilizes the same side of the disk for illumination and detection [Kino *et al.* , 1988], [Kino, 1989], [Kino & Xiao, 1990] and [Xiao & Kino, 1987], [Xiao *et al.*, 1988]. This configuration has the advantage that it does not need alignment of conjugate

pinholes. Nevertheless light reflected off the surface of the spinning disk may increase background noise and decrease resolution when viewing some low contrast biological samples.

Most Nipkow type confocal microscopes use polychromatic (white) light sources, in contrast to object or beam scanning confocal microscopes that employ a laser as the light source. In a laser confocal microscope a point source (diffraction limited spot) is used for illumination. The source is focused inside the sample volume and the reflected (or transmitted) light is focused onto a point detector. The result is a dramatic reduction of out-of-focus scattered light and improved resolution both in the lateral (x-y) plane, as well as in the axial (z or optical axis) direction. The theory describing the principles of confocal microscopy was more rigorously developed in the late 1970s and 1980s [Sheppard & Choudhury, 1977], [Sheppard & Wilson, 1981], [Hamed & Clair, 1983], [Wilson & Sheppard, 1984], [Wilson, 1985], [Kimura & Munakata, 1989], [Drazic, 1992]. It is now widely accepted that the confocal microscopes be classified into two types: Type-1 and Type-2. Type 1 imaging is incoherent or partially coherent, while Type 2 is coherent. The main difference between the two types is the size of the detector. Type-2 employs a point detector and offers superior lateral resolution and depth discrimination than Type-1, which employs a large area detector and has lateral resolution equivalent to that of a conventional microscope. Type-1 confocal microscopes still exhibit depth discrimination but to a lesser degree than Type-2 ones.

2.3 Implementation Specifics

In designing and building a confocal scanning laser microscope a number of considerations should be taken into account. These have to do with the problem of image formation, illumination methods (transmission or reflection - referred to also as epi-illumination) and contrast mechanisms (i.e. intensity, phase, polarization or wavelength contrast). Next, the different techniques employed in design and construction of different confocal microscopy systems are presented.

2.3.1 Scanning Arrangements.

Image formation in a confocal microscope involves a scanning arrangement that illuminates and detects the (reflected or transmitted) light from only one point of the object at a time. Therefore one of the ways that confocal microscope arrangements can be

categorized is based on the scanning system they employ to form the object's image onto the detector (or eyepieces for those allowing direct viewing).

2.3.1a Tandem Scanning or Spinning Nipkow Disk Arrangement.

Tandem scanning is the method originally used by Egger & Petran [1967], and is the one that allows real time imaging and direct viewing though eyepieces. The direct viewing and real time imaging capability are what makes this configuration the most popular for biological studies and more specifically in vivo ones. Using this type of arrangement, real time stereoscopic image pairs ([Boyde, 1985], [Boyde, 1987] [Maly & Boyde, 1994]) of the sample under observation can be acquired. The main drawback of such systems is light efficiency; only about 1-2% of the source light reaches the detector.

2.3.1b Beam Scanning

With the use of rotating [Stelzer, 1989] [Carlsson, 1990] or vibrating mirrors or a rotating-polygon mirror [Webb & Hudges, 1981], [Webb *et al.*, 1987] & [Merkle *et al.*], the source beam can be scanned over the stationary specimen through the objective lens. The major advantage of these techniques is small scanning times (usually 2-3 s/2D image). The major drawback is complex optical design since off-axis lens aberrations must be minimized and corrections are required for the off-axis light transmission reduction. These requirements generally complicate the lens design. Most commercial systems use this type of scanning arrangement. In most beam scanning systems the object (or the objective) is scanned along the z (optical) axis for acquiring image slices at different depths [Dixon, *et al.*, 1991]. Beam scanning is generally faster than the object (stage) scanning (described next) but it does not usually offer real time imaging that is highly desirable for observation of dynamic phenomena. The only beam scanning arrangements that perform true real-time microscopy are the ones using acousto-optic beam deflectors [Goldstein *et al.*, 1989] or a combination of an acousto-optic deflector for scanning the fast axis and a rotating mirror for the slow axis [Draaijer & Houpt, 1987 & 1988].

2.3.1c Object(Stage) Scanning

Scanning the object in a raster-like fashion in front of the illumination beam foci was the arrangement proposed originally by Minsky in his patent and the one employed in some of the first confocal laser scanning microscopes[Brakenhoff *et al.*, 1979], [Sheppard and Wilson, 1980]. The main advantage of the object scanning over the beam scanning

arrangement is that the light path is always along the optical axis of the objective lens, thus reducing the off-axis optical aberrations. Object scanning also allows the acquisition of variable magnification images without the need for changing the objective lens. Additionally, since only the middle of the objective is used for image acquisition the point-spread function (psf) of the microscope is stationary over the image field. This allows for application of linear deconvolution techniques for image restoration and enhancement [Bertero *et al.*, 1989 & 1990], [Doukoglou *et al.*, 1987]. Beyond the disadvantage of longer scanning times (usually more than 10 s/2D image), object scanning can produce some unwanted motion artifacts to certain biological preparations (i.e. in solution).

2.3.1d Optics Scanning

Optics scanning arrangements require the scanning of the objective lens in front of the point source, thus translating the illumination point at the sample space. The first optics-only scanning microscope is described in [Davidovits & Egger, 1969]. Recently a complete optics scanning microscope based on compact disk technology has been presented in [Benschop *et al.*, 1989] and [Benschop & Van Rosmalen, 1991].

In practice, most microscopes usually use a hybrid scanning arrangement. An example (frequently employed) is a beam scanning arrangement in the x-y plane and an object scanning arrangement along the z-axis. Another combination is scanning of the object in the x-y plane and scanning of the objective lens along the z (optical) axis.

2.3.2 Illumination Methods

The illumination and detection optics can both be located at the same side with respect to the specimen or on opposite sides. Therefore confocal microscopes are divided into a) reflection mode types when the illumination and detection optics are located at the same side of the object and b) transmission mode varieties where the illumination and detection are on either side of the object. Certain microscope designs allow for operation both in reflection and in transmission (i.e. [Dixon *et al.*, 1991]).

2.3.2a Reflection (Epi-illumination)

In reflection-mode confocal microscopes, the same lens serves both as an objective and as a collector. Source and detector are both located on the same side of the sample under observation. The advantage of this configuration is simpler optical design and easier

alignment, at the expense of reduced light efficiency in the case of weakly reflecting (scattering) objects. This arrangement is the one used for observation of opaque objects and the one employed in most non-biological applications (i.e. silicon chip metrology, inspection and profilometry).

2.3.3b Transmission

Transmission-type microscopes have the objective and collector lenses located on opposite sides of the sample. The image is formed by detecting the source light after it has passed though the specimen. Confocal microscopes operating in transmission are more difficult to align but they offer a higher light throughput (especially with transparent or semi-transparent objects). They cannot be used with opaque objects and their main use is in the studies of biological tissue[Brakenhoff *et al.*, 1979], [van der Voort *et al.*, 1985], [Hunter *et al.*, 1990]. Such arrangements also offer greater versatility in the use of different aperture shape combinations (i.e. circular, rectangular, annular) on the illumination and detection side.

2.3.3 Contrast Mechanisms

In any imaging system increased resolution is desirable but also a suitable contrast mechanism is essential for detection of the structures of interest. Image formation in a microscope involves the measurement of the spatial distribution of quantities such as intensity, phase and polarization of the reflected (or transmitted) light. These quantities can be associated with such sample properties as reflectivity, optical density, refractive index changes or even structural (geometric) changes. Different forms of microscopy arrangements allow the detection of some or most of these parameters. In general these quantities can be measured either as:

a) Absolute values, with respect to the value of the equivalent parameter in the probe beam.

b) Relative changes, where the measurement is the differential of the given parameter at each image point along a predetermined spatial direction.

More specifically, a specimen modulated probe beam can be described by its amplitude (U) phase(φ) and polarization orientation (P), and spectral distribution. Different contrast mechanisms arise depending on which parameter the photodetector output (D) is a function of.

The purpose of contrast mechanisms is to increase visibility (in the acquired image) or even allow detection of certain characteristics of an object under observation. Selection of the proper contrast mechanism will depend on the type of studies or measurements that must be performed on the object. A-priori knowledge of the object structure and how it will affect the parameters of the probe beam is also necessary. Therefore if an object property is expected to alter the polarization of the probe beam rather than its amplitude or phase a polarization contrast mechanism would be more suitable for imaging this object. The most versatile confocal scanning laser microscopes offer more than one contrast mode. Brakenhoff, for example, described a system that is capable of intensity, interference contrast, differential contrast (amplitude and phase) and finally fluorescence imaging modes [Brakenhoff, 1979]. Next the contrast mechanisms offered on different confocal microscopy apparati are outlined.

2.3.3a Intensity Contrast

In microscopy, intensity contrast arises from the different ways that the various volume elements (voxels) of the specimen interact with the source illumination. The interaction mechanisms include absorption, scattering, refraction, reflection and fluorescence. The combined contribution of all these mechanisms gives rise to the intensity contrast image. More specifically, intensity contrast imaging results when the photodetector output is proportional to the amplitude squared of the specimen modulated probe beam ($D \propto f(U^2)$). This imaging mode is the one that most (if not all) confocal microscopes offer. By measuring other properties of the reflected (or transmitted) light, such as phase and polarization, the contrast modes mentioned next arise.

2.3.3b Fluorescence Microscopy

This is perhaps the second most frequently used imaging mode in confocal microscopy. A lot of work has been done in acquiring high contrast fluorescent images with simultaneous reduction of the image flare. In studies of biological tissue, fluorophores may be introduced into the specimen. These agents (fluorescent dyes) selectively adhere to certain structures of the specimen that are to be imaged. By exciting the fluorophore structures, light at a wavelength different from the excitation wavelength is emitted from the specimen. By detecting the fluorescent wavelength an image of the structures of interest can be acquired [Stelzer & Wijnaendts var Resandt, 1990]. Parameters of interest are primarily the spatial distribution of the fluorescing dye and the intensity of fluorescence, although other parameters can also be observed (depolarization, intensity

ratios, etc.). Flare from neighboring structures is one of the major problems when fluorescent imaging is performed with conventional microscopes. Using a confocal microscope the image flare is drastically reduced and true 3D volumetric images of the specimen can be acquired at the same time.

2.3.3c Differential Amplitude Contrast

By measuring relative light amplitude changes (from two sample regions very close together) a differential amplitude image is formed. More specifically differential amplitude contrast (DAC) imaging results when the photodetector output is proportional to the derivative of the specimen modulated probe beam amplitude ($D \propto \frac{dU}{dx}$), along a predetermined lateral coordinate. DAC imaging is a simple and efficient method for producing edge-enhanced images [Hamilton & Wilson, 1984a]. Using a large area split or quadrature detector, differential amplitude and phase contrast images can be acquired through a two-mode optical fiber by properly adjusting the phase delay between the two fiber modes [Wilson *et al.*, 1994][Juskaitis and Wilson, 1992a, b]. When amplitude differentiation is performed not on the image plane but along the optical axis ($D \propto \frac{dU}{dz}$ where z is the microscope's optical axis), very accurate measurement of the distance between the lens and sample can be done [Corle *et al.*, 1987]. Longitudinal DAC imaging can therefore be utilized for very high accuracy (0.01 nm) profilometry.

2.3.3d Phase Contrast

By measuring the phase changes of the source light after it has interacted with the specimen, phase contrast images are acquired. In phase contrast imaging the photodetector output is proportional to the phase ($D \propto f(\varphi)$) of the beam reflected (or transmitted) from the sample. This contrast mode is important for weakly scattering specimens, something not so uncommon for biological preparations. The Zernike phase contrast technique is the one most frequently employed in microscopy. In this method the 0^{th} order (DC) frequency of the Fourier spectrum of the image is phase retarded by $\pi/2$ so that the detected image represents phase variation as intensity. Kimura describes such a confocal arrangement in his U.S. patent [Kimura, 1993]. Also, by integration of differential phase contrast images, absolute phase images can be obtained [Hamilton & Wilson, 1984b]. By using a novel electro-optic phase modulator, Kino and his colleagues implemented a close equivalent to the Zernike phase contrast mechanism in a confocal microscope arrangement [Kino *et al.*, 1988a, b].

2.3.3e Differential Phase Contrast

Phase variations (of the probe beam modulated by the sample) can be measured with respect to a reference mean phase value, or as relative changes within a sample's voxel. In the later case differential phase contrast (DPC) imaging results [Atkinson & Dixon, 1994], [Atkinson *et al.*, 1992], [Hamilton & Sheppard, 1984]. In DPC the photodetector output is a function of the phase differential ($D \propto \frac{d\varphi}{dx}$) along a spatial coordinate. A split detector arrangement for DPC imaging was originally proposed for Scanning Electron microscopy by Dekkers & deLang [Dekkers & deLang, 1974]. In scanning optical microscopy, DPC is used either for very accurate surface profilometry or acquisition of images with significant edge enhancement. Benschop [1988] reports a comparison of conventional with confocal differential phase contrast imaging, and gives applications to silicon wafer profilometry. Hamilton & Sheppard [1984] compared differential phase contrast with the Nomarski differential technique (mentioned in the next section). They found that using a split detector results in pure differential phase imaging. On the other hand, the Nomarski method is a complex mixture of a number of contrast mechanisms (phase and interference), whose relative strength can be varied by adjusting the compensator.

Simultaneous detection of differential phase and amplitude images can also be performed through a two-mode optical fiber by adjusting the phase difference between the two fiber modes and the use of a quadrature detector [Juskaitis and Wilson, 1992a][Wilson *et al.*, 1994].

2.3.3f Interference & Differential Interference Contrast

Interferometric arrangements are the most complex ones but they offer a significant increase in sensitivity and contrast. By using multiple detectors or by controlling the phase, amplitude (and even polarization) of the reference beam, both intensity and absolute phase contrast images can be obtained with an interferometric arrangement. Apart from the widely-used Nomarski differential interference technique that uses a Nomarski-modified Wollaston prism [Corle & Kino, 1990], a number of other interferometric arrangements of the Michelson type (reflection) [Hamilton and Sheppard, 1982] or Mach-Zehnder type (transmission) [Brakenhoff, 1979] have been employed in different confocal scanning microscopes. In [Hunter *et al*, 1988] a confocal interference

microscope that can selectively be used in a Michelson as well as in a Mach-Zehnder configuration is presented.

An equivalent to the Nomarski differential interference technique, which uses an electro-optical Bragg cell and heterodyne detection is described by Jungerman *et al.* [1984]. The interferometric arrangements can also be classified as homodyne [Stelzer et al, 1986] or heterodyne [Offside & Somekh, 1992]; the difference being that in the heterodyne systems the reference beam is frequency shifted (using an acousto-optic modulator), and the interference signal is detected at the difference frequency between the reference and sample probe beams. The advantage of this AC detection is the very good separation of the interference with the non-interference signals. Differential heterodyne interference systems are also described by Holmes & Somekh, [1994] and Laeri & Strand, [1987] and are used for sub-nm resolution profilometry and surface characterization. An overview of the different interferometric systems appearing in the confocal microscopy literature, together with the field in which they have been applied, is given in Table 2.1.

	Homodyne	Heterodyne
Michelson	[Hamilton & Sheppard, 1982] profilometry [Hamilton & Mathews, 1985] profilometry [Mathews *et al.*, 1986] profilometry [Davidson *et al.*, 1987] [Hunter *et al*, 1988] biological studies [Tychinsky *et al.*, 1989], profilometry [Doukoglou, *et al.*, 1992], biological	[Offside & Somekh, 1992] surface characterization. [Jungerman *et al.*, 1984] profilom. [Holmes & Somekh, 1994] differential interference.
Mach-Zehnder	[Hunter *et al*, 1988] biological studies [Stelzer *et al.*, 1986] biological [Brakenhoff, 1979] biological	[Sawatari, 1973]

Table 2.1. *Different interferometric confocal microscope apparatuses grouped with respect to their optical configuration.*

2.3.3g Polarization Contrast

By illuminating the sample with light of different polarizations and measuring the polarization of the detected light, an image of the sample's polarization anisotropy can be

obtained. Such images might contain information regarding different molecular organizations in the sample. Polarization contrast is not a very common imaging mode. In [Juang *et al.*, 1988] a very sensitive differential polarization scanning microscope is presented. Hunter *et al.* [1988] presents a microscope where the source polarization angle could be controlled and in conjunction with orthogonal polarization resolving detectors polarization contrast images could be acquired. Finally in [Kimura & Wilson, 1994] a dark field confocal scanning polarization microscope, which detects the edge diffracted waves whose polarization differs from that of the incident beam, is described.

2.3.3h Spectroscopic Configurations

Most of the previously-mentioned systems measure properties of photons that have been elastically scattered off the sample (Rayleigh photons).There are photons, though, which interact with the sample's molecules and exchange energy. By detecting these photons and measuring their properties, an absorption spectrum [Sasaki *et al.*, 1992] or even a Raman spectrum for each sample point can be obtained. A complete Fourier Transform Raman confocal microscope system is described in [Brenan & Hunter, 1994].

2.3.4 Aperture Shape (Pinhole vs. Slit).

The improved resolution and the depth discrimination property of the confocal arrangement is due to the aperture placed in front of the light detector. Although most systems use circular pinholes as the detector aperture, a number of confocal scanning arrangements use narrow slits [Sheppard & Mao, 1988], [Koester *et al.*, 1993], [Maurice, 1973] in order to increase light efficiency and reduce scanning time. In such systems the point detector is replaced by a detector array, and cylindrical-type lenses are used in the place of the more common circular aperture ones.

2.4 Conventional Bulk Optics vs. Optical Fiber Based

Recently, a new class of confocal scanning microscopes has been reported where bulk optical components are being replaced by optical fiber based ones. Since there is an increasing trend towards fiber-based, smaller and integrated confocal microscopes, some of the work done in this field is mentioned next.

The simpler of the optical fiber-based confocal scanning microscopes are the ones which use optical fiber to replace some open air links. In fiber-based optical arrangements it is possible to scan the optical fiber end (used both for illumination and detection) in all

three axes [Dabbs & Glass, 1992] in front of a stationary objective lens. This is equivalent to the optics-scanning arrangements mentioned before. By scanning the fiber end, the inertia of the moving parts is minimized, but the fiber end is scanned a distance proportionally greater than the field of view on the sample, depending on the demagnification of the lens. When the objective lens is scanned, the scanning distance equals that of the required field of view, but a relatively more massive objective lens has to be moved around. Both of the above techniques place severe requirements on the off-axis performance of the objective lens. Therefore, one very recently developed prototype [Sheard *et al.*, 1993] integrates the optics in a thin film optical waveguide with fiber connections for illumination and detection. Dickensheets & Kino, [1994] report an optical fiber-based confocal microscope which integrates both an electrostatic scanning mechanism and the objective lens, in a package approximately 1 mm in diameter. In Chapter 6 of this thesis, a novel optical fiber based, spherical coordinate scanning, confocal laser microscope prototype is presented.

Fiber-based microscopes [Shigeharu & Wilson, 1991], [Kimura & Wilson, 1991], [Delaney *et al.*, 1994], [Gu & Sheppard, 1993], [Juskaitis *et al.*, 1993], [Wilson, 1993] offer a number of advantages over conventional ones:

- The detection system can be remotely located from the light source and the object.
- The fiber core can serve as the source and detector pinhole, minimizing alignment requirements.
- The number of optical components and their mass can be drastically reduced since there are fiber-based components that can replace many bulk optics ones.
- With miniaturization and integration of the objective lens with the fiber, use of confocal scanning setups in endoscopic applications is now feasible.

2.5 Image Processing

For most confocal scanning microscope systems, the acquired images are already in digital form. Powerful digital image processing and enhancement techniques are thus immediately applicable. Histogram equalization, median filtering and contrast enhancement are some of the methods applied to the images. To further improve the images various techniques which deconvolve the influence of the optical system from the acquired images can be employed. Wiener filtering for image restoration [Bertero *et al.*, 1989 & 1990], deconvolution using correlation functions [Doukoglou *et al.*, 1988], constrained iterative deconvolution [Agard *et al.*, 1989], 3D inverse filtering [Erhardt, *et*

al., 1985] and iterative reconstruction [Conchello & Hansen, 1989] are some of the methods used.

The significant advantage of the confocal arrangement is its capability of acquiring true 3D images. The 3D image can be reconstructed from a series of 2D images taken either along the optical axis of the microscope (x-y sectioning) or along one of the image axes (x-z or y-z sectioning).

There are numerous methods to extract the desired (or useful) information from these 3D images and present it to the viewer in a meaningful way. Many of the methods are problem oriented (i.e. extraction of fiber-like structures from 3D cell images [Vepsalinen, 1990]) but a few are more general. 3D reconstruction by tessellation [Schormann & Jovin., 1990], data reduction by employing vector representation to describe the 3D neuron morphology [Forgren, 1987], [Wallen *et al.*, 1988], and solid modeling of chromosomes [Jones *et al.*, 1990] are a few of the techniques applied to confocal 3D data sets.

Final visualization of the 3D data can be done by segmentation and then volume rendering [Carlsson *et al.*, 1985], [Masters & Paddock, 1990] or ray-tracing techniques [Montag *et al.*, 1990]. Lately, commercial software packages such as VoxelView®* VoxBlast®** and ImageVolumes®*** are available for performing automated volume rendering and 3D visualization.

More recently, with computer memory becoming cheaper and CPU performance increasing rapidly, 4D images (3D images that change dynamically in time) from confocal microscopes have been reported [Inoué, 1989a,b].

2.6 Advantages of Confocal Scanning Microscopy

From the literature on confocal microscopy the following can be summarized to be the main advantages of confocal scanning microscopy over conventional microscopy that complement the list given by Minsky in his patent.

- Lateral resolution superior to that of conventional microscopy.

* VoxelView is a registred trade mark of the Vital Images Inc., Fairfield, IA.
** VoxBlast is a registered trademark of Vaytek Inc.
*** ImageVolume is a registered trademark of Minnesota Datametrics, St. Paul, MN.

- Optical sectioning or depth discrimination property with rejection of out-of-focus information, allowing for true 3D image acquisition.
- Variable magnification without the need to change objectives (object scanning arrangements).
- Fluorescence imaging with greatly reduced image fogging.
- Minimal spherical and off-axis aberrations (object scanning type).
- Insignificant chromatic aberration when laser is used as a source.
- Very high dynamic range in the detectors and consequently in the acquired images.
- For most system images are already in digital form, allowing immediate application of powerful digital image processing techniques.

2.7 Applications of Confocal Scanning Microscopy

Confocal scanning microscope arrangements have been employed in a multitude of fields, some of which are listed next. For some of the applications references will be given. The following list is not intended to be exhaustive but merely a good indication of the various fields in which confocal scanning microscopy has been and is being used successfully. Nevertheless, as more people find out about the capabilities of this new form of microscopy, the more it is being applied in diverse areas of research. Just to give the reader an idea of this trend, on March 1994 and for a period of one year before that, a quick search gave us more than 1,000 references dealing with applications of confocal microscopy.

2.7a Biological Applications

The whole issue of *Scanning* **16**(3), 1994 is devoted to biological applications of confocal microscopy. The most common biological applications of confocal microscopy are listed next. For some applications related references are given. These are not the only ones but are merely given as examples.

- Non-invasive serial optical sectioning of excised blocks of tissue (mentioned also as microtomoscopy) [Stelzer & Wijnaendts van Resandt, 1987]
- In vivo imaging of intact tissue [Webb & Hughes, 1981]
- Fluorescence imaging without image flare [Wijnaendts van Resandt *et al.*, 1985].
- Imaging of cytoskeletons [Wallen *et al.*, 1988].
- Localization of immunofluorescently labeled proteins in cell cultures

- Chromosome microscopy [Jones *et al.*, 1990].
- x-z sectioning of cellular structures
- 3-D and 4-D (time evolving 3D imaging) image reconstruction of biological tissue.

2.7b Semiconductor, and Integrated Circuit Related

A number of SPIE conferences were devoted to this field, and the proceedings (e.g. **565** Micron and Submicron Integrated Circuit Metrology, **921** Integrated Circuit Metrology, Inspection and Control, **749** Metrology: Figure and Finish) of these conferences offer a wealth of information regarding the various applications of confocal scanning microscopy to semiconductor circuit metrology and inspection.

- Imaging of passive defects and quality control
- High resolution and high contrast imaging of circuit topography
- In-process critical dimension measurements [Stallard & Bukhman, 1987], [Zarf & Wijnaendts van Resandt, 1988]
- Imaging of residual photoresist [Bennett *et al.*, 1988].
- Imaging of active defects (using optical beam induced current imaging) [Awamura *et al.*, 1988].
- Line width (trace) measurements and consistency, [Wijnaendts van Resandt *et al.*, 1988].

2.7c Material Science Applications

- Surface roughness measurements [Offside & Somekh, 1992]
- Profilometry [Fieguth & Staelin, 1994].
- Material defects characterization [Wolf, 1988]
- Surface coating imaging and thickness measurements.
- Non-invasive imaging of material (no staining or coating needed as in electron beam microscopy) [Krug *et al.*, 1993].

2.8 Overview

In this chapter an extensive literature review summarizing the development of the confocal microscope, and the different types of scanning confocal microscopes developed to date was presented. In addition to this literature review an extensive "*Bibliography on*

Confocal Microscopy and Its Applications" was compiled by Prof. Alan Boyde and it appears in Scanning, vol. 13, pages 33-56, 1994. A smaller bibliography appears in the end of the book "*Textbook of Biological Confocal Microscopy*," edited by Prof. James B. Pawley (Plenum Press, New York, 1989) and compiled by Prof. R.H. Webb. A rigorous theoretical description of the theory governing scanning confocal microscopy is presented in the book by Profs Colin Sheppard and Tony Wilson, "*Theory and Practice of Scanning Optical Microscopy*," (Academic Press, London, 1984). More recent developments in the field of confocal microscopy are presented in the book edited by Prof. Tony Wilson, "*Confocal Microscopy*," (Academic Press, London, 1991). At the end of this thesis there is a bibliography section containing a list of other publications that have not been referred to in this chapter and are related to the field of confocal microscopy. A great number of articles dealing with the theoretical aspects of confocal microscopy can be found there.

2.9 References

Agard, D.A., Hiraoka, Y. & Sedat, J.W. (1989), "Three-dimensional microscopy: image processing for high resolution subcellular imaging," *Proceedings SPIE*, **1161** New Methods in Microscopy and Low Light Imaging, pp. 24-30.

Atkinson, M.R., Dixon, A.E. & Damaskinos, S. (1992), "Surface-profile reconstruction using reflection differential phase-contrast microscopy," *Applied Optics*, **31** (31), pp. 6765-6771.

Atkinson, M.R. & Dixon, A.E. (1994), "Single-pinhole confocal differential phase contrast microscopy," *Applied Optics*, **33**(4), pp. 641-653.

Awamura, D., Ode, T. & Yonezawa, M. (1988), "Scanning color laser microscope," *Proceedings SPIE*, **921** Integrated Circuit Metrology, Inspection and Process Control, pp. 388-394.

Bennett, S.D., Peltzer, E.A. & Smith, I.R. (1988), "Ultraviolet confocal metrology," *Proceedings SPIE*, **897** Scanning Microscopy Technology and Applications, pp. 75-82.

Benschop, J.P.H. (1988), "Phase detection using scanning optical microscopy," *Proceedings SPIE*, **921** Integrated Circuit Metrology, Inspection and Process Control, pp. 123-130.

Benschop, J.P.H., Ossekeppele, M. & van Rosmalen, G. (1989), "Miniature scanning optical microscope based on compact disk technology," *Proceedings SPIE*, **1139** Optical Storage and Scanning Technology, pp. 110-116.

Benschop, J.P.H. & van Rosmalen, G. (1991), "Confocal compact scanning optical microscope based on compact disc technology," *Applied Optics*, **30** (10), pp. 1179-1184.

Bertero, M., Boccacci, P., Brakenhoff, G.J., Malfanti, F. & van der Voort, H.T.M. (1989), "Three-dimensional image restoration in fluorescence confocal microscopy," *Proceedings SPIE*, **1139** Optical Storage and Scanning Technology, pp. 86-91.

Boyde, A. (1985), "Stereoscopic images in confocal (Tandem scanning) microscopy," *Science*, **230** (Dec. 13), pp. 1270-1272.

Boyde, A. (1987), "Colour-coded stereo images from tandem scanning reflected light microscope (TSRLM)," *Journal of Microscopy*, **146** (2), pp. 137-142.

Brakenhoff, G.J., Blom, P. & Barents, P. (1979), "Confocal scanning light microscopy with high aperture immersion lenses," *Journal of Microscopy*, **117** (2), pp. 219-232.

Brakenhoff, G.J. (1979), "Imaging modes in confocal scanning light microscopy," *Journal of Microscopy*, **117** (2), pp. 233-242.

Brenan, C.J.H. & Hunter, I.W. (1994), "Chemical imaging with a confocal scanning Fourier-transform-Raman microscope," *Applied Optics.*, **33**(31), pp. 7520-7528.

Carlsson, K., Danielsson, P.F., Lenz, R., Liljeborg, A., Majlof, L. & Aslund, A. (1985), "Three-dimensional microscopy using a confocal laser scanning microscope," *Optics Letters*, **10** (2), pp. 53-55.

Carlsson, K. (1990), "Scanning and detection techniques used in confocal scanning laser microscope," *Journal of Microscopy*, **157** (1), pp. 21-27.

Conchello, J.-A. & Hansen, E.W. (1989), "Three-dimensional reconstruction of noisy confocal scanning microscopy images," *Proceedings SPIE*, **1161** New Methods in Microscopy and Low Light Imaging, pp. 279-285.

Corle, T.R., Fanton, J.F. & Kino, G.S. (1987), "Distance measurements by differential confocal optical ranging," *Applied Optics*, **26**(12), pp. 2416-2420.

Corle, T.R. & Kino, G.S. (1990), "Differential interference contrast imaging on a real time confocal scanning optical microscope," *Applied Optics*, **29**(26), pp. 3769-3774.

Dabbs, T. & Glass, M. (1992), "Fiber-optic confocal microscope: FOCON," *Applied Optics*, **31** (16), pp. 3030-3035.

Davidson, M., Kaufman, K., Mazor, I. & Cohen, F. (1987), "An application of interference microscopy to integrated circuit inspection and metrology,"

Proceedings SPIE, **775** Integrated Circuit Metrology, Inspection and Process Control, pp. 233-247.

Davinovits, P. & Egger, M.D. (1969), "Scanning laser microscope," *Nature*, **223**, Aug. 23, p. 831.

Dekkers, N.H. & deLang, H. (1974) "Differential phase contrast in STEM," *Optik*, **41**, pp. 452-456.

Delaney, P.M., Harris, M.R. & King, R. (1994), "Fiber optic laser scanning confocal microscope suitable for fluorescence imaging," *Applied Optics*, **33**(4), pp. 573-577.

Dickensheets, D. & Kino, G.S. (1994), "A scanned optical fiber confocal microscope," *Proceedings SPIE*, **2184** Three dimensional microscopy, pp. 39-47.

Dixon, A.E., Damaskinos, S. & Atkinson, M.R. (1991), "A scanning confocal microscope for transmission and reflection imaging," *Nature*, **351**, pp. 551-553.

Doukoglou, T.D., Hunter, I.W., Kearney, R.E., Lafontaine, S. & Nielsen, P.F. (1988), "Deconvolution of Laser Scanning Microscope Images using System Identification techniques," *Proceedings Canadian Medical and Biological Engineering Conference*, **14**, pp. 105-106.

Doukoglou, T.D., Hunter, I.W. & Brenan, C.J.H., (1992) "Myocardial Fiber Studies using Interference Confocal Microscopy," *Scanning*, **14**(suppl. II), pp. II-72 - 74.

Draaijer, A. & Houpt, P.M. (1987), "A real time confocal laser scanning microscope (CSLM)," *Proceedings SPIE*, **809** Scanning Imaging Technology, pp. 85-89.

Draaijer, A. & Houpt, P.M. (1988), "A standard video-rate confocal laser scanning reflection and fluorescence microscope," *Scanning*, **10** (4), pp. 139-145.

Drazic, V. (1992), "Dependence of two- and three-dimensional optical transfer functions on pinhole radius in a coherent confocal microscope," *Journal of the Optical Society of America A*, **9**(4), pp. 725-731.

Egger, M.D. & Petran, M. (1967), "New reflected-light microscope for viewing unstained brain and ganglion cells," *Science*, **157**, pp. 305-307.

Fieguth, P.W. & Staelin, D.H. (1994), "High-accuracy profiler that uses depth from focus," *Applied Optics*, **33**(4), pp. 686-689.

Forgren, P.-O. (1987), "Using vector representation to display 3D data from a confocal laser scanning microscope," *Proceedings of fifth Scandinavian Conference on Image Analysis*, pp. 367-374.

Goldstein, S.R., Hubin, T., Rosenthal, S. & Washburn, C. (1989), "A video-rate confocal laser beam scanning light microscope using image dissector," *Proceedings SPIE*, **1161** New Methods in Microscopy and Low Light Imaging, pp. 268-278.

Gu, M., & Sheppard, C.J.R. (1993), "Fiber-optical confocal scanning interference microscopy," *Optics Communications*, **100**(1-4), pp. 79-86.

Hamed, A.M. & Clair, J.J. (1983), "Studies on optical properties of confocal scanning optical microscope using pupils with radially transmission ρ^n, distribution," *Optik*, **65** (3), pp. 209-218.

Hamilton, D.K. & Sheppard, C.J.R. (1982), "A confocal interference microscope," *Optica Acta*, **29** (12), pp. 1573-1577.

Hamilton, D.K. & Sheppard, C.J.R. (1984), "Differential phase contrast in scanning optical microscopy," *Journal of Microscopy*, **133** (1), pp. 27-39.

Hamilton, D.K. & Wilson, T. (1984a), "Edge enhancement in scanning optical microscopy by differential detection," Journal of Optical Society of America A, 1(3), pp. 322-323.

Hamilton, D.K. & Wilson, T. (1984b), "Two-dimensional phase imaging in the scanning optical microscope," *Applied Optics*, **23** (2), pp. 348-352.

Hamilton, D.K. & Mathews, H.J. (1985), "The confocal interference microscope as a surface profilometer," *Optik*, **71** (1), pp. 31-34.

Holmes, R.D. & Somekh, M.G. (1994), "Extended-focus phase imaging with an interferometric confocal microscope," *Applied Optics*, 33(4), pp. 654-661.

Hunter, I.W., Lafontaine, S., Nielsen, P.M.F. & Hunter, P.J. (1988), "An apparatus for laser scanning microscopy and dynamic testing of muscle cells," Proceedings SPIE, **1028** Scanning Imaging Technology, pp. 152-159.

Hunter, I.W., Lafontaine, S., Nielsen, P.M.F., Hunter, P.J. & Hollerbach, J.M. (1990), "Manipulation and dynamic mechanical testing of microscopic objects using a tele-micro-robot system," *IEEE Control Systems Magazine*, **10**, pp. 3-9.

Inoué, S. (1989a), "Whither video microscopy?. Towards 4D imaging at the highest resolution of the light microscopy." in *Digitized Video Microscopy*, Herman, B. & Jacobson, K. (eds), Alan R. Liss, NewYork.

Inoué, S. (1989b), "Foundations of Confocal Scanned Imaging in Light Microscopy," in Handbook of Biological Confocal Microscopy, Pawley, J.B. (ed.), Plenum Press, New York.

Jones, S.J., Taylor, M.L., Baarslag, M.W., Krol, J.J., Mosterd, B., Mans, A., Brakenhoff, G.J. & Nanninga, N. (1990), "Image processing techniques for 3-D chromosome analysis," *Journal of Microscopy*, **158** (2), pp. 235-248.

Juang, C., Finzi, L. & Bustamante, C.J. (1988), "Design and application of a computer-controlled confocal scanning differential polarization microscope," *Review of Scientific Instruments*, **59**(11), pp. 2399-2408.

Jungerman, R.L., Hobbs, P.C.D. & Kino, G.S. (1984), "Phase sensitive scanning optical microscope," *Applied Physics Letters*, **45** (8), pp. 846-848.

Juskaitis, R. & Wilson, T. (1992a), "Differential confocal scanning microscope with a two-mode optical fiber," *Applied Optics*, **31**, pp. 898-902.

Juskaitis, R. & Wilson, T. (1992b), "Surface profiling with scanning optical microscopes using two-mode optical fibers," *Applied Optics*, **31**, pp. 4569-4574.

Juskaitis, R., Rea, N. & Wilson, T. (1993), "Fiber-optic based confocal microscopy using laser detection," *Optics Communications*, **99**(1-2), pp. 105-113.

Kimura, S. & Munakata, C. (1989), "Calculation of three-dimensional optical transfer function for a confocal scanning fluorescent microscope," *Journal of the Optical Society of America A*, **6**(7), pp. 1015-1019.

Kimura, S. & Wilson, T. (1991), "Confocal scanning optical microscope using single-mode fiber for signal detection," *Applied Optics*, **30**(16), pp. 2143-2150.

Kimura, T. (1993), "Confocal scanning type of phase contrast microscope and scanning microscope," U.S. Patent No. 5,241,364.

Kimura, S. & Wilson, T. (1994), "Confocal scanning dark-field polarization microscopy," *Applied Optics*, **33**(7), pp. 1274-1278.

Kino, G.S., Corle, T.R. & Xiao, G.Q. (1988a), "New types of scanning optical microscopes," *Proceedings SPIE*, **921** Integrated Circuit Metrology, Inspection and Process Control II, pp. 116-122.

Kino, G.S., Corle, T.R. & Xiao, G.Q. (1988b), "The scanning optical microscope: an overview," *Proceedings SPIE*, **897** Scanning Microscopy Technology and Applications, pp. 32-42.

Kino, G.S. (1989) "Intermediate optics in Nipkow disk microscope," in *Handbook of Biological Confocal Microscopy*, (Ed. Pawley, J.B.), Plenum Press.

Kino, G.S. & Xiao, G.Q. (1990), "Real-time scanning optical microscopes," in *Confocal Microscopy* (Ed. Wilson, T.), Academic Press.

Koester, C.J., Auran, J.D., Rosskothen, H.D., Florakis, G.J. & Tackaberry, R.B. (1993), "Clinical Microscopy of the cornea utilizing optical sectioning and a high-

Krug, R., Würfel, P. & Ruppel, W. (1993), "Material Characterization with a simple laser scanning microscope," *Applied Optics*, **32**(32), pp. 6458-6463. (CSMA)

Laeri, F. & Strand, T.C. (1987), "Angstrom resolution optical profilometry for microscopic objects," *Applied Optics*, **26** (11), pp. 2245-2249.

Lukosz, W. (1966), "Optical systems with resolving powers exceeding the classical limit," *Journal of Optical Society of America*, **57**, p. 1190.

Maly, M. & Boyde, A. (1994), "Real-time stereoscopic confocal reflection microscopy using objective lenses with linear longitudinal chromatic dispersion," *Scanning*, **16**, pp. 187-192.

Masters, B.R. & Paddock, S.W. (1990), "Three-dimensional reconstruction of the rabbit cornea by confocal scanning optical miscroscopy and volume rendering," *Applied Optics*, **29** (26), pp. 3816-3822.

Masters, B.R. (1992), "A historical perspective on confocal microscopy," *Scanning*, **14**(suppl. II), pp. II-51-52.

Mathews, H.J., Hamilton, D.K. & Sheppard, C.J.R. (1986), "Surface profiling by phase locked interferometry," *Applied Optics*, **25** (14), pp. 2372-2374.

Maurice, D.M. (1973), "A scanning slit optical microscope," *Investigative Ophthalmology*, **13**, pp. 1033-1037.

Merkle, F., Bille, J., Hunklinger, S., Karte, T., Wijnaendts, R.W. & Kaplan, R. (1988), "Laser-scanning inspection microscope system," pp. ThA2-1 to -4.

Minsky, M. (1961), "Microscopy apparatus," *U.S. Patent # 30313467* (Filed Nov. 7, 1957).

Minsky, M. (1988), "Memoir on inventing the confocal scanning microscope," *Scanning*, **10**, pp. 128-138.

Montag M., Spring, H., Trendelenburg, M.F. & Kriete, A. (1990), "Methodical aspects of 3-D reconstruction of chromatin architecture in mouse trophoblast giant nuclei," *Journal of Microscopy*, **158** (2), pp. 225-233.

Offside, M.J. & Somekh, M.G. (1992), "Interferometric scanning optical microscope for surface characterization," *Applied Optics*, **31** (31), pp. 6772-6782.

Pawley, J.B. (ed) (1989), *Handbook of Biological Confocal Microscopy*, Plenun Press, New York.

Sasaki, K., Koshioka, M., & Masuhara, H. (1992), "Confocal laser-induced absorption microscope," *Journal of the Optical Society of America A*, **9**(6), pp. 932-936.

Sawatari, T. (1973), "Optical Heterodyne Scanning Microscope," *Applied Optics*, **12**(11), pp. 2768-2772.

Schormann, T. & Jovin, T.M. (1990), "Optical sectioning with a fluorescence confocal SLM: procedures for determination of the 2-D digital modulation transfer function and for 3-D reconstruction by tessellation," *Journal of Microscopy*, **158** (2), pp. 153-164.

Sheard, S., Suhara, T. (1993), "Integrated-Optic Implementation of a Confocal Scanning Optical Microscope," *IEEE Journal of Lightwave Techniques*, II(8), pp. 1400-1403.

Sheppard, C.J.R. & Choudhury, A. (1977), "Image formation in scanning microscope," *Optica Acta*, **24** (10), pp. 1051-1073.

Sheppard, C.J.R. & Wilson, T. (1980), "Fourier imaging of phase information in scanning and conventional optical microscopes," *Philosophical Transactions of the Royal Society of London A*, **295**, pp. 513-536.

Sheppard, C.J.R. & Wilson, T. (1981), "Effects of high angles of convergence in V(z) in the scanning acoustic miscroscope," *Applied Physics Letters*, **38** (11), pp. 858-859.

Sheppard, C.J.R. & Mao, X.Q. (1988), "Confocal microscopes with split apertures," *Journal of Modern Optics*, **35** (7), pp. 1169-1185.

Shigeharu, K. & Wilson, T. (1991), "Confocal scanning optical microscope using single-mode fiber for signal detection," *Applied Optics*, **30** (16), pp. 2143-2150.

Stallard, B. & Bukhman, Y. (1987), "Use of a confocal scanning laser microscope for measurement of submicrometer critical dimensions," *Proceedings SPIE*, **775** Integrated Circuit Metrology, Inspection and Process Control, pp. 60-67.

Stelzer, E.H.K., Marsman, H.J.B. & Wijnaendts van Resandt, R.W. (1986), "A setup for a confocal scanning laser interference miscroscope," *Optik*, **73** (1), pp. 30-33.

Stelzer, E.H.K. & Wijnaendts van Resandt, R.W. (1987), "Nondestructive sectioning of fixed and living specimens using a confocal scanning laser fluorescence microscope: microtomoscopy," *Proceedings SPIE*, **809** Scanning Imaging Technology, pp. 130-137.

Stelzer, E.H.K. (1989), "The Intermediate optical system of laser-scanning confocal microscopes," in *Handbook of Biological Confocal Microscopy*, (Ed. Pawley, J.B.), Plenum Press.

Stelzer, E.H.K. & Wijnaendts van Resandt, R.W. (1990), "Optical cell splicing with the confocal fluorescence microscope: microtomoscopy," in *Confocal Microscopy*, T.Wilson (ed.), pp. 199-212.

Tychinsky, V.P., Masalov, I.N., Pankov, V.L. & Ublinsky, D.V., (1989), "Computer phase microscope for submicron structure topology monitoring," *Proceedings SPIE*, **1139** Optical Storage and Scanning Technology, pp. 2-5.

van der Voort, H.T.M., Brakenhoff, G.J., Valkenburg, A.C. & Nanninga, N. (1985), "Design and use of a computer controlled confocal microscope for biological applications," *Scanning*, 7 (2), pp. 66-78.

Vepsalainen, A.M. (1990), "Extraction of fiber-like objects from 3D images of cells," *Proceedings SPIE*, **1350** Imaging Algebra and Morphological Image Processing, pp. 201-208.

Wallen, P., Carlsson, K., Liljeborg, A. & Grillner, S. (1988), "Three-dimensional reconstruction of neurons in the lamprey spinal cord in whole-mount, using a confocal laser scanning microscope," *Journal of Neuroscience Methods*, **24**, pp. 91-100.

Webb, R.H. & Hughes, G.W. (1981), "Scanning laser ophthalmoscope," *IEEE Transactions on Biomedical Engineering*, **BME-28**, pp.488-492.

Webb, R.H., Hughes, G.W. & Delori, F.C. (1987), "Confocal scanning laser ophthalmoscope," *Applied Optics*, **23**, pp. 1492-1499.

Wijnaends van Resandt, R.W., Marsman, H.J.B., Kaplan, R., Davoust, J., Stelzer, E.H.K. & Stricker, R. (1985), "Optical fluorescent microscopy in three dimensions: microtomoscopy," *Journal of Microscopy*, **138** (1), pp. 29-34.

Wijnaends van Resandt, R.W., Zapf, Th., Fangerau, M. & Piepenstock, R. (1988), "Laser scanning optical inspection and metrology," *Proceedings SPIE*, **921** Integrated Circuit Metrology, Inspection and Process Control II, pp. 78-84.

Wilson, T. & Sheppard, C.J.R. (1984) *Theory and practice of Scanning Optical Microscopy*, Academic Press.

Wilson, T. (1985), "Scanning optical microscopy," *Scanning*, 7 (2), pp. 79-87.

Wilson, T. (ed.) (1990), *Confocal Microscopy*, Academic Press, New York.

Wilson, T.(1993), "Image formation in 2-mode fiber-based confocal microscopes," *Journal of the Optical Society of America A-Optics & Image Science*, **10**(7), pp. 1535-1543.

Wilson, T., Juskaitis, R. & Tan, J.B. (1994), "Differential imaging in confocal microscopy," *Journal of Microscopy*, **175**, pp. 1-9.

Wolf, W.E. (1988), "Characterizing birefringent crystal wafers with scanning laser microscope," *Proceedings SPIE*, **1004** Automated Inspection and High Speed Vision Architectures II, pp. 142-150.

Xiao, G.O. & Kino, G.S. (1987), "A real-time confocal scanning optical microscope," *Proceedings SPIE*, **809** Scanning Imaging Technology, pp. 107-113.

Xiao, G.O., Corle, T.R. & Kino, G.S. (1988), "Real-time confocal scanning optical microscope," *Applied Physics Letters*, **53** (8), pp. 716-718.

Zarf, Th. & Wijnaendts van Resandt, R.W. (1988), "VLSI metrology using an automatic beam-scanning confocal laser microscope," *Scanning*, **10** (4), pp. 157-162.

CHAPTER 3

Theory of Confocal Scanning Laser Microscopy

This chapter presents a brief analysis of the theory governing the operation of the confocal scanning laser microscope (CSLM) arrangement. The optical performance of such systems is investigated in terms of their transverse and depth response functions. Simple models describing the influence of the size of the detector on the depth and transverse responses are developed. Finally, a brief description of some of the imaging modes available in CSLMs is followed by an analysis of the error introduced due to refractive index mismatches while performing 3D volumetric image acquisition.

3.1 Overview-Basic Principles

The basic principle of confocal optical microscopy is summarized in Figure 3.1. Light is focused to a diffraction limited spot on the sample via an objective lens. At the rear focal point of the objective, a pinhole is placed and behind it a photodetector. Light emanating from within the focal volume of the objective is imaged onto the detector pinhole. Light from out-of-focus structures reaches the detector greatly attenuated. Therefore, a spatially filtered detection of the backscattered light occurs. The properties of confocal arrangement depend highly on the size of the photodetector, or more specifically the size of the pinhole aperture placed in front of the photodetector. In subsequent sections the terms 'detector size' and 'pinhole size' are used interchangeably.

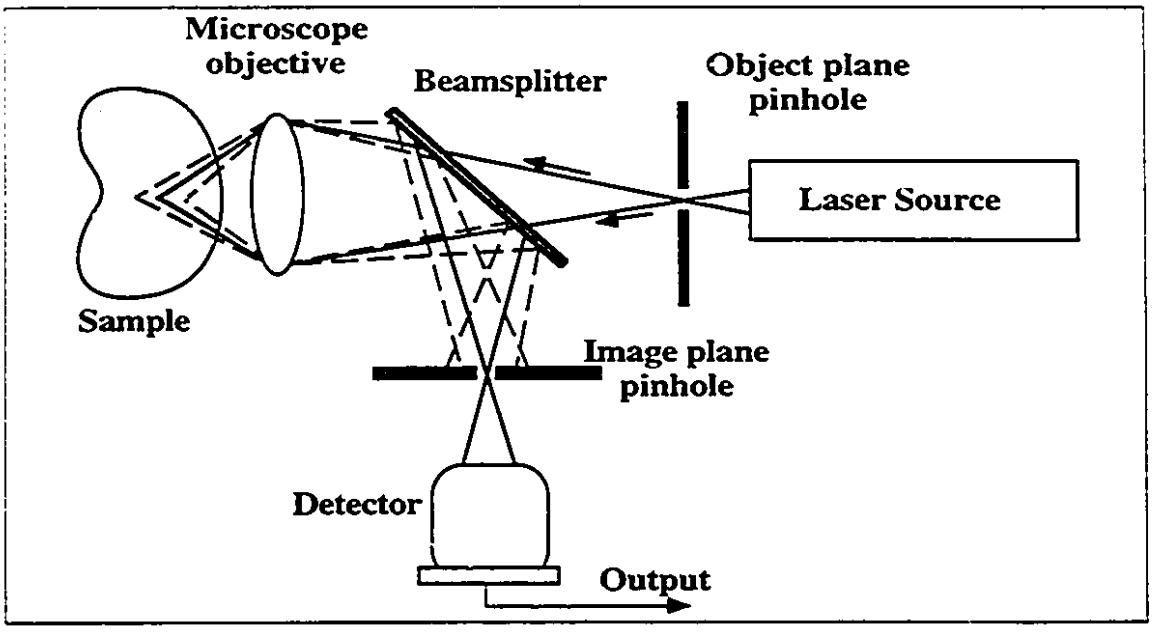

Figure 3.1 *The principle of confocal microscopy is demonstrated here in a reflection mode confocal microscope configuration. Light from the focal volume of the objective is focused onto the detector pinhole. Light outside the objective's focal volume arrives at the pinhole plane defocused and therefore its measured intensity is greatly attenuated.*

Currently, the classification of confocal microscopes into Type 1 and Type 2 has become widely accepted. Type 2 confocal microscopes employ a point source and a point detector, resulting in spatially coherent imaging. When a large source or a large area photodetector is used, the imaging is partially coherent and is referred to as Type 1. Confocal Type 2 arrangements offer superior lateral and axial resolution to that of conventional arrangements. Confocal Type 1 arrangements offer lateral resolution similar to that of conventional microscopes but still exhibit improved axial resolution (depth discrimination). In this thesis work, care was taken to ensure that the confocal scanning laser arrangements behave like Type 2 configurations, in order to take advantage of the improved imaging capabilities.

By using Fourier imaging theory it can be shown that when an object (with complex transmittance t(x,y,z)) is imaged onto a point (infinitely small) detector, as depicted in Figure 3.2. The intensity of the light reaching the detector is given by [Sheppard & Wilson, 1984, p. 47]:

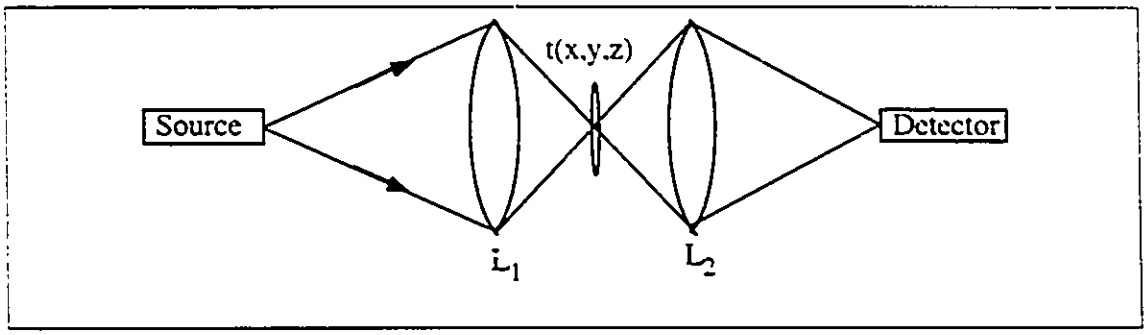

Figure 3.2 *Optical arrangement of a scanning microscope. A Type 2 confocal arrangement results when the detector is reduced to a point. A large detector or source results in a Type 1 confocal arrangement with properties similar to those of a conventional microscope (L_1: objective lens, L_2: collector lens, t(x,y,z): complex object transmittance).*

$$I(.) = |h_{L1}(.)\, h_{L2}(.) \otimes t(.)\,|^2 \quad . \tag{3.1}$$

where $\otimes$ denotes convolution and $h_{L1}(.)$, $h_{L2}(.)$ are the point spread functions of the two lenses (Equation (3.3) below). For a reflection mode confocal microscope like the one depicted on Figure 3.1, $h_{L1}(.) = h_{L2}(.)$, since the same lens is used as the objective and the collector.

When the area of the detector becomes large, imaging is not coherent. In the extreme case of an infinitely large detector, the intensity of the detected light is given by:

$$I(.) = |(h_{L1}(.)t(.)) \otimes h_{L2}(.)|^2 \quad . \tag{3.2}$$

Equations (3.1) and (3.2) are very important since they summarize the main difference between Type 2 confocal and conventional microscopes in terms of their optical behavior.

The point spread function $h_L(.)$ of a lens, (in Equations (3.1) and (3.2) above) is given by the Debye integral [Born & Wolf, 1959], and it is, theoretically, an even function:

$$h(u,v) = \int_0^1 P(\rho)\, e^{(\frac{1}{2} j u \rho^2)}\, J_0(v\rho)\, \rho\, d\rho \quad , \tag{3.3}$$

where P(.) is the pupil function of the lens, $J_0(.)$ is a 0^{th} order Bessel function of the first kind, and u, v are the normalized optical coordinates (defined in Equations (3.5) and (3.6)

below). Equation (3.3) is an approximation to the more general expression of a plane wave's angular spectrum.

3.2 Confocal Imaging Theory

Without undertaking an extensive analysis, this section presents the imaging theory governing confocal arrangements. The analysis is based on Fresnel / Kirchhoff diffraction theory, using also the Fraunhofer approximation. The goal is the derivation of a mathematical representation for the depth and transverse response functions of a confocal arrangement as a function of the optical system parameters.

The field amplitude U(.) at a focal plane point Q(x,y,z) due to a lens with a circular aperture of radius w_0 and focal distance f , fully illuminated by a monochromatic point source is given by [Born & Wolf, 1959, p. 438]:

$$U(Q) = -\frac{\pi w_0^2}{\lambda f} e^{j\left(\frac{f}{w_0}\right)^2 u} \, 2 U_0 \int_0^1 J_0(v\rho) e^{-\frac{1}{2} j u \rho^2} \rho \, d\rho \quad , \tag{3.4}$$

where

$$u = \frac{2\pi}{\lambda}\left(\frac{w_0}{f}\right)^2 z \equiv \frac{8\pi}{\lambda}\sin^2\left(\frac{a}{2}\right) z \quad , \tag{3.5}$$

z being the actual distance on the optical axis and sin(a) the numerical aperture of the lens, and

$$v = \frac{2\pi}{\lambda} \frac{w_0}{f} \sqrt{x^2 + y^2} \equiv \frac{2\pi}{\lambda} \sin(a)\, r \quad , \tag{3.6}$$

where $r = \sqrt{x^2 + y^2}$ and x, y are the coordinates in the plane transverse to the optical axis.

Equation (3.3) holds for $f > w_0 \gg \lambda$ and $\frac{w_0^2}{f\lambda} \gg 1$ (paraxial ray approximation).

It is useful to consider separately the real and imaginary parts of Equation (3.4):

$$2 \int_0^1 J_0(v\rho) e^{-\frac{1}{2} j u \rho^2} \rho \, d\rho = C(u,v) - j\, S(u,v) \quad , \tag{3.7}$$

where

$$C(u,v) = 2 \int_0^1 \cos\left(\frac{1}{2} u \rho^2\right) J_0(v\rho) \, \rho \, d\rho \quad , \tag{3.8}$$

and

$$S(u,v) = 2\int_0^1 \sin(\tfrac{1}{2}u\rho^2)\, J_0(v\rho)\, \rho\, d\rho \quad . \tag{3.9}$$

In an optical system the intensity I(.) is the quantity usually measured, and since I(.)= |U(.)|^2 then:

$$I(u,v) = I_0 [\, C^2(u,v) + S^2(u,v) \,] \quad . \tag{3.10}$$

$$\text{where } I_0 = \left(\frac{\pi w_0^2}{\lambda f} U_0\right)^2 \quad . \tag{3.11}$$

3.2.1 Transverse Response - Point Detector

The transverse response of a confocal arrangement on the focal plane can be derived by letting u=0 in Equation (3.10). Then, the intensity on the focal plane is given by:

$$I(0,v) = I_0 [\, C^2(0,v) + S^2(0,v)] \quad . \tag{3.12}$$

Since sin(0)=0 and S(0,v) = 0,

$$I(0,v) = I_0\, C^2(0,v) = I_0\left[2\int_0^1 J_0(v\rho)\, \rho\, d\rho\right]^2 \quad , \tag{3.13}$$

using the fact that $\int J_0(t)tdt = tJ_1(t)$ and $J_1(0) = 0$:

$$I(v) = I_0\left[\frac{2J_1(v)}{v}\right]^2 \quad , \tag{3.14}$$

where J_1 is a Bessel function of the first kind and of order 1.

Note that the ratio $\frac{I(v)}{I_0} = \left[\frac{2J_1(v)}{v}\right]^2 = h_L(0,v)$: the lens impulse response in the v plane.

Substituting Equation (3.14) in Equation (3.1), and by assuming circular apertures and identical objective and collector lenses; the image of an ideal point object represents the lateral response for the confocal Type 2 confocal microscope configuration:

$$I(v) = I_0\left[\frac{2\,J_1(v)}{v}\right]^4 \quad . \tag{3.15}$$

Type 2 confocal arrangements offer up to 27% higher lateral resolution compared to either a Type 1 or a conventional microscope arrangement. Note that an estimate of the lateral resolution for a conventional microscope arrangement may be obtained by using the Rayleigh's criterion ($d_v = \frac{1.22\,\lambda}{NA_{obj}+NA_{cond}}$) for visually resolving two equally bright points.

Better imaging performance is possible with the use of annular aperture lenses that offer a higher cut-off spatial frequency. Nevertheless, since the design and construction of the CSLMs arrangements presented in subsequent chapters of this work, only considers circular aperture lenses, this case is not investigated. The interested reader is directed to the extensive literature found in the bibliography section at the end of the thesis and in [Sheppard & Wilson, 1984].

3.2.2 Depth (Axial) Response-Point Detector

The behavior of the depth response of a confocal arrangement can be investigated using Equation (3.10) when v=0, the intensity along the microscope's optical axis is given by:

$$I(u,0) = I_0\,[\,C^2(u,0) + S^2(u,0)] \quad , \tag{3.16}$$

since $J_0(0) = 1$,

$$I(u) = I_0\left[\left(2\int_0^1 \cos(\tfrac{1}{2}u\,\rho^2)\,\rho\,d\rho\right)^2 + \left(2\int_0^1 \sin(\tfrac{1}{2}u\,\rho^2)\,\rho\,d\rho\right)^2\right] \quad . \tag{3.17}$$

By defining $g = \frac{1}{2}up^2$, carrying out the integration, and using the fact that $2\sin^2(\frac{A}{2}) = 1 - \cos A$ it follows that the intensity distribution along the optical axis is given by:

$$I(u) = I_0\left[\frac{\sin(u/4)}{u/4}\right]^2 \quad . \tag{3.18}$$

Note that the ratio $\frac{I(u)}{I_0} = \left[\frac{\sin(u/4)}{u/4}\right]^2 = h_L(u,0)$: the lens impulse response along the optical axis (u).

From Equation (3.1), it follows that the depth response of a Type 2 confocal arrangement when intensity is measured only on the optical axis (v=0) is the square of Equation (3.18). Nevertheless, the depth response of CSLM arrangements is measured by axially scanning a planar reflector (mirror) through the focal point of the objective lens. From Figure 3.3 it is apparent that the depth response for a plane reflector is half that of the point response. Furthermore, since the object is not a point, but rather a uniformly reflecting infinitely large plane (its Fourier transform is given by a delta function) the planar depth response can be estimated by:

$$I_{plane}(u) = \int I_{point}(2u,v)\, v\, dv \quad , \tag{3.19}$$

and for two circular pupils the previous equation becomes:

$$I_{plane}(u) = I_0\left[\frac{\sin(u/2)}{u/2}\right]^2 \quad , \tag{3.20}$$

where I_0 in this case is the integrated intensity on the lateral (v) plane.

Sheppard and Wilson [1981] estimated the complex amplitude of the depth response using paraxial theory and by taking into account high angles of convergence. For the sake of completeness the result of their derivation is also included here:

$$U(u) = U_0 \frac{\sin(u/2)}{u} \exp\left[\frac{ju}{2} - \frac{2ju}{\sin^2 a}\right] \quad . \tag{3.21}$$

The transverse and depth responses for the confocal arrangement, as described by Equations (3.15) and (3.20), are valid when the detector is assumed to be a single point and is mathematically represented by a Dirac delta function ($\delta(r_p)$). A finite size detector influences both the depth and the transverse response of the confocal microscope. The depth response is, however, affected less drastically by an increase in the detector size.

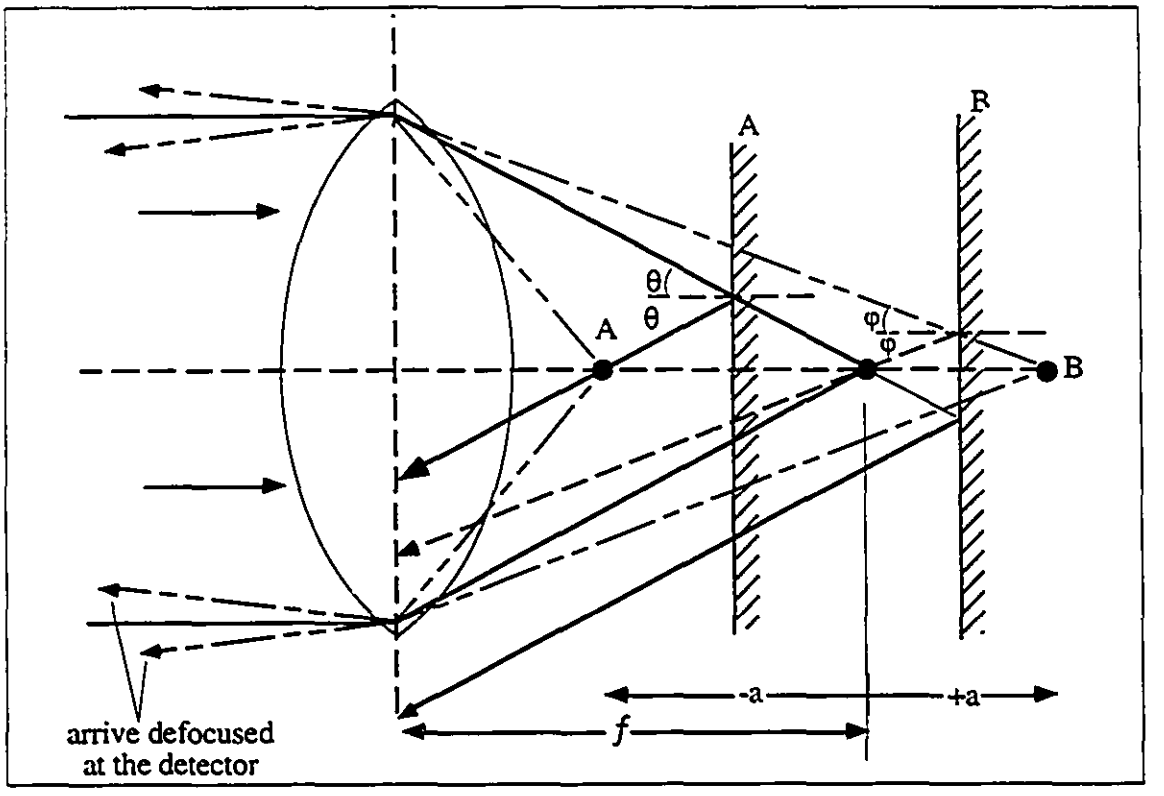

Figure 3.3 *Comparison of a point vs. a planar depth response. It can be seen that the full width half maximum (FWHM) for the point depth response should be double that of the planar one. Also, the planar depth response due to apodization is expected to be asymmetric. When the mirror is moved away from the focal point and the objective, less light is reflected back through the lens (smaller collection stereo angle for a>0) as opposed to when it approaches the lens, in which case most of the light is reflected back through the lens.*

In the case of a finite size detector, the magnification of the optical system (M) is introduced in the definition of the normalized coordinates v given by Equations (3.6). The definition of the normalized coordinate v becomes:

$$v=\frac{2\pi}{\lambda}\frac{r}{M}r\equiv\frac{2\pi}{\lambda}\frac{\sin(a)}{M}r \qquad (3.22)$$

The expression for the normalized coordinate u is given by Equation (3.5).

The magnification of the optical system for the case depicted in Figure 3.1 is that of the objective lens. In a parallel beam system, as shown in Figure 3.4(b) below, a condenser lens is used to focus the light reflected off the object onto the photodetector. The

magnification is then defined as the ratio of the object to the image size. It can be shown that the ratio of the F numbers (F#) of the condenser and objective lenses can be used as the magnification factor. The F# of a lens is given by:

$$F\# = \frac{f}{2w_0} \cdot \equiv \frac{1}{2\sin(a)} \quad . \tag{3.23}$$

Alternatively, when using Gaussian beam approximation, the magnification can be defined as the ratio of the beam waists for the objective and condenser lenses.

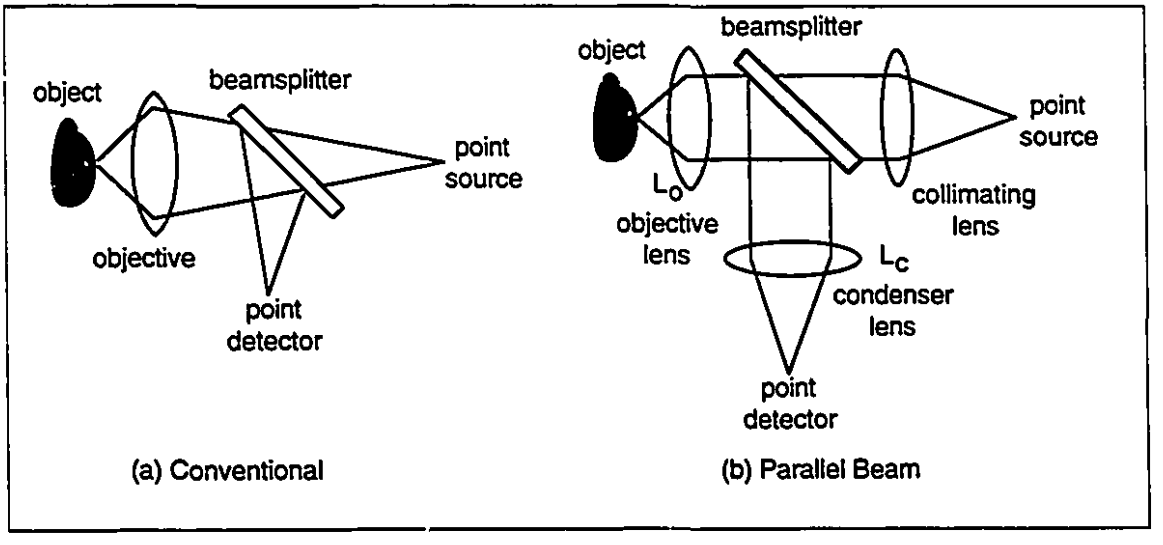

Figure 3.4 *(a) Conventional and (b) parallel beam configuration of a confocal scanning laser microscope. In the latter case a condenser lens (L_C) is employed to focus the light reflected off the object onto the detector.*

The parallel beam configuration (Figure 3.4b) has a lower optical efficiency than the conventional configuration (Figure 3.4a) since there are four additional surfaces (the two collimating lenses) where light loss could occur. Nevertheless, the parallel beam configuration offers greater flexibility in introducing additional optical components and varying the magnification of the optical system. The importance of the magnification factor in determining the confocality of a scanning optical microscope is outlined in the next section.

3.2.3 Transverse Response - Finite Size Detector.

When a pinhole of radius v_p is placed in front of the large area detector (Figure 3.1), the effective detector size becomes equal to the size of the pinhole. Considering a point

source, and back-projecting the pinhole on the focal plane of the objective lens, the transverse response of the confocal arrangement on this plane (u=0) is given by:

$$I(v) = h_{L1}^2(v)\left(h_{L2}^2(v) \otimes d_p(v)\right) \quad , \tag{3.24}$$

where h(u,v) is the point spread function of the lens and is given by Equation (3.3), $d_p(v)$ is the detector sensitivity function and $\otimes$ denotes the convolution operation. This is a 2D convolution operation defined on the v plane:

$$\int_{+\infty}^{\infty}\int_{+\infty}^{\infty} h_L(\zeta,\eta)\, d_p(x-\zeta,y-\eta)\,d\zeta d\eta \quad , \tag{3.25}$$

where x, y are orthogonal coordinates on the v plane.

The limits of the $d_p(v)$ are set by the size of the detector pinhole. If the sensitivity of the detector is assumed to be uniform and equal to 1, and that the pinhole is circular with radius v_p, then $d_p(v)$ becomes a circ(.) function:

$$d_p(v)=\text{circ}\left(\frac{v}{v_p}\right) = \begin{cases} 1 \text{ for } v \le v_p \\ \\ \text{and 0 elsewhere} \end{cases} \quad . \tag{3.26}$$

Following the derivation presented in Section 3.2.1 and by assuming the lens to be focused on the object plane, therefore, constraining the analysis on the u=0 plane, $h_L(0,v)$ becomes:

$$h_L = \left(\frac{2J_1(v)}{v}\right)^2 \quad , \tag{3.27}$$

where J_1 is a Bessel function of the 1st kind and of order 1.

The transverse response of a confocal arrangement can be estimated for different detector pinhole sizes (v_p), by numerically evaluating Equation (3.24). The results of this simulation are plotted in Figure 3.5 below. The results are very similar to those presented by Wilson and Carlini [1987], who solved the convolution integral of Equation (3.24) analytically in polar coordinates. The small deterioration in the transverse response for

values of $v_p \equiv 4$ (observed by Wilson and Carlini) is not apparent in Figure 3.5. This is possibly due to the loss of accuracy in estimating the convolution integral numerically. It can also be seen in Figure 3.5, that for a normalized pinhole radius of $v_p \leq 0.5$, the detector is small enough to be considered a point, resulting in Type 2 operation. The above value of v_p is referred to as the confocality criterion and is used to establish if a confocal arrangement is likely to behave as Type 2.

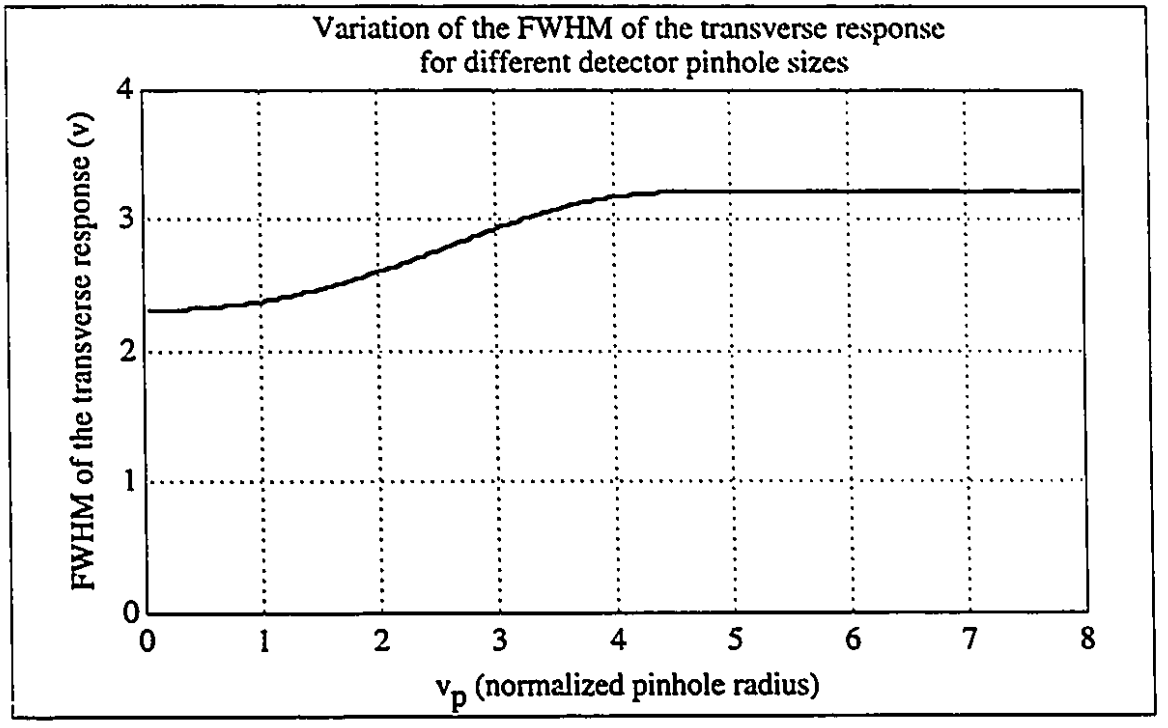

Figure 3.5 *FWHM of the transverse response of a confocal arrangement as a function of the normalized pinhole radius.*

Introduction of the optical system's magnification factor (M) into the normalized coordinates is very important. M plays a significant role in determining the confocality of a scanning optical arrangement. When the Type 2 operation criterion ($v_p \leq 0.5$) is used to assess the performance of a microscope, it is important that the revised normalized coordinate definition (Equation 3.22) be used. It can be seen from Equation (3.22) that when objectives with similar numerical aperture (NA) but different magnification factors are used, the objective with the lower magnification can be combined with a larger size pinhole without violating the confocality criterion. *The above fact is not emphasized in the confocal microscopy literature.*

3.2.4 Depth (Axial) Response - Finite Size Detector.

The dependency of the axial response on the size of the detector pinhole can be investigated by carrying out a similar analysis. A planar reflector is again considered as the object to estimate the axial response of a confocal arrangement. Considering a mirror as the object allows comparison of the theoretical results with actual measurements from the confocal system described in the next chapter.

The planar depth response is estimated from Equation (3.3) or (3.10) and by back-projecting the detector pinhole onto the object plane:

$$I_{plane}(u)= \int_0^{v_p} |h(2u,v)|^2 \, v \, dv \quad . \tag{3.28}$$

The integration can be performed numerically by either using Equation (3.3) or by separating the real and imaginary parts of the h(2u,v) and estimating the modulus of the result. In the simulation that follows, Equation (3.3) was numerically evaluated (see Appendix 3 for the computer subroutine). The pupil function P(.) was assumed to be circular and equal to one.

$$I_{plane}(u) = \int_0^{v_p} \left(\int_0^1 P(\rho) \, e^{(j u \rho^2)} \, J_0(v\rho) \, \rho \, d\rho \right)^2 v \, dv \quad . \tag{3.29}$$

The full width half maximum (FWHM) of depth response as a function of the normalized pinhole radius is plotted in Figure 3.6(b) below. The estimated normalized responses for different values of v_p are also plotted on Figure 3.6(a). The responses were estimated for both positive and negative values of u. In Figure 3.6(a) only the positive parts of $I_{plane}(u)$ are shown, because the depth responses are symmetric around u=0 (even functions). The computer program that evaluates Equation (3.29) is included in Appendix 3.

From Figure 3.6 it can be seen that if the normalized pinhole radius (v_p) is less than 2.5 the system will behave as a Type 2 configuration with regard to the longitudinal (depth) resolution. The modeling of the depth and transverse responses presented above is based on scalar paraxial theory. The determination of these models requires intensive computation.

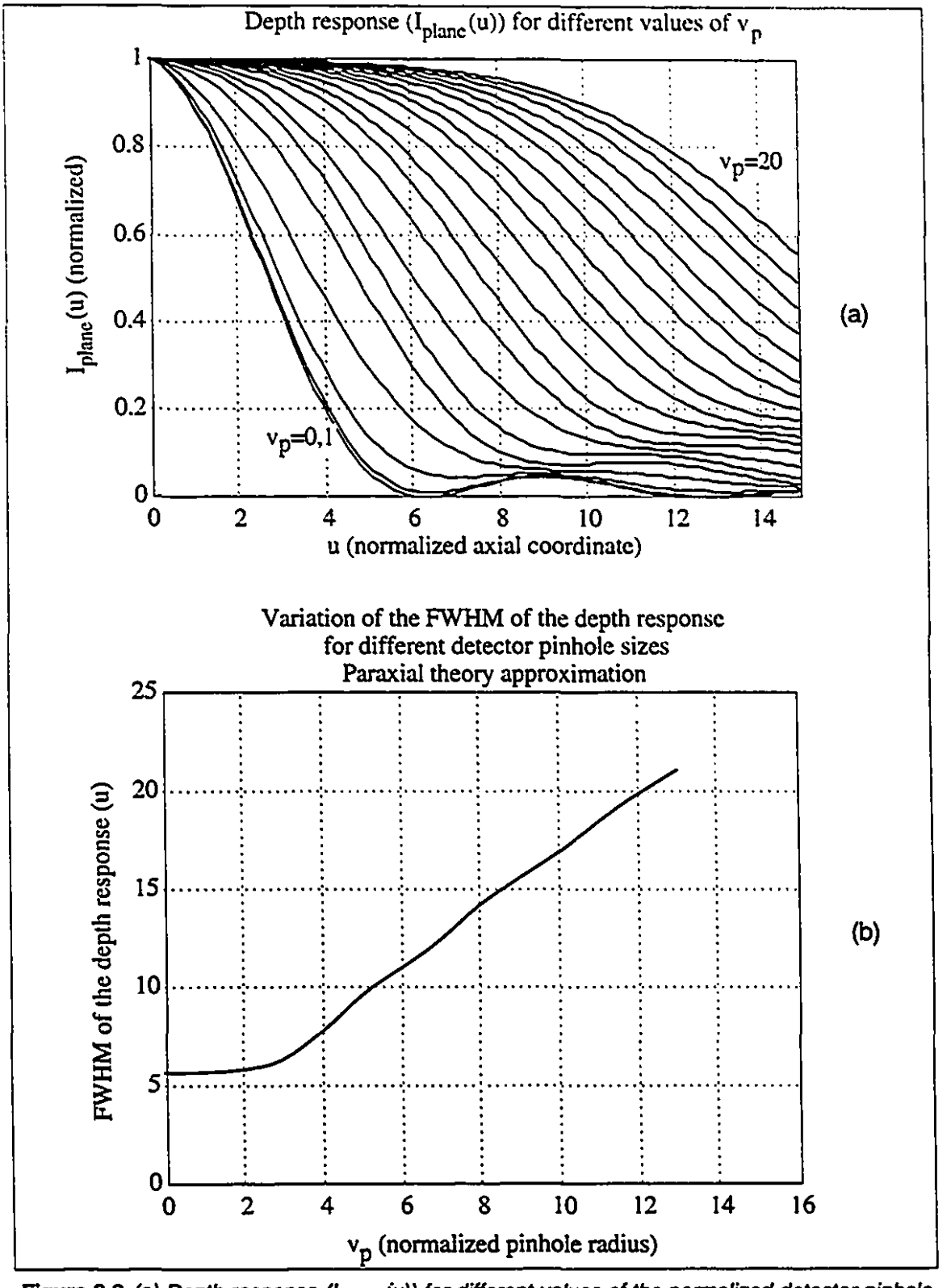

Figure 3.6 *(a) Depth response ($I_{plane}(u)$) for different values of the normalized detector pinhole radius, and (b) the FWHM of the depth response of a confocal arrangement as a function of the normalized pinhole radius.*

3.2.5 Depth Response - Geometric Optics Model with Gaussian Beam Weighting.

A simple, less computationally demanding, geometric optics model with Gaussian beam weighting, is used to investigate the effect of the detector pinhole size on the longitudinal response of a confocal arrangement. The model can give a quick estimate of the expected depth resolution for different detector pinhole sizes (Appendix 3). This information is useful during the design stage of a confocal microscope arrangement.

The optical arrangement used in the analysis that follows is depicted in Figure 3.7. A beam with a diameter of $2w_0$ is focused onto the object by the objective lens (L). In the parallel beam case (Figure 3.4(b)) the objective and condenser lenses have been collapsed into a single lens (L). The new object and image distances are the object distances from the objective and the image distance from condenser, respectively.

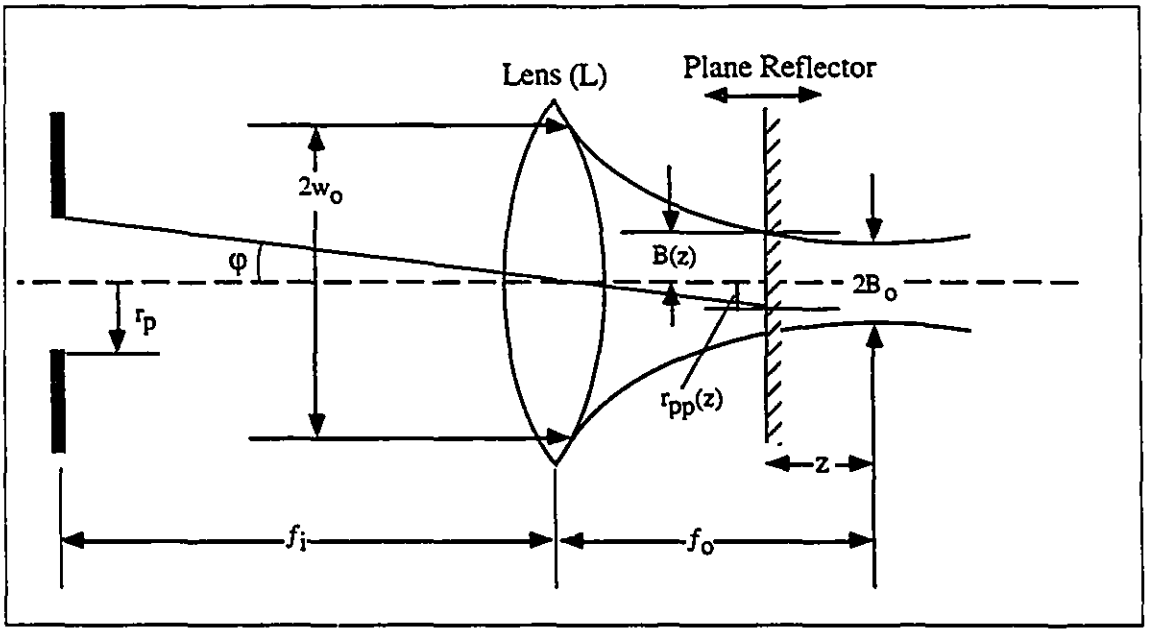

Figure 3.7 *The optical arrangement for the geometric optics model with Gaussian beam weighting.*

The front focal distance is the focal distance of the objective (f_o) and the back focal distance is equal to that of the condenser lens (f_i). The beam waist radius, B_o, at the focal point of the objective is given by:

$$B_o = \frac{2}{\pi} \lambda F_{\#} \quad , \tag{3.30}$$

where $F_{\#}$ is given by Equation (3.23).

The beam waist radius, B(z), at a distance z from the focus is given by:

$$B(z) = B_o \sqrt{\left(1 + \left(\frac{z}{z_R}\right)^2\right)} \quad . \tag{3.31}$$

where z_R is known as the Rayleigh range.

The beam waist radius at the focus as a function of the Rayleigh range is given by:

$$B_o = \sqrt{\frac{\lambda z_R}{\pi}} \quad , \tag{3.32}$$

from Equation (3.30) and (3.31) it can be seen that for z= 0: $B(0)=B_o$.

The projected pinhole radius (r_{pp}) due to a pinhole of radius r_p, can be estimated (Figure 3.7) using the principal ray passing from the center of the lens:

$$r_{pp}(z) = (f_o - z)\tan\varphi \quad , \tag{3.33}$$

where $\tan\varphi = \frac{r_p}{f_i}$.

The depth response function should be proportional to the power of the reflected light beam contained within the limits of the back-projected pinhole radius (r_{pp}). For a Gaussian beam the power contained within a radius r is given by:

$$P(r) = P_{total}\left[1 - \exp\left(\frac{-2r^2}{B^2(0)}\right)\right] \quad , \tag{3.34}$$

therefore,

$$I_{plane}(z) \equiv \left[1 - \exp\left(\frac{-2r_{pp}^2(z)}{B^2(z)}\right)\right] \quad . \tag{3.35}$$

An equivalent approach is to work in the image plane of the condenser lens. The radius of the illuminating Gaussian beam is then projected onto the image (pinhole) plane. In this case, the detected intensity is proportional to the field power contained within the detector pinhole radius (r_p).

The previous analysis does not describe the shape of the depth response very accurately, because it does not account for zeros along the u axis. The usefulness of this model relies on its simplicity in providing an estimate of the depth discrimination (in terms of the FWHM points of the depth response) for various pinhole sizes. Experimental measurements presented in Chapter 6, indicate that, for low numerical aperture objectives the model describes closely the measured depth response of the microscope. This is expected since the assumptions and approximations intrinsic to the geometric optics approach are best satisfied in this case. The estimated FWHM of the depth response, as a function of the normalized detector pinhole radius, for the geometric optics model, is shown in Figure 3.8.

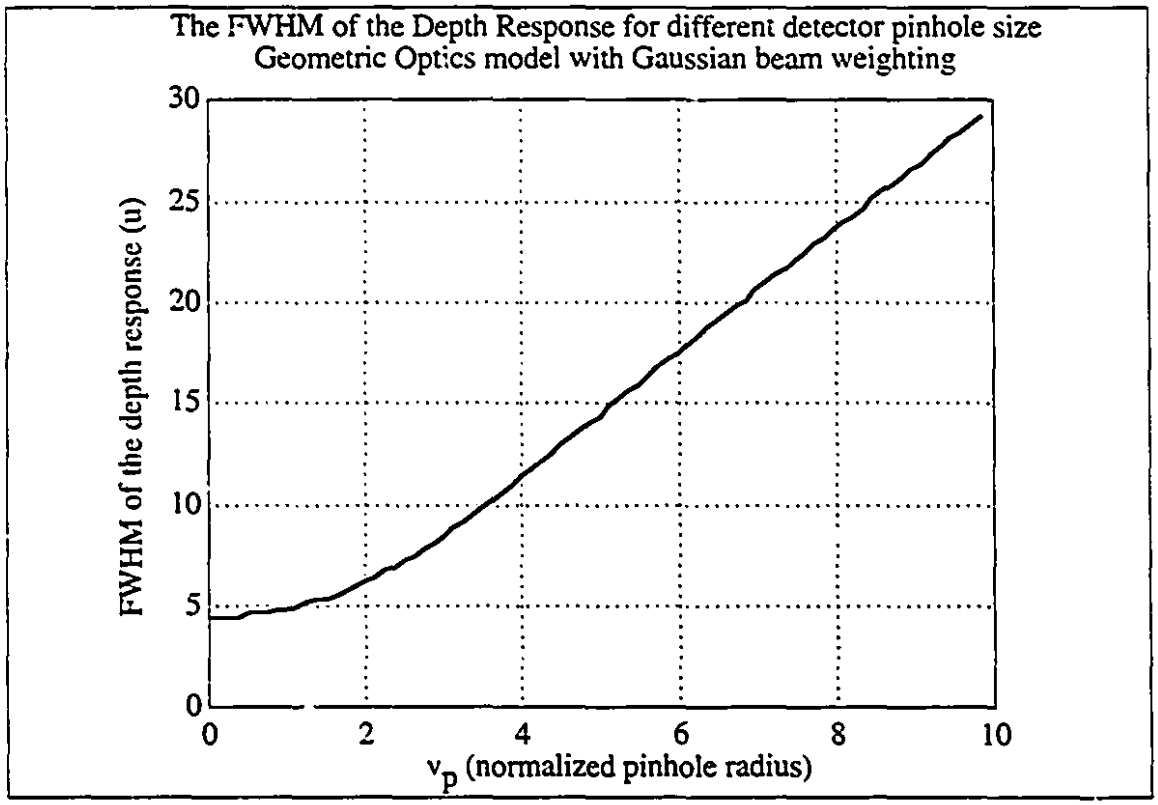

Figure 3.8 *Variation of the FWHM of the depth response as a function of the pinhole radius for the Gaussian beam model.*

3.2.6 Model Comparison.

The models presented in Sections 3.2.3, 3.2.4 and 3.2.5 are simple but give a useful insight into how a confocal arrangement will behave as imaging changes from being coherent to non-coherent by gradually increasing the detector size. Quantitatively, the difference between the two imaging modes is in the detected intensity:

$$I=|h_L|^2 \otimes |t|^2 \quad , \tag{3.36}$$

for the incoherent case.

$$\text{and } I=|h_L \otimes t|^2 \quad , \tag{3.37}$$

for the coherent case.

For lenses with high numerical apertures (> 0.7), the assumptions and approximation made do not hold and therefore more sophisticated models should be used in these cases [Sheppard & Wilson, 1981], [Wolf, 1959], [Richards & Wolf, 1959].

Estimates for the FWHM of the depth response as a function of the normalized pinhole radius, obtained using the models presented in Sections 3.2.4 and 3.2.5 are plotted together in Figure 3.9. Experimental measurements of the depth response for different pinholes sizes (from the confocal microscope presented in Chapter 4) are also shown.

In Figure 3.9 it can be seen that neither model fits the measurements very well. For the smallest pinhole size the paraxial theory model predicts the measured value quite well. For the intermediate values of v_p, though, the Geometric optics/Gaussian beam model provides a better approximation to the experimental measurements. It should be noted that for similar measurements, performed by Wilson and Carlini [1988], the slope of the measurement curve for large pinhole values is greater than the one for the scalar paraxial theory model, in a manner similar to that of the Geometric optics/Gaussian beam model. The reasons stated for the disagreement between theory and measurement are numerous; some of the reasons for the inadequacy of the models can be attributed to:

a) The nominal values for NA and magnification, as given by the manufacturer of the objective lens, and used to estimate the normalized coordinates, may differ from the real ones. This has been also the experience of other researchers [Sheppard, 1992],[Wilson, 1990]. For one of the objective lenses used in the microscope presented in Chapter 4 it was found that the NA was slightly less than the 0.7 value given by the manufacturer (more specifically it was measured to be approximately 0.68)

b) For high NAs, (> 0.7) scalar paraxial theory is not adequate and a theory that takes into account the high angles of convergence should be used [Sheppard & Wilson, 1981].

c) The pupil function was assumed to be constant across the aperture area. Nevertheless, this is not entirely true, and, as it is pointed out by Wilson [1990] and Corle *et al.* [1986], the transmission of the pupil function was found to fall off towards the periphery of the aperture. The same can be seen in the quantum efficiency versus position curves provided by some lens manufacturers. This is particularly apparent in objectives with high NA.

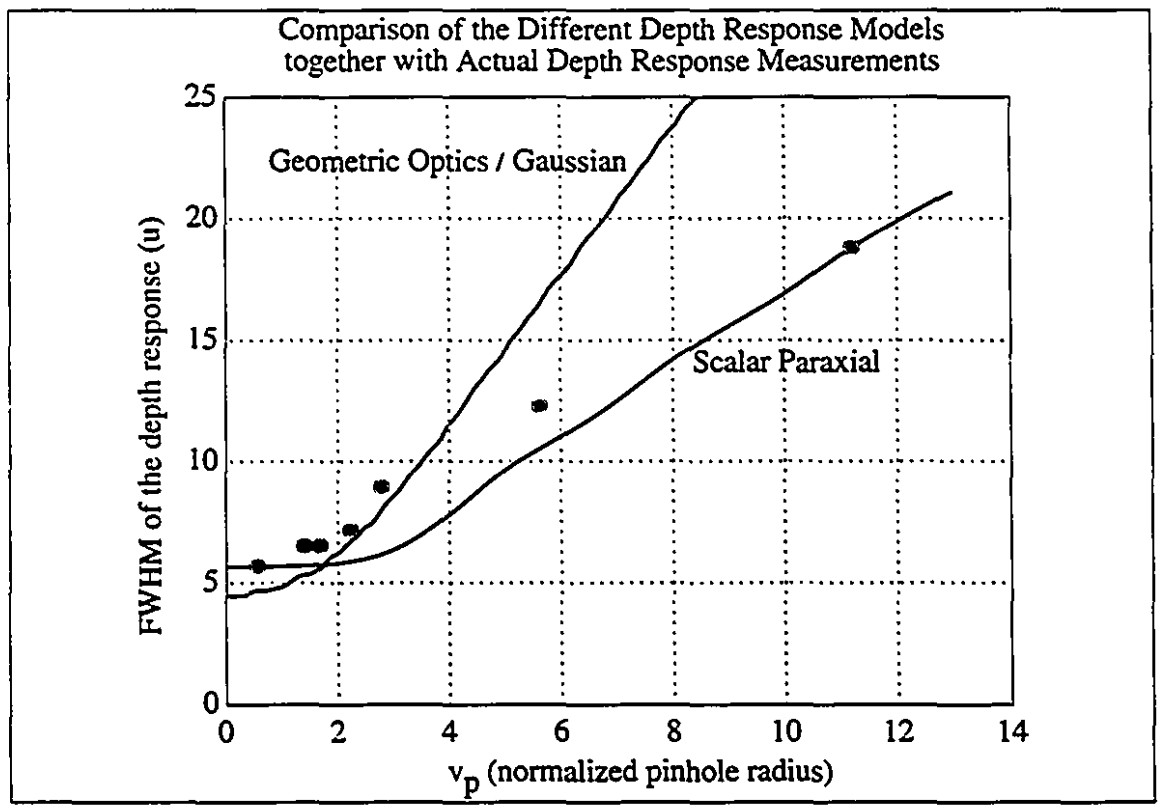

Figure 3.9 *Comparison of the results obtained from the paraxial and Gaussian beam models together with actual measurements (●) performed with the confocal microscope arrangement described in Chapter 4.*

From the above reasons, it is obvious, that the models presented here should be used with caution, and only to get an estimate of the expected performance of a confocal microscope system during the design phase. Nevertheless, these models are important since they do show how the various experimental (physical) parameters (e.g., λ, M, NA) determine the confocal microscope's depth and transverse response.

3.3 Imaging Modes in Confocal Scanning Laser Microscopes.

As mentioned in Chapter 2 CSLM systems offer a number of image contrast modes. These modes include intensity, amplitude, phase, and in some cases, polarization contrast imaging. Although CSLMs can acquire high contrast images of biological samples using only intensity detection, occasionally phase detection is desirable since a number of biological specimens exhibit weaker intensity but stronger phase contrast (variation). Phase detection can be achieved using, among others, interferometric and differential phase contrast arrangements. The CSLM presented in Chapter 4 offers these two modes of operation. The principles of interferometric and differential phase contrast CSLM are presented next, but only briefly, since these two modes are not the most important in the current CSLM design.

3.3.1 Confocal Interference Arrangements

In intensity contrast CSLMs, the detector measures the intensity of the light reflected from or transmitted through the object under observation. Therefore, only the amplitude modulation of the source light is detected. If on the other hand, the phase modulation of the source light must be measured with respect to a reference phase value, an interferometric setup should be used.

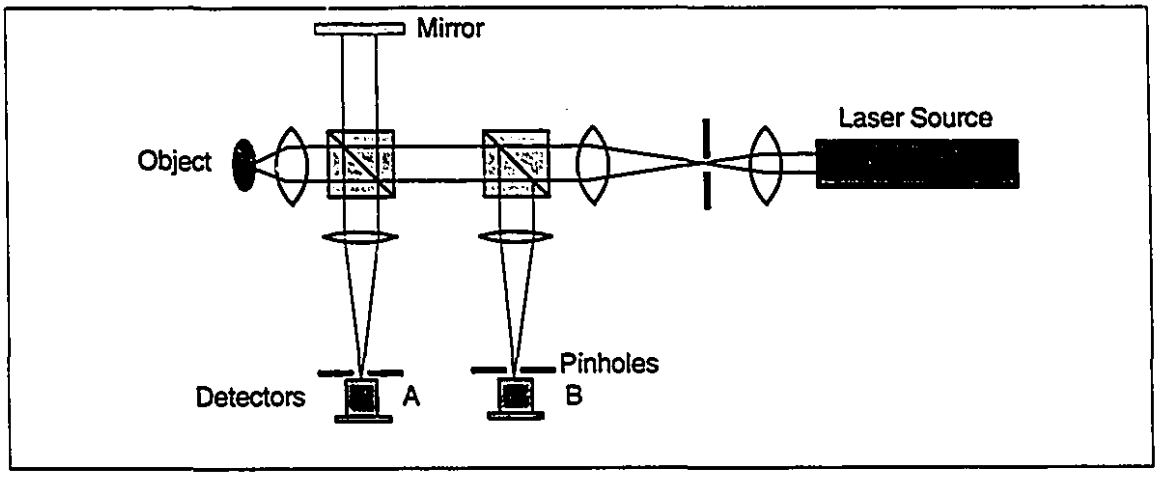

Figure 3.10 *Optical configuration of a two detector Michelson type interferometric arrangement.*

In an interferometric arrangement, such that shown in Figure 3.10, light reflected off the object is combined with a well defined wave reference reflected from a mirror. The resulting beam contains phase as well as amplitude information. To decouple the amplitude and phase information, a number of techniques can be used. A two-detector

interferometric arrangement for measuring the intensity as well as the phase of the light reflected off a sample is described in Chapter 4. The general theoretical formulation of such an arrangement is presented here.

In a confocal interferometric arrangement the confocal complex amplitude image (U) is combined with a reference beam (R) to give the interference image I (measured as the current in the photodetector circuit) :

$$I=|U+R|^2 = U^2 + R^2 + 2Re[R^*U] \quad . \tag{3.38}$$

where R^* denotes the complex conjugate of R, and Re[.] denotes the real part.

The goal is to isolate and measure the spatial distribution of the quantities U^2 and $2Re[R^*U]$. The first one is the conventional intensity image and the second is the phase contrast image (measured modulo 2π).

In order to recover these two terms either a two-detector arrangement [Hamilton & Sheppard, 1982], [Hamilton & Mathews, 1985], [Offside & Somekh, 1992], [Doukoglou *et al.*, 1992] or a phase modulation / demodulation scheme [Wilson *et al.*, 1994] can be used. In a Mach-Zehnder type interference arrangement [Stelzer *et al.*, 1986], the intensity and interference components can be recovered using a single detector but two measurements (for two different amounts of phase retardation of the reference beam) for each image point. Finally, in a similar Mach-Zehnder configuration [Brakenhoff, 1979], the amplitude and phase components are recovered by controlling the ratio of the relative phase and amplitude of the reference beam with the probe beam.

It can be shown from power conservation considerations, that when two optical beams are combined in a beam splitter, the two resulting beams are proportional to the sum and difference of the original ones. Therefore, from the interference of the probe beam (reflected from the sample) with the reference beam, the light intensity reaching the two photodetectors is given by:

$$I_A=|U+R|^2 = U^2 + R^2 + 2Re[R^*U]$$
$$I_B=|U- R|^2 = U^2 + R^2 - 2Re[R^*U] \tag{3.39}$$

The sum of the two detector signals is a function of U, and their difference is proportional to the interference component. The sum ($I_{(+)} = U^2 + R^2$) is the confocal image superimposed on a constant brightness background. The difference ($I_{(-)} = 4Re[R^*U]$) is the interference signal modulated with the conventional confocal signal. By assuming that:

$U=U(v)\exp(j\theta(v))$ and $R=R_0 \exp(j\varphi)$

the difference signal can be estimated to be:

$$I_{(-)} = 4\, U(v)\, R_0 \cos(\theta(v)-\varphi) \qquad (3.40)$$

which is proportional to the phase of the object beam, assuming weak amplitude variations (U(v)=constant) and strong phase variations ($\theta(v)$). For the highest phase detection sensitivity φ should be chosen to be $\equiv \frac{\pi}{2}$.

If the amplitude variations are not weak, it is difficult to differentiate amplitude from phase variations imposed by the object on the probe beam, since phase variations are measured as intensity variations by the detector. Nevertheless, this assumption does not reduce the usefulness of the technique for imaging weakly scattering objects that mainly alter the phase of the probe beam. More details regarding the interference contrast mode in confocal microscopy can be found in [Wilson & Sheppard, 1984, Section 4.3].

3.3.2 Differential Phase Contrast Arrangement.

In interference confocal microscopy, the phase change of the probe beam is measured against the phase of the reference beam, giving potentially, an absolute phase measurement (modulo 2π). When relative phase measurements are required, differential phase contrast (DPC) imaging is used. Using split or quadrature detectors, in a method that was originally-proposed for Scanning Electron Microscopy (SEM) [Dekkers & deLang, 1974], the phase differential of the probe beam can be detected. It should be noted that the originally proposed DPC arrangements rely on the use of a large area split detector, at the expense of depth discrimination. In a modification of the original design, the beam can be split in two parts, each of which is focused onto a point detector, thus allowing DPC imaging while preserving significant depth discrimination. Another approach is the use of a large enough pinhole that allows differential phase measurements while at the same time preserving a reasonable degree of optical sectioning [Atkinson &

Dixon, 1994]. The advantage of DPC lies with its ability to detect very small phase changes of the probe beam. DPC has been used for high accuracy surface profilometry and measurement of small refractive index variations in the object plane. A brief description of the DPC theory follows.

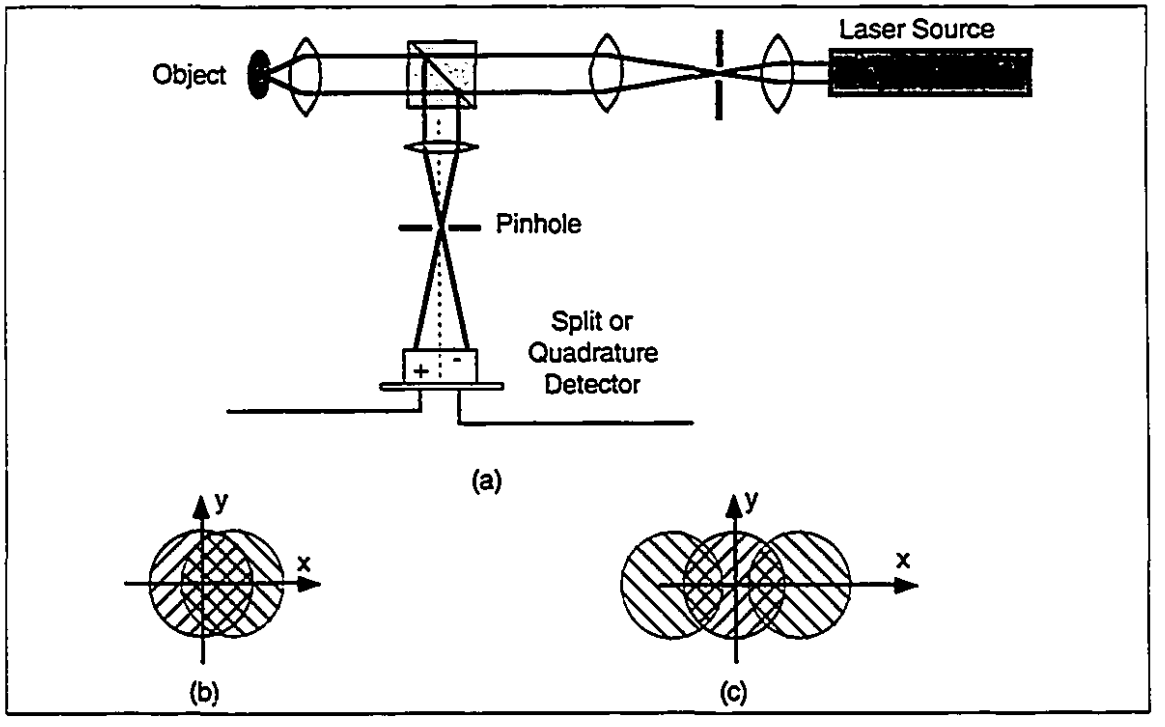

Figure 3.11 *(a) Optical configuration of a differential phase contrast confocal arrangement. (b) Field in the detector plane for the non diffraction case, where the cross-hatched area indicates the region of non-zero field. (c) Case where diffraction is taken into account and the cross hatched areas indicate the areas that the two diffracted beams interfere with the undiffracted one. In both cases the detector is centered on the origin of the coordinates system and is split along the y-axis.*

Ignoring diffraction effects, and assuming an object with complex transmittance (or reflectance) t(x) which exhibits variations along only the x-axis:

$$t(x)=U(x)\,e^{\varphi(x)} \quad . \tag{3.41}$$

It was shown [Hamilton & Wilson, 1984] that by using a split detector and taking the difference signal of the two halves, the measured intensity can be approximated by:

$$I_d(x) \cong U^2(x)\,\frac{d\varphi(x)}{dx} \quad . \tag{3.42}$$

The sum of the two detector halves yields:

$$I_s(x) = U^2(x) \quad . \tag{3.43}$$

Equation (3.42) holds, providing the phase variations are weak and the amplitude is slowly varying or constant. Under these circumstances, the ratio of Equations (3.42) and (3.43) results in a pure DPC measurement ($\propto \frac{d\varphi(x)}{dx}$). Special care should be taken when the sum signal is very small, in which case the ratio can have extremely large values. This situation arises when a very large phase variation is encountered or when the local reflectivity of the sample is very small. DPC, in this case, can be understood as a shift of the object-modulated beam at the detector plane due to phase (or surface height) variation at the object plane. The difference signal from the two detector halves is then proportional to this shift, and consequently, to the phase (or height) variations of the object (Figure 3.11(b)). The analytical derivation for a reflection mode parallel beam system can be found in [Atkinson & Dixon, 1994].

By taking into account diffraction effects, the object's complex transmittance can be described as:

$$t(x) = e^{\beta \cos(2\pi\xi x)} \quad , \tag{3.44}$$

where ξ is the spatial frequency, and β is, in general, a complex quantity to account for absorption.

In this case, the expressions for the detected intensity, when the difference and the sum of the two detector halves is measured, are more complex and can be found in [Hamilton & Wilson, 1984]. The DPC signal at the detector plane is now considered to be the interference of three wave fronts, two diffracted and one undiffracted (Figure 3.11(c)). The two diffracted parts are located on each side of the detector (along the x-axis) and they partially interfere with the undiffracted one. If an unaberrated pupil is assumed [Wilson & Sheppard, 1984] then the intensity at the left area of interference is proportional to:

$$I_{left}(x) \propto (1 + Re[\beta\, e^{-j2\pi\xi x}]) \quad , \tag{3.45}$$

and that of the right is proportional to:

$$I_{right}(x) \propto (1 + Re[\beta\, e^{+j2\pi\xi x}]) \quad . \tag{3.46}$$

The assumption made above is that β is small (which is representative of many biological specimens). For pure phase objects, β can be considered to be imaginary. In practice, usually the imaginary part is much larger than the real part. The opposite is true for amplitude objects.

From equations (3.45) and (3.46) it can be seen that when β is imaginary ($\beta_m \exp(-j\frac{\pi}{2})$), the two signals are opposite in phase, while when β is real, they are in phase. This is consistent with the fact in transmission pure phase objects should not alter the total amount of optical power. The different response for phase and amplitude objects indicates that by adding and subtracting the two halves of the detector, respectively, amplitude and phase information is being imaged.

The CSLM prototype presented in Chapter 4 offers DPC as one of its imaging modes. Although the DPC mode is not essential for the imaging system of the organ mapping setup, it is useful in other applications of the CSLM (i.e. profilometry), and can enhance the image contrast for certain biological specimens.

3.4 Error Analysis in 3D Volumetric Image Acquisition with a CSLM.

One of the big advantages of a confocal arrangement is its optical sectioning property. Due to refractive index miss-match, when volumetric images of transparent or semi-transparent objects are acquired, the actual position of each optical slice does not correspond to the actual displacement imposed on the object (or optics) along the optical axis. This could lead to severe miscalculation of the object's size (or geometry) [Visser & Oud, 1994] [Doukoglou & Hunter, 1995]. In this section the phenomenon is described and an analytical formula is given to correct for this error.

This situation is depicted in Figure 3.12. The distance that the object is displaced along the optical axis is δ_0 but the focal volume is located at $\delta_0+\varepsilon$ (or l_1) below the object's surface. What must be estimated, for a given displacement of δ_0 units along the optical axis, is the actual position of the slice being imaged (l_1) with respect to the object's surface.

3.4.1 Formulation

It is required to estimate the position of the optical slice (l_1) as a function of the mechanical (requested) translation of the object (δ_0). The situation can be simplified by assuming $n_1 > n_0$ (use of a dry objective) and n_1 being constant inside the object under observation. It should also be assumed that $f > l_0$ for the focal point to be inside the material. The numerical aperture of the objective lens is $NA_{obj} = \sin\theta_0$.

According to Snell's law,

$$n_0 \sin\theta_0 = n_1 \sin\theta_1 \Rightarrow \theta_1 = \arcsin\left(\frac{n_0}{n_1}\sin\theta_0\right) \quad . \tag{3.47}$$

From Figure 3.12: $\tan\theta_0 = \frac{d_1}{\delta_0}$ and $\tan\theta_1 = \frac{d_1}{l_1}$

$$\Rightarrow l_1 \tan\theta_1 = \delta_0 \tan\theta_0$$

$$\Rightarrow l_1 = \frac{\delta_0 \tan\theta_0}{\tan\theta_1} \tag{3.48}$$

also, from Figure 3.12: $\tan\theta_0 = \frac{d_0}{f}$. (3.49)

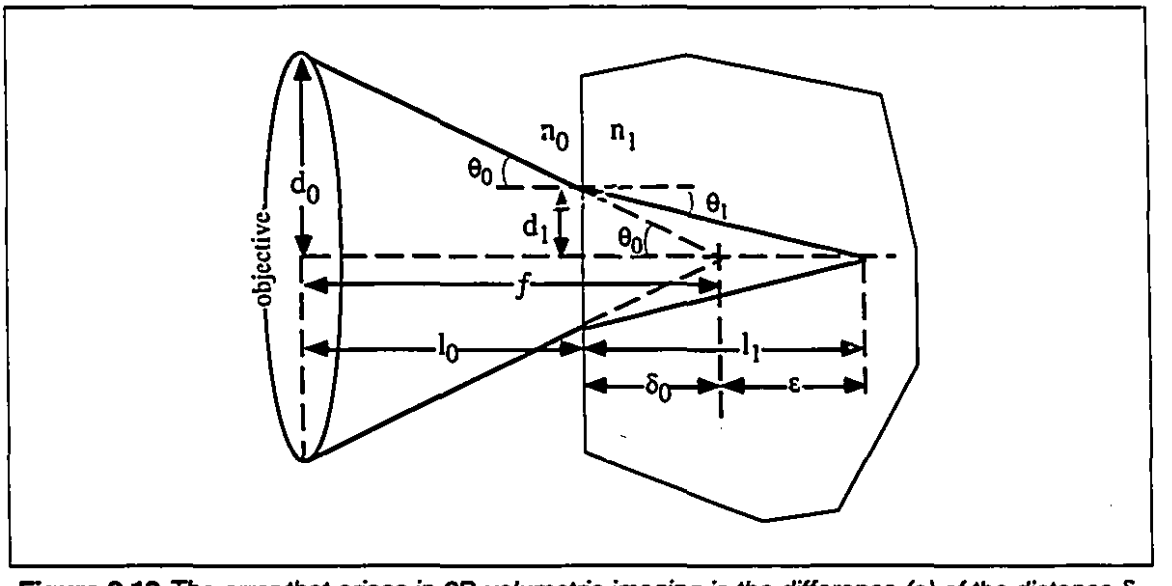

Figure 3.12 *The error that arises in 3D volumetric imaging is the difference (ε) of the distance δ_0 ($= f - l_0$) that the object (or optics) is displaced along the optical axis, and the actual position ($l_0 + l_1$) of the focal volume.*

From Equations 3.48 and 3.49:

$$l_1 = \frac{\delta_0 \frac{d_0}{f}}{\tan\left(\arcsin\left(\frac{n_0}{n_1}\sin\theta_0\right)\right)} \quad . \tag{3.50}$$

Therefore, the apparent error is $\varepsilon = l_1 - \delta_0 = \dfrac{\delta_0 \left[\frac{d_0}{f} - \tan(\arcsin(\frac{n_0}{n_1}\sin\theta_0)) \right]}{\tan(\arcsin(\frac{n_0}{n_1}\sin\theta_0))}$. (3.51)

When using a dry objective (n_0=1), Equation 3.51 is simplified to

$$l_1 = \frac{\delta_0 \frac{d_0}{f}}{\tan(\arcsin(\frac{NA_{obj}}{n_1}))} \quad , \tag{3.52}$$

or

$$\delta_0 = \frac{l_1 f}{d_0} \tan(\arcsin(\frac{NA_{obj}}{n_1})) \quad . \tag{3.53}$$

To verify the above, the following experiment was performed. A microscope glass cover slip of known thickness (~ 154 μm) and refractive index ($n_1 \cong 1.5$) was used as the object. A depth scan was performed by moving the cover slip along the optical axis of the CSLM and through the focal volume of the objective lens. The glass surface is perpendicular to the microscope's optical axis. The front and the rear surfaces of the cover slip can be detected from the intense reflection that the air-to-glass interface exhibits. Given l_1=154 μm, NA_{obj}=0.7, f=3.6 mm, d_0=3 mm and n_1=1.5 and using Equation (3.53) one can estimate $\delta_0 = 97.5$ μm.

From the result of the depth scan using the cover slip as an object, it was found that δ_0 = 95.12 μm. The small difference can be attributed to deviation in the original calculation of l_1, or even in small deviations in the specifications of the objective lens. The photodetector's signal produced from scanning the glass cover slip through the focal point of the CSLM objective lens is shown in Figure 3.13.

Another measurement was performed where two glass cover slips, separated by a known air gap were imaged. The depth profile of this structure was measured by detecting the position of the reflected signal peaks along the optical axis. In agreement with the previous measurement the apparent thickness of the cover slips and the air gap was different from the actual one. As expected the transition from an optically thin (low refractive index) object to an optically denser one (higher refractive index) resulted in a considerable decrease of the apparent thickness. Exactly the opposite is true for a high to

low refractive index transition. The apparent thickness for the two glass layers was 91.8 and 94.1 μm and for the air gap 108.2 μm. The actual thicknesses were 152 μm, 154 μm and 94 μm, respectively.

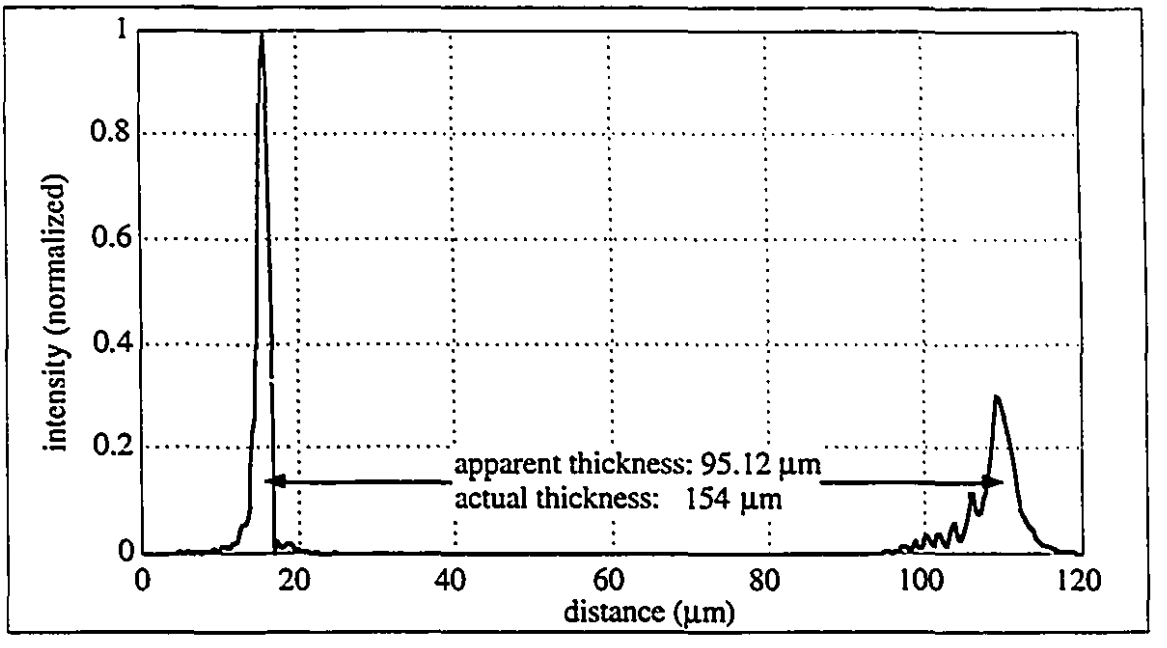

Figure 3.13 *The error that arises in 3D volumetric imaging is measured for a glass cover slip of 154 μm thickness. The peaks correspond to the front and rear surfaces of the glass. The additional side lobes in the signal produced by the rear surface can be attributed to spherical aberrations. The apparent cover slip thickness was 95.12 μm and the theoretical expected outcome was 97.5 μm.*

Therefore, when 3D volumetric imaging is performed, the reconstructed 3D model (of the object under observation) can be inaccurate along the optical axis. The error depends on the spatial distribution and the magnitude of the refractive index changes inside the object. From the formulation above, it can be seen that the volume miscalculation error can be high (38 % in the first experiment described above). The error decreases significantly when corrections are applied by taking into account Equation (3.52). For biological tissue, assuming n_1=1.3 (refractive index of water) is a good first approximation. Furthermore, the use of a water immersion objective will decrease the error significantly. A priori knowledge of the specimen's refractive index and how this index can change within the material (i.e. possible air gaps) can also help in improving the accuracy of the reconstruction.

For surface geometry reconstruction the refractive index mismatch error does not come into effect. This is because in surface profilometry the imaging is performed inside the same medium, unless the surface is embedded in a material different than the imaging medium. The result of the reconstruction can therefore be very accurate (within certain error limits that depend on the size of the depth response for the CSLM).

3.5 Summary

In this chapter an overview of the optical theory governing the operation of a confocal arrangement was briefly presented. Based on scalar paraxial theory, equations describing a confocal arrangement with respect to its transverse (lateral) and depth (longitudinal) response were presented. The effect of the detector size on these responses was also studied using both scalar paraxial theory and a simpler Gaussian beam model. Comparison of the theoretical calculations with actual measurements was also performed. Finally, the error imposed (due to refractive index mismatches) on the acquired 3D volumetric data, and leading to object size miscalculation, was theoretically modeled. An experiment was also conducted to verify the theoretical findings.

3.6 References

Atkinson, M.R. & Dixon, A.E. (1994), "Single-pinhole confocal differential phase contrast microscopy," *Applied Optics*, **33**(4), pp. 641-653.

Born, & Wolf, (1959), *Principles of Optics*, Pergamon Press, Oxford.

Brakenhoff, G.J. (1979), "Imaging modes in confocal scanning light microscopy," *Journal of Microscopy*, **117** (2), pp. 233-242.

Corle, T.R., Chou, C.-H. & Kino, G.S. (1986), "Depth response of confocal optical microscopes," *Optics Letters*, **11** (12), pp. 770-772.

Dekkers, N.H. & deLang, H. (1974) "Differential phase contrast in STEM," *Optik*, **41**, pp. 452-456.

Doukoglou, T.D., Hunter, I.W. & Brenan, C.J.H., (1992) "Myocardial fiber studies using interference confocal microscopy," *Scanning*, **14**(suppl. II), pp. II-72 - 74.

Doukoglou, T.D. & Hunter, I.W. (1995), "Volumetric image distortion due to refractive index mismatch in 3D confocal scanning laser microscopy," *Accepted in IEEE Engineering in Medicine and Biology Conference*, Sept. 1995.

Hamilton, D.K. & Mathews, H.J. (1985), "The confocal interference microscope as a surface profilometer," *Optik*, **71** (1), pp. 31-34.

Hamilton, D.K. & Sheppard, C.J.R. (1982), "A confocal interference microscope," *Optica Acta*, **29** (12), pp. 1573-1577.

Hamilton, D.K. & Wilson, T. (1984b), "Two-dimensional phase imaging in the scanning optical microscope," *Applicd Optics*, **23** (2), pp. 348-352.

Offside, M.J., Somekh, M.G. (1992), "Interferometric scanning optical microscope for surface characterization," *Applied Optics*, **31** (31), pp. 6772-6782.

Richards, B. &Wolf, E. (1959), "Electromagnetic diffraction in optical systems I. Structure of the image field in an aplanatic system," *Proceedings of the Royal Society of London Series A*, **253**, pp. 358-379.

Sheppard, C.J.R., & Wilson, T. (1981), "Effects of high angles of convergence in V(z) in the scanning acoustic microscope," *Applied Physics Letters*, **38** (11), pp. 858-859.

Sheppard, C.J.R. (1992), Personal communication during the Scanning 1992 conference.

Stelzer, E.H.K., Marsman, H.J.B. & Wijnaendts van Resandt, R.W. (1986), "A setup for a confocal scanning laser interference microscope," *Optik*, **73** (1), pp. 30-33.

Visser, T.D. & Oud, L.J. (1994), "Volume measurements in three-dimensional microscopy," *Scanning*, **16**, pp. 198-200.

Wilson, T. & Sheppard, C.J. R. (1984), *Theory and Practice of Scanning Optical Microscopy*, Academic Press, London.

Wilson, T. & Carlini, A.R. (1987), "Size of the detector in confocal imaging systems," *Optics Letters*, **12**, pp. 227-229.

Wilson, T. & Carlini, A.R. (1988), "Three-dimensional imaging in confocal imaging systems with finite size detectors," *Journal of Microscopy*, **149** (1), pp. 51-66.

Wilson, T. (1990), "The role of the pinhole in confocal imaging systems," Chapter 11, *Textbook of Biological Confocal Microscopy*, (Ed. Pawley, J.B.), Plenum Press, New York, pp. 113-126.

Wilson, T., Juskaitis, R. & Rea, N.P. (1994) "Scanning interference microscopy," in *Proceedings SPIE*, Electronic Imaging Science and Technology, pp.199.

Wolf, E. (1959), "Electromagnetic diffraction in optical systems I. An integral representation of the image field," *Proceedings of the Royal Society of London Series A*, **253**, pp. 349-357.

CHAPTER 4

A Confocal Scanning Laser Microscope - Design and Construction

4.1 Introduction - Overview

In this chapter the design and construction of a confocal, reflection mode, object scanning laser microscope is being presented. As mentioned in the introduction the confocal scanning laser microscope (CSLM) is built as the imaging system of a 3D organ mapping apparatus; the other subsystem being the tissue cutting (removing) subsystem. The imaging system is used to acquire detailed 3D volumetric images of the specimen. The tissue machining subsystem will subsequently remove the already-imaged piece of tissue so that the next section of the specimen is exposed for imaging. Initial versions of the CSLM are briefly described in [Doukoglou *et al.*, 1992a,b]. Initial consideration for the design of the tissue cutting subsystem (under construction) are presented in the next chapter.

The most important aspect of the CSLM optical design is the fact that it allows the acquisition of intensity contrast, interference and differential phase contrast images without any change or realignment of its optical components. The design considerations for the CSLM are given first, followed by construction and layout details. The descriptions of the various CSLM subsystems, namely the optical, the mechanical and the computer subsystem are given separately. A list of the CSLM's image acquisition modes

together with example images is also included. Finally some applications of the CSLM outlining its functionality as an independent microscopy apparatus are included in the end of this chapter. Operational details as well as an extensive characterization of the CSLM and its main subsystems are presented in the chapter that follows this one.

4.2 CSLM Design & Construction

The models presented in Chapter 3 (Sections 3.2.3-3.2.6) are important in that they indicate how the critical optical parameters (i.e. numerical aperture(NA), magnification, wavelength, detector size) influence the performance of a confocal optical arrangement. Equations 3.15, 3.20 and 3.22 together with the design criteria listed below were used to select the important components of the optical subsystem, such as the objective and condenser lenses, the detector pinhole, and the laser source. The other components were selected so that signal-to-noise ratio, sensitivity and dynamic range are kept high and optical power losses are kept low.

4.2.1 Design Criteria

The general design criteria of the CSLM are outlined in the Introduction but they are also repeated here.

- Cellular and sub-cellular level imaging capability for biological structures. This translates to submicron lateral resolution.
- Three-dimensional image acquisition capabilities. For the case of a confocal microscope this means that it should exhibit depth discrimination along the optical axis. Depth discrimination in the order of a few μm (≅ 2-3 μm) is desired.
- Acquire images in digital form, so that further processing is possible to extract the information of interest (i.e. cell orientation, tissue density, cell size, isolation of various structures via segmentation, etc.)
- Modular design that allows the incorporation of a tissue removal subsystem, if imaging of the whole organ without the need for sectioning is not possible.

It should be noted that speed of image acquisition is not a design criterion since the specimen studies will be done in vitro. This is not the case for in vivo imaging where the image acquisition should be fast to avoid any image distortion due to motion.

Next an overview of the design and capabilities of the CSLM is presented. In the next chapter an extensive evaluation of the CSLM is performed in order to verify that its performance conforms to the design criteria.

The design of the CSLM is highly modular and consists of three major subsystems. The optical subsystem (Section 4.3), the mechanical/scanning subsystem (Section 4.5) and computer subsystem (Section 4.6). A schematic diagram of the CSLM and the various subsystems is shown in Figure 4.1. At the end of this chapter, photographs of the apparatus are also included.

4.3 The Optical Subsystem

The optical subsystem of the CSLM consists of the following components:

a) A 10 mW HeNe Laser (λ=632.8 μm), is used as the light source.

b) A spatial filter for beam expansion and attenuation of high spatial frequency components.

c) Two beam-splitters. The first one is chosen to be polarizing, so that in conjunction with the $\lambda/4$ plate it can function as an optical isolator and increase the signal reaching the first photo detector (D_1). The second beam-splitter is non-polarizing.

d) Two condenser lenses that focus the light reflected from the sample onto the two photodetectors.

e) Two photodetectors. Three different types of photodetectors were used in the CSLM. Namely, photomultipliers, Si-photodetectors with integrated amplifiers, and avalanche photo diodes (APDs). The APDs were selected because of their small size, high sensitivity and their easily adjustable internal gain.

f) Two pinhole apertures, placed in front of the photodetectors; Different size pinholes determine the effective size of the photodetectors.

g) A microscope objective. Infinity corrected objectives are used in the CSLM. The infinity corrected objective in combination with the secondary (condenser) lens that focuses the reflected light onto the pinhole, offer greater control over the magnification factor (M) of the optical system. The important role M plays in determining the confocality of a scanning microscope setup was discussed in chapter 3. The ability to control M is an important advantage of the CSLM optical arrangement.

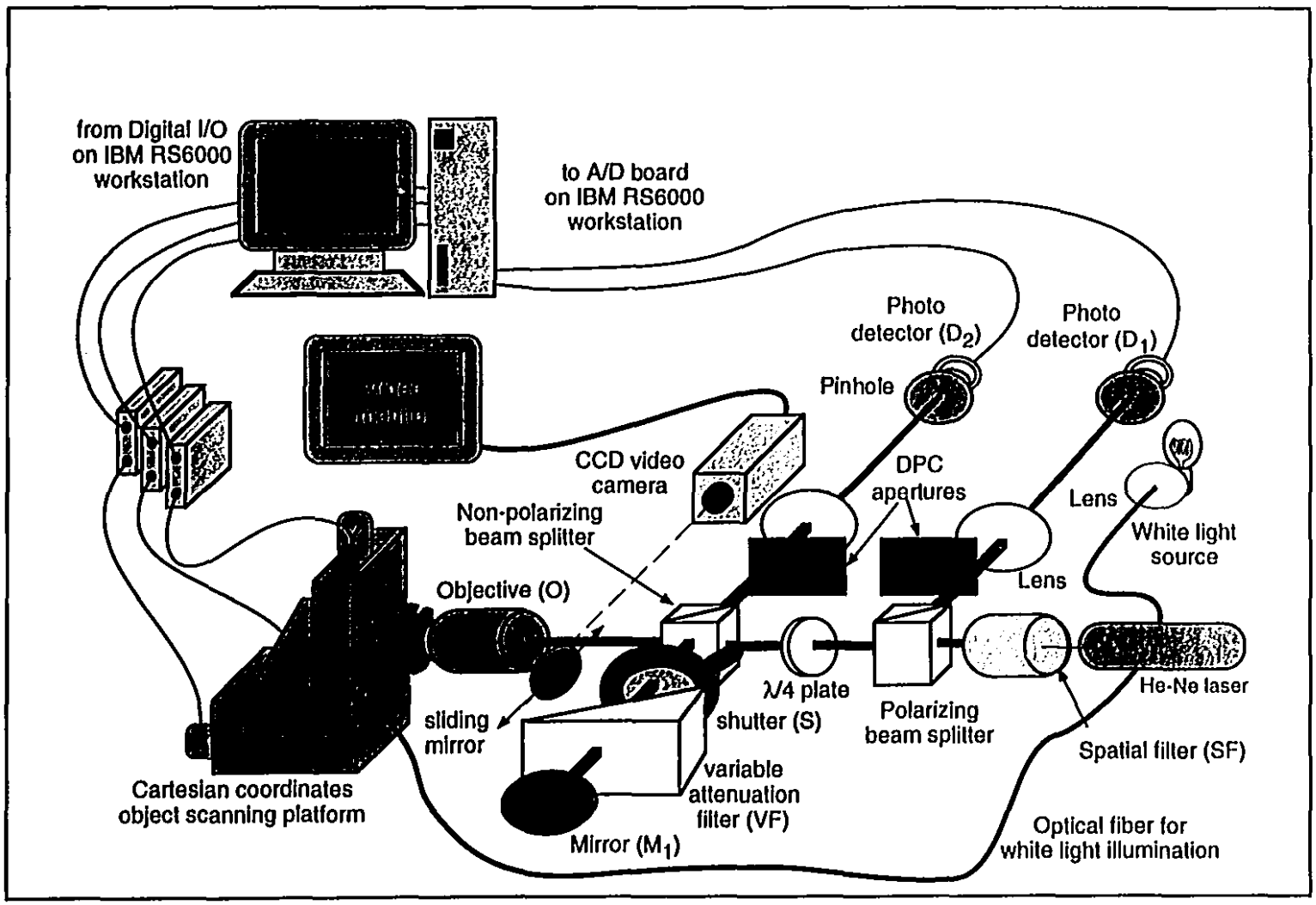

Figure 4.1 *Schematic of the confocal scanning laser microscope.*

For the interference contrast mode of operation the following components are also required:

h) A variable attenuation filter that is located in the interferometer reference beam path. It is used to balance the light power between the two scales of the interferometer.

i) A mirror for the reference beam of the Michelson type interferometric arrangement.

j) A shutter that blocks the reference beam in the non-interference contrast modes of operation.

For the differential phase contrast mode the following components are required:

k) A set of two apertures, placed between the beam-splitters and the condenser lenses, partially blocking the beam wavefront reflected from the sample.

The vertically polarized He-Ne laser beam is expanded to 6 mm in diameter via the spatial filter so that it fills the aperture of the objective lens. After passing through the two cube beam-splitters, one path of the interferometer beam is focused on the specimen by the objective(O). Microscope objectives (dry, water or oil immersion) with different NAs can be used in the CSLM. The reference beam is reflected from the mirror (M_1) after passing through a shutter (S) and a variable attenuation neutral density filter (VF). The beam reflected from the specimen is combined in the two beamsplitters with the reference beam and detected by the two APDs (D_1,D_2). Special attention was given so that the path length of the two arms of the interferometer are equal. The reference beam of the interferometer can be blocked by closing the shutter (S). With S closed, the CSLM operates in a conventional intensity contrast mode. Proper placement of the two apertures in the detection paths of the CSLM, results in a differential phase contrast (DPC) mode of operation. The CSLM optical modes of operation and example images, are presented in Section 4.4.

The CSLM also includes an optical fiber-based white light illumination arrangement. An incoherent white light source is focused onto the core of an optical fiber that delivers the light either behind the specimen holder or very close to the specimen's surface. A sliding mirror can then block the light from the laser source and direct the transmitted (or reflected) white light onto the charge coupled device (CCD) array detector of a video camera. The white light image can then be viewed on a video monitor. The white light illumination arrangement allows for quick investigations of the specimen. The output signal from the CCD camera can also be sent to a frame grabber board installed in the

computer system. White light images of a particular specimen region thus can be digitized and stored in the computer's hard disk.

The optical subsystem is laid out on an optical table supported on four pneumatic cylinders (air bearings) that provide environmental isolation from the building and floor vibrations. A custom-built environmental isolation enclosure [Brenan *et al.*, 1992] is lowered onto the optical table using four pneumatic actuators (pistons) during image acquisition. The enclosure is built around a wooden frame covered with lead and copper sheets. Both the lead (mainly) and the copper layer provide isolation from low frequency acoustical noise. The copper layer also provides insulation against high frequency electromagnetic radiation. The enclosure is lowered onto a square aluminum tubing manifold attached to the optical table. The manifold's function is to establish electrical contact between the optical table and the enclosure and to provide feed-through connections to the components on the optical table. Photographs of the system with the environmental isolation enclosure can be found at the end of this chapter.

4.4 Operating Modes of the Optical Subsystem

The optical subsystem of the CSLM was designed to offer three distinct modes of operation. These are: a) confocal Type 1 and Type 2 intensity contrast mode, b) interferometric contrast mode and c) differential phase contrast mode. The optical configurations for the three different modes of operation are summarized in Figure 4.2. The intensity contrast mode is the most important and also the most frequently used one. The other two modes of operation were included in order to allow phase detection in the case of weakly scattering biological specimens that would exhibit mainly phase contrast. Furthermore, the interferometric mode (in non-confocal configuration) has proven very useful (for position measurements) in the extensive characterization of the scanning subsystem. A fourth contrast mode considered but not implemented in this current prototype is polarization contrast. Polarization contrast can be useful for imaging the anisotropic structure for certain types of tissue.

It can be seen that the CSLM offers these three distinct image contrast modes, with only a few adjustments in the optical subsystem and without realignment of any optical components. This is a unique aspect of the CSLM design that led to the adoption of the optical configuration presented above. The following sections (4.4.1-4.4.3) discuss the three optical modes of operation, and present example images highlighting the differences of the three contrast modes.

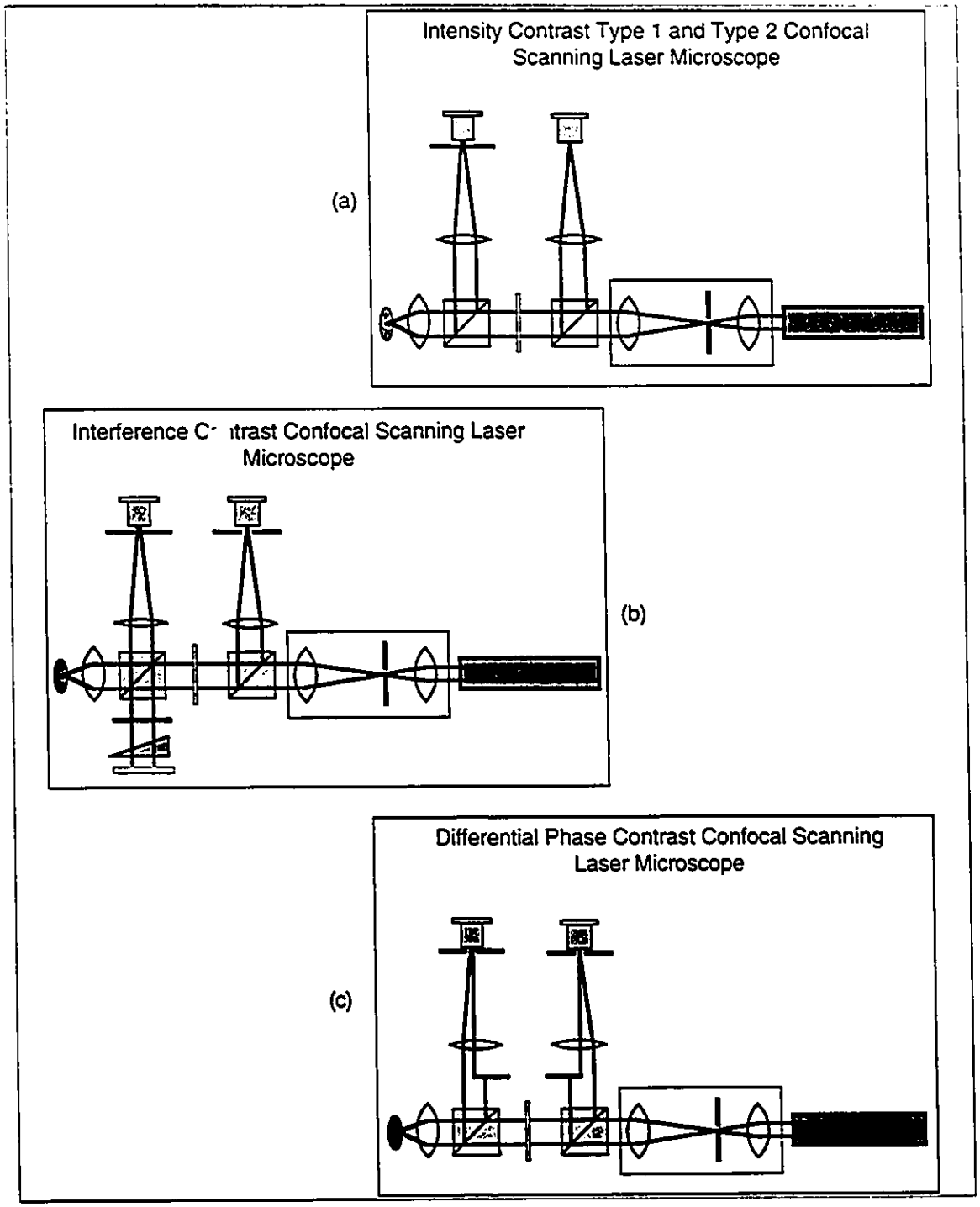

Figure 4.2 *The three different optical modes of operation of the CSLM. (a) confocal Type 1 and Type 2 intensity contrast mode, (b) interference contrast mode and (c) differential phase contrast mode.*

4.4.1 Confocal Type 1 and Type 2 Intensity Contrast Mode.

The intensity contrast mode is shown in Figure 4.2 (a). In this mode of operation, light reflected from the specimen is focused onto the two photodetectors. The first photodetector has no pinhole in front of it so the resulting optical arrangement is that of a Type 1 confocal scanning microscope. The second photodetector has a small pinhole (typically 10 µm in diameter) placed in front of it. By choosing the pinhole size and the magnification factor appropriately, a Type 2 confocal operation can be achieved. Figure 4.3 presents an example of the difference in the resulting image from the two photodetectors.

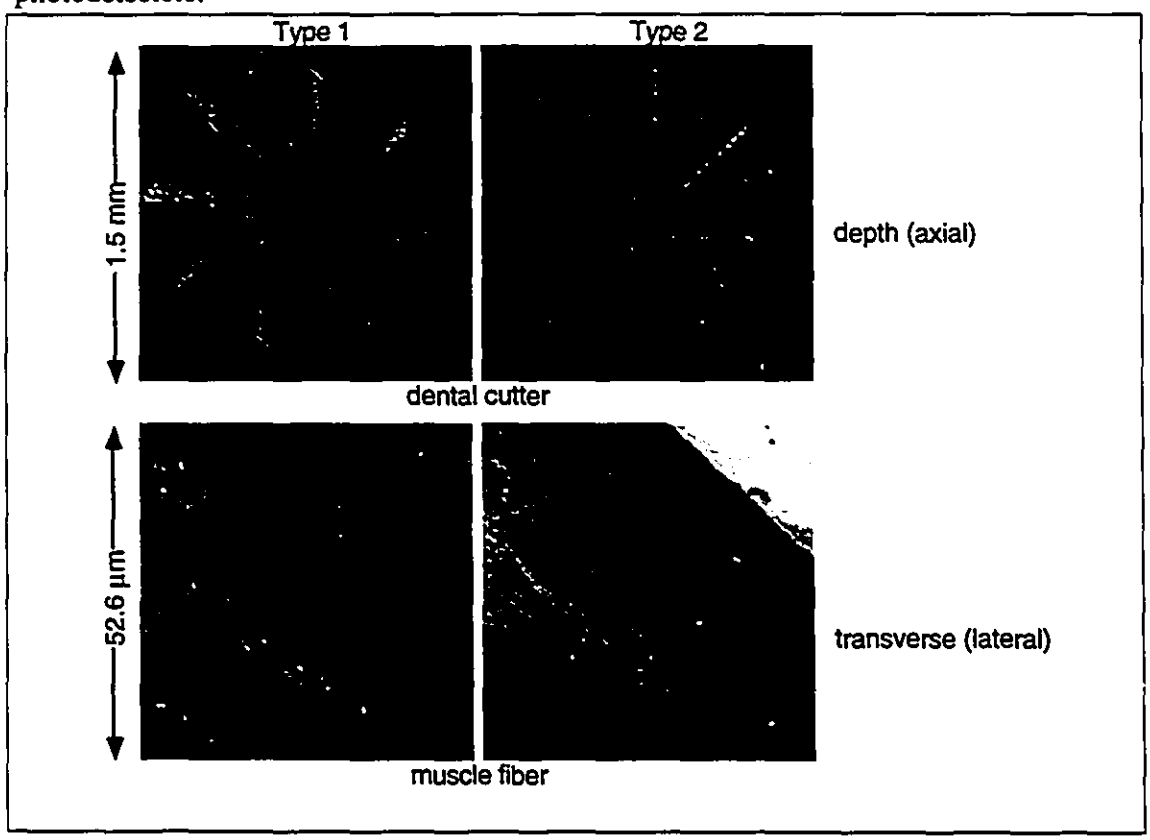

Figure 4.3 *Images acquired with the Type 1 vs. Type 2 intensity contrast mode of operation. Note the improved depth and lateral resolution for the Type 2 mode compared with Type 1.*

The images shown in Figure 4.3 are acquired with the first prototype of the CSLM. The only difference with the currently used one is that the photodetectors were photomultiplier tubes with a large active area. Currently, the difference between the images acquired by the two photodetectors, although significant, is not as drastic. This is because the active area of the APDs (currently used as the photodetectors) is limited to an

area of approximately 250 μm in diameter. The confined active area of the APDs is therefore acting as a detector plane aperture.

4.4.2 Interference Contrast Mode.

To select the interference contrast mode of operation, the optical subsystem must be modified by opening of the S (shutter) and by introducing a second pinhole in front of the detector (D_1). D_1 was used for Type 1 imaging in the intensity contrast mode. The optical arrangement for this mode of operation is shown in Figure 4.2 (b). It is that of a reflection mode confocal interference scanning laser microscope of the Michelson geometry [Hamilton & Mathews, 1985], [Hamilton & Sheppard, 1982]. Both detectors are used in this mode of operation. Light reflected off the sample interferes with the reference beam and is detected in the two photodetectors (D_1, D_2). It can be shown that from power considerations, the signals emerging from the beamsplitter are proportional to the sum and the difference of the input signals [Sheppard & Wilson, 1980]. Therefore, due to the optical arrangement of the microscope, the signal on the two photodetectors exhibits a 180° phase difference and can be described by:

$$I_{D1,D2} = |t|^2 + |r|^2 \pm 2\mathrm{Re}[t \cdot r^*] \quad , \tag{4.1}$$

where t and r are the amplitudes of the object and reference beams, respectively, and * denotes complex conjugate.

Clearly, from the two photodetector signals, both an intensity contrast and an interference contrast image (that contains phase information) can be acquired, by respectively adding and subtracting the two signals.

The interferometric arrangement is very sensitive to external disturbances. The photodetector output will change from maximum (+10V) to minimum (0V) value with a 316.4 nm length change in any of the interferometer arms. Hence even the smallest length change in any of the two arms of the interferometer will generated a fluctuation in the output signal that cannot be attributed to the specimen properties. The arm length changes are caused by both mechanical vibrations or low frequency thermal (temperature) variations. It is thus essential that the apparatus be enclosed in the environmental isolation enclosure (described above) to improve its performance. Example images acquired using the interference contrast mode are shown in Figure 4.4.

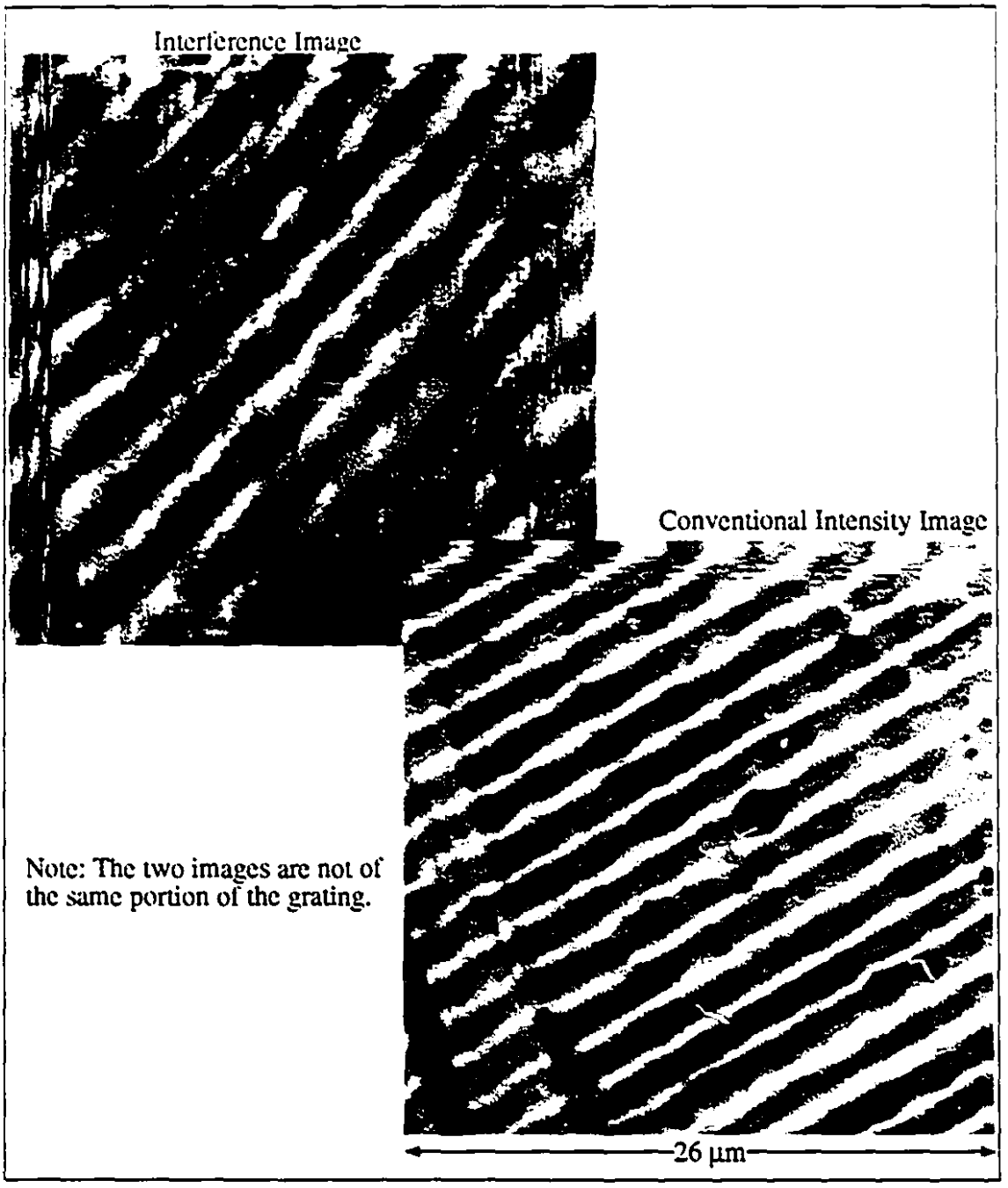

Figure 4.4 *Conventional vs. Interference images of a phase diffraction grating. The spacing of the grating is 13200 lines/inch (1.92 µm line spacing). Note that in the intensity image the transition between the regions of different refractive index is brighter. Conversly, the interference image despite a higher contrast and dynamic range suffers from a poor signal-to-noise ratio.*

The interference image has a higher dynamic range and contrast but with reduced signal-to-noise ratio. The conventional image is less prone to external disturbances but exhibits less contrast. Also the conventional image mainly registers the transition between regions of different refractive indices. The difference of the brightness levels I(x,y) between two regions in the image normalized with respect to the image's average brightness, is the measure of contrast C(I), used to compare the two images.

$$C(I) = \frac{\Delta I(x,y)}{\text{mean}[I(x,y)]} \qquad (4.2)$$

4.4.3 Differential Phase Contrast Mode.

The optical arrangement for the differential phase contrast (DPC) mode of operation is shown in Figure 4.2 (c). The theory behind DPC arrangements has been studied by either ignoring or considering diffraction effects. A brief summary of the theory was presented in Chapter 3. The principle behind a two detector DPC optical arrangement is described in detail in [Atkinson & Dixon, 1994]. The alternative to the two-detector DPC arrangement is the split detector arrangement.

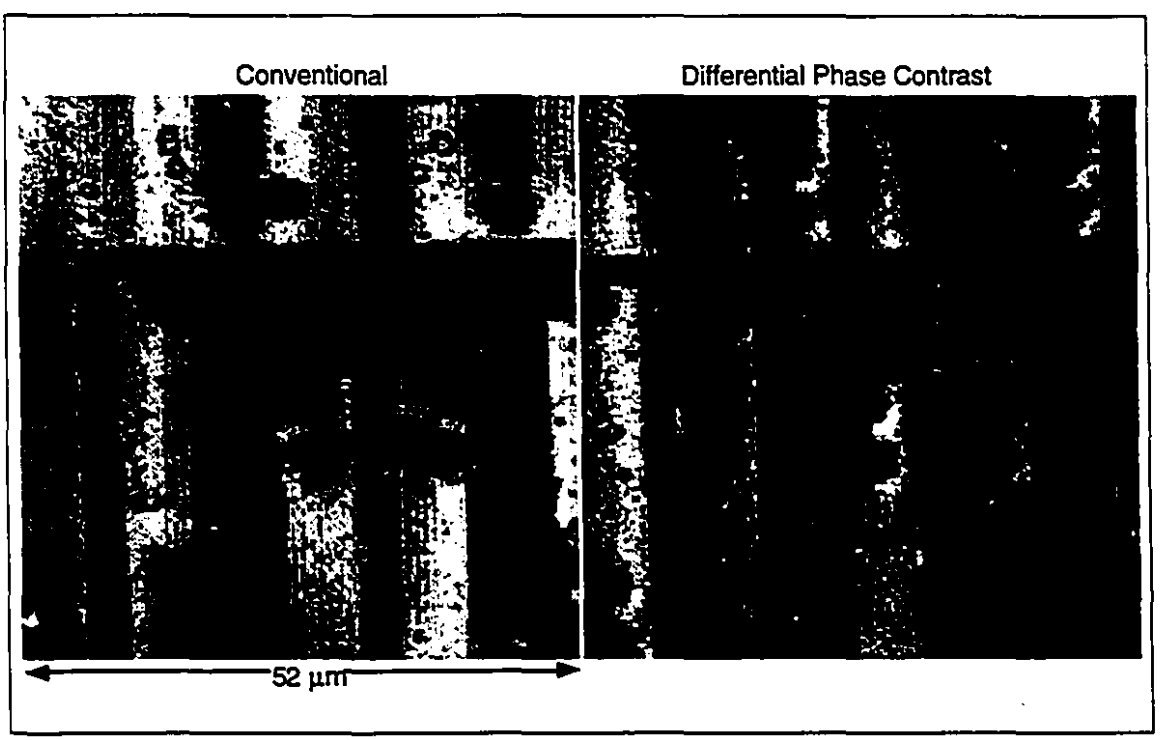

Figure 4.5 *Intensity vs. differential phase contrast images from the CSLM. The DPC image contains information regarding the geometry of the surface. Bright regions indicate positive slope and dark regions negative slope.*

The DPC contrast mode is very useful for visualizing the shape (i.e. surface geometry) of the object and enhancing contrast of point and line features. For DPC imaging, the only modification performed to the optical subsystem is the introduction of the two DPC apertures. The apertures block two opposing beam halves for each of the two photodetectors. For this configuration the shutter (S) is closed, and therefore the reference beam (needed for the interference contrast mode) is blocked.

4.5 Mechanical Subsystem

The mechanical subsystem of the CSLM (see Figure 4.1) is used to translate (scan) the object under observation through the focal point of the objective lens and consists of the following components.

a) A motorized 3-axis linear translation stage. The rotary motion is converted into linear via a 508 μm pitch lead screw. To minimize backlash the stages are preloaded.

b) Three stepping motors (one per linear translation axis) with resolution of 200 steps/revolution.

c) Three microstepping controllers with resolution of 250 microsteps/step for the x and y axis and variable resolution of 1 to 125 microsteps/step for the z (optical) axis.

The command signal to the microstepping motor controllers is generated using custom control software. It is sent to the motor controllers via the digital I/O port of the workstation's data acquisition card. Currently, the translation stage is controlled open loop (without position feedback). Measurements of the accuracy, repeatability and backlash for the linear translation stages were performed by means of laser interferometry. The stage minimum addressable position increment is:

$$\frac{508\ \mu\text{m/rev pitch}}{(200\ \text{steps/rev} * 250\text{microsteps})} = 10.16\ \text{nm}$$ for the x- and y-axes,

and similarly up to 20.32 nm for the z-axis.

The spatial resolution in all three axes was measured to be at least 50.8 nm, for a scan range of less than 250 μm. The resolution of the scanning subsystem was better along the fast axis (x) than the slow one (y) and remained the same even for longer scan ranges (3-4 mm). The repeatability of the scanning subsystem was measured to be better than 158 nm

($\equiv \lambda/4$) for a displacement range of 100 μm over 256 trials. An extensive characterization of the scanning subsystem appears in the next chapter.

The main drawback of the mechanical subsystem is its speed. To improve the positioning accuracy and scanning speed while data acquisition is being performed, the stages must be accelerated to the proper speed and must also be decelerated to a full stop, before changing the direction of motion. Therefore, for a useful scan distance of 100 μm, the actual traveled distance was almost double, depending on the acceleration profile used (linear, parabolic etc.). A detailed description about the operation of the scanning subsystem is given in the next chapter where operational details of the CSLM are discussed.

An alternative 3-D scanning arrangement was designed and is presented in Appendix 2 of the thesis. Only one axis of the design was built and evaluated [Brenan *et al.*, 1993]. This 1D scanning arrangement is presented in the paper included as part of Appendix 2. The novel scanning arrangement design is based on a direct parallel drive scheme that utilizes linear actuators [Hunter *et al.*, 1990]. The scanning platform design discussed in Appendix 2 is not used in the CSLM since the full 3-axis version is not completed yet.

4.6 Computer & Data Acquisition Subsystem

The computer subsystem consists of a UNIX workstation (IBM RS/6000 model 320), equipped with a Digital/Analog I/O card (BurrBrown model PCI 602W). The data I/O card supports up to eight differential, 12-bit, variable gain and range analog-to-digital (A/D) channels, two 16-bit digital-to-analog (D/A) channels, two 8-bit wide digital I/O ports, a counter, a burst generator, and an external trigger input. For operating the CSLM two A/D channels for sampling the photodetector signal and the two digital I/O ports for driving the 3-axis translation stage are required.

4.6.1 Computer Software

The control of the CSLM functions is performed via a custom software package written in the C programming language. The CSLM software is driven using a multi-window graphical user interface. Under software control the CSLM can offer a multitude of image acquisition modes. It can acquire 2D and 3D images as well as image sequences with user specified spatial arrangement. These different image acquisition modes are described next. Appendix 1 presents how the different image acquisition modes can be selected, and

how the various image parameters are specified. A brief description of the graphical user interface and its functionality is also included in Appendix 1. A simplified block diagram of the CSLM user interface software shown in Figure 4.6. The purpose of some of the CSLM software blocks (appearing in Figure 4.6) becomes apparent in the sections that follow.

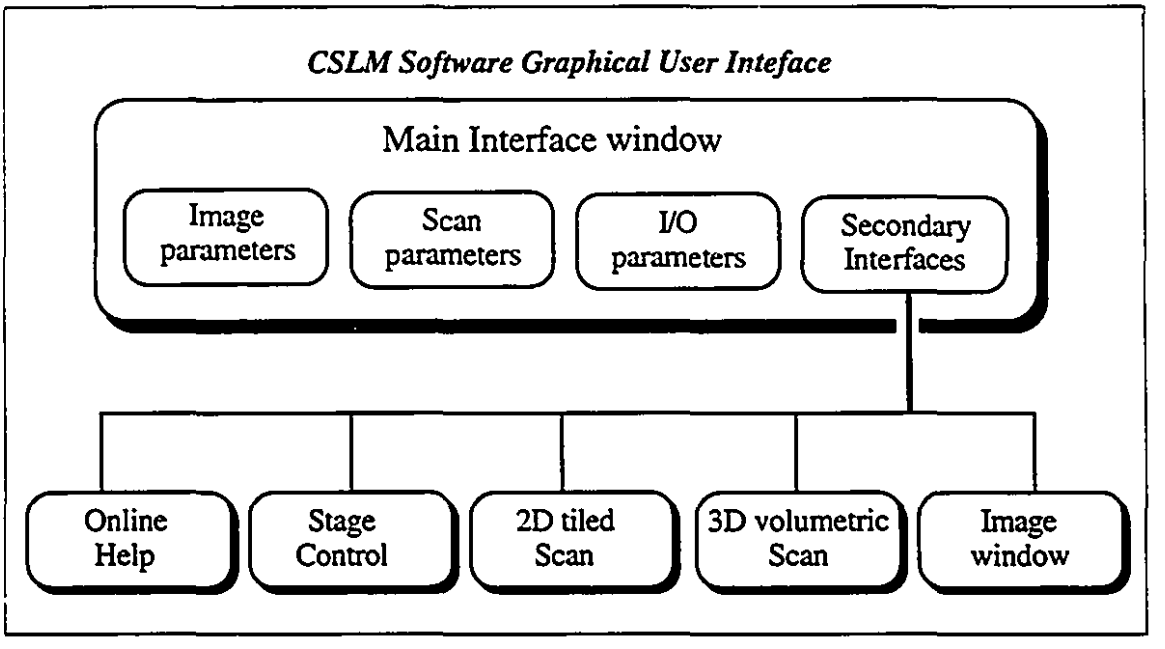

Figure 4.6 *The CSLM graphical user interface (GUI) block diagram.*

4.6.2 The Image Acquisition Modes

The data acquisition protocol of the CSLM is software-controlled. Via its software the CSLM provides of a number of different image acquisition modes. 2D and/or 3D images, as well as measurements of the optical sectioning capabilities of the optical subsystem, can be performed without any hardware or software modification.

4.6.2a Two Dimensional Image Acquisition Mode

In this mode the CSLM acquires images of the specimen that are on the plane which is transverse to the optical axis of the microscope. The size and resolution of the images can be specified by the user. The image size is limited by the amount of the available RAM in the computer system and the resolution by the smallest motion increment of the motion/scanning subsystem. The user-specified image resolution is the spatial distance between the image pixels and is completely independent of the resolution of the optical subsystem which is the minimum distance between two points that can be resolved as

separate. When the specified image resolution is smaller than the resolution of the optical subsystem, blurring occurs. If an image is acquired with resolution smaller than the optical resolution, deconvolution may be performed to reconstruct (partially) the attenuated higher spatial frequencies of the image [Doukoglou, 1989]. During this mode of operation the user can specify other parameters (i.e. speed of scanning, direction of scanning) that are described in greater detail in Appendix 1, where a brief overview of the CSLM software graphical user interface is given.

4.6.2b Two Dimensional Tile Mode

The two-dimensional tile mode permits the acquisition of a sequence of 2D images. All images are on the plane transverse to the optical axis of the CSLM. The spatial distribution of these 2D images is user specified but their spatial relation resembles that of floor tiles, hence the name tile mode. One example of such an image is shown in Figure 4.7. The size of the grid is variable and the only limit is the amount of secondary storage (hard disk, magnetic tape) of the computer system. The 2D tile mode is more suitable for acquiring a high resolution image of a large area of the specimen. It is also useful for measuring the spatial distribution of a specimen property (i.e. fiber orientation, density) over a large area. In the later case each image tile is processed individually in order to determine the value of the desired property within the tile. By knowing the spatial relation between the image tiles, a spatial distribution map of the measured property can then be reconstructed. Appendix 1 describes how the parameters that control the spatial distribution of the tiles (i.e. size of the tile grid, amount of overlap if any between the tiles).

4.6.2c Three Dimensional Surface-Tracing Mode

In the surface tracing mode of operation, the depth discrimination property of the CSLM is utilized to measure the surface geometry and reflectivity of an object. Although this mode is more appropriate for imaging opaque objects, it can nevertheless be used with transparent and semi-transparent objects. During the 3D surface tracing mode, at each image pixel location, the scanning system searches along the optical axis for the highest reflectivity value. The acquired image has 2 values per pixel which correspond to the reflectivity of the surface at that point and the coordinate along the optical axis where the maximum reflectivity occurs. The information in each image can then be used to reconstruct a 3D model of the image surface. An example of this type of image set is shown in Figure 4.8.

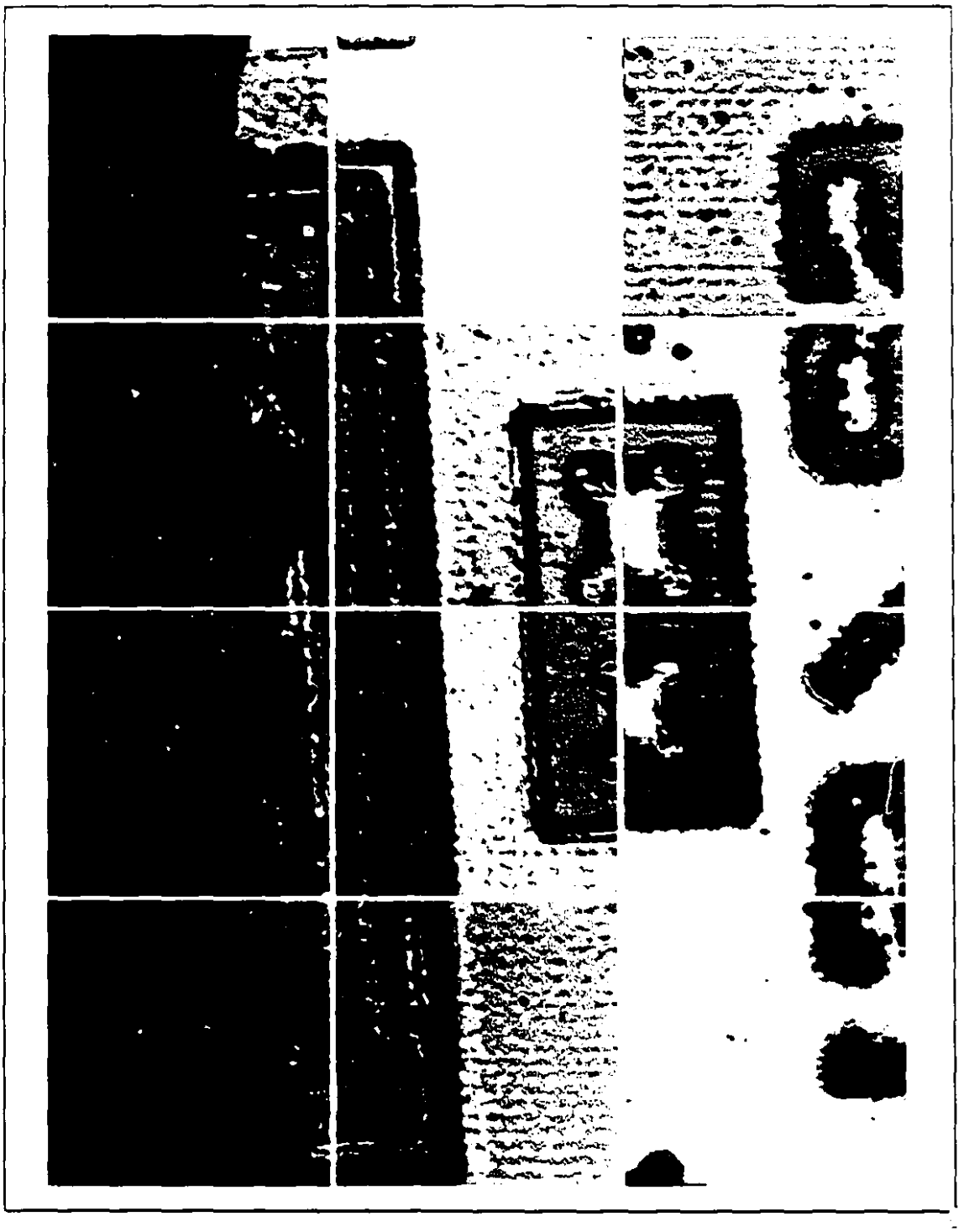

Figure 4.7 *Example of a tile mode image. The composite image consists of 12 smaller images each 256 x 256 pixels at 0.1 µm/pixel resolution arranged in a 4x3 grid.*

4.6.2d Three Dimensional Volumetric Image Acquisition Mode

The optical sectioning property (depth discrimination) of the CSLM is again utilized in the three dimensional volumetric image acquisition mode of operation in order to acquire a sequence of 2D (x,y) images along the microscope's optical axis. An example from such a sequence of images is shown in Figure 4.9. This image acquisition mode is useful in visualizing the 3D geometry of a specimen. The image sequence along the optical axis can be processed to retrieve information regarding the surface geometry and internal structure of transparent and semi-transparent specimens. From this information a 3D geometric model of the specimen can be reconstructed. Due to refractive index mismatches (between the refractive indices of the imaging medium and the specimen), the accuracy of the reconstruction is limited. The error (due to refractive index mismatch) that affects the accuracy of the 3D reconstruction and how it can be corrected was discussed in detail in Chapter 3.

4.6.2e Depth Response Investigation Mode

The most frequently performed operations with the CSLM is the acquisition of 2D (x,y) images. During the construction phase another frequent measurement is that of the CSLM's depth response. The depth response is measured every time a change is applied to the optical or mechanical subsystems of the CSLM. It is a quick way to check whether the modification had the desired effect. Furthermore, the depth investigation mode is useful before a volumetric image acquisition is performed. The reflected light intensity for a 1D scan along the optical axis of the CSLM is measured first. The resulting 1D signal indicates the position of the front surface, and gives a good indication of how deep inside the specimen an image slice can be acquired before the SNR is too low or the reflected intensity becomes too weak to be detected.

4.6.3 Data Processing

The acquired digital images may be subjected to numerous image processing techniques. This section describes the data processing methods required to present the acquired images on the workstation screen and to reconstruct the 3D surface profile of the specimen. The more general 2D image processing techniques applied to the CSLM images are presented in the next chapter.

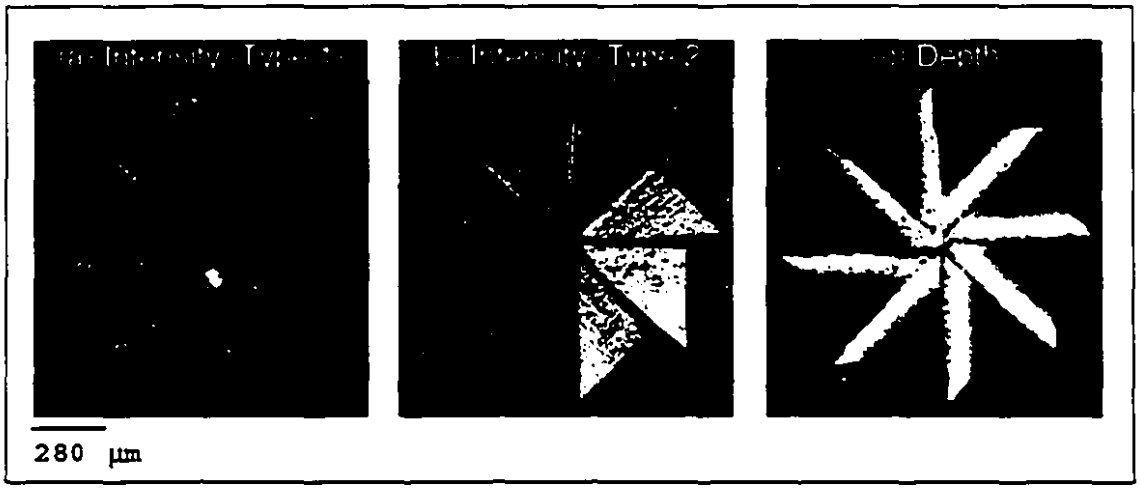

Figure 4.8 *Example of a surface tracing image acquisition mode of the CSLM. The picture is that of the tip of a dental tool. The intensity images represent the reflectivity of the surface when using Type 1 and Type 2 configurations. The depth image represents the geometry of the surface (brightness is proportional to surface height).*

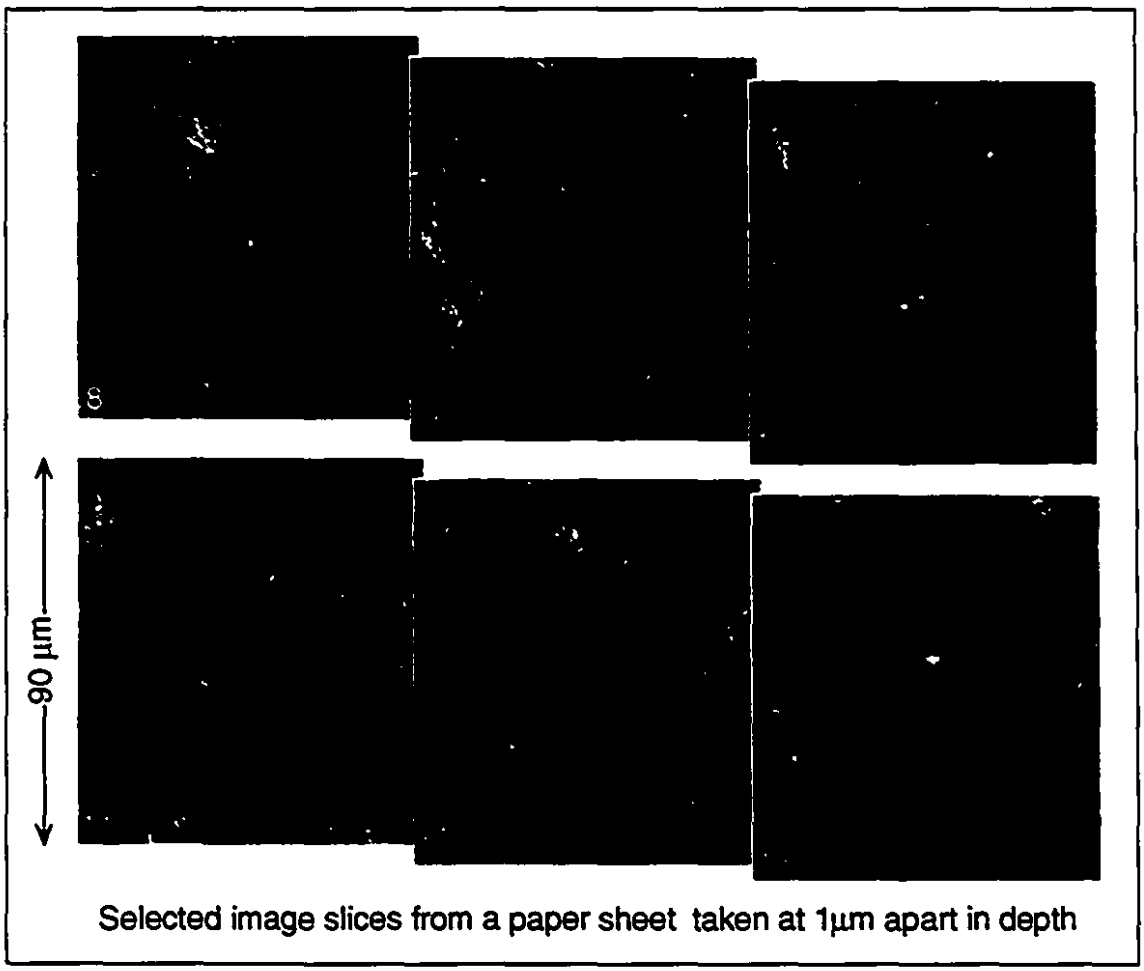

Figure 4.9 *Example of volumetric image acquisition from the CSLM. Images are that of a paper sheet and are 320 x 320 pixels at 0.2 µm/pixel resolution. Slices are spaced 1 µm apart. Lower slice index indicates larger distance from the objective lens.*

Using a sequence of N two-dimensional CSLM images acquired along the optical axis of the microscope, the surface geometry of the object under observation can be reconstructed. For the sequence of N 2D images, and for each (x,y) location, the highest intensity value and the location along the optical (z) axis where this highest value occurs are found. Using this procedure, the sequence of the N images is reduced to two 2D images: one representing the surface reflectivity ($S_r(x,y)$) and the other the surface geometry ($S_g(x,y)$). $S_r(x,y)$ is also referred to as the extended focus image.

More rigorously, the above process can be described as:

for $i_k(x,y)$ k=1...N, and for each (x,y) position

$$S_r(x,y) = \max_{k=1...N}[i_x(x,y)] \quad ,$$

and $$S_g(x,y) = \mathrm{Loc}(\max_{k=1...N}[i_x(x,y)]) \quad , \qquad (4.3)$$

where the Loc(.) function returns the value of k for which the $\max_{k=1...N}[i_x(x,y)]$ occurs.

When applying the surface reconstruction process to a sequence of images, it is assumed that the maximum reflectivity occurs at the surface of the object. This is true for most opaque and semi-transparent objects but this method should be used with caution with fluorescent and transparent specimens. In the latter case, 3D volume-rendering algorithms can be used to reconstruct not just the surface but the complete volume geometry of the specimen.

When doing surface reconstruction, it is also assumed that there is adequate registration between subsequent images. Adequate registration means misalignment of less than one pixel between consecutive images. Sub-pixel miss-registration correction, although possible using Fourier Transform interpolation techniques, is not used in the CSLM images mainly due to storage requirements. For integer pixel miss-registration, cross-correlation based methods can be used to align the image slices. For the case of the CSLM images registration is usually adequate and therefore there was no need for correction.

A brief mention of deconvolution methods that can be used to reduce the influence of the optical system from the acquired images can be found in [Doukoglou *et al.*, 1988]. Deconvolution can be used to increase image resolution and contrast. Details regarding the other 2D image processing operations frequently applied to the CSLM images are presented in the next chapter.

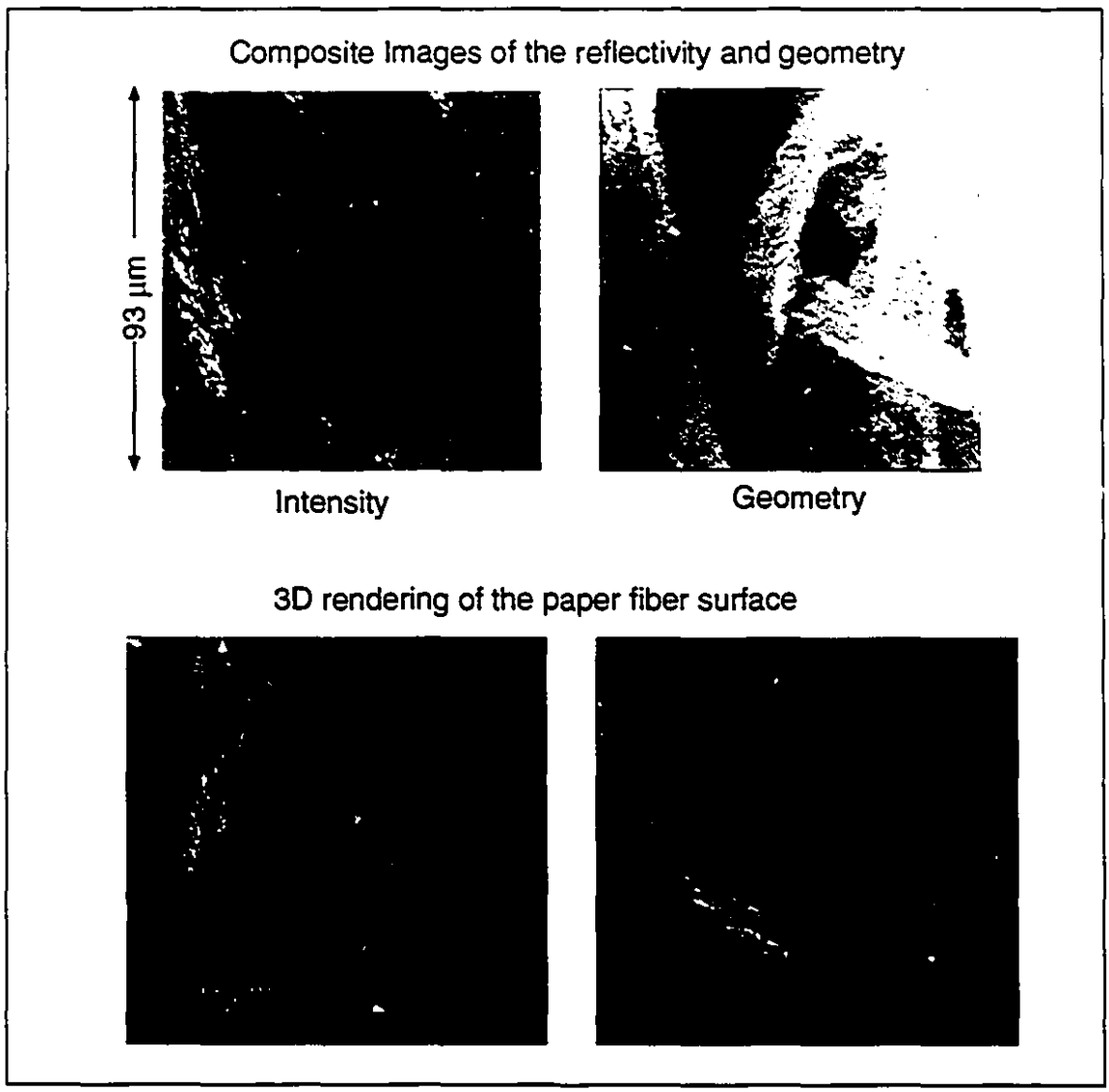

Figure 4.10 *Example of 3D surface reconstruction from a series of CSLM optical slices along the optical axis.*

4.7 Applications of the CSLM

The confocal microscope presented in this chapter is designed as the imaging system of a 3D organ mapping apparatus (still under development). Nevertheless, the CSLM by itself is a complete microscope system with its multi-window user interface (see Appendix 1), thus making it an attractive tool in the study of various materials (such as dental tissue or micro-fabrication structures). The CSLM even in its initial stages of development was used for acquisition of microscopic images of a variety of specimens (biological and non). Some of the applications that were used and are going to be used in the near future are presented next.

4.7.1 Dental Studies

Confocal microscopy has been used to observe features like osteocyte lacunae and canaliculi in bone and prism boundaries in dental enamel [Boyde *et al.*, 1983] and dental caries [Jones & Boyde, 1987]. The CSLM developed in this thesis was used to image a number of dental samples. The samples (prepared by Dr. Ivan Stangal of McGill University, Department of Dentistry) were from tooth enamel and the properties to be investigated are the size and density of the tubules that penetrate through the enamel and into the dentin. The surface of the samples was smeared from the cutting. Therefore images should be acquired below a thin (2-3 μm) surface layer. Some preliminary images from these samples are shown in Figure 4.11 below. Additionally, surface characterization (i.e. roughness and thickness of residual surface film) can also be measured in these samples.

4.7.2 Micro-Fabrication Structure Imaging

One other project in progress in the Biorobotics laboratory at MIT is the development of a novel micro-fabrication method based on either spatially constrained electro-deposition [Madden & Hunter, 1994], or Excimer laser machining. In order to assess the success and usefulness of these techniques quantitative measurement of the fabricated structures should be performed. The CSLM was already shown to be an excellent non-contact micron resolution profilometer for opaque structures and was used successfully to measure. Using it in the interferometric mode, the measurement accuracy can be increased to sub-micron resolutions. An example of a 3D image of a 1.7 μm high feature from a silicon EPROM chip, that demonstrates the capabilities of the CSLM, is shown in Figure 4.12 below.

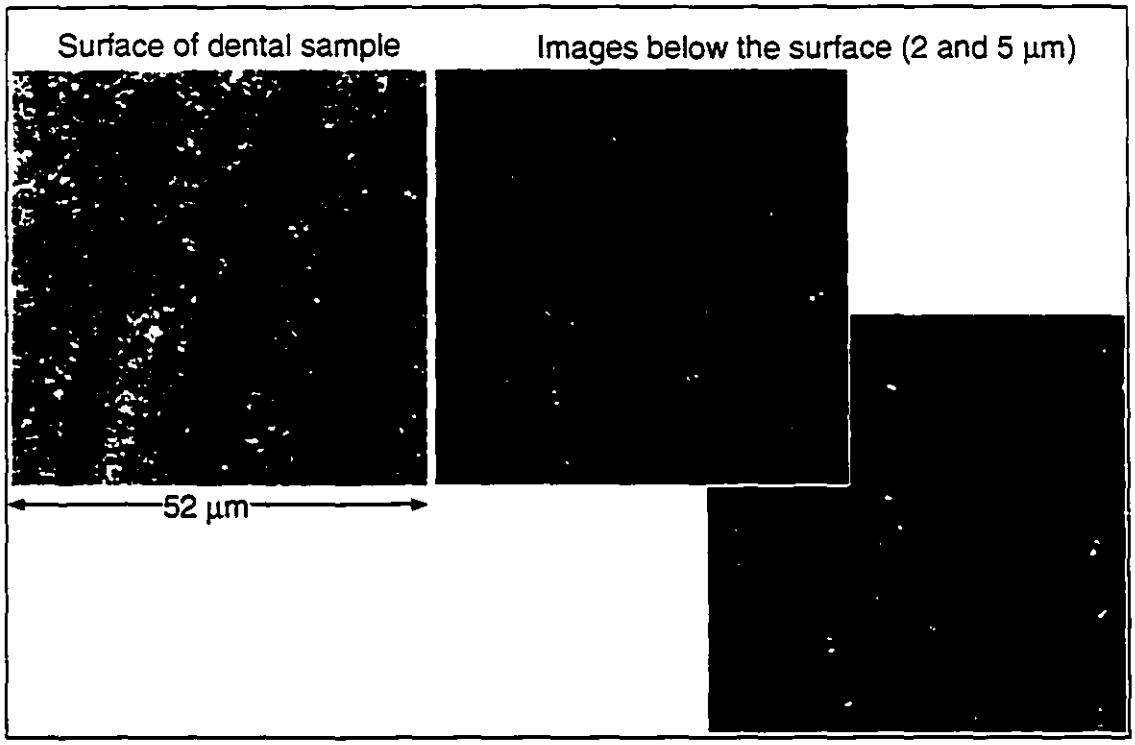

Figure 4.11 *Images of dentine surface (on the right) and 2 and 5 μm bellow the surface of the enamel. The bright spots are tubules that penetrate through the enamel into the dentin. The size and concentration of these tubules are of interest .*

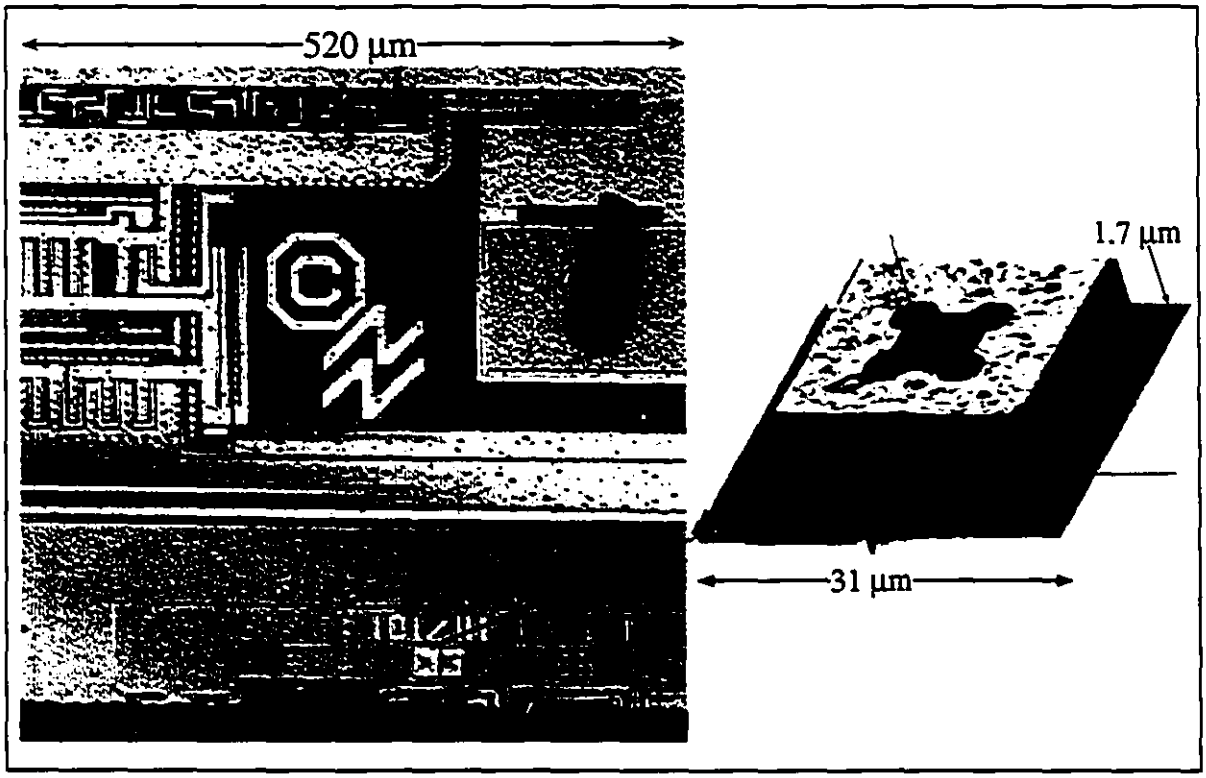

Figure 4.12 *(a) Image of a small portion of a silicon chip and (b) a 3D volumetric image of a 1.7 μm height feature. The 3D image is a magnification of the outlined section of the image on the right.*

4.8 Conclusions

A complete, reflection-mode, object scanning confocal scanning laser microscope system, capable of operating in three distinct modes, was presented. The CSLM is capable of confocal Type 1 and Type 2 intensity, interference and differential phase contrast imaging. The computer controlled CSLM can perform image acquisition in different formats (i.e. 2D or 3D). Example images from different modes of operation were presented. The CSLM is designed for performing studies of biological organs (structures) at the cellular level. It is also the imaging subsystem of a more complex apparatus that would allow the 3D imaging of whole organs (organ-mapping system).

In designing and building the CSLM, a number of related products have been developed and tested. In Appendix 2, a novel scanning arrangement design is presented. A prototype of one axis [Brenan *et al.*, 1993] of the 3-axis design was built and is used for scanning the mirror in an FT Raman microscope [Brenan & Hunter, 1994]. Furthermore, a simplified and miniaturized spherical coordinate scanning confocal microscope [Doukoglou & Hunter, 1995] is presented in Chapter 6 of the thesis. This microscope is very well suited for imaging of organs exhibiting quasi-spherical shape (e.g. the eye). In the chapter that follows, important details regarding the operation and characterization of the CSLM system are presented.

4.9 References

Boyde, A., Petran, M. & Hadravsky, M. (1983), "Tandem scanning reflected light microscopy of internal features in whole bone and tooth samples," *Journal of Microscopy*, **132**, pp. 1-7.

Brenan, C.J.H., Charette, P.G. & Hunter, I.W. (1992), "Environmental isolation platform for microrobot system development," *Review of Scientific Instruments*, **63** (6), pp. 3492-3498.

Brenan, C.J.H., Doukoglou, T.D., Hunter, I.W., & Lafontaine, S. (1993), "Characterization and use of a novel optical position sensor for microposition control of a linear motor," *Review of Scientific Instruments*, **64** (2), pp. 349-356.

Brenan, C.J.R. & Hunter, I.W. (1994), "Chemical imaging with a confocal scanning FT-Raman microscope", *Applied Optics*, **33**(31), pp. 7520-7528.

Dekkers, N.H. & deLang, H. (1974), "Differential phase contrast in STEM," *Optic*, 41, pp. 452-456.

Doukoglou, T.D. & Hunter, I.W. (1995), "A spherical-coordinate scanning confocal laser microscope," *Optical Engineering*, **34**(7), pp. 2103-2108.

Doukoglou, T.D., Hunter, I.W. & Brenan, C.J.H., (1992a) "Myocardial Fiber Studies using Interference Confocal Microscopy," *Scanning*, **14**(suppl. II), pp. II-72 - 74.

Doukoglou, T.D., Hunter, I.W. & Brenan, C.J.H. (1992b) "Confocal Scanning Laser Microscopy for Muscle Fiber Orientation Studies," in *Proceedings of Canadian Medical and Biological Engineering Conference*, **18**, pp. 106-107.

Doukoglou, T.D. (1989), "Non-parametric system identification techniques for numerical deconvolution of scanning laser microscope images," *Master Thesis*, Dept. of Electrical and Biomedical Eng., McGill University.

Doukoglou, T.D., I.W. Hunter, R.E. Kearney, S. Lafontaine & P.F. Nielsen (1988), "Deconvolution of Laser Scanning Microscope Images using System Identification techniques," *Proceedings Canadian Medical and Biological Engineering Conference*, **14**, pp. 105-106.

Hamilton, D.K. & Mathews, H.J. (1985), "The confocal interference microscope as a surface profilometer," *Optik*, **71** (1), pp. 31-34.

Hamilton, D.K. & Sheppard, C.J.R. (1982), "A confocal interference microscope," *Optica Acta*, **29** (12), pp. 1573-1577.

Hunter, I.W., Lafontaine, S., Nielsen, P.M.F., Hunter, P.J. & Hollerbach, J.M. (1990), "Manipulation and dynamic mechanical testing of microscopic objects using a tele-micro-robot system," *IEEE Control Systems Magazine*, **10**, pp. 3-9.

Jones, S.J. & Boyde, A. (1987), "Scanning microscopy observation on dental caries," *Scanning Microscopy*, **1**, pp. 1991-2002.

Madden, J. & Hunter, I.W. (1994), "3D Micro-fabrication by localized electrochemical Deposition," *Journal of Microelectromechanical Systems*, in press.

Sheppard, C.J.R., & Wilson, T. (1980), "Fourier imaging of phase information in scanning and conventional optical microscopes," *Philosophical Transactions of the Royal Society of London A*, **295**, pp. 513-536.

Plate 4.1 *Picture of the CSLM setup where the optical table, environmental isolation enclosure and computer systems are shown.*

Plate 4.2 *Picture of the CSLM's optical subsystem.*

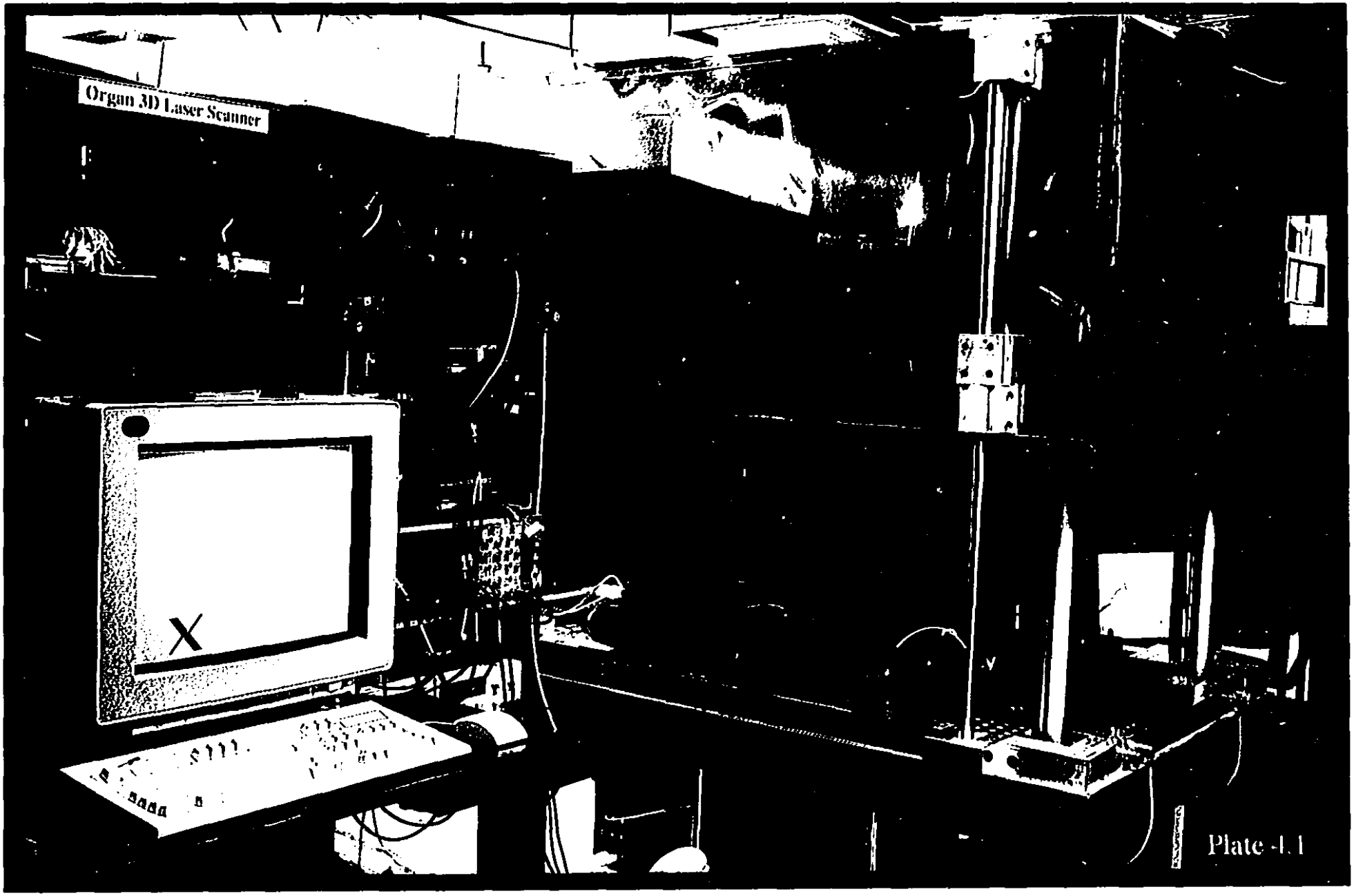

Plate 4.1

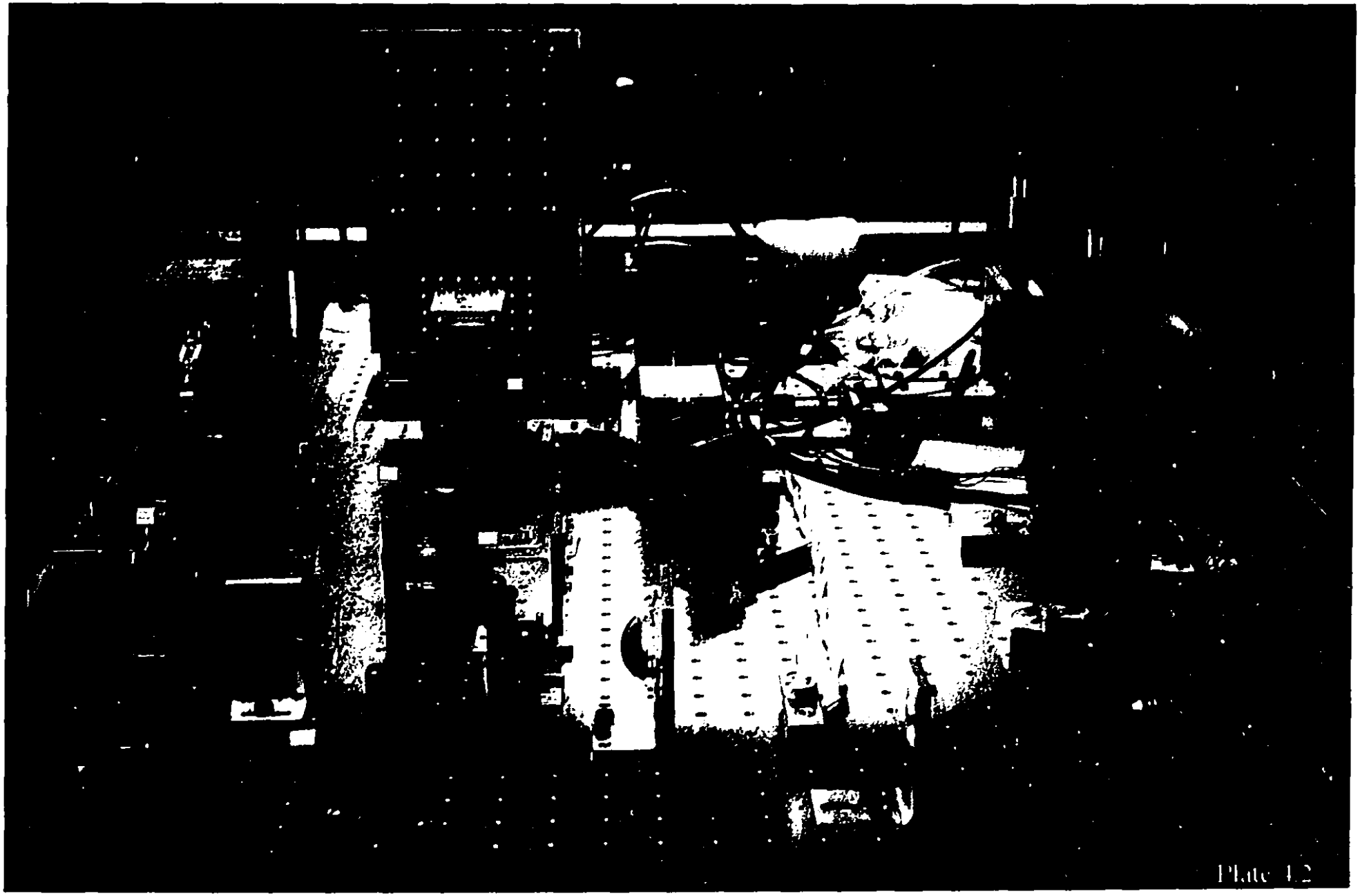

Plate 1.2

CHAPTER 5

Operation and Characterization of the CSLM

5.1 Preface

This Chapter presents operational details and an extensive characterization of the different subsystems of the CSLM. One very important property of the CSLM design is the capability of acquiring intensity, interference and differential phase contrast images without the need for realigning optical components or for significant modifications to the optical subsystem. The only change required is the opening and closing of a shutter (for the interference mode) or the introduction of two apertures in two predetermined positions (for the differential phase contrast mode). The way these changes can be easily implemented is presented in the first section of this chapter. Subsequently, results from characterizing the CSLM in terms of its depth and transverse point spread functions (PSFs) and for the different contrast modes of operation are shown. The measured PSFs are also compared to theoretical ones generated via the models presented in Chapter 3.

Details concerning the proper use of the scanning subsystem, as well as results of characterizing the system in terms of its resolution and accuracy, are also included. Finally, the image processing algorithms most frequently applied to the acquired 2D images, together with details regarding the coordinate system of the CSLM and image file format, are found in the last section of this chapter.

5.2 Operation of the Optical Subsystem

The CSLM is a complex modular device that integrates a number of components which have to operate in synchronism to ensure proper operation in the acquisition of high quality images. Each device used in the CSLM has to be properly integrated with the rest of the CSLM components. Therefore, great effort went into ensuring that the different components operate according to their specifications (i.e. the response of the A/Ds is linear, the signal-to-noise ratio (SNR) is high, the sensitivity, gain and frequency response of the photodetectors is adequate etc.), and the components integrate properly with each other. Each component was tested and characterized before being integrated into the CSLM. The measurements were performed with the CSLM's computer subsystem (an IBM RISC/6000 workstation) by either using the resident data acquisition board or separate external test and measurement equipment (i.e. HP 3562A dynamic signal analyzer) controlled via a general purpose interface bus (GPIB). The characterization of only the main CSLM components is presented next. Nevertheless, operation details for all the subsystems whose role is critical in the proper functioning of the CSLM, will be given. Such subsystems are the optical and the scanning subsystems.

5.2.1 Alignment of the Optical Subsystem

An important aspect of the CSLM is its flexible design that provides control over the magnification factor of the optical subsystem (whose role is critical in determining the confocal properties of the CSLM). Equally important is the capability of acquiring intensity, interference and differential phase contrast images without any significant change in its optical configuration. The three optical configurations of the CSLM are shown in Figure 4.2. The conversion from one configuration to the next is described below. Details concerning alignment requirements are also included.

5.2.1a Intensity Contrast Mode

The optical arrangement for this mode of operation is shown in Figure 4.2(a). The alignment of the optical components is performed starting from the laser source and moving towards the objective lens and the photodetectors. Different size pinholes can be used in front of the detectors. They are aligned using a mirror as an object and a voltmeter for monitoring the output of the photodetectors. On the optical axis the pinhole is positioned close to the photodetector's surface (and at the focal plane of the collector lens), making sure at the same time that the light emerging from the pinhole falls inside the active area of the photodiodes. The pinhole is then translated along the optical axis, in

the plane transverse to the optical axis, and is also tilted about two orthogonal directions until maximum signal output is achieved. The photodetector, that is also attached on a three degrees-of-freedom optical mount, is moved as close as possible to the pinhole surface and translated in the lateral (to the optical axis) plane until the output signal reaches a maximum value.

5.2.1b Interference Contrast Mode

In this mode of operation a second (reference) beam reflecting off a mirror is introduced into the system (Figure 4.2(b)) to form a Michelson interferometer. The two beams interfere in the first beamsplitter. For easier alignment of the interferometer the parallel laser beam can be changed to be mildly divergent. In this case the wavefront pattern in front of the detectors is a small number (2-3) of concentric alternating dark/bright rings. The detector pinholes are aligned as before and to the center (bull's eye) of the pattern. After the Michelson interferometer is aligned, the laser beam can be made parallel, and intensity or interference contrast mode of operation can be selected by just closing or opening the shutter that blocks the reference beam. Special care must be taken so that the two interfering beams are of equal intensities. This is done by first blocking the reference beam and measuring the photodetectors' output. Subsequently the object beam is blocked and the variable attenuation filter (placed in the path of the reference beam) is adjusted until the photodetector's output is the same as the one obtained in the previous step.

5.2.1c Differential Phase Contrast Mode

For the DPC mode of operation the shutter (S) is closed so that the reference beam used for the interference mode is blocked. Two apertures are now introduced between the two beamsplitters and the two collector lenses. The apertures are inserted in predetermined positions along the x or y axis, each blocking half the beam wavefront (see Figure 4.2(c)). The position of the apertures is initially determined as follows. A mirror is used as the object of the CSLM. Care should be taken so that the mirror is exactly perpendicular to the optical axis of the microscope. This can be verified by acquiring a 2D x-y image of the mirror and adjusting the tilt so that the image exhibits a uniform intensity throughout. The output of the photodetectors is measured and the apertures are slowly translated further inside the beam, until the reading from the photodetectors' output is reduced by half. The final position of the apertures is then marked for future quick positioning. The axis (x or y), along which the apertures are introduced defines the axis along which the differentiation is performed.

5.2.2 Characterization of the Optical Subsystem

The CSLM was extensively characterized in terms of its depth response and its transverse step response functions for the different modes of operation. The characterization of the microscope was performed using an Olympus MA50 metallurgical, infinity corrected microscope objective with numerical aperture (NA) of 0.7. The size of the pinhole in front of the photodetectors was 10 μm. Under these circumstances and using the confocality criteria presented in Chapter 3 the system should behave like a Type 2 confocal arrangement ($v_p \approx 0.5$). The 3D composite depth point-spread function and transverse step-response of the microscope were measured by imaging a sharp edge as it was translated through the focal point of the objective lens. The result of this measurement is shown in Figure 5.1(a). By differentiating the result along the transverse direction the 3D point-spread function of the CSLM can be estimated. Since differentiation is an inherently noisy process, the derivative was estimated by first fitting a parabola to every five points of the measured step response and then calculating the derivative for this region analytically. The outcome is shown in Figure 5.1 (b). Subsequently the measured lateral and axis responses of the CSLM were compared against the theoretically-estimated ones. The results of this comparison are presented next.

5.2.2a Transverse Step Response Function

In Chapter 3 the transverse point spread function of an ideal Type 2 confocal arrangement is given by,

$$h_t(v) = \left(\frac{2J_1(v)}{v}\right)^4 , \qquad (5.1)$$

where $v = \frac{2\pi}{\lambda} r \sin(a)$ is the normalized optical distance, $J_1(.)$ is a first-order Bessel function of the first kind, r is the distance in the x-y plane and sin(a) is the NA of the objective lens, 'a' being the extreme ray incident angle.

The step-response of a confocal scanning microscope is given by the integral [Eykhoff, 1974]:

$$h_{tsrf}(v) = \int_{-\infty}^{\infty} h_t(v)dv \ . \qquad (5.2)$$

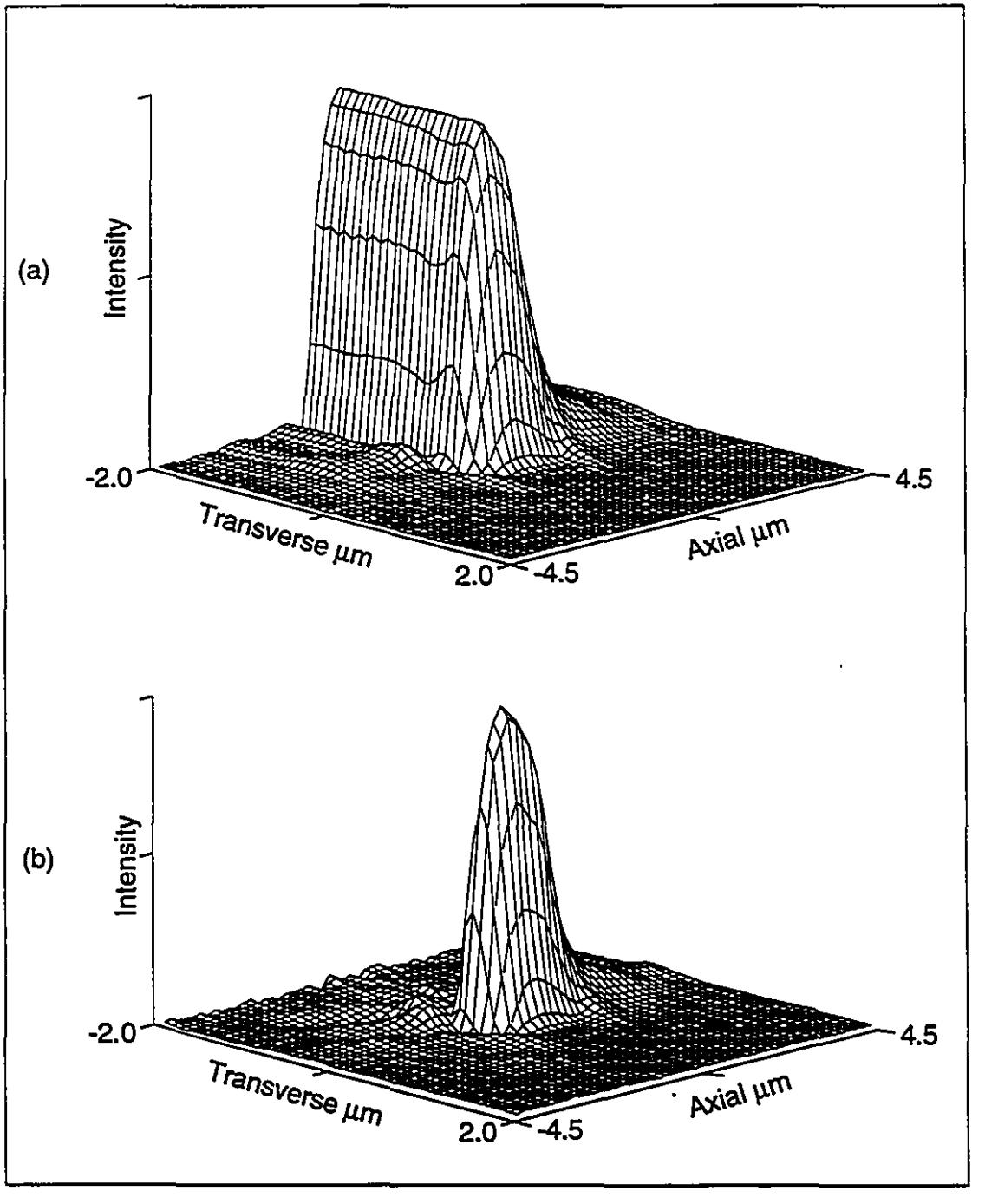

Figure 5.1 *(a) 3D composite depth point-spread function and transverse step-response function of the CSLM. (b) 3D point-spread function of the CSLM estimated via numerical differentiation along the transverse direction.*

The transverse intensity step-response function (SRF) of the CSLM was measured by scanning the sharp edge of a glass plate along the x or y axis through the focal point of the objective. Prior to performing the measurement the glass edge was aligned so as to be perpendicular to the scan axis. This is done by acquiring a 2D x-y image of the edge and rotating the plate around the optical axis until the edge is at 90° angle to the scan (differentiation) direction.

In Figure 5.2(a) the theoretical step-response, together with the measured one are shown. The 10% to 90% distance is 330 nm and the noise equivalent displacement (NED) is approximately ±1.2 nm. The error is 0.36%. NED is defined as the standard deviation (SD) of the output signal at a point (in V) converted into displacement. For example, in the case of the transverse intensity step-response the SD of the output signal around a point where the signal is stationary is 12.47 mV. The mean value of the signal changes from 4.25 V to 0.0 V; or when considering the 10% to 90% signals these are 3.825 V to 424.8 mV respectively. The NED can be calculated to be:

$$\text{NED} = \frac{\Delta d \times \text{SD(V)}}{\Delta V} = \frac{330\ \text{nm} \times 12.47\ \text{mV}}{(3.825 - 0.425)\ 10^3\ \text{mV}} \cong 1.2\ \text{nm}. \qquad (5.3)$$

where Δd is distance traveled and ΔV is the measured voltage difference.

By numerical differentiation of the step response function, the transverse point-spread function of the CSLM was estimated and is shown in Figure 5.2(b), together with the theoretical ones for the Type 1 and Type 2 configurations. Since numerical differentiation is an inherently noisy process, in order to get a good point-spread function estimate, three different step response measurements were first averaged. The derivative was then estimated by first fitting a parabola to every five points of the averaged step response and then calculating the derivative analytically [Scheid, 1989, pp. 245-246].

5.2.2b Depth Response Function (Intensity Contrast)

In Chapter 3 the planar depth response function (PDRF) of a confocal microscope, $h_d(z)$, as a function of displacement z, along the optical axis is estimated to be:

$$h_d(u) = \left(\frac{\sin(u/2)}{(u/2)}\right)^2 , \qquad (5.4)$$

where $u = \frac{8\pi}{\lambda} z \sin^2(\frac{a}{2})$ and sin(a) is the NA of the objective lens.

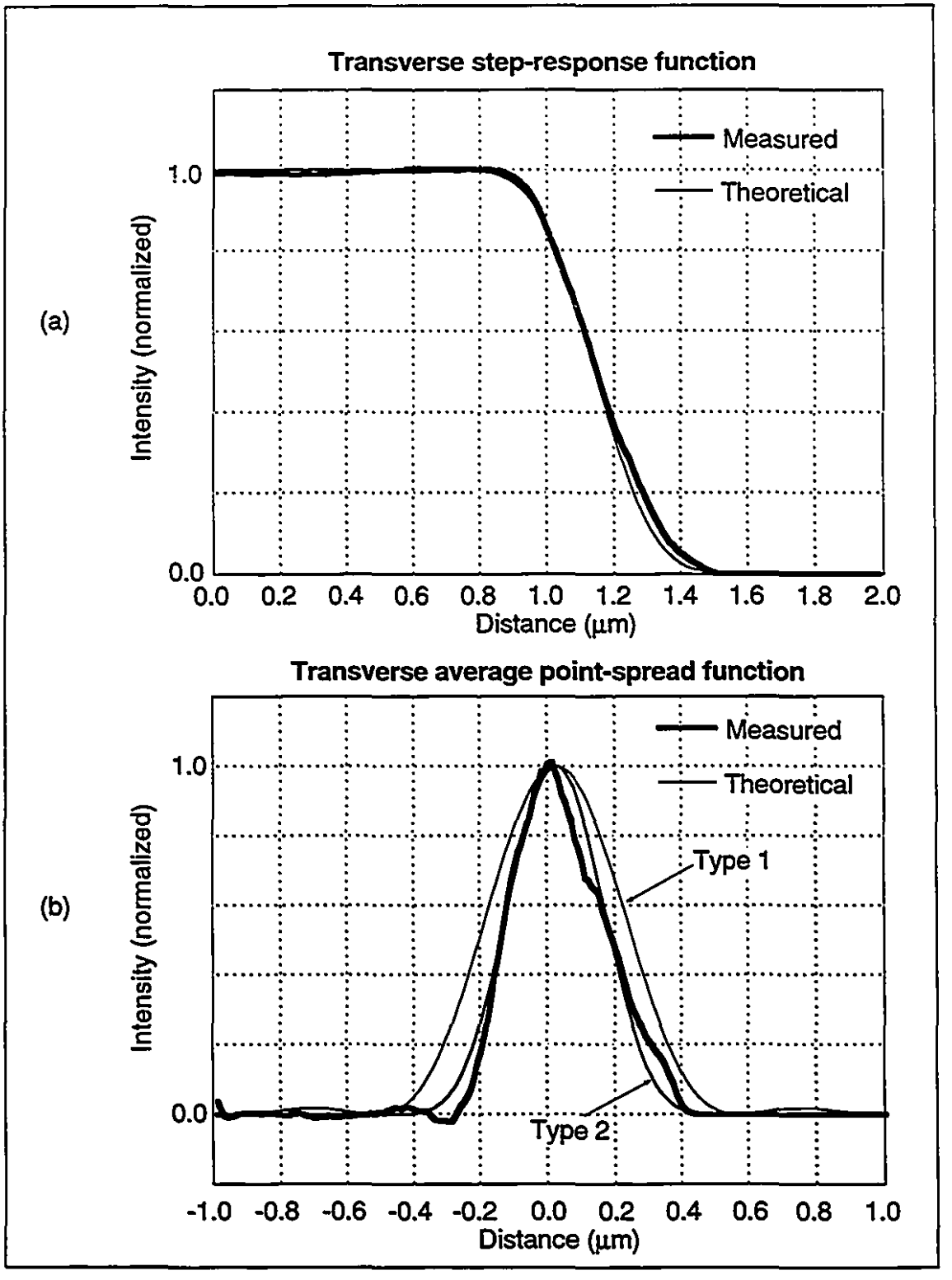

Figure 5.2 *(a) Measured transverse intensity step-response function of the CSLM together with the theoretical one for Type 2 configuration. (b) Measured transverse point-spread function estimated using numerical differentiation together with theoretical responses for Type 1 and Type 2 confocal arrangements.*

By using a plane mirror as the object, the microscope's PDRF was measured. The results are shown in Figure 5.3, together with the PDRF that was theoretically estimated using Equation (5.4). The extremely close agreement between the theoretical and measured PDRF is obvious. The full width half maximum (FWHM) distance is approximately 1.0 μm. The NED is approximately ±1.1 nm. The error is 0.1%.

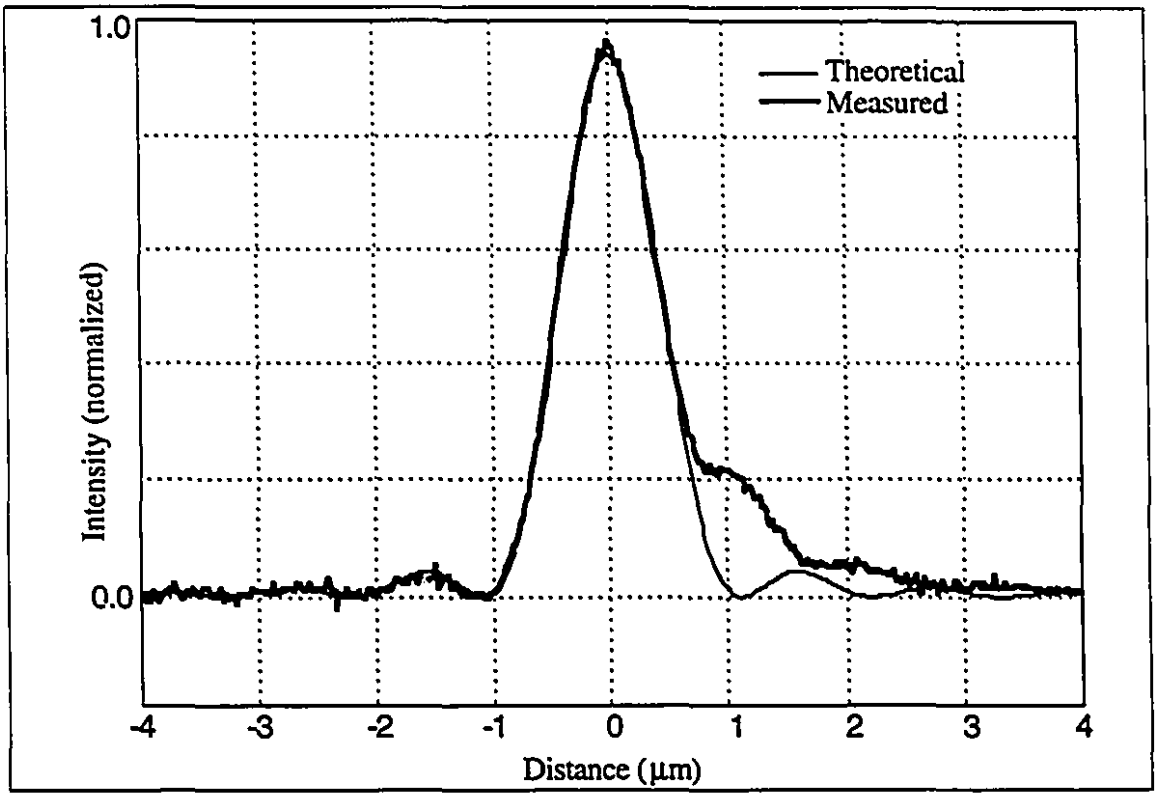

Figure 5.3 *The measured and theoretical planar depth response functions.*

The deviation between the theoretical and measured PDRF at approximately +1.0 μm away from the peak can be attributed to spherical aberrations. This behavior has been observed by other researchers and was also studied theoretically [Sheppard & Gu, 1991] , [Sheppard & Wilson, 1979].

The PDRF of the CSLM were also measured for different size detector pinholes. The FWHM points as a function of the pinhole diameter are plotted in Figure 5.4. It can be seen that for small pinhole sizes the FWHM distance increases slowly. The slope of the curve increases as the pinhole's size increases and imaging properties change from coherent to partially coherent. This is consistent with the theory presented in the previous chapter and the work of Wilson and Carlini [Wilson and Carlini, 1987].

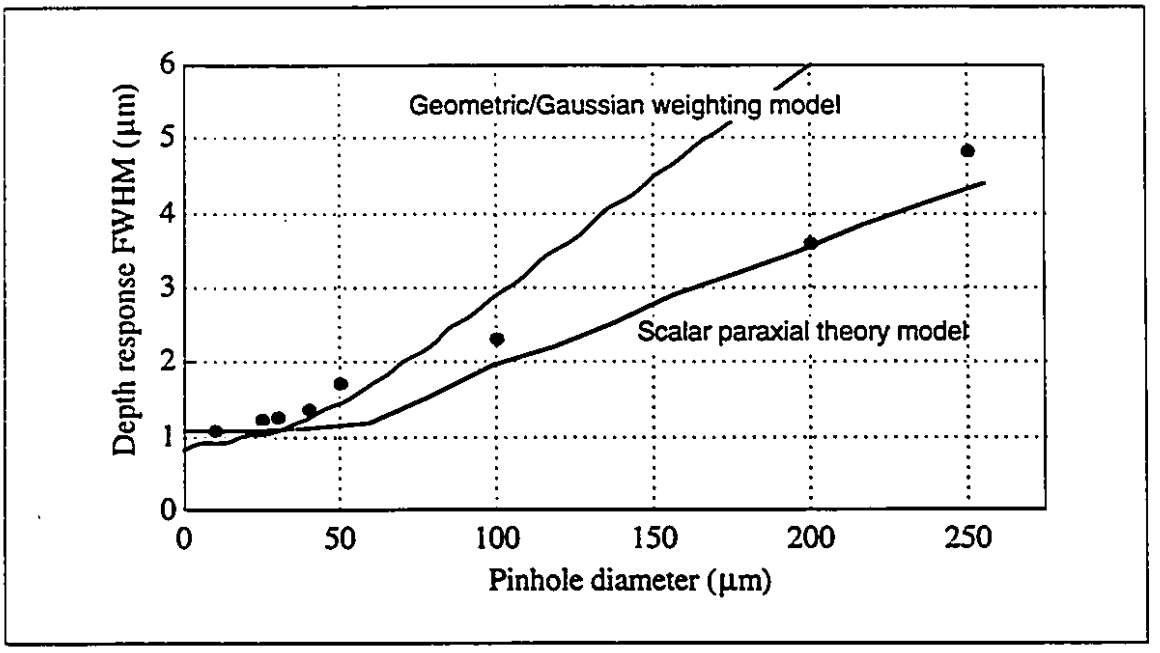

Figure 5.4 *The measured FWHM distance as a function of the detector pinhole diameter.*

5.2.2c Depth Response Function (Interference Mode)

The planar depth response of an interference contrast confocal microscope, $h_i(z)$, is described as an interference term multiplied by an envelope function. The envelope is a sinc(.) function and is given by Equation (5.4). The PDRF was measured by using a plane mirror as the object which was translated along the optical axis (z) and through the focal point of the objective lens. The signal of the two photodetectors (with the DC term subtracted) is shown in Figure 5.5. Note that as predicted by the theory the two photodetector signals are 180° out of phase.

By allowing the reference beam to be represented by $R=R_0\exp(j\varphi)$

and recalling that the complex amplitude of the defocus signal is given by (Equation 3.21):

$$U(u) = U_0 \frac{\sin(u/2)}{u} \exp\left[\frac{ju}{2} - \frac{2ju}{\sin^2 a}\right] \text{ for } u=\frac{2\pi}{\lambda}\sin^2(a) \quad , \tag{5.5}$$

the expression for the difference signal of the two detectors can be found to be:

$$I_{(-)}(u) = I_A - I_B = 4U_0R_0 \frac{\sin(u/2)}{u/2}\cos\left(\frac{u}{2} - \frac{2u}{\sin^2 a} - \varphi\right) \quad , \tag{5.6}$$

where the first part is the confocal depth response multiplied by an interference term ($\cos(P(u,\varphi))$).

It can be seen in Figure 5.6(b) that the difference of the two detector output signals is an interference term multiplied with an envelope function proportional to the confocal depth response function, as described by Equation (5.6). By normalizing the waveform shown in Figure 5.6(b) with the one on Figure 5.6(a), $\cos(P(u,\varphi))$ can be estimated.

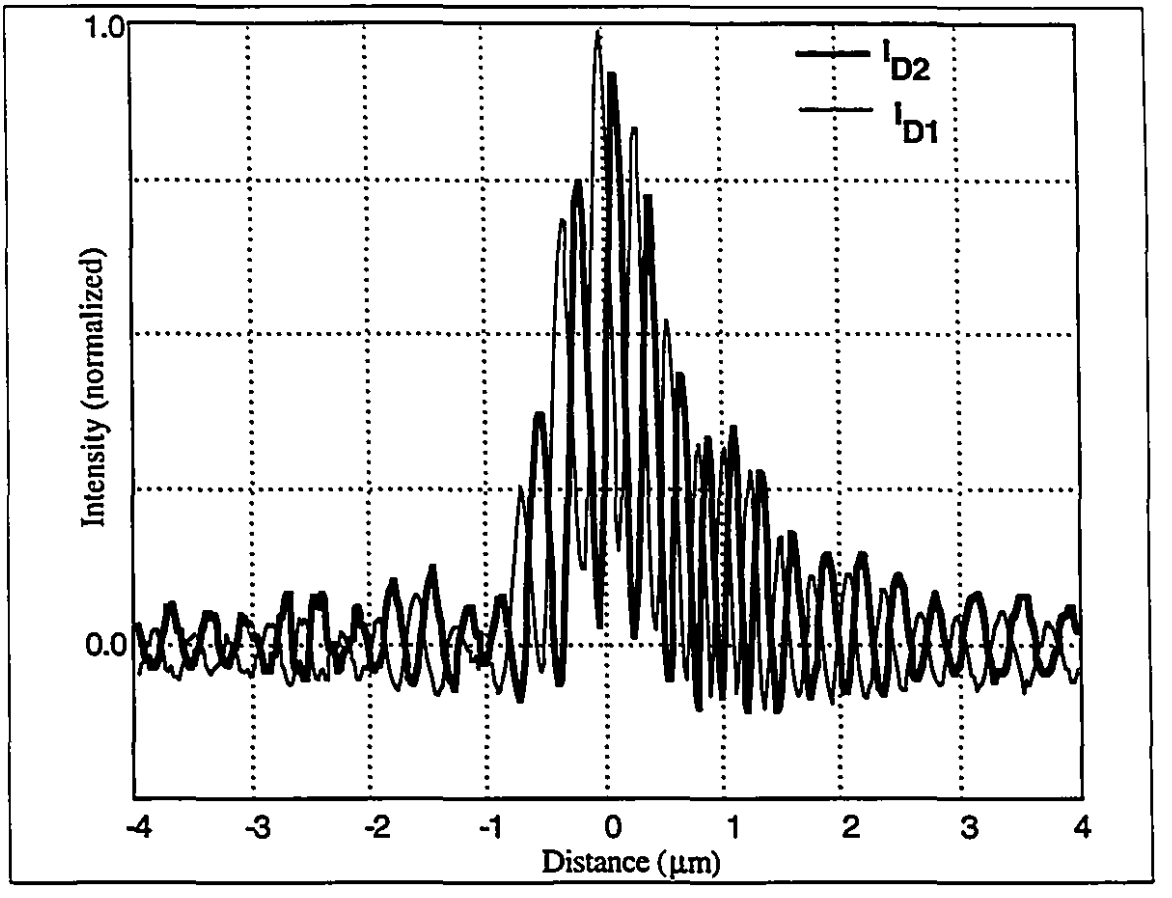

Figure 5.5 *The signals of the two photodetectors when measuring the interference depth-response function of the CSLM*

From the signal of the two photo detectors (described by Equation 3.37), the intensity and the interference term of the depth-response function (Equation 5.6) can be reconstructed. The estimated magnitude and interference signals are shown in Figure 5.6(a) and (b) respectively. The reconstructed magnitude of the depth response function (after subtracting the DC offset) is plotted together with the theoretical one. It can be seen that the agreement between the two curves is high.

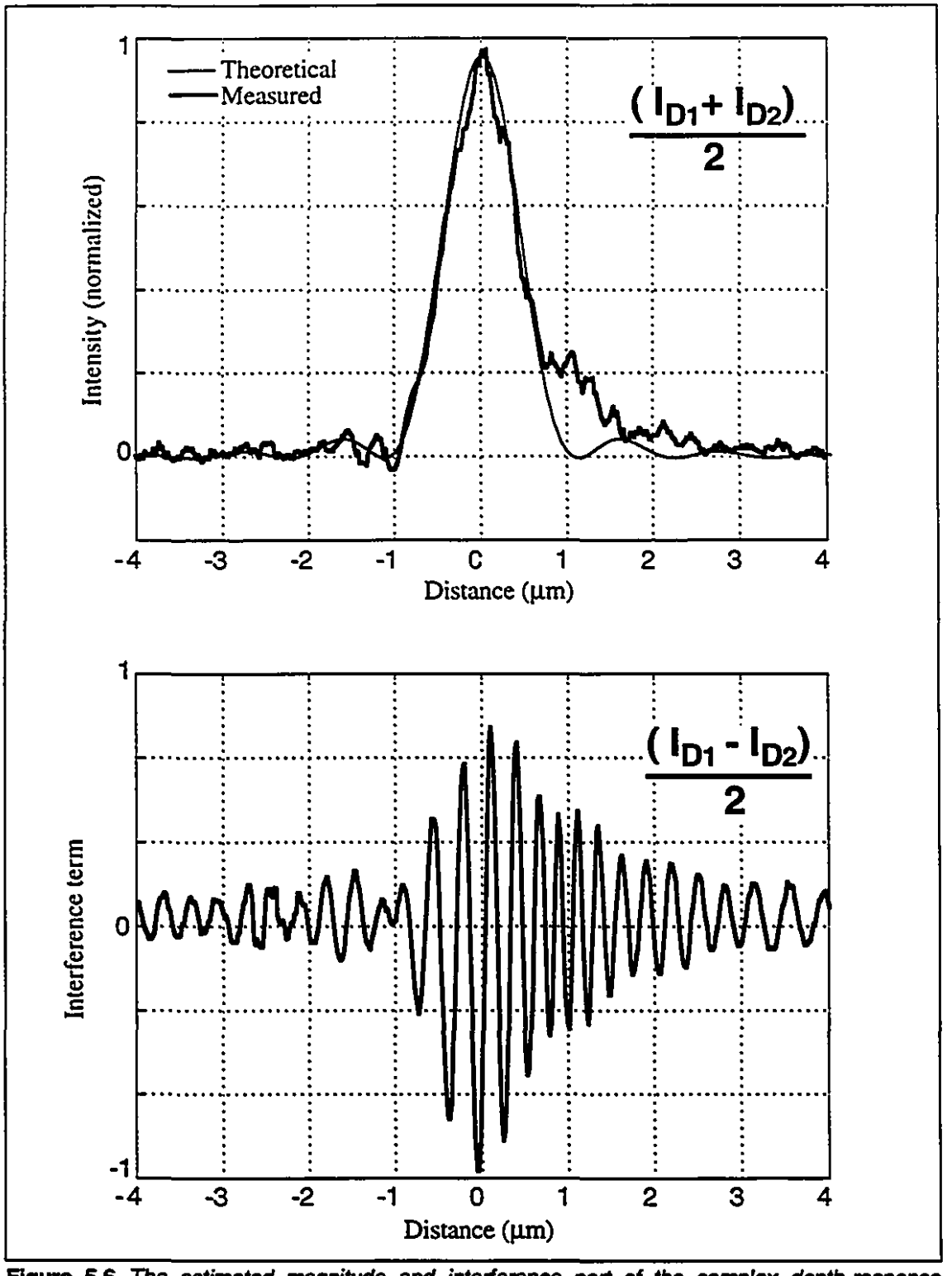

Figure 5.6 *The estimated magnitude and interference part of the complex depth-response function of the CSLM.*

5.2.2d Depth Response Function - DPC mode

The PDRF for the DPC mode should be zero if the planar reflector is exactly perpendicular to the optical axis of the CSLM. If the signals of the two photodetectors are added, a measurement of the conventional (intensity contrast) depth response results (see Section 3.3.2).

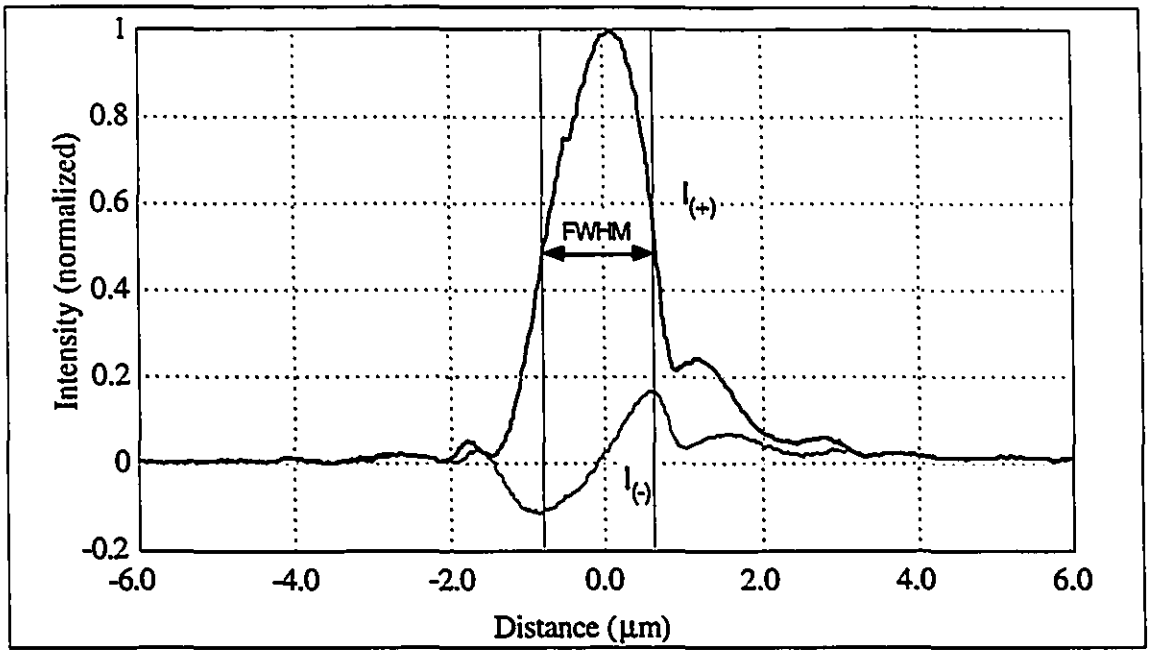

Figure 5.7 *The measured DPC depth-response function of the CSLM. Both the sum and the difference of the two detector signals are plotted.*

In Figure 5.7, it can be seen that the difference signal is not zero. This is due to a small tilt of the mirror target or slight misalignment of the two pinholes (the peak intensity does not occur at exactly the same mirror position for the two detectors). The fact that the difference signal is not zero provides an indication of the DPC sensitivity to small surface height variation on the object plane (or small phase changes within the focal volume). The mirror was aligned to the lateral (to the optical axis) plane by acquiring 2D x-y images and tilting the mirror until a constant reflectivity was present throughout the image. The non-zero difference signal indicates that the small surface tilt or pinhole placement difference (~ 60 nm), although not apparent in the intensity contrast image, was adequate to generate a DPC signal. Figure 5.6 also shows that even in DPC mode the CSLM exhibits a significant depth discrimination. The FWHM of the PDRF for the DPC mode is 1.6 μm.

In the above extensive characterization of the CSLM it should be noted the very good agreement between the theoretical models and the experimental measurements. Furthermore the results of the characterization indicate that:

a) The performance of the CSLM's optical subsystem fulfills the desired specifications (namely submicron lateral and 1 μm depth resolutions).

b) The theoretical models presented in Chapter 3 are adequate in predicting the performance of a confocal microscope system and therefore are very useful in its design phase since they indicate how different physical parameters (i.e. NA, λ, M) influence the performance of the CSLM.

5.2.3 Sensitivity of the Detectors' Subsystem.

In the previous sections the alignment details and the spatial response of the optical system were presented. Another component of the optical subsystem that influences the quality of the acquired images is the detection system. Initially in the CSLM photomultipliers were used as detectors. They were replaced by silicon avalanche photodiodes (APD) to reduce space. The important features of the APDs are their small size and their internal gain mechanism that can amplify very small signals over the thermal noise level thus producing a very high signal-to-noise ratio (SNR). However when a high gain is used (> 1000) then the shot noise is also amplified resulting in a reduction of the SNR.

From the approximately 10mW of power of the HeNe Laser source, only about 3.5 mW reached the sample*. Biological material may reflect as little as 10^{-4} of the incident light [Davidovits & Egger, 1971]. Suppose that only a fraction of this light emanates from within the narrow 1 μm slice of interest (perhaps as little as 10^{-2}). Due to the beamsplitter behind the objective lens only half of this power reaches the detector pinhole. Therefore, the optical power that eventually reaches the detectors can be in the worst case in the order of 1.8 nW. The APDs' sensitivity at 632 nm and unity gain is 0.3 A/W. The APDs were operated at a gain of approximately 100 (which, according to the manufacturer, is the one that offers optical SNR ≅ 10^5 and dark current of ≅ 10^{-10} A). For the worse case scenario of a very weakly reflecting biological specimen the expected SNR is:

$$\text{SNR} = \frac{100 \times 1.8^{-6}\,\text{mW} \times 0.3\,\text{mA/mW}}{10^{-7}\,\text{mA}} = 540\,.$$

* Measured using the Newport 815 series digital light power meter.

It can be seen that even for weakly scattering biological specimens the photodetectors offer a reasonable SNR. A more typical SNR of 10^4 though, spans a dynamic range of 16 bits. Unfortunately the available A/D converters had only 12 bits resolution. Therefore, although the sensitivity of the photodetectors is more than adequate (for imaging of biological specimens), the performance of the CSLM was compromised by the low dynamic range of the A/D converters. The limited dynamic range of the A/Ds became more of a problem in 3D volumetric image acquisition. Frequently the gain of the APDs had to be reduced when imaging the top specimen slices, thus preventing acquisition of images with reasonable SNR from deeper layers. If the gain was adjusted (increased) to image specimen layers deep below the surface, the signal level from the top layers was beyond the range of the A/Ds.

5.3 Operation and Characterization of the Mechanical Subsystem

5.3.1 Linear Stage Optimal Motion Profile.

In object scanning confocal microscopes the image acquisition time depends on how fast the object can be scanned in front of the laser beam, assuming that the output of the photodetectors can be sampled equally fast. Since the maximum conversion speed of the A/Ds is fixed (100 Ksamples/s/channel), considerable effort went into trying to minimize the image scan time. The scanning subsystem of the CSLM is based on a micro-stepping motor driven 3-axis linear translation stage. To ensure the best possible position accuracy, stepping motor manufacturers suggest a trapezoidal motion profile like the one shown in Figure 5.8(b) [Parker, 1991-92],[Newport, 1994]. The stage has to be accelerated to a constant velocity, and subsequently decelerated before changing direction or coming to a full stop. In the CSLM, to minimize image distortion, data acquisition takes place while the translation stage is traveling at constant velocity. It is therefore important to bring the translation stage to a constant velocity motion as quickly as possible.

For stepping motors the units used for speed and acceleration are steps/s and steps/s^2, respectively. These units can be converted to m/s and m/s^2 by knowing the specification of the stepping motors in terms of number of steps/revolution and the pitch of the lead screw. For the stages and stepping motors used in the CSLM, these specifications can be found in the previous chapter (Section 4.5).

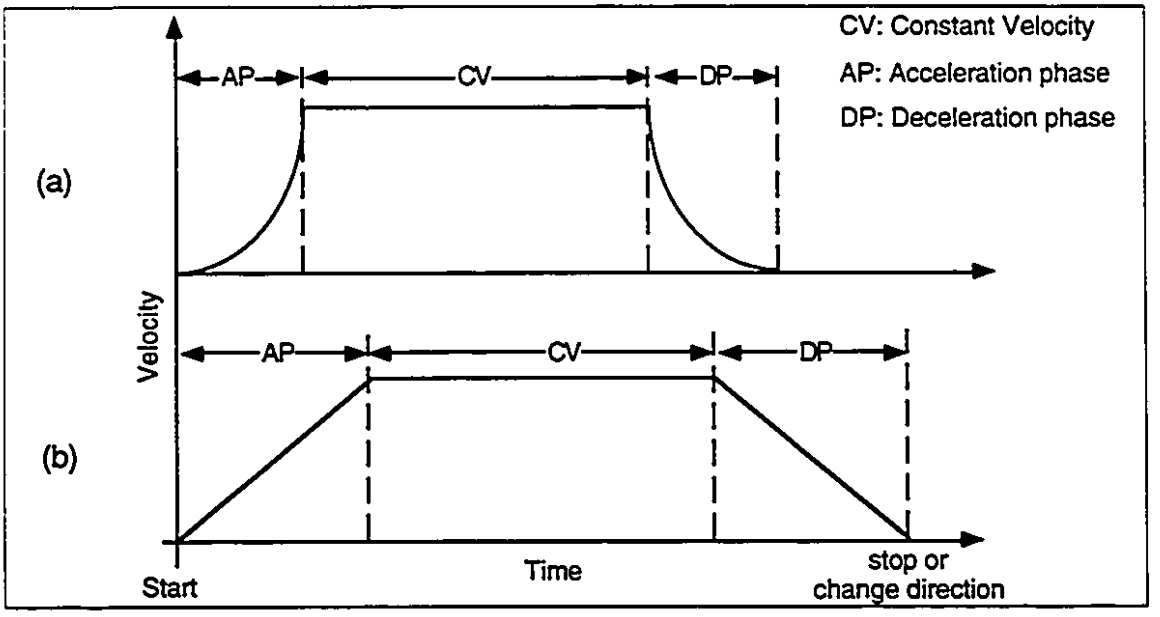

Figure 5.8 *The suggested motion profile for stepper-motor driven linear stages in order to achieve best position accuracy. (a) Motion profile when using acceleration increasing linearly with time and (b) when using constant acceleration.*

The motion profile shown in Figure 5.8(b), assumes constant acceleration. Considering an acceleration of α steps/s^2, the time to reach constant speed is $t = \frac{v_0}{\alpha}$ s where v_0 is the desired constant velocity, and the distance traveled while the stage is accelerating is $d = \frac{{v_0}^2}{2\alpha}$ steps.

Parameters t and d can be minimized by increasing α, but there is always an upper limit beyond which the stepping motor will behave erratically and may even stall (i.e. by exceeding the maximum motor torque). Therefore, in order to minimize the time it takes to accelerate the stages to a constant velocity, a parabolic motion profile (shown in Figure 5.8(a)) can be used. In this case the acceleration is not constant but increases linearly with time:

$\alpha = \beta t$ (where β is given in steps/s^3 and is the rate of acceleration). (5.7)

The time that it takes to reach a constant speed is $t_p = \sqrt{\frac{2v_0}{\beta}}$ s and the constant speed can be reached in $d_p = \frac{1}{3} v_0 \left(\sqrt{\frac{2 v_0}{\beta}} \right)$ steps.

The stepping motor performs a step each time its controller receives an input pulse. The timing between pulses is critical if the motor is to accelerate properly and move smoothly without stalling. The time delay between pulses while accelerating (or decelerating) the motor is

$$\delta t_{n+1} = \sqrt{\frac{2}{\alpha}} \left(\sqrt{n+1} - \sqrt{n} \right) \text{ s for the case of constant acceleration, and} \qquad (5.8)$$

for the case of the linear acceleration motion profile:

$$\delta t_{n+1} = \sqrt[3]{\frac{6}{\beta}} \left(\sqrt{n+1} - \sqrt{n} \right) \text{ s} \quad , \qquad (5.9)$$

where n indicates the n^{th} motor step since the motor started its accelerating motion.

β should be chosen to be large enough, in order to reduce the acceleration and deceleration time of the motion system. For a given maximum rate of constant acceleration α, β should be chosen to be:

$$\beta \geq \frac{2\alpha^2}{v_0} \quad . \qquad (5.10)$$

Equations (5.8) and (5.9) are used by the computer software in order to estimate the time delay between the pulses. If the computer is fast enough these times can be estimated at run time (as in the case of the CSLM). Alternatively they can be estimated in advance and used in the form of a look-up table.

5.3.2 Characterization of the Scanning (Motion) Subsystem.

The performance of a motion system can be characterized in terms of its resolution, accuracy, repeatability and backlash. Using laser interferometry, the performance of the CSLM's scanning subsystem (as described by these quantities) was measured. Interferometry was used because of its high accuracy and since it was already available as an operating mode of the optical subsystem. The CSLM optics in the interferometric (non-confocal) arrangement were thus used for performing the various tests. Proper characterization of the scanning system is important since the measured characteristics give an indication of the upper limit for the CSLM performance.

5.3.2a Resolution

The resolution of a scanning system is defined as the smallest addressable position increment. In the CSLM the object scanning is performed in a raster-like fashion. Therefore, there is a fast and a slow-scanning axis. Although, as mentioned in the previous chapter, the smallest addressable position increment for the scanning system is 10.16 nm, this can only be achieved along the fast-scanning axis (x) of the CSLM, and only while the stages are moving with constant velocity. On the slow axis (y) the theoretical resolution is 20.32 nm and the smallest repeatable and reliable positioning increment was measured to be approximately 50 nm.

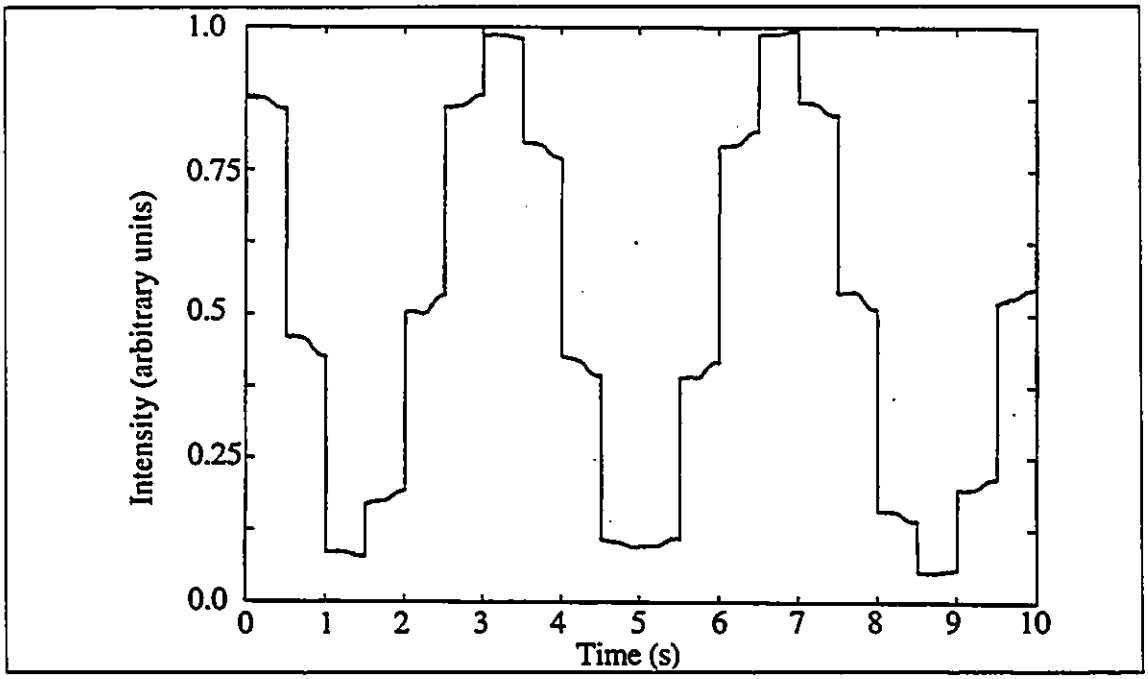

Figure 5.9 *The interferometer output that indicated the position resolution of the scanning subsystem to be 50 nm.*

The difference in the behavior between the slow and fast axes is due to stiction (static friction). When an idle stepping motor is commanded to move by one microstep, it will not move unless its torque is enough to overcome the stiction (and load inertia). By receiving more microstep commands that increase the voltage gradient between the motor phases, torque is accumulated. The motor starts to move when the accumulated torque can overcome the stiction threshold at which point it will jump to the proper position. Once motion has commenced the torque required to move by one microstep is smaller (depends on the load) and therefore it is possible that the motor will move by one

microstep each time a command to do so is received. For the fast axis the stiction and load inertia are overcome in the acceleration phase and therefore the smallest position increment is the same as the smallest addressable increment. This is not the case for the slow axis which has to start moving each time a new image line is to be acquired.

The resolution measurements were performed by commanding the system to move a certain distance, wait for a certain period of time (during this time the fast axis would be scanning) and then repeating the same command. The commanded distance was gradually increased until the distance traveled for each command was constant over the total travel range. An example of the interferometer output when performing this type of measurements is given in Figure 5.9. The stage was requested to move in 50 nm increments and to wait 500 ms between each position increment.

5.3.2b Accuracy

Accuracy in a motion system is defined as the difference (error) between the commanded and actual final position over repeated trials. It should be noted that accuracy is a statistical measure and that the position error follows a probability distribution whose mean is considered to be the accuracy of the system. Using interferometry, the accuracy of the CSLM's scanning system was measured to be ≅ 0.02 %. That is, for a requested motion of 50 μm, the actual motion was approximately 50±0.1 μm. It should also be noted that accuracy depends on the distance traveled, and the relation is not necessarily linear. The given accuracy estimate was for displacements from a few μm to approximately 500 μm. For longer distances the accuracy improved (as a percentage of the total distance traveled).

5.3.2c Repeatability

For a positioning system, repeatability can be defined as follows: if the position error is a statistical quantity that has a mean (m_0) and a standard deviation (σ_0), then repeatability is measured as the standard deviation of the error between the desired (commanded) and actual positions over repeated trials. Repeatability depends mainly on the distance traveled but also on the speed of motion. The repeatability of the CSLM's scanning system was measured to be better than 0.158 μm ($\lambda/4$) for 256 trials and for a 50 μm travel range. Longer travel distances did not affect the outcome significantly.

5.3.2d Backlash

Backlash is the difference between the forward and backward paths for the same commanded position. In this type of measurement, the CSLM's scanning system performed the worse. Its backlash was measured to be $\equiv 4\lambda$ (λ=632 nm) around the middle of the traveling range, and it was independent of the distance traveled. This large backlash of the scanning system necessitated the acquisition of image lines while the linear translation stage was moving always in the same direction (unidirectional scanning). Unidirectional data acquisition is imperative when the desired image resolution is less than 2λ / pixel or the application is critical.

Although the use of a parabolic motion profile (described above) reduces the image scan time, due to the significant backlash of the scanning system data acquisition was performed while the stage was moving always in the same direction. This ensured that subsequent image lines were aligned properly. However this unidirectional scanning resulted in a doubling of overall scan time.

5.4 Operation Details for the Computer Subsystem

Most functions of the CSLM are computer controlled. The motion of the scanning platform is synchronized with the data acquisition via software control. The acquired images are also stored in the workstation memory for further off-line processing. In this section a few unique aspects of the computer and software subsystem which are essential for complete understanding of the CSLM operation are presented

5.4.1 The CSLM Coordinate Systems

The CSLM is the imaging subsystem of an organ mapping system. The purpose of the organ mapping system is to automate the acquisition of information needed to build a 3D anatomical map of small organs. This will be done by acquiring a sequence of 3D volumetric images that when put together will enable a 3D picture of the full organ to be reconstructed in great detail. The small images will be arranged in a 3D grid. The data from all the 3D images will not be kept but after processing only the properties of interest (i.e. cell size, orientation etc.) for each location will be retained. This information is then used to build the 3D property distribution map (model). The data acquisition process necessitates the use of two coordinate systems. The global (organ) and the local (image) coordinate systems. The relation of these coordinate systems is depicted in the Figure 5.10

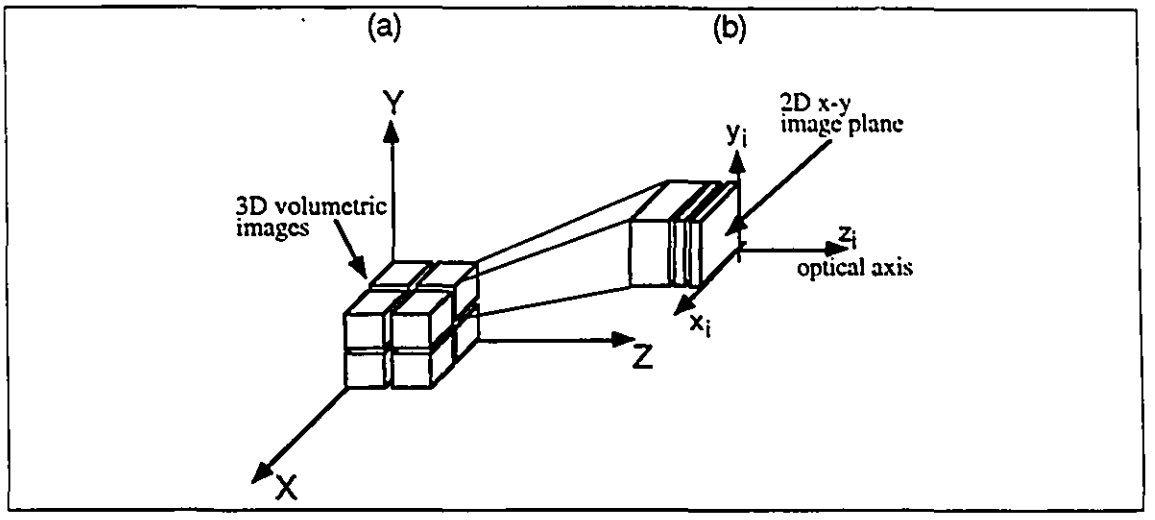

Figure 5.10 *The two coordinate systems of the CSLM and the organ mapping system. (a) The organ or world and (b) the local or image coordinate systems.*

In accordance with the requirements of the organ mapping system, within the working space of the CSLM, there are defined two coordinate systems: a world coordinate system (WCS) and an image coordinate system (ICS). The software that controls the CSLM keeps track and updates the current (scanning or focal point) position with respect to the two coordinate systems. The ICS origin always reflects the origin of the image that was last acquired by the CSLM. The WCS origin reflects the user-specified origin of the CSLM workspace. The ICS usually lies within the WCS, and the origin of the ICS is defined with respect to the origin of WCS. At any time the user can set (or reset) the current position as the origin of the WCS or the ICS. The actual working space of the CSLM in the transverse (image) plane is 38 by 38 mm. Along the optical axis the range depends on the working distance of the objective lens. Furthermore, tracking of the scan position along the optical axis is important since a collision of the object onto the objective lens should be avoided in order to prevent both object distortion and possible damage to the microscope objective.

5.4.2 The CSLM Image File Format

Images acquired using the CSLM are usually 2D (3D images are a sequence of 2D ones) and are stored in a number of file formats. The most frequently used formats are Matlab®* and TIFF. These file formats are used, so that the images can be imported into other software packages either for further processing or visualization. The images can

* Matlab is a trademark of MathWorks Inc.

also be stored in a custom file format. Each file contains the actual image data and additional information regarding the image parameters. In the header of the custom file format the resolution for each image axis and the image size both in pixels and micrometers is included. The resolution needs to be specified for each axis individually since the CSLM can acquire non-square pixel images. In the file header are also stored the image's WCS position. The images are monochrome and are stored as 16 bit (short integer) values. In Appendix 1 the way the various image parameters can be specified prior to acquisition is described.

5.4.3 Basic Image Processing

The CSLM images are monochrome and have a depth of 12 bit/pixel. However, the human eye cannot differentiate all 4096 shades of gray [Gonzalez & Wintz, 1987, p. 190], and the workstation screen on which they are presented does not support more that 256 levels of gray. Therefore (for display purposes only) the acquired images were mapped to 256 gray level intensities represented by the integer numbers from 0 to 255. The reduction from 12 bit/pixel to 8 bit/pixel was not done by eliminating the 4 least significant bits for each pixel but the whole dynamic range of the image $i_m(x,y)$ was optimally mapped to the 8-bit range:

$$i_m(x,y) = 255 * \frac{i(x,y) - \min[i(x,y)]}{\max[i(x,y)] - \min[i(x,y)]} \tag{5.11}$$

where min[.] and max[.] return the minimum and maximum levels for i(x,y).

Depending on the information that needs to be extracted from the images, different digital image processing techniques can be applied to the acquired images. Next, two of the 2D image processing algorithms that are used to improve visibility of different image structures are presented. Regarding 3D image processing, the surface geometry determination algorithm was already presented in the previous chapter. For additional processing techniques the user is referred to the extensive literature of 2D and 3D digital signal processing [Gonzalez & Wintz, 1987].

5.4.3a Gamma Correction

The most frequently employed image transformation is gamma correction which belongs to a more general class of operations that remaps the image pixels to different entries in the color-map table. Other operations of this class are histogram equalization, dynamic

range expansion and pseudo-coloring [Rosenfelt & Kak, 1982]. For the CSLM images, the color-map table has 256 entries with 0 representing black and 255 white. Gamma correction (or transformation) can selectively increase the contrast of the darker portions of the image and reduce it around the brighter portions. The overall image appears brighter and more details become visible in the darker regions. An example of gamma correction applied to a CSLM image is presented in Figure (5.11).

Mathematically the process is described as follows.

For $0 \leq I(x,y) \leq R$ and for every x,y the gamma corrected image $I_g(x,y)$ is given by:

$$I_g(x,y) = \text{gamma} \cdot R\left(\sqrt{\frac{I(x,y)}{R}}\right) + (1\text{-gamma}) \cdot I(x,y) \quad , \qquad (5.12)$$

where $0 \leq \text{gamma} \leq 2.0$ and R is the dynamic range of the image.

The transformation can be applied to the actual image itself or to the color (gray level) lookup table of the computer graphics hardware/software. The second method is usually faster and is the one employed in the CSLM software.

5.4.3b Median Filtering

Median filtering is a non-linear operation that belongs to a larger class of operations called kernel or neighborhood-based transformations [Gallagher & Wise, 1981][Ataman *et al.*, 1980]. The value of each pixel in the output image is a function of the pixel values in an N by N neighborhood around the equivalent pixel in the original image. In the median filtering operation the value of the output pixel is chosen to be the median value of its neighborhood. Specifically,

$$I_m(x,y) = \text{median}[I(x-\frac{N}{2} \ldots x+\frac{N}{2}, y-\frac{N}{2} \ldots y+\frac{N}{2})] \quad , \qquad (5.12)$$

where N is an odd number and $\frac{N}{2}$ is the integer division of N by 2.

The process can be implemented as follows: for each pixel at (x,y) location, the pixel values lying in the N×N subimage centered around (x,y) are sorted in a non-decreasing order. These values are stored in an N^2 length temporary array. The value of the output image pixel at location (x,y) is the value at index $\frac{N^2}{2}$ of the temporary array.

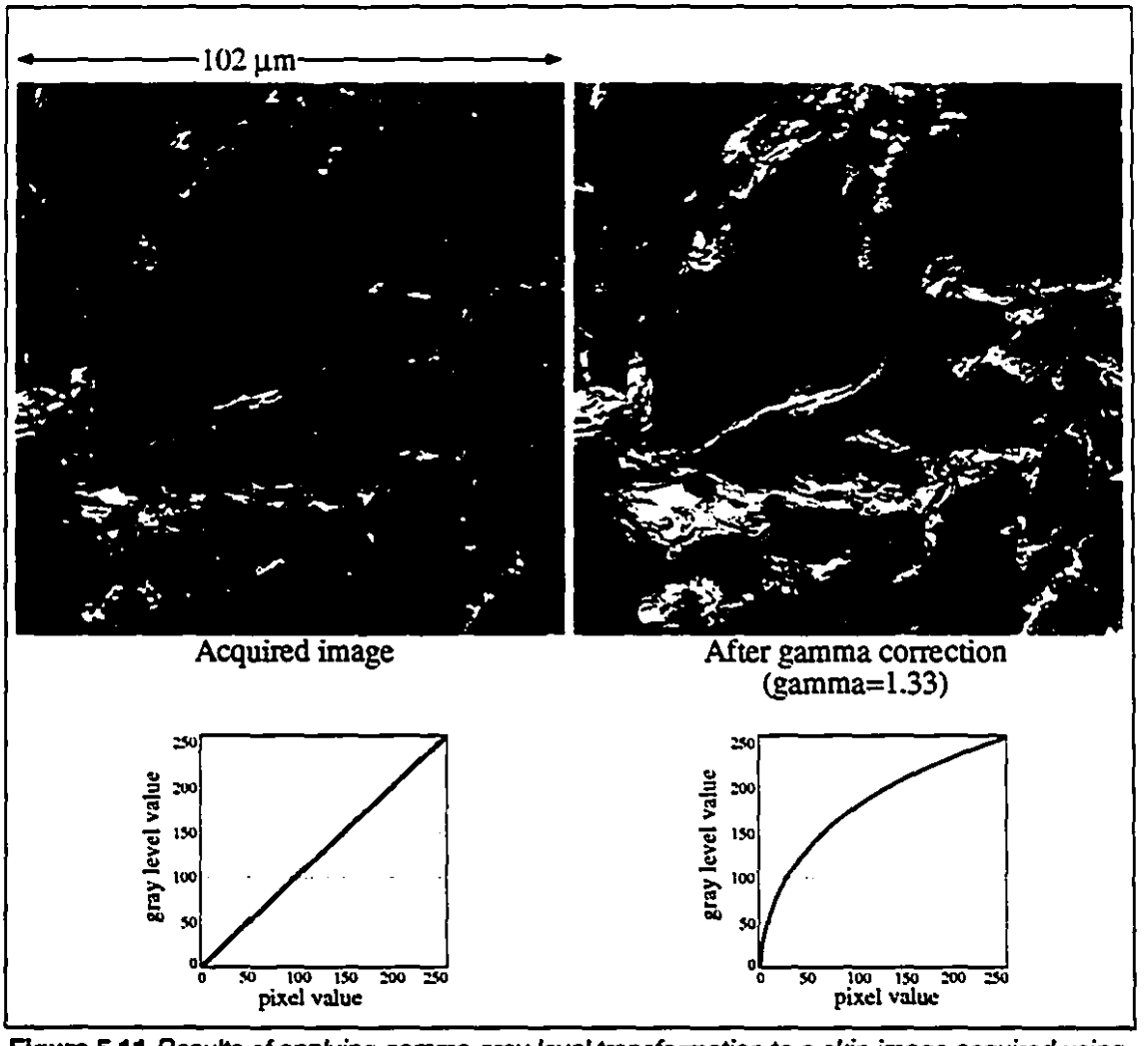

Figure 5.11 *Results of applying gamma gray level transformation to a skin image acquired using the CSLM.*

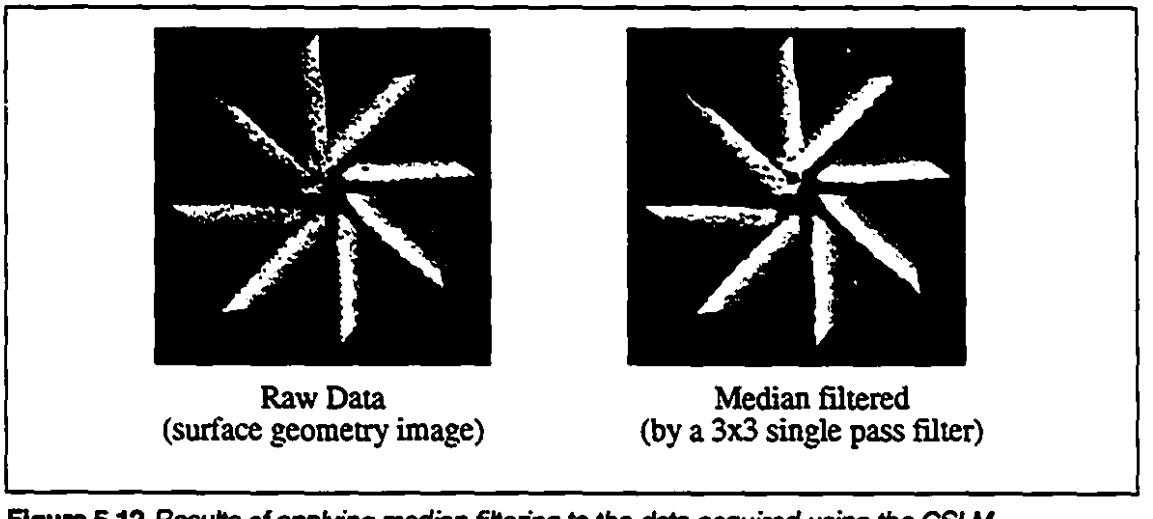

Figure 5.12 *Results of applying median filtering to the data acquired using the CSLM*

The main advantage of median filtering is the drastic reduction of random spike noise while preserving edge gradients. This type of noise is encountered when object surface reconstruction is performed at places where the surface reflectivity is very low. In these regions the surface geometry estimate is erroneous. A 3x3 one-pass median filter was used in the surface geometry image of the dental tool which appears in Figure 5.12. The filter has a negligible effect on the surface geometry image but it drastically reduces the random spike noise that is apparent on the dark background.

5.5 Specimen Preparation and Tissue Cutting Considerations

As mentioned in the introduction, the CSLM is designed as the optical subsystem of an organ mapping apparatus. The organ mapping system includes a cutting mechanism for tissue machining as well. Some preliminary considerations dealing with the issues of tissue preparation and tissue cutting are presented in Appendix 4. Objective quality of muscle tissue images (more specifically visibility and contrast of the sarcomeres) was used as the criterion for evaluating the various methods for tissue preservation. The most appropriate method was found to be the one using potassium citrate in a phosphate buffer and 5% formaldehyde. The method is described in Section a4.2.2. An extended focus image of a striated muscle fiber that was fixated using this technique is shown in Figure 5.13. The visibility of the sarcomeres (without any staining) should be noted. The extended focus images was reconstructed from 6 confocal (x,y) image slices acquired with the CSLM.

The cutting subsystem of the organ mapping apparatus is being developed in parallel with the imaging subsystem. The subjective quality of the tissue surface (clean or contaminated from tissue residues) after a tissue layer was removed, was used as a criterion for preliminary evaluation of the different cutting techniques. The most appropriate one was found to be ablation via an Excimer layer. More details regarding the tissue machining methods can be found in Appendix 4 (Sections a4.3). The organ used in the preliminary evaluation of tissue machining methods was adult mice hearts. The motivation behind using this type of tissue is the need for a detailed 3D anatomical map of the myocardium [Doukoglou *et al.*, 1992] to be used for the development of a heart surgical robot (HSR-1) analogous to the ophthalmic MSR-1 presented in Chapter 1.

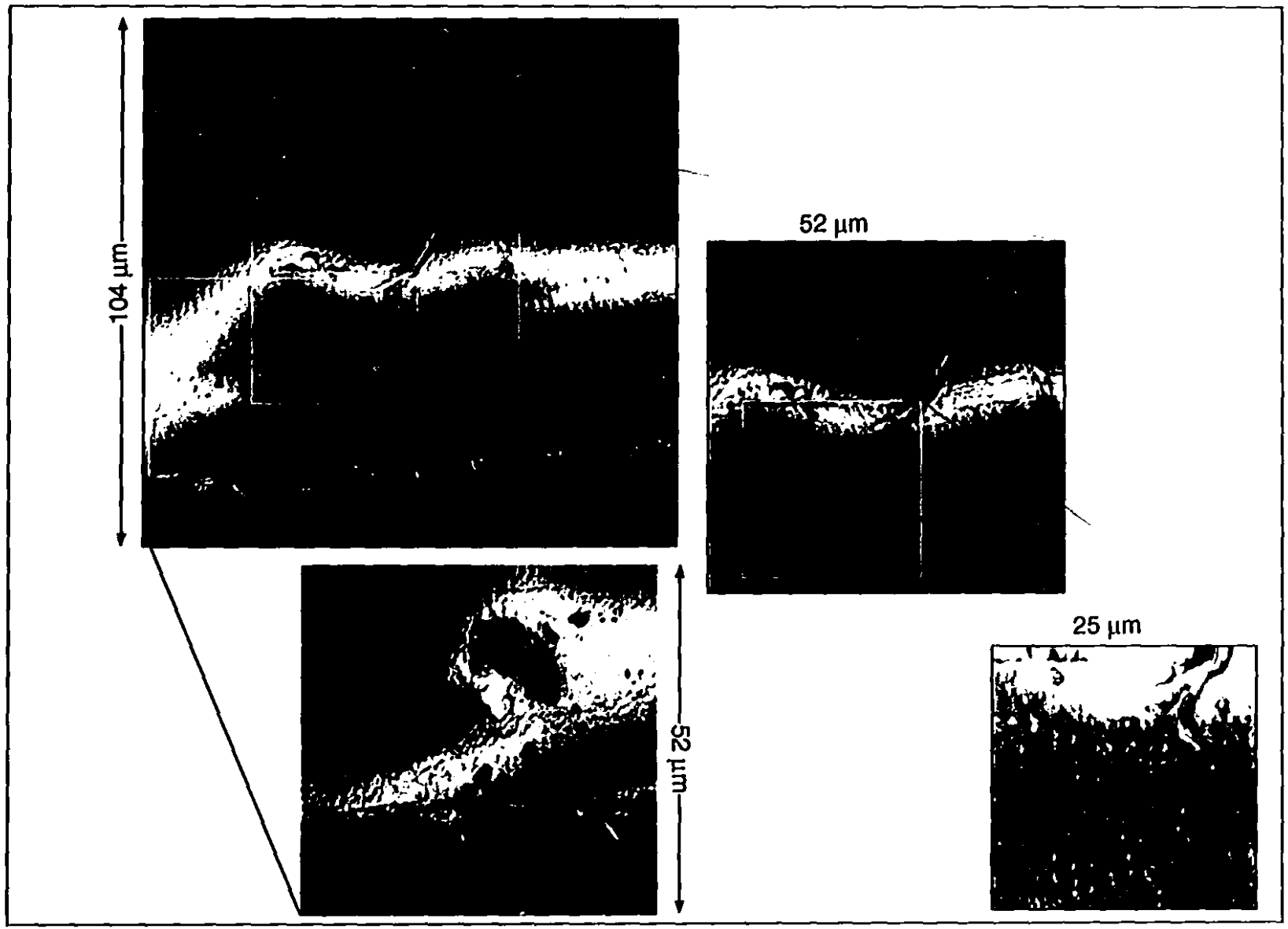

Figure 5.13 *Image of a striated muscle fiber. The sarcomeres are clearly visible. This is an extended focus image and is generated by a series of 6 confocal image slices spaced at 1 µm apart.*

5.6 Summary

In this chapter operational details as well as important results of characterizing the CSLM were presented. More specifically the CSLM optical subsystem was characterized in terms of its depth and transverse response function. A very close agreement between the measured and theoretically estimated performance was observed. An extensive characterization of the scanning subsystem with respect to its resolution, accuracy, repeatability and backlash, was also presented. Details regarding some frequently applied 2D image processing techniques, together with image examples, were also presented. Finally, considerations regarding tissue preservation and tissue machining methods were discussed.

5.7 References

Ataman, E., Aatre, V.K. & Wong. K.M. (1980), "A fast method for real-time median filtering," *IEEE Transcactions on Acoustics, Speech and Signal Processing*, **ASSP-28**(4), pp. 415-241.

Davidovits, P. & Egger, M.D. (1971), "Scanning Laser Microscope for Biological Investigations," *Applied Optics*, **10**(7), pp. 1515-1619.

Doukoglou, T.D., Hunter, I.W., Brenan, C.J.H. (1992), "Myocardial Fiber Studies using Interference Confocal Microscopy," *Scanning*, **14**(suppl. II), pp. II-72 to 74.

Eykhoff, P. (1974), *System Identification, Parameter and State Estimation*, John Wiley, New York.

Gallagher, N.C. & Wise, G.L (1981), "A theoretical analysis of the Properties of median filters," *IEEE Transactions on Acoustics, Speech and Signal Processing*, **ASSP-29**(6), pp. 1136-1141.

Gonzalez, R.C. & Wintz, P. (1987), *Digital Image Processing*, second edition, Adison-Wesley.

Newport Corporation (1994), *The 1994 Newport Catalog*, pp. 4.9-4.10.

Parker Hannifin Corporation (1991-92), *Positioning Control Systems and Drives Catalog*, pp. A63-A65.

Rosenfeld, A. & Kak, A.C. (1982), "Section 6.2: Gray scale modification" in *Digital Picture Processing* (second edition), Academic Press, New York, pp. 223-237.

Scheid, F. J. (1989), Schaum's outline of theory and problems of numerical analysis, 2nd edition, McGraw-Hill.

Sheppard, C.J.R., & Wilson, T. (1979), "Effects of spherical aberration on the imaging properties of scanning optical microscopes," *Applied Optics*, **18**(7), pp. 1058-1063.

Sheppard, C.J.R., & Wilson, T. (1981), "Effects of high angles of convergence in V(z) in the scanning acoustic microscope," *Applied Physics Letters*, **38** (11), pp. 858-859.

Sheppard, C.J.R., & Gu, M. (1991), "Aberration compensation in confocal microscopy," *Applied Optics*, **30**(25), pp. 3563-3568.

Wilson, T. & Carlini, A.R. (1987), "Three-dimensional imaging in confocal imaging systems with finite size detectors," *Journal of Microscopy*, **149** (1), pp. 51-66.

CHAPTER 6

A Spherical-Coordinate Scanning Laser Microscope

Preface

As mentioned in the Introduction (Chapter 1) the scope of this thesis work is dual. Beyond the design and construction of an imaging subsystem of the small organ mapping system, the applicability of confocal arrangements as an imaging tool for the microsurgical robot (presented in Chapter 1) is investigated. This Chapter presents a system prototype that a) performs the scanning in non-Cartesian coordinate fashion and b) uses optical fiber for replacing some of the open air links (and bulk optical components) in the microscope design. These two novel design choices are intended for a) improving the image signal-to-noise ratio for organs that exhibit a sphere-like shape (i.e. the eye) and b) allowing the miniaturization of the optical system so that can ultimately be integrated (as an imaging tool) in one of the microsurgical robot's Slave limb.*

* The format of this chapter deviates slightly from the format used for the rest of the thesis chapters since it follows the guidelines for submiting to the Journal of Optical Engineering. A paper similar in form to this chapter was published in the Journal of Optical Engineering with T.D. Doukoglou and I. W. Hunter as its authors:
Tilemachos D. Doukoglou & Ian W. Hunter (1995), "A Spherical-coordinate Scanning Confocal Laser Microscope," *Optical Engineering*, 34(7), pp. 2103-2108.

Abstract. We will present the design, construction and characterization of a spherical-coordinate scanning, reflection mode confocal laser microscope (SCSLM). Two system designs will be presented, namely a conventional bulk optics object-scanning design and a preliminary optical fiber based 2-axis optics/1-axis object scanning version. The bulk-optics design is characterized with respect to its optical sectioning property. Sample 3D images acquired using the SCSLM are also presented, including a reconstruction of an ex-vivo pig's cornea. The bulk optics design offers a higher light throughput but it can not be easily miniaturized for future integration in a microsurgical robot design. The fiber based design has a reduced signal-to-noise ratio (SNR) but can be potentially made lightweight and small enough to be integrated as the imaging subsystem of a microsurgical robot.

Subject terms: confocal microscope; spherical-coordinate scanning; optical fiber based; 3D imaging.

6.1 Introduction

In designing a microsurgical robot for performing surgery on small organs, like the eye[1], detailed knowledge of the organ operated upon, such as detailed structural and mechanical models, is required. Having as our objective a) investigating the use of non-rectilinear coordinate scanning in developing an imaging system capable of gathering high resolution 3D corneal images and b) integration of such a system into the microsurgical robot for acquisition of 3D corneal images during microsurgery, we have lately constructed two confocal scanning laser microscope prototypes. These systems can acquire 3D volumetric images, and they utilize a spherical-coordinate scanning scheme to make them better suited for observation of objects that can be considered to have a roughly spherical-shape.

Confocal scanning microscopes (CSM)[2] have been and are used for acquiring volumetric three dimensional (3D) high resolution images of ocular tissue. More specifically they are used for retinal[3] and corneal imaging. Corneal studies are performed ex-vivo[4], or insitu ex-vivo[5] , but also non-real-time in vivo[6] and more recently real-time in vivo[7]. These systems are very well suited for the ocular tissue studies they are designed for. However, mainly due to their size, existing ophthalmic CSMs cannot be easily integrated as part of a microsurgical robot design.

In the case of corneal imaging, scanning in Cartesian coordinates means the surface normal increasingly deviates from the microscope's optical axis as the objective moves away from the corneal center, because of the cornea's quasi spherical shape. This results in a reduced signal-to-noise ratio (SNR), and image quality degradation towards the periphery of the cornea. Master and Thaer in their system design[7] addressed the problem by moving the whole microscope along two angular and one linear coordinates to ensure that the optical axis of the microscope is almost perpendicular to the tangent of the corneal surface.

In our case we have chosen to perform the scanning in spherical coordinates. Using this scheme we can move along the surface of the cornea, while the optical axis of the microscope does not deviate significantly from the cornea's surface normal. Finally utilizing the optical sectioning property of a confocal arrangement we can construct 3D images of the cornea surface from a series of 2D concentric spherical coordinate slices. For final integration of such an imaging system into the microsurgical robot a miniaturized optics scanning, optical fiber based arrangement, that incorporates ideas used in other optical fiber based systems[8,9], is required. This is due to the fact that optical fiber based microscopes allow the positioning of the imaging optics away from the light source and detection system and the optical components can be small and fewer in number. Additionally, when optics scanning rather than object scanning is required, fiber based systems are more suitable, since the imaging end of the fiber together with the imaging optics can be easily scanned (even in spherical coordinates).

6.2 Microscope Design

Before attempting a fiber based system design, we built a bulk optics SCSLM in order to investigate the other aspects of microscope operations (i.e. depth discrimination, acquisition of spherical coordinate optical slices, and 3D reconstruction from these slices).

6.2.1 SCSLM Bulk optics design

The bulk optics configuration of the SCSLM is shown in Figure 6.1. Its design is highly modular consisting of three main subsystems: the optical subsystem, the mechanical (scanning) subsystem and the computer subsystem. A 10 mW, 670 nm wavelength laser

diode (Lasermax Inc.) is used as the light source. The vertically polarized beam, after being corrected for astigmatism in the beam shaping optics, is expanded to 5 mm diameter. An objective (with a 0.25 numerical aperture (NA) - Olympus MA10) focuses the beam on to the object, which is scanned in θ,φ,ρ spherical coordinates using 2 rotary and 1 linear motorized stages. The motion of the stages is achieved using microstepping motors with resolution of up to 25000 steps/revolution.

The smallest addressable motion increment is less than 1 mdeg for the rotary axes and 50 nm for the linear axis. The unidirectional accuracy of the positioning system is 0.06 deg for the φ axis, 0.05 deg for the θ axis and 0.1 μm for the ρ axis. The range of motion for the translation stages is continuous (>360 deg) for the φ axis, 110 deg for the θ axis and 50 mm for the ρ axis. The speed of the φ axis (fast axis) is 10 Hz, thus the total scan time for acquisition of a 2D (φ,θ) image is proportional to the number of image lines along the θ axis.

The reflected light, after emerging from the polarizing beam splitter, is focused by a plano-convex lens (k=200 mm) and detected with an avalanche photo diode (APD - Hamamatsu Type no. 2381). A $\lambda/4$ wave plate mounted between the sample and the polarizing cubic beam splitter is used for optical isolation and to maximize the amount of light reaching the detector. A pinhole is placed in front of the APD to reduce out-of-focus light detection. The size of the pinhole can be selected to be from 10 μm up to about 200 μm. The signal of the APD is discretized, quantized, and stored in the computer memory. The computer (IBM RS6000 workstation) is equipped with a data I/O card (Burr Brown PCI 602W) providing 12 bit analog to digital (A/D) converters and 16 digital I/O lines. The motion of the stages is also computer controlled to synchronize the scanning with the data acquisition. Most functions of the microscope are software controlled via custom software written in the C programming language. The acquired images contain intensity as well as information regarding the object's 3D geometry. The intensity information of the acquired images can be displayed on the workstation screen. An example image of an eye shaped aluminum calibration target is shown in Figure 6.5. The concentric spherical coordinate slices are shown in Figure 6.5(a) and the 3D reconstructed geometry as well as the geometry superimposed with the reflectivity are shown in Figure 6.5(c).

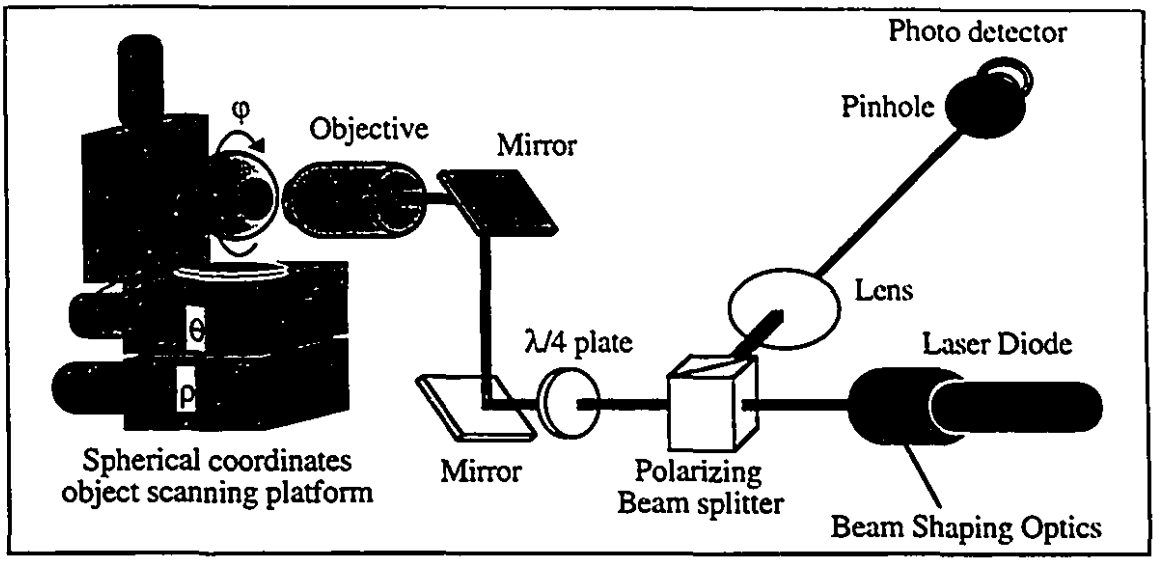

Fig. 6.1 *Conventional configuration of the spherical-coordinate scanning laser microscope system.*

Currently the SCSLM's resolution is limited by the low NA objective used. Mechanical design limitations (size and shape of the eye-socket) require an objective lens with a long working distance (> 15 mm). To accommodate this requirement a 0.25 NA microscope objective with a working distance of 18 mm is used. The linear resolution (arc-length inter-pixel distance) of the 2D φ,θ images varies along the θ axis (decreases for larger θ values). The decrease in linear resolution can be compensated for by increasing the radial resolution along the φ axis for increasing θ values.

6.2.2 SCSLM fiber design

A revised version the SCSLM is designed as the fiber based configuration that is shown in Figure 6.2. Optical fiber based confocal microscopes [8-15] including fiber bundle based versions[16] have been reported recently. They offer a number of advantages compared to bulk optics designs. The detection system and light source can be remote from the imaging optics and the object under observation. The optics can be miniaturized and their number reduced since there are a number of bulk optical components that can be replaced with fiber based ones (i.e. mirrors, beam-splitters). The optical-fiber core can serve as both a detector and source pinhole minimizing alignment requirements. In our design we have isolated the scanning system from the detection and laser source and minimized the mass of the moving parts by using a fiber optics based spherical-coordinate hybrid scanning arrangement (2 axes for the optics and 1 axis for the object).

Light is delivered to the objective lens using a single-mode optical fiber whose core (diameter of 3.8 μm with NA=0.1) also serves as the source and detector pinhole required for the confocal arrangement. A 10 mW, 670 nm wavelength laser diode was used as the light source. The vertically polarized beam, after being corrected for astigmatism in the beam shaping optics, was expanded to 5 mm diameter. We used an objective of 0.25 NA to focus the beam on to the object, which was scanned in the φ spherical coordinate using a rotary stage. The optics were scanned in the other two axis (θ, ρ) using one rotary and one linear motorized stages. Two lenses (L_1 and L_2) with NA matching that of the optical fiber were used to launch and collect the light of the optical fiber. The collimating lens L_2 controls the confocality properties of the arrangement. When its NA is lower than that of the fiber then we have higher depth discrimination (narrower depth response). This is achieved at the expense of the amount of light reaching the sample[12]. An image of a spherical object acquired with this arrangement is shown in Figure 6.3.

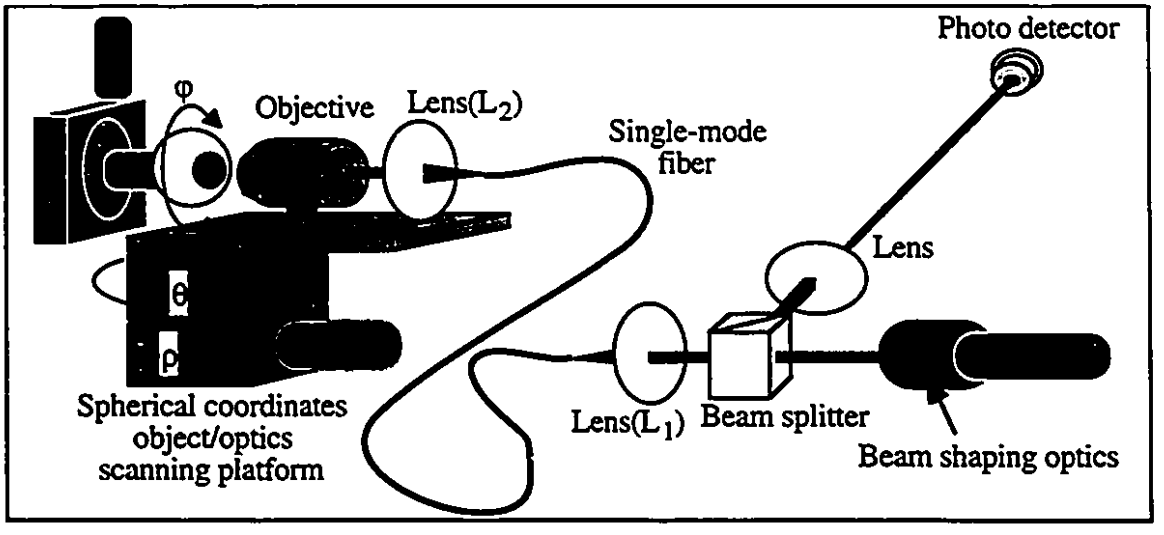

Fig. 6.2 *Optical fiber based spherical-coordinate scanning laser microscope where the core of the single-mode optical fiber is used as the source and detector pinhole.*

Despite its numerous advantages, our optical fiber based configuration needs further improvements. One problem was that the fiber core drifted out of alignment during scanning (possibly due to vibration from the scanning system). This problem can be seen in the images of Figure 6.3 where the signal deteriorates in the lower part of the square φ,θ image (Figure 6.3a). Also the amount of light that reaches the object is less compared with the bulk optics configuration. We are currently investigating faster and more reliable fiber (optics) scanning arrangements based on beam bending direct drive technology (non-stepping motor) similar to the one in Reference 17.

6.3 Data Processing

After acquisition, the images (from both SCSLM designs) are stored in the computer hard disk for further offline processing. We have enhanced the images by using standard image processing techniques. When necessary, median filtering is applied to the images to reduce random spike noise. The 2D (φ,θ) intensity image is difficult to interpret unless the topographical and intensity information is properly mapped into 3D (x,y,z) space (Figure 6.3). Using the spherical to Cartesian coordinate transformation,

$$x = \rho \sin\theta \cos\varphi,\ y = \rho \sin\theta \sin\varphi,\ z = \rho \cos\theta \quad , \tag{1}$$

we can reconstruct a realistic 3D model of the object under observation.

To visualize the 3D model a surface rendering custom visualization package (written utilizing the GL library), was used and run on an IBM RS6000 workstation equipped with a 3D graphics card. The 3D image can be rotated interactively to obtain views of the various sides of the object. Pseudo coloring can be applied to the images to improve differentiation of various structures.

Surface geometry information can be extracted from a sequence of concentric spherical coordinated images as follows. A sequence of N 2D (φ,θ) images are acquired along the ρ axis. Axis ρ is parallel with the optical axis of the SCSLM. From the sequence of the N 2D (φ,θ) images and for each φ,θ location (pixel) we find the highest intensity value and the location along the ρ axis where this highest value appears (Equation 2). By applying the above process to the sequence of N concentric spherical coordinate images (refer to Figure 6.5a) we construct two new 2D (φ,θ) images. One represents the surface reflectivity ($I(\varphi,\theta)$) and the other the object's geometry ($D(\varphi,\theta)$) in spherical coordinates (refer to Figure 6.5(b)). Using then these two images and by applying the spherical to Cartesian coordinate transformation we can build a 3D representation of the object under observation (refer to Figure 6.5c).

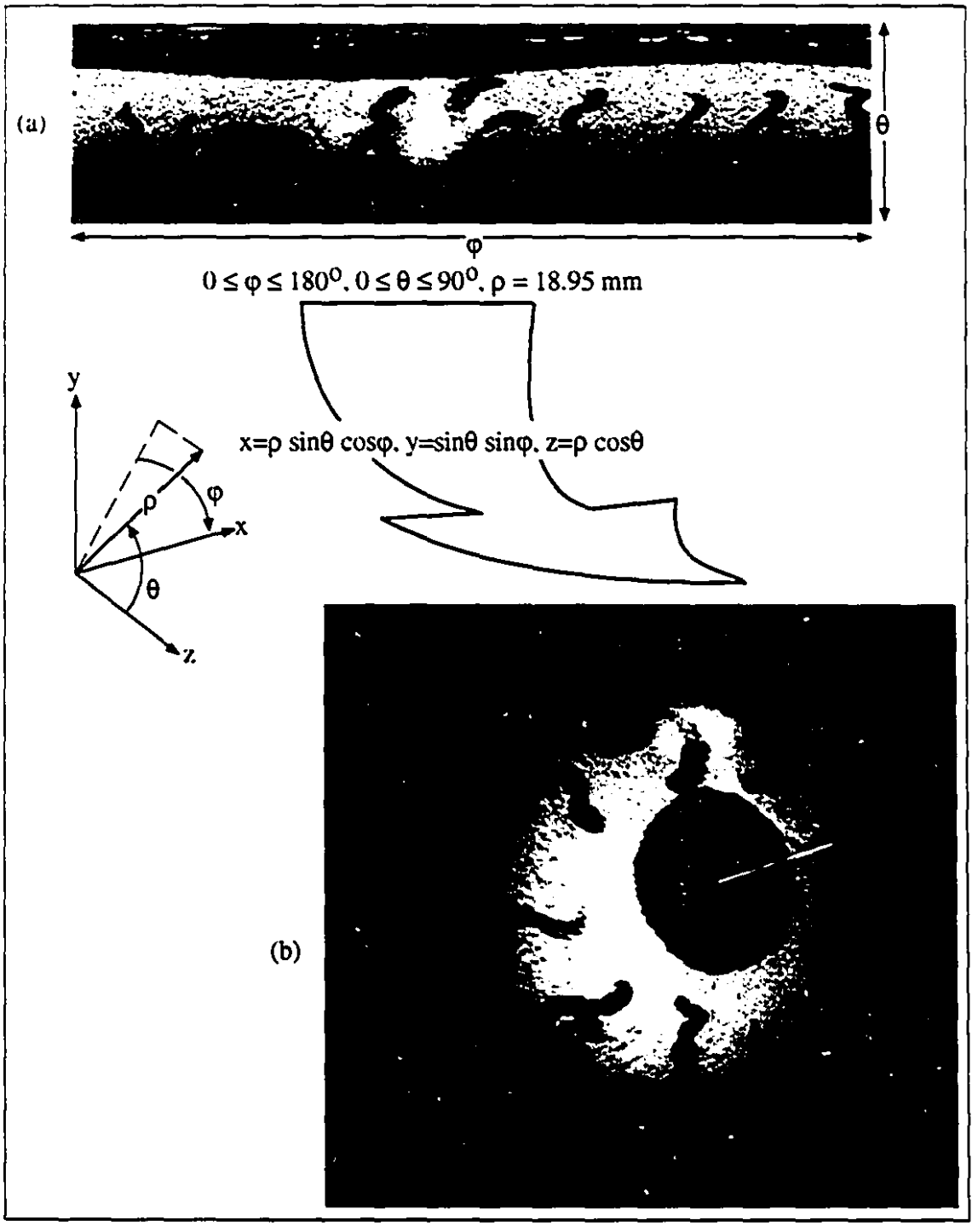

Fig. 6.3 *(a) Sample 2D θ,φ (ρ=constant) intensity image from the optical fiber arrangement of the SCSLM and (b) the acquired image visualized after being mapped properly in the 3D x,y,z coordinate space.*

More rigorously, for a sequence of N concentric spherical coordinate images $i_k(\varphi,\theta)$

$$I(\varphi,\theta) = \max_{k=1...N}[i_k(\varphi,\theta)]$$

and $$D(\varphi,\theta) = \mathrm{Loc}(\max_{k=1...N}[i_k(\varphi,\theta)]) \quad \text{for } k=1...N\ , \qquad (2)$$

where the Loc( ) function returns the value of k for which $\max[i_k(\varphi,\theta)]$ occurs.

In order to reconstruct not just the object's surface geometry, but also its internal structure voxel based volume rendering[4] techniques (now being offered also by commercial packages) should be applied to the data after they are converted from spherical to Cartesian coordinate space.

6.4 Characterization

For a confocal microscope arrangement, we define as the normalized pinhole radius (v_p)

$$v_p = 2\pi\, r_p \sin(a)/\lambda \quad , \qquad (3)$$

where r_p is actual pinhole radius scaled by the optical magnification ($r_p = r/M$) and sin(a) is the effective NA of the objective lens.

The confocality criteria[18] dictate that $v_p \leq 0.5$ for the lateral resolution to be indistinguishable from that of a scanning microscope with a true point detector (Type 2 confocal). The equivalent criterion for the depth response (to be indistinguishable from that of a confocal microscope with a true point detector) is that $v_p \leq 2.5$.

In our case, the smallest pinhole used has a diameter of 10 μm , $v_p \cong 0.65$. Consequently, the lateral resolution of the SCSLM is worse than that of a Type 2 confocal arrangement. Nevertheless, with the 10 μm pinhole the SCSLM should exhibit depth discrimination (optical sectioning) equivalent to that of a Type 2 confocal microscope.

The (bulk optics configuration) SCSLM axial depth response was measured by scanning a mirror through the focal point of the objective lens. The objective used was an Olympus ×10, 0.25 NA lens. The effective NA though was less (≅ 0.14) since we did not completely fill the objective's aperture. A plano-convex lens (k=200mm) was used as the collector lens. We have varied the pinhole size from 10 to 200 μm. The normalized depth responses for the different pinhole sizes are shown in Figure 6.4(a).

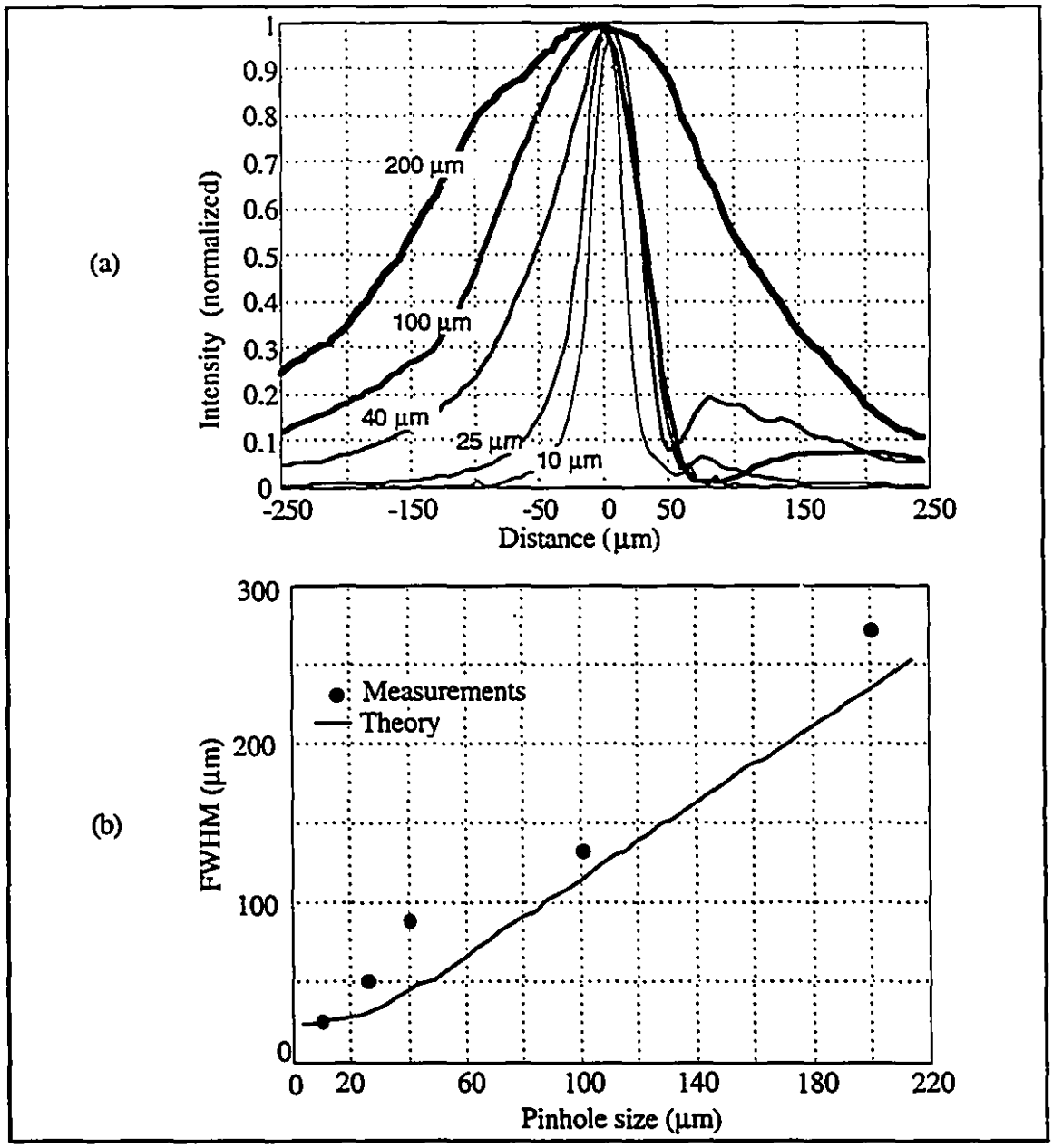

Fig. 6.4 *(a) Depth response measurements for the SCSLM arrangement for various pinhole diameters and (b) plot of the FWHM of the depth response vs. pinhole diameter.*

The depth response function of a confocal microscope arrangement for a planar reflector is approximated[2] by

$$\left[\frac{\sin(u/2)}{u/2}\right]^2 \qquad \text{where } u=\frac{8\pi}{\lambda}\rho\sin^2(a/2) \quad , \tag{4}$$

and ρ the actual distance along the optical axis.

For the SCSLM and with a 10 μm pinhole the theoretical 3dB distance (FWHM) according to Equation (4), should be approximately 30 μm. The measured value was 28 μm, indicating good agreement between the theoretically expected value and the measured response.

The full width half maximum (FWHM) distance for each of the curves as a function of the pinhole size is plotted in Figure 6.4(b). Although the FWHM measurements, for various pinholes sizes, follow the trend of the theoretically estimated ones, experimental FWHM measurements were found to be larger. The theoretical values were calculated using a geometric optics model with Gaussian beam weighting (shown with the solid line in Fig. 4b). This disagreement (between theory and experiment) is similar to what Wilson and Carlini[18] observed with their measurements and the scalar paraxial theory model they used (for $v_p > 2$). The disagreement was attributed to aberrations (i.e. spherical, astigmatism and coma), whose combined effects result in a non-symmetrical depth response.

To calibrate further the system we have constructed an aluminum target (using a Mazak 15MS, 0.5 μm precision turning center) having an eye like shape/size and we have tried to reconstruct the surface geometry and reflectivity using the SCSLM. This way we could check the accuracy of the reconstruction against a known object. The images acquired are shown in Figure 6.5 together with the 3D model of the target.

The reconstruction was successful within the error imposed by the system design criteria. The surface geometry was reconstructed with a resolution of 90 μm (which was the distance between the acquired concentric slices). The resolution can be increased at will by first narrowing the depth response of the SCSLM (choosing a smaller pinhole and/or also using a higher NA objective) and at the same time acquiring concentric slices with a smaller radial (ρ) distance increment. The resolution of the acquired image in the transverse plane is governed mainly by the diffraction limit of the objectives used and the positioning accuracy of the scanning system. In the previous measurements we have operated well above these limits.

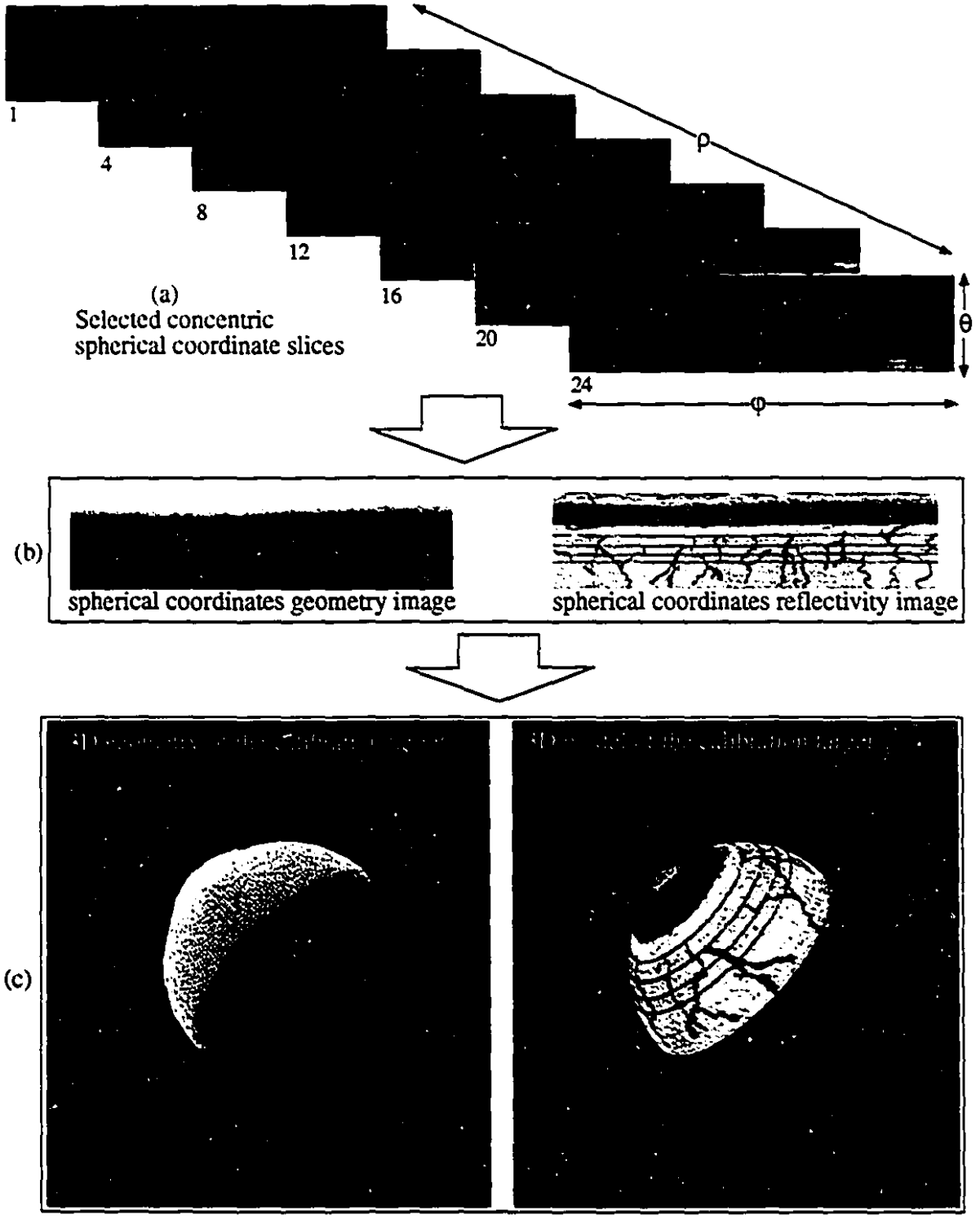

Fig. 6.5 *(a)Concentric confocal slices of the Al calibration target, (b) the resulting reflectivity and geometric information images, and (c) the 3D model of the target.*

6.5 Application to eye studies

Using the SCSLM we have also scanned the corneas of ex-vivo pig's eyes. The extracted eyes were cleaned of the surrounding tissue (muscles, skin). They were then mounted in an aluminum elliptical socket we machined on the Mazak 15MS turning center. Different socket sizes were constructed to accommodate different eye sizes.

Each socket consists of two `semi-spherical' shells that fit together to form the eye-holder. Both parts have a hole on the center. The top part for allowing the cornea (and some of the sclera) to be exposed for imaging and the lower for injecting Ringer solution to prevent eye drying. The two parts are held together with three small screws. The lower part is also attached to an adaptor ring that allows mounting of the whole socket on the scanning system.

When the eye-mounting socket was attached on the scanning system the range of motion of the θ axis was reduced to 72 deg. The eye-mounting platform also imposed limits to the working distance of the objective lens. An objective lens with a working distance of > 15 mm is needed to utilize the available range of motion of the scanning system. These limitations dictated the used of the low NA objective, instead of a higher NA one that would have also provided a higher depth discrimination and be able to observe corneal cell layers at the same time.

At regular time intervals the eye was sprayed with Ringer solution to avoid drying and to slow tissue degradation. An image of a whole pig cornea acquired by the SCSLM is shown in Figure 6.6. We acquired 26 concentric slices at 100 μm radial increments. These slices were then processed to construct the surface geometry and intensity images shown in Figure 6.6(b). These two images mapped in Cartesian space coordinates are shown in Figure 6.6(c). The spikes that appear on the section of the sclera that surrounds the cornea (Figure 6.6(c)) are due to the inadequacy of the rendering algorithm to properly select the surface normal for that section of the image. Although the acquired images do not have the highest possible resolution, the purpose of the above experiment was to investigate the feasibility of acquiring accurate 3D images of small organs that exhibit a roughly spherical shape (such as the eye), by using non-Cartesian scanning and a confocal microscope arrangement.

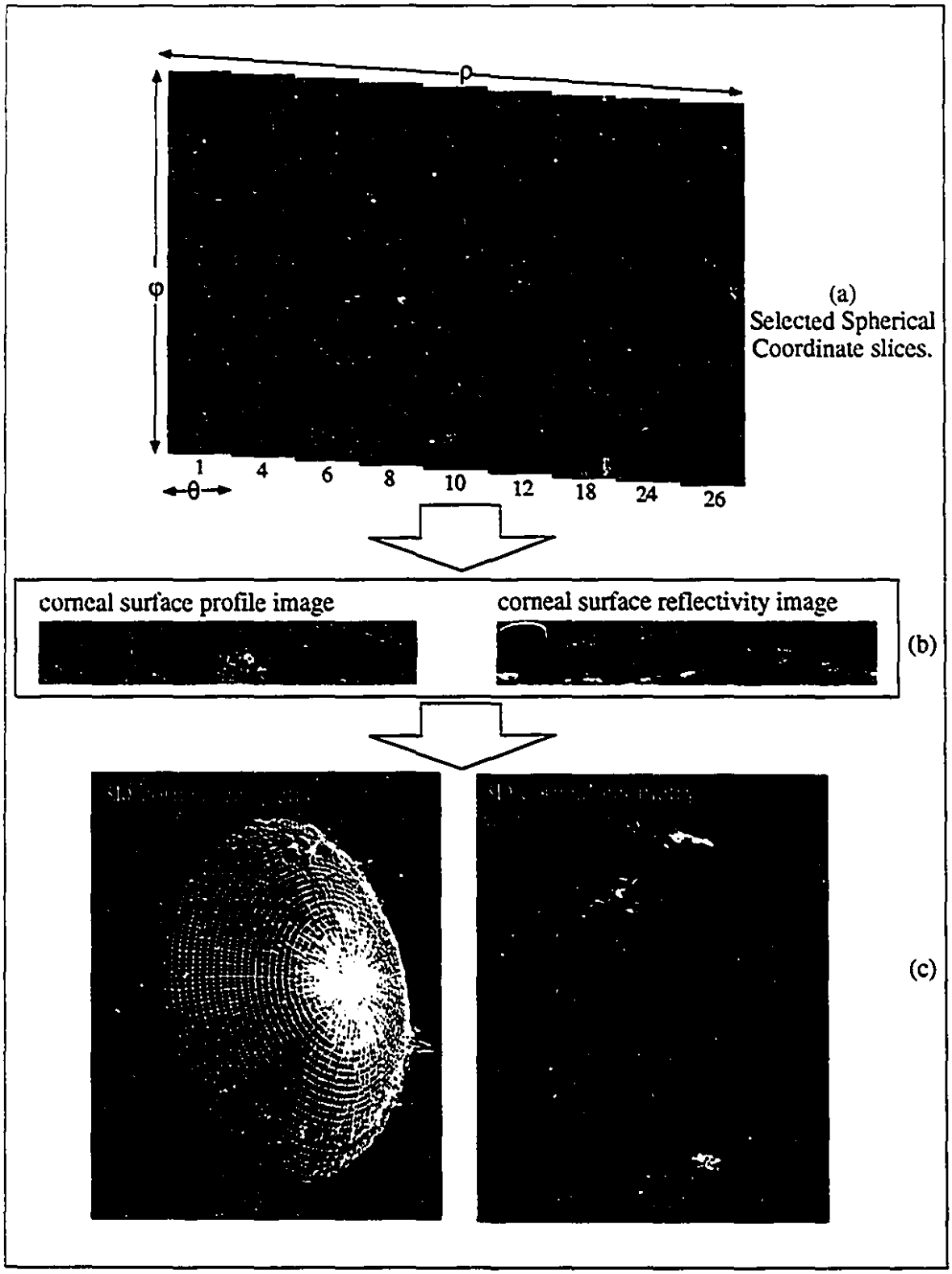

Fig. 6.6 *(a) Selected spherical coordinate image slices. (b) Retrieved cornea geometry and reflectivity images and (c) the 3D reconstucted model of the cornea.*

Improvement of the lateral resolution and the depth discrimination of the SCSLM (by using a higher NA objective lens) will allow acquisition of both high resolution volumetric images of small sections of the cornea, as well as very accurate topographical images of the whole corneal geometry. As it is indicated in Figure 6.6 due to system design limitations only the later is currently possible. To perform eye-surgery and more specifically radial keratotomy (using the microsurgical robot), visibility of the corneal cell layers is not essential. Information regarding corneal topography is highly desirable. Even though the SCSLM prototype is not designed to be used like a conventional corneal mapping system[19,20], it compares favorably with the most commonly used corneal topography techniques[21], that offer radial resolutions of ~100 μm. Furthermore, although SCSLM in its current state cannot achieve the depth resolution offered by coherent optical domain reflectometry[22] (OCDR), confocal OCDR arrangements can greatly benefit (in terms of SNR) by incorporating spherical-coordinate scanning (similar to the one used in the SCSLM) when performing ocular tissue imaging.

A problem that arises in in-vivo eye-imaging applications is blurring artifacts due to eye motion. In the anticipated use of the SCSLM as an imaging subsystem of the microsurgical robot, the eye is tethered during the surgical procedure (as in radial keratotomy) thus preventing motion.

6.6 Summary

We have developed a spherical coordinate scanning confocal laser microscope. The constructed prototypes are (1) a bulk optics, object scanning confocal arrangement and (2) an optical fiber based, optics/object scanning arrangement. We have used the bulk optics configuration to acquire accurate 3D geometric and optical information from various test objects as well as motionless ex-vivo pig's corneas. The information from these volumetric images may be used for the development of realistic geometric models of the object under observation. The system was built to investigate the suitability and usefulness of non-Cartesian scanning arrangements as imaging systems for the microsurgical robots[1]. Preliminary results are encouraging, but further development is needed. The next step is to integrated the optics into a very low mass and low volume package suitable for being mounted on a microsurgical robot to provide real time imaging at the microsurgical robot tool tip.

Acknowledgments

This research started while both authors were at McGill University of Montréal, Canada. We would like to thank the Institute for Robotics and Intelligent Systems, one of the Canadian Networks of Centres of Excellence and the Medical Research Council of Canada for funding the above project.

6.7 References

1. I.W. Hunter, T.D. Doukoglou, S.L. Lafontaine, P.G. Charette, L.A. Jones, M.A. Sagar, G.D. Mallinson and P.J. Hunter, "A teleoperated microsurgical robot and associated virtual environment for eye surgery," *PRESENCE* **2**, 265-280 (1993).
2. B.R. Masters, "Confocal microscopy of ocular tissue," Chap. 11 in *Confocal Microscopy*, T. Wilson, Ed., pp. 305-324, Academic Press, New York, (1990).
3. R.H. Webb, G.W. Hughes and F.C. Delori, "Confocal scanning laser ophthalmoscope," *Applied Optics* **23**, 1492-1499 (1987).
4. B.R. Masters and S.W. Paddock, "Three-dimensional reconstruction of the rabbit cornea by confocal scanning optical microscopy and volume rendering," *Applied Optics* **29**, 3816-3822 (1990).
5. B.R. Masters and M.A. Farmer, "3-Dimensional confocal microscopy and visualization of the insitu cornea," *Computerized Medical Imaging and Graphics* **17**, 211-219 (1993).
6. C.J. Koester, J.D. Auran, H.D. Rosskothen, G.J. Florakis and R.B. Tackaberry, "Clinical Microscopy of the cornea utilizing optical sectioning and a high-numerical-aperture objective," *Journal of the Optical Society of America-A-Optics and Image Science* **10**, 1670-1679 (1993).
7. B.R. Masters and A.A. Thaer, "Real time scanning slit confocal microscopy of the in vivo human cornea," *Applied Optics* **33**, 695-701 (1994).
8. D. Dickensheets & G.S. Kino, "A scanned optical fiber confocal microscope," in *Proceedings SPIE* **2184** Three-dimensional microscopy, 39-47 (1994).
9. L. Giniunas, R. Juskaitis, and S.V. Shatalin, "Endoscope with optical sectioning capability" *Applied Optics* **32**, 2888-2890 (1993).
10. K. Shigeharu and T. Wilson, "Confocal scanning optical microscope using single-mode fiber for signal detection," *Applied Optics* **30**, 2143-2150 (1991).
11. S. Kimura and T. Wilson, "Confocal scanning optical microscope using single-mode fiber for signal detection," *Applied Optics* **30**, 489-494 (1991).

12. T. Dabbs and M. Glass, "Fiber-optic confocal microscope FOCON," *Applied Optics* **31**, 3030-3035 (1992).

13. P.M. Delaney, M.R. Harris and R. King, "Fiber optics laser scanning confocal microscope suitable for fluorescence imaging," *Applied Optics* **33**, 573-577 (1994).

14. M. Gu and C.J.R. Sheppard, "Fiber-optical confocal scanning interference microscopy," *Optics Communications* **100**, 79-86 (1993).

15. T. Wilson, "Image formation in 2-mode fiber based confocal microscopes," *Journal of Optical Society of America A-Optics and Image Science* **10**, 1535-1543 (1993).

16. A.F. Gmitro and D. Aziz (1993), "Confocal microscopy through a fiber optic imaging bundle," *Optics Letters* **18**, 565-567 (1993).

17. I.W. Hunter, S.L. Lafontaine, P.F.M. Nielsen, P.J. Hunter and J.M. Hollerbach, "Manipulation and dynamic testing of microscopic objects using a tele-micro-robot system," *IEEE Control Systems Magazine* **10**, 3-9 (1990).

18. T. Wilson and A.R. Carlini, "Size of the detector in confocal imaging systems," *Optics Letters* **12**, 227-229 (1987).

19. J.J. Roswey, A.E. Reynolds and R. Brown, "Corneal Topography," *Archives of Ophthalmology*, **99**, 1093-1100 (1981).

20. S.D. Klyce, "Computer-assisted corneal topography. High-resolution graphic representation and analysis of keratoscopy," *Investigative Ophthalmology & Visual Science*, **25**, 1426-1435 (1984).

21. J.D. Doss, R.L. Hutson, J.J. Rawsey and D.R. Brown, "Methods for Calculation of Corneal Profile and Power Distribution," *Archives of Ophthalmology*, **99**, 1261-1265 (1981).

22. J.A. Izzat, M.R. Hee, D. Huang, J.G. Fujimoto, E.A. Swanson, C.P. Lin, J.S. Schuman and C.A. Puliafito, "Optical coherence tomography for medical diagnostics," in *Medical Optical Tomography: Functional Imaging and Monitoring*, G. Miller, B. Chance, R. Alfano, S. Arridge, J. Beuthan, E. Gratton, M. Kaschke, B Masters, S. Svanberg and P. van der Zee, Eds, pp. 450-472, **IS11**, SPIE Optical Engineering Press, pp. (1993)

Plate 6.1 *Picture of the bulk optics prototype of the SCSLM.*

Plate 6.2 *Picture of the fiber optics based prototype of the SCLM.*

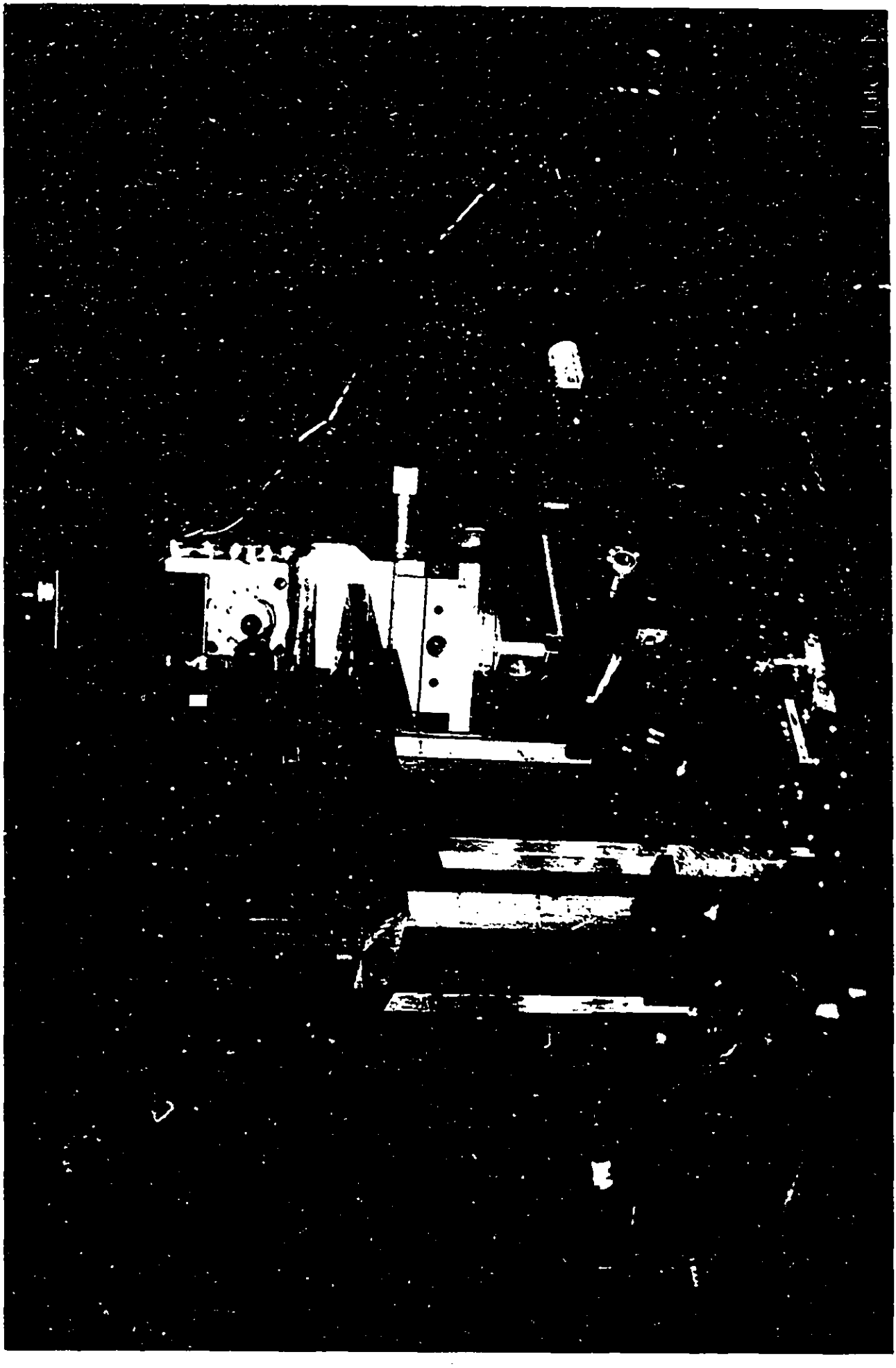

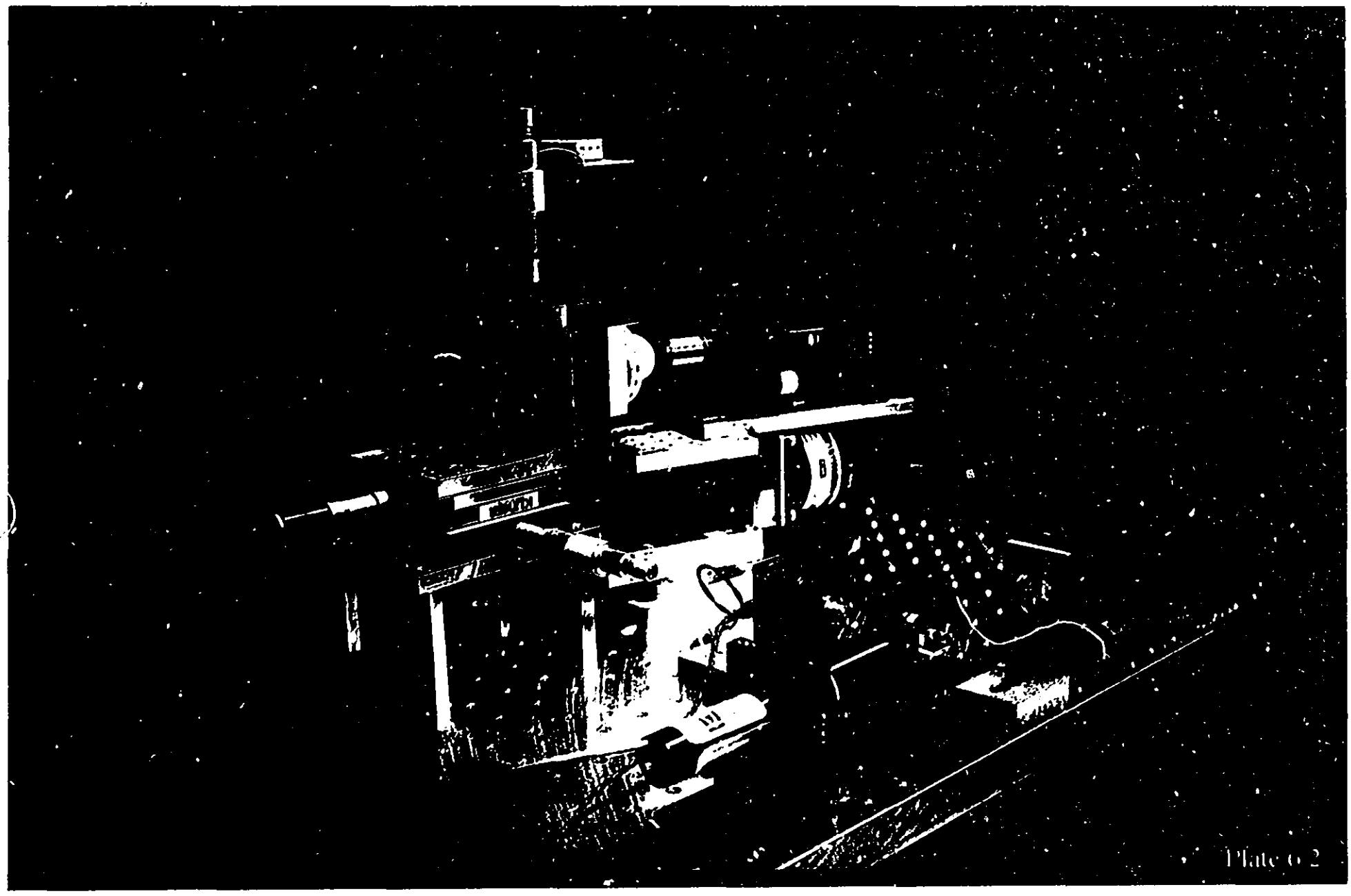

Plate 6.2

CHAPTER 7

Conclusion

After a brief overview of what has been presented in this thesis, the original contributions of this work are listed, followed by a discussion on the possible directions for the continuation of this research project. Some of the tasks mentioned in the future work section have been attempted but not in a rigorous manner. Nevertheless, some understanding of the problems, and the advantages and disadvantages for a number of these tasks were made possible.

7.1 Overview

A justification for this research project was given in Chapter 1. The current work was positioned within the general framework of the research in-progress in the Biorobotics laboratory of McGill University and the Newman laboratory of the Massachusetts Institute of Technology. The main theme of this research is the development of microsurgical robotic systems.

The main impetus behind this research project is the development of an imaging system as part of a complete organ mapping apparatus. The apparatus would be capable of sectioning an organ as well as acquiring 3D volumetric images with cellular level details for each section, until a complete map of the organ can be built. Additionally, the possibility of using confocal microscopy as an imaging modality for the microsurgical robot is also investigated.

The imaging system of the organ mapping apparatus was chosen to be a confocal scanning laser microscope. Therefore, a historical overview, as well a thorough literature review, of the development of various forms of confocal scanning laser microscopes was presented in Chapter 2.

A brief overview of the theory describing the function of the confocal microscope arrangement was presented in Chapter 3. Simplified geometric optics and scalar paraxial theory models describing the depth response properties of a confocal arrangement were developed and presented.

The design, construction, and characterization of a Confocal Scanning Laser Microscope (CSLM) was described in Chapters 4 and 5. The microscope's novel design allows for a multitude of image contrast modes (intensity, phase and interference), without rearrangement of its physical components. Confocal microscopes configurations improve image resolution, contrast and dynamic range over conventional microscopes. Existing microscopes usually optimize one or two of these quantities. The microscope presented in Chapters 4 and 5 is optimized so as to improve all three quantities simultaneously. This is reflected on the quality of the acquired images also presented in these chapters. In Chapter 6 a novel non-Cartesian scanning microscope prototype suited for corneal studies, built to investigate the possible integration of such a system in the microsurgical robot, was presented.

Details which supplement the contents of Chapters 3, 4 and 5 are found in four Appendices. More specifically, Appendix 1 contains information about the CSLM software graphical user interface; Appendix 2 presents a novel 3D scanning design and Appendix 3 presents two computer routines used to evaluate the theoretical models developed in Chapter 3. Finally, Appendix 4 contains the result of a preliminary study that investigated various tissue preservation and tissue machining methods, that are to be used in the organ mapping apparatus.

7.2 Original Contributions

The work presented in this thesis is considered to be original in the following aspects:

i) Design and construction of a computer controlled confocal scanning laser microscope that offers three distinct imaging modes: (a) Type 1 and Type 2 confocal intensity contrast, (b) interference contrast, and (c) differential phase contrast mode. Consistent

with the original requirements, the microscope is capable of obtaining cellular level 3D images of biological tissue.

ii) Design, construction and characterization of a spherical-coordinate confocal scanning laser microscope suited for studies of organs (or parts of organs) exhibiting quasi-spherical shape (i.e. the eye and more specifically the cornea).

iii) Theoretical modeling and measurement of the error involved in 3D volumetric imaging through media layers that exhibit a refractive index mismatch.

iv) Development and comparison of two models for estimating the depth response of a confocal scanning laser microscope: (a) a geometric-optics model with Gaussian-beam weighting, and (b) a model based on scalar paraxial theory.

v) Design, construction and complete characterization of a novel micro-positioning system that serves as the prototype for the development of a parallel drive scanning arrangement (Appendix 2). This work was performed by the author in cooperation with Dr. Ian W. Hunter who had the idea of using a confocal optical sensor as a position transducer, Mr. Colin Brenan, who developed and characterized the closed loop configuration and performed the long term stability measurements, and Mr. Serge Lafontaine who offered useful insight and information on the implementation of the closed loop control circuitry.

7.3 Future Work

The work presented in thesis can be continued to accommodate the following future work that can be classified as immediate and long term.

Immediate - Optimization of the CSLM System

The confocal microscope system presented in Chapter 4 is fairly complex and quite large in size. Incorporation of a cutting mechanism (most probably based on a Excimer laser) would be difficult without first simplifying and rearranging the current optical configuration. It would also be advantageous to miniaturize the entire microscope by replacing some of the bulk-optics with fiber-optic based components. The fiber-optic-

based design of the spherical coordinates scanning laser microscope (presented in Chapter 6 of this thesis) represents a step in that direction.

Currently, the CSLM offers three distinct contrast modes. A polarization contrast mode that was briefly attempted but was not incorporated in the prototype should be further investigated. This contrast mode can be very useful for imaging the anisotropic mechanical structure of tissue such as muscle.

When the CSLM prototype was originally designed and built, each subsystem was implemented having in mind availability, simplicity, and ease of use. As a result, some of the subsystems are not optimal. One of these subsystems is the scanning arrangement; the other is the data acquisition hardware. An upgrade of these will greatly improve the performance of the CSLM.

a) Improved Scanning Arrangement

Microstepper driven translation stages, although simple to use and adequate for general positioning requirements, suffer from significant backlash. The resolution vs. scanning speed trade-off is also a limiting factor. Therefore, a significant improvement is expected with the use of a faster scanning subsystem. An alternative would be to implement an optics scanning design coupled with an optical-fiber-based system. The hybrid optics/object scanning arrangement prototype described in Chapter 5 is such an attempt.

b) Faster Data Acquisition

Frequently, image acquisition speed was slowed down by the conversion speed of the A/Ds. The maximum data acquisition speed for 2 channels was slightly less than 19 Ksamples/sec. With the CPU speeds and data bus bandwidths ever increasing, an upgrade to a higher throughput computer is likely. A VXI-based I/O system can also offer an immediate improvement.

Long Term - Development of the Tissue Machining Subsystem

Although in Appendix 4 preliminary consideration regarding the cutting subsystem of the organ mapping system are given, a number of issues remain to be resolved. Specifically: (a) Fluency level for different tissues should be determined, (b) the amount of tissue

removed for a given amount of optical power level should be accurately measured and (c) the tissue machining arrangement should be integrated with the CSLM.

Final Goal - Development of Organ Finite Element Model

Upon completion of the organ mapping system, the acquisition of the necessary data to build an accurate 3D anatomical map (at the cellular level) of small biological organs, would be possible. The 3D anatomical map can then serve as the basis for the development of a finite element model of the organ. This model can be used for pre-operation surgical procedure rehearsal, surgical training and student surgeon objective assessment.

APPENDICES

Appendix 1

a1.1 The CSLM software Graphical User Interface

In this appendix the graphical user interface (GUI) that was designed for the CSLM is presented. This is not a complete reference of its full functionality but mainly a brief summary of its capabilities and a brief introduction for someone who would like to use the interface. The GUI is running on a Unix workstation (IBM RS 6000) running X-Windows / Motif. The GUI was programmed in C using also an interface builder. The main interface window (Figure a1.1(a)) is what the user sees when the program is initiated. This main interface window has four areas, each one containing the parameters that control different aspects of the functionality of the CSLM.

a1.1.1 The Main Window

By default the CSLM will acquire a 2D x,y image of the object under observation. From the main window of the GUI (shown in Fig. a1.1 (a)) the user can modify the parameters that control the acquisition of the images by the CSLM, initiate a scan with the desired specifications, and also interrupt one. The three main groups of parameters that the user can modify are:

a) Images Parameters

These parameters control the image size (number of pixels in x and y dimensions) and resolution along these axes. For convenience, in the same area an option is given to perform a depth response measurement for the microscope. The acquisition of a 2D image and a depth response measurement are the most frequently-performed ones. In the case of low signal-to-noise ratio (SNR) the user can request the acquisition of more samples per image point (pixel). These measurements can then be averaged to improve the SNR.

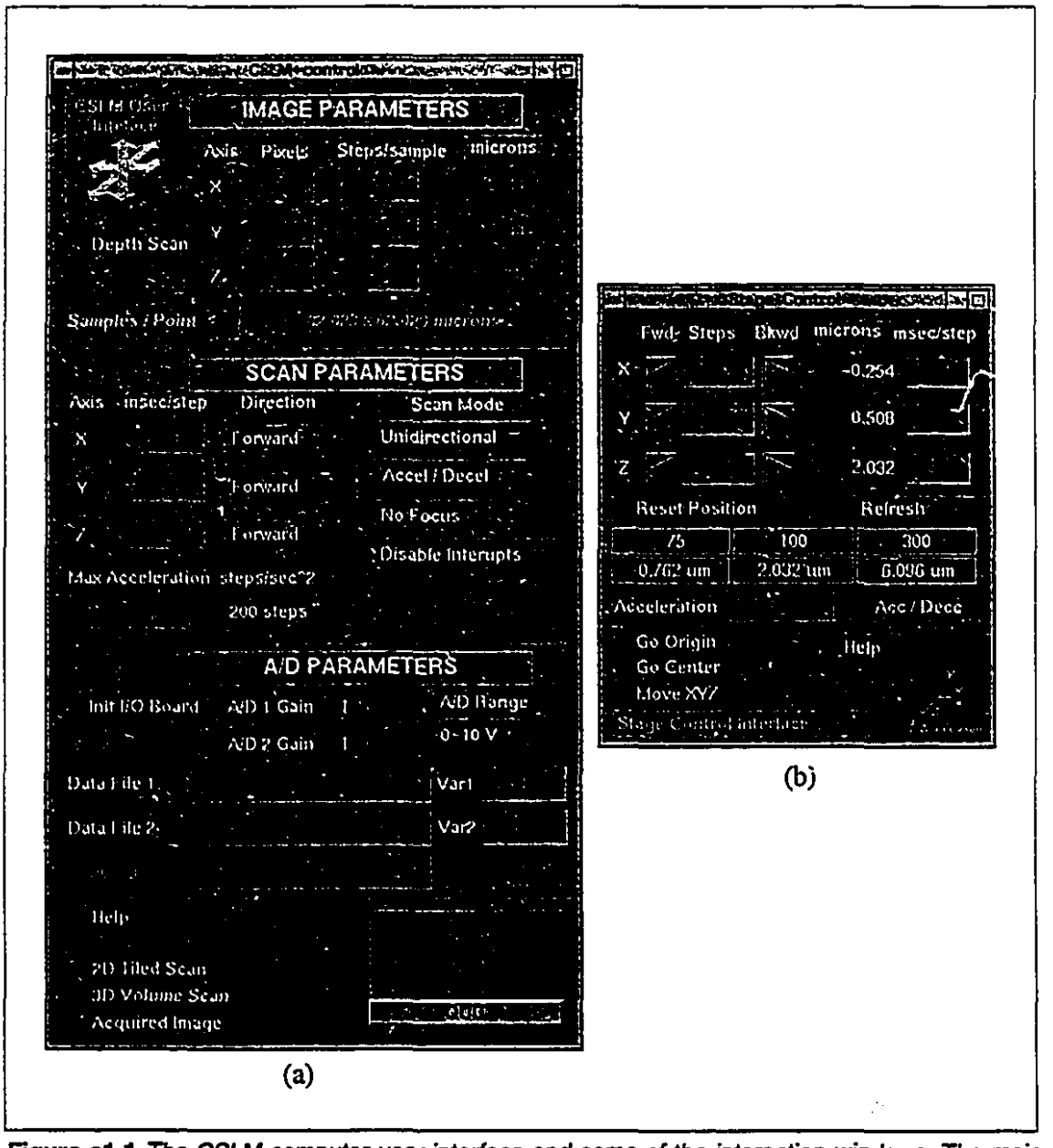

Figure a1.1 *The CSLM computer user interface and some of the interaction windows. The main window (a), and the scanning stage control window (b).*

b) Scan Parameters

These parameters specify:

a) The scanning speed and direction of motion along each axis.

b) The motion profile of the stage (i.e. constant velocity or accelerating and decelerating motion for each scan line) and

c) The scanning mode, or more specifically whether unidirectional or bi-directional scanning should be performed. In the unidirectional scanning mode, the stage returns to the origin of the fast scanning axis, before acquiring the next image line. In the case of bi-directional scanning data are acquired both in the forward and return path of the stage motion.

Within the scan parameters the user can specify focusing of the CSLM on the surface of the sample for each image point. This results in long scan times but a surface profile of the object is retrieved. This mode of operation is also mentioned as auto-focus mode.

Finally the user can specify whether the user interrupts should be disabled while an image is acquired. The disabling of the user interrupts is highly desirable for multi-user and multi-tasking systems. During image acquisition timing is critical and therefore all the system resources should be allocated to the CSLM control process. User interrupts are enabled as soon as the image is acquired. Since there is no way for the process to be stopped when the user interrupts are disabled a hardware interrupt button (wired to the workstation's parallel port) is constructed so that the user can stop the acquisition of an image (even when the interrupts are disabled) and return the process control to the main interface without loosing the position (in the world and image coordinate systems).

c) I/O Parameters.

These parameters specify the gain of the A/D channels (that sample the photodetectors' signal), the range of the A/Ds (i.e. 0-5 V or -10 to +10 V) and the file names where the acquired images are to be saved.

In the lower part of the main interface window the "START" (for starting the image acquisition), "STOP" (stopping any process that is in progress) and "QUIT" (quit the interface) buttons are located. Also a number of toggle buttons are included in this lower part of the interface that control the pop-up of the secondary interface windows described in the next section.

a1.1.2 The Secondary Windows

a) The Online Help Window (Figure a1.2 (c)).

This window offers online help regarding the interface and also the way the inputs and outputs of the Digital I/O board should be connected.

b) The Stage Control Window (Figure a1.1 (b)).

This is the second most important window and is used to control interactively the motion of the stages. The user can move each individual axis or all of them by a certain distance. The user can also select the speed of motion and the motion profile (i.e. constant speed or accelerated/decelerated motion). The motion can be performed with respect to the two coordinate systems described in Chapter 4 of this thesis. Namely, the image coordinate system and the world coordinate system. The Stage Control Interface window contains also some position status labels that indicated the current stage position in word and image coordinates. The user can reset the origins of the world and user coordinate systems at will by using the "Reset Position" button.

c) 2D Tiled Scan Window (Figure a1.2 (b)).

With this window the user can perform a 2D tiled scan. A series of 2D images arranged in a 2D tiled fashion can be acquired. The grid size is user selectable as well as the amount of overlap (if any) between neighboring images. To give an example, the user can acquire 12 images 256 by 256 pixels each arranged in a 3 by 4 grid.

d) The 3-D Volumetric Image Acquisition Window (Figure a1.2 (a)).

Within this window the user can specify the parameters that govern the acquisition of a sequence of images along the optical axis of the microscope (Z-axis). More specifically the number of 2D images (slices), the distance between the slices and the numbering of the slices can be specified. These image slices are then processed so that a 3D volumetric image of the object or a topographical map of its surface can be reconstructed.

e) The Acquired Image Window (not shown).

This is the window used for visualization of the acquired image. This part of the GUI should not be used any more. The user can use other programs to view the acquired

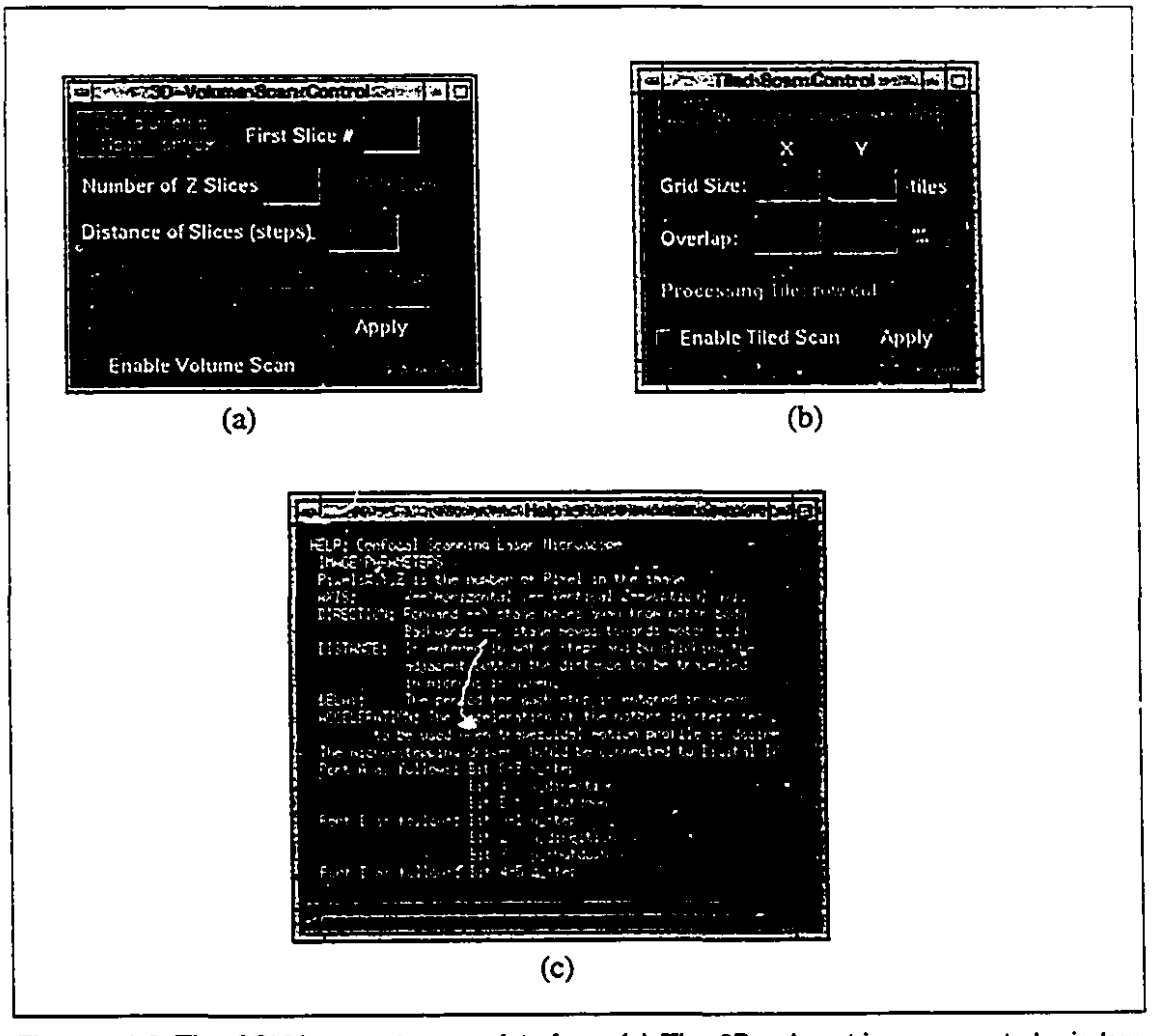

Figure a1.2 *The CSLM computer user interface: (a) The 3D volumetric scan control window, (b) the tile mode control window and (c) the online help window.*

images (i.e. Matlab®* , xv©** or xvg [Charette, 1994]). These programs offer a number of utilities for image processing (i.e. filtering, Fourier transform) and gray level manipulation (i.e. gamma correction, contrast enhancement, histogram equalization).

a1.2 References

Charette, P.G. (1994), *A method for full-field mechanical testing of biological membranes based on electronic speckle pattern interferometry (ESPI)*, Ph.D. thesis, McGill University.

* Matlab is a registered trademark of the MathWorks Inc.
** xv is a copyright of John Bradley from the University of Pennsylvania (bradley@cis.upenn.edu)

Appendix 2

a2.1 A Novel Scanning Arrangement.

In an effort to replace the stepping motor driven stage scanning arrangements that were used both in CSLM and SCSLM (Chapters 4 and 6 above) we have designed the scanning arrangement shown in Figure a2.1. It is a parallel drive arrangement utilizing beam bending (like to the one in [Hunter *et al.*, 1990]). The difference is that is this case a novel confocal displacement transducer is used for position feedback. A single axis of this arrangement was designed, built and characterized extensively. The results of the evaluation are published in [Brenan *et al.*, 1993]. The constructed single-axis arrangement is currently used for scanning the mirror in a Fourier transform Raman spectrometer.

The single-axis arrangement had a resolution of approximately 60 μm and a scan range of ~800 μm. Although the resolution is adequate. the scan range is limited for the applications for which the CSLM was built. These instruments should allow the acquisition of wide-field low-resolution images as well as narrow-field very high-resolution ones. The used stepping motor controlled translation stages offer this requirement at the expense of speed and bi-directional repeatability. The scanning arrangement shown in Figure a2.1 can achieve higher scanning speeds, higher accuracy and bi-directional repeatability at the expense of a limited scan range. A good approach would be a hybrid arrangement in which the translation stages are used for large displacements and the direct drive arrangement proposed in this appendix for small fast displacement. Another approach in the case of a optical fiber based design is to have the optics scanned using the direct drive scanning arrangement and the object (for large displacements) using translation stages like the ones used in the CSLM described in Chapter 4.

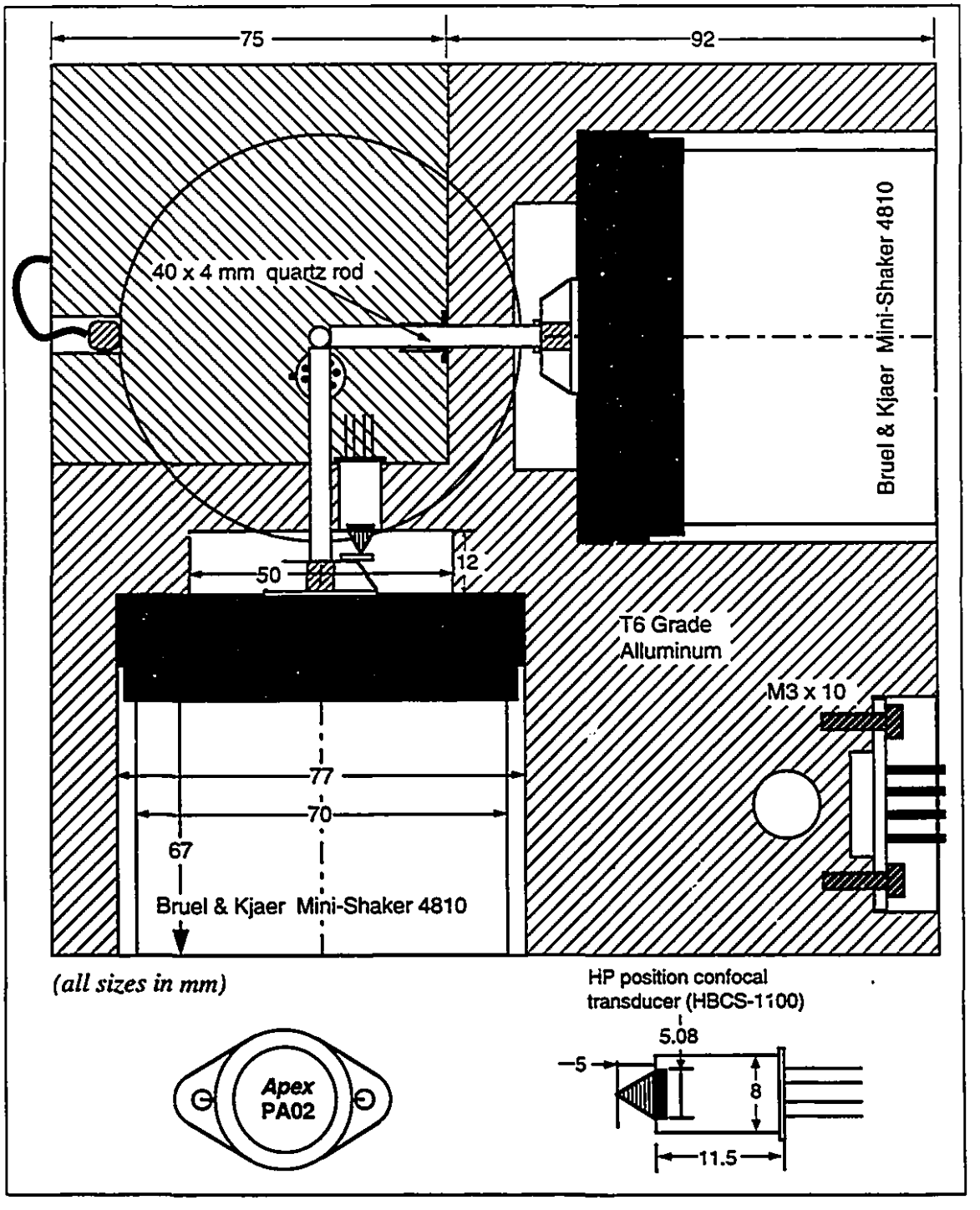

Figure a2.1 *Alternative parallel drive scanning arrangement based on beam bending and the use of a novel position transducer (HP HBCS-1100).*

The contribution of each author to the design, construction and characterization of the single axis prototype is as follows: T.D. Doukoglou designed and built the experimental setup; he also did the preliminary evaluation and characterization. C. Brenan, with some assistance from T.D. Doukoglou, was responsible for the complete characterization of the system and he is currently using it in his Fourier Transform Raman spectrometer. Dr. I.W. Hunter had the insight of using the confocal detector as a position transducer and built a number of devices (including micro-actuators) using it. S. Lafontaine provided the information on how to build the feedback circuitry.

a2.2 References

Hunter, I.W., Lafontaine, S., Nielsen, P.F.M., Hunter, P.J. & Hollerbach, J.M. (1990), "Manipulation and dynamic mechanical testing of microscopic objects using a tele-micro-robot system," *IEEE Control Systems Magazine*, **10**, pp. 3-9.

Brenan, C.J.H., Doukoglou, T.D., Hunter, I.W., & Lafontaine, S. (1993), "Characterization and use of a novel optical position sensor for microposition control of a linear motor," *Review of Scientific Instruments*, **64** (2), pp. 349-356.

Appendix 3

a3.1 Depth Response of CSLM for Finite Size Detector: Computer Code

Next we include the code for evaluating the depth response function of a confocal arrangement for different sizes of normalized pinhole radius. The code of both the scalar paraxial theory model as well as of the Gaussian beam model are given. For the theoretical formulation please refer to Chapter 3 of this thesis.

a3.1.1 Computer Code for Paraxial Theory Model

```
%  TDD 28 Oct. 1994
%  Estimation of the depth response function of a Confocal arrangement
%  as a function of the detector pinhole size.....
%  Paraxial ray approximation
%              / 1
%    h(u,v)= |  P(r) exp(0.5*i*u*r^2) J0(v*r) r dr
%            / 0
% for the radial coordinate on the transverse plane....
r=[0.0:0.02:0.98];
length(r)
for vp=1:1:10      % normalized pinhole radius.....
%vp should never be more than max(v)
% be careful also with the u limits. It should not go beyond
%                                          kfo*(sina)^2
 for u=-15.0:0.15:15.0
   for v=0.2:0.2:20.0
     % estimate the transverse Intensity distr.(should be spinned around
     % for more accurate results.....
     hv(v/0.2)=abs(sum((exp(i.*u.*r.^2).*bessel(0,v.*r).*r)))^2;
   end
   % integrate from 0 to vp the transverse intensity distribution.
   vz(u/0.15)=sum(hv(1:vp/0.2).*[0.2:0.2:vp]);
 [vp u]
 end
 eval(['Vz',int2str(vp),'=vz']);
 eval(['save Vzu15_', int2str(vp) ,'.mat Vz',int2str(vp)])
% plot(vz/max(vz))
end
xlabel('vp: normalized pinhole radius')
ylabel('Intensity of Depth Response')
title('Pinhole radius from 0 to 15')
```

a3.1.2 Computer Code for Geometric Optics & Gaussian Beam Weighting Model

```
function [vp , p3db] = dep_Gmodel(points,increment,sina,Num)
% USE:  h=dep_model(points, increment [sina], Num);
%       Depth response of a type II confocal scanning laser microscope
%       for a perfect plane object (Gaussian beam approximation theory).
%       T.D. Doukoglou 25 Oct. 1994
%       Copyright(c) tdd.
%
ri=zeros(1,points);
pai=3.14159;
lambda=632.*10^(-9);
p3db=zeros(1,Num);

fo=3.6e-3; w0=3.0e-3; fi=300e-3; rp=10.0e-6;

fo=w0/tan(asin(sina))          %estimate of focal distance for given sina
sina=sin(atan(w0/fo))
Magnif=fi/(2*w0)*2*sina        % Ratio of F#s for lenses
pinhole_incr=1.25e-6;
Bo=(2/pai)*lambda/(2*sina);    % Gaussian beam waist
zR=(Bo^2) * pai/lambda;        % Rayleigh range


for j=1:Num
 rp=j*pinhole_incr;
 tanq=rp/fi;
 for i=1:points
   dist=(i-points/2)*increment;
% For Geometric Model
%      Bz=w0*dist/fo;
% For Gaussian beam model
    Bz=Bo*sqrt(1+(dist/zR)^2);          % beam radius
    rpp=abs(tanq*(fo+dist));            % projected pinhole radius

% power of beam within radius rpp
    ri(i)=(1-exp(-2*(rpp^2)/(Bz^2)));
 end
 ri=ri/max(ri);
 plot(ri); pause
% find the FWHM points and store them.
 error=0.3;
 for k=1:points/2
     if (abs(ri(k)-0.5)<=error)
       p3db(j)=2*(points/2-k);
     end
     error=min(error,abs(ri(k)-0.5));
   end
end
vp=[1:1:Num]*pinhole_incr*2*pi/lambda*sina/Magnif;
p3db=p3db*increment*8*pi/lambda*sin(asin(sina)/2)^2;
%use [vp p3dp]=dep_model(400,0.025e-6,0.624,40);
```

Appendix 4

a4.1 Tissue Preservation and Tissue Machining Techniques

The organ mapping apparatus (OMA) which includes the CSLM as a subsystem also incorporated a tissue cutting (machining) subsystem. For proper development of the latter different tissue preservation and cutting methods, were attempted. This Appendix present preliminary result from the evaluation of different tissue preservation and tissue machining methods in order to access their suitability for use in the OMA.

4.2 Techniques for Tissue Preservation

There are various method for preserving and preparing tissue for microscopic observation [Luna (ed.), 1960], [Thompson & Hunt, 1966]. Some of the methods tried on tissue that was subsequently imaged using the CSLM are described next. The methods were tried in order to assess their suitability for tissue machining and observation using the CSLM. The organ used in the experiments was mice heart and the features that were observed was contrast and visibility of the sarcomeres in myocardial fibers. The reason being that the spacing and orientation of sarcomeres can give information about the fiber orientation in the myocardium. Building of a detailed fiber orientation map of the myocardium is one of the applications for the OMA.

a4.2.1 Freezing with Dry Ice

The organ (mouse heart) was extracted and then immediately washed both externally and internally by pumping saline solution through the aortic valve. A solution of 20 to 100 % alcohol was then used to disperse the water and prepare the tissue for freezing. The cleaned tissue was embedded in dry ice and allowed to freeze for 10 minutes. The frozen sample was then immersed in a cubic container with embedding media (Tissue-Tek O.C.T. compound) to form a block suitable for dissection in a cryotome. The advantage of this technique is that the tissue closely resembles the state of fresh tissue. The main problem with this technique was that, due to the use of alcohol, the water contained in the muscle fibers was drained (due to osmotic pressure) and the sarcomeres were no longer visible under the microscope. This made the observation of the various structural characteristics of the cardiac tissue very difficult.

a4.2.2 Fixation using Formaldehyde

A whole fresh mouse heart was cleaned using saline solution injected through the aortic valve. After the cleaning a 15% potassium citrate in a phosphate buffer was injected through the aortic valve and at the same time 5% formaldehyde was injected in the coronary circulation. Immediately the heart is lowered in bath of 5% formaldehyde and let to set for 20 minutes to 2 hours. The fixated tissue was either frozen to allow use of a cryotome or was embedded in a silicon rubber block that enables cutting using a microtome. A gelatin solution of different concentrations (from 4% to 10 %) was also used for tissue embedding but was not proven very practical during the cutting. This method gave the best images of muscle fibers; the sarcomeres were clearly visible and accurate measurement of the muscle fiber orientation was possible. An image of a striated muscle fiber that was fixated using this technique is shown in Figure 5.13. Note that the muscle fiber images in Figure 5.13 are extended focus images that were reconstructed from 6 confocal image slices.

a4.2.3 Fixation using Glutaraldehyde

This technique is similar to the one mentioned above, with the only difference being that the fixating agent is 3% and then 8% glutaraldehyde. In this case, after a tissue is cleaned with saline solution it is immersed in a bath of glutaraldehyde and left to set overnight. Even though, the results looked similar to the ones obtained using the technique described in a4.2.2, it is believed that glutaraldehyde is less drastic than formaldehyde and preserves tissue morphology better.

a4.2.4 Wax Embedding Techniques

This procedure was performed by an outside specialized lab. It involves fixation of the tissue and final embedding into a block of wax. The process is fairly involved and long but optional staining can be applied to the tissue to enhance visibility of certain structures. The main problem with this technique is the complete drying of the tissue before the embedding. As a result, the cells shrink, and consequently drastically reduce the visibility of certain structures (in this case muscle fibers and sarcomeres). Cleaning of the wax using xylene in increasing concentrations and finally rehydration of the tissue was performed before imaging. A problem that was encountered with this method was the quick drying of the tissue surface that made acquisition of a consistent set of images

difficult. An example of muscle tissue fixated using this technique is the fiber shown in Figure 4.3(b).

a4.3 Tissue Machining Techniques

The next problem to be resolved is that of tissue cutting. For whole organ imaging, a layer of tissue needs to be removed after being imaged to expose the next underlying layer of tissue for further processing. A number of tissue cutting methods were tried; the most promising is the ablation using an excimer laser. The attempted techniques are outlined next.

a4.3.1 Cryotome / Microtome

Tissue samples fixated using the method referred in Section a4.2.1 can be sliced and very thin surface layers ($\leq 2\ \mu m$) can be removed. The removed tissue is disposed of; this is exactly the opposite to what usually happens in histological studies where the cut slice is mounted on a microscope glass slide for visualization. The advantage of this technique is that the exposed surface is clean and suitable for imaging. The disadvantage is the high price of a good cryotome, its proper integration into the microscope and the fact that the table where the organ is to be mounted should be kept at very low temperature ($\leq -20\ ^{o}C$) to avoid melting of the tissue. The same principle can be used with wax embedded specimens. In this case cutting is performed with a microtome. The advantage of microtome cutting is that there is no need for temperature controlled specimen holder, compensating in a way for the more elaborate fixation method.

a4.3.2 Inertial Cutting

Both a microtome and a very high speed spinning mill (15,000 - 20,000 revs/min) were tried in order to slice tissue layers. These cutting methods were used with samples fixated using methods described in Sections a4.2.2 and a4.2.3 above. Although the surface of the tissue appeared clean to the eye, under the microscope the muscle fibers appeared smeared and distorted. Small pieces of the cut tissue also appeared on the freshly-cut surface, requiring additional cleaning and complicating possible automation of the whole process. Fine tuning of the technique is essential before it can be used for whole organ cutting and imaging. The big advantage of the technique is its simplicity and the low price of the components required.

a4.3.3 Ablation via Excimer Laser

A 248 nm wavelength krypton-fluoride Excimer Laser (MPB model PSX 100) was used to ablate myocardial tissue that was fixated using the methods described in Sections a4.2.2 and a4.2.3 above. Uv photon energy is sufficient to break co-valent bonds in the tissue [Shukov & Smith, 1988]. The bond destruction is accompanied by ejection of the free molecules due to local volume changes. This process is called ablation and it allows for cleaner cuts (compared with ones obtained with infra-red laser or mechanical cutting) [Poulin *et al.*, 1988].

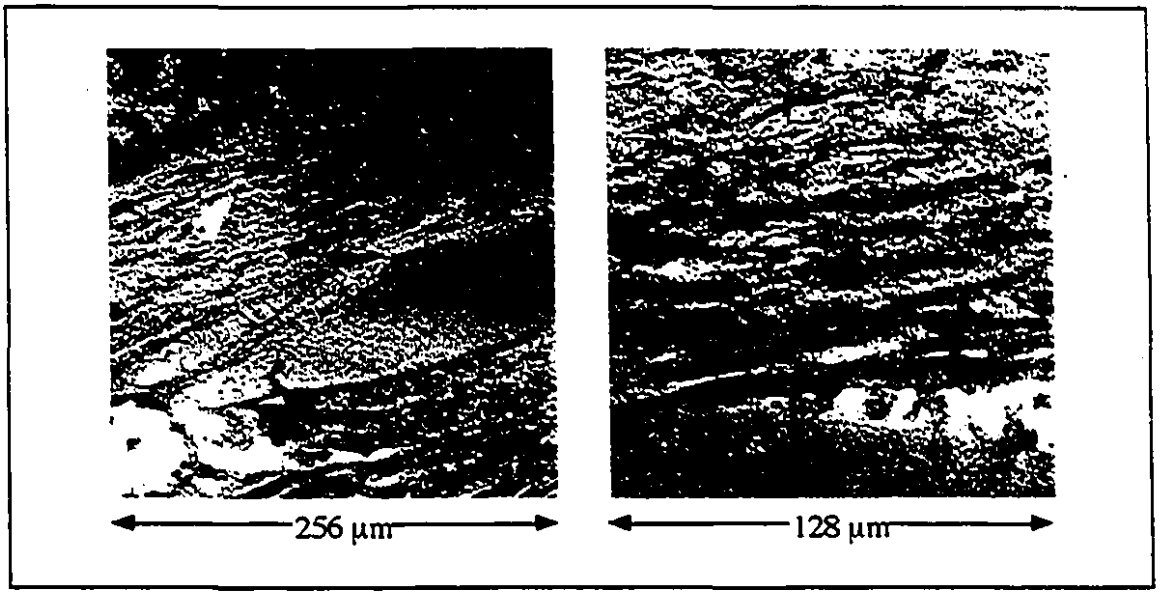

Figure a4.1 *Image of a mice myocardium slice whose top surface layer was ablated using a pulsed Excimer laser. The image was acquired using the CSLM described in Chapter 3 & 4.*

The Excimer laser used is a pulsed laser so the energy delivered (and thus the depth of cutting) can be accurately controlled. Pulsed mode offers itself for complete computerized control. Tissue removal can be done in parallel (if enough energy is available), or sequentially using a focused beam. Even though there are no exact figures on how uniform the cutting depth is, the quality of the cut appeared excellent under a white light conventional microscope. The tissue was also imaged using the CSLM but its narrow depth response did not allow for quick evaluation of the quality of the exposed surface. An example image of myocardium tissue after the top surface layer was ablated is shown if Figure a4.1. From this preliminary evaluation, tissue ablation via Laser appears to be the best suited method for the OMA.

a4.4 Summary

A brief overview of tissue preservation and cutting techniques, were presented. The motivation of such a study was the identification of a suitable tissue preservation and machining method to be implemented in the OMA. A subsystem of the OMA is the confocal scanning laser microscope presented and characterized in Chapters 3 and 4 of this thesis. Preliminary results indicate that tissue fixation via Formaldehyde and tissue machining using a pulsed Excimer laser suitable for implementation in the OMA.

a4.5 References

Luna, L.G.(ed.) (1960), *Manual of Histologic Staining Methods of the Armed Forces Institute of Pathology*, 3rd edition, McGraw Hill.

Poulin, G., Darcy, G. & Eisele, P (1988), "A versatile excimer laser processing system," in *Proceedings SPIE*, **998**, pp. 17-23.

Schukov, G. & Smith, A.. (1988), "Micromachining with excimer lasers," *Lasers and Optics*, **9**, pp. 75-77.

Thompson, C.C. & Hunt R.D. (1966), *Selected Histochemical and Histopathological Methods*, Charles C. Thomas Publisher.

Bibliography

This section contains important publications in the field of confocal microscopy, which are not referred in the body of the thesis. They are grouped by subject and are given in the interest of completeness.

b1. General Reviews

Galloway, J.W. (1987), "The new microscopy," *New Scientist*, Jul. 2, pp. 39-42.

Hoke, F.(1994), "New confocal systems allow real-time views of cells," *Scientist*, **8**(4),p. 18.

Lichman, J.W. (1994), "Confocal Microscopy," *Scientific American*, Aug. 94, pp. 40-45.

Wilke, V. (1985), "Optical scanning microscopy - the laser scan microscope," *Scanning*, **7**(2), pp. 88-96.

Wilson, T. (1985), "Scanning optical microscopy," *Advances in Microscopy*, pp. 103-113.

Wickramasinghe, H.K. (1988), "Some history and technology of scanning microscopy," *Proceedings SPIE*, **897** Scanning Microscopy Technology and Applications, pp. 2-6.

Yamamoto, Y., Horikawa, Y. & Yamamoto, M. (1990), "Features and applications of the laser scanning microscope," *Journal of Modern Optics*, **37**(11), pp. 1691-1701.

b2. Theory of Confocal Microscopy

Aguilar, J.F. & Mendez, E.R. (1989), "Numerical simulation of images of perfectly conducting rough surfaces in scanning microscopy," *Proceedings SPIE*, **1161** New Methods in Microscopy and Low Light Imaging, pp. 286-296.

Brakenhoff, G.J. & van der Voort, H.T.M. (1989), "Illumination and detection strategies for confocal microscopy," *Proceedings SPIE*, **1139** Optical Storage and Scanning Technology, pp. 117-120.

Conchello, J.-A. & Lichtman, J.W. (1994), "Theoretical analysis of a rotating-disk partially confocal scanning microscope," *Applied Optics*, 33(4), pp. 585-596.

Courderc, H. & Marraud, A. (1985), "Three-dimensional imagery methods in light microscopy," *Proceedings SPIE*, **602** Biostereometrics, pp. 58-62.

Dilworth, D.S., Leith, E.N. & Lopez, J.L. (1990), "Imaging absorbing structures within thick diffusing media," *Applied Optics*, **29**(5), pp. 691-698.

Dilworth, D.S., Leith, E.N. & Lopez, J.L. (1991), "Three-dimensional confocal imaging of objects embedded within thick diffusing media," *Applied Optics*, **30**(14), pp. 1796-1803.

Drazic, V. (1993), "3-Dimensional transfer function of coherent confocal microscopes with extended source and detector (vol. 39, pg. 1777, 1992)," *Journal of Modern Optics*, **40**(3), pp. 547-548.

Drazic, V. (1993), "3-Dimensional transfer function analysis of a confocal fluorescence microscope with a finite size detector," *Journal of Modern Optics*, **40**(5), pp. 879-887.

Frieden, B.R. (1967), "Optical transfer of the three-dimensional object," *Journal of the Optical Society of America A*, **57**(1), pp. 56-66.

Fujii, Y. & Takimoto, H. (1976), "Imaging properties due to the optical heterodyne and its applications to laser microscopy," *Optics and Electronics I*, **18**(1), pp. 45-47.

Gan, X.S. & Sheppard, C.J.R. (1993), "Detectability: A new criterion for evaluation of confocal microscope," *Scanning*, **15**, pp. 187-192.

Gan, X.S. & Sheppard, C.J.R. (1993), "Imaging in a confocal microscope with one circular and annular lens," *Optics Communications*, **103**(3-4), pp. 254-264.

Gu, M. & Sheppard, C.J.R. (1994), "Effects of defocus and primary spherical aberration on image of a straight edge in confocal microscopy," *Applied Optics*, **33**(4), pp. 625-630.

Gu, M., & Sheppard, C.J.R. (1993), "3-Dimensional coherent transfer function for confocal imaging with unequal annular lenses," *Journal of Modern Optics*, **40**(7), pp. 1255-1272.

Gu, M. & Sheppard, C.J.R. (1993), "Effects of a finite-size pinhole on 3D image formation in confocal 2-photon fluorescence microscopy," *Journal of Modern Optics*, **40**(10), pp. 2009-2024.

Gu, M., Sheppard, C.J.R. & Zhou, H. (1993), "Optimization of axial resolution in confocal imaging using annular pupils," *Optik*, **93**(2), pp. 87-90.

Hamed, A.M. (1983), "Compromising resolution and contrast in confocal microscopy using a novel obstruction of circular pupils," *Optica Applicata*, **XIII**(3), pp. 265-271.

Hamilton, D.K., Sheppard, C.J.R. & Wilson, T. (1984), "Improved imaging of phase gradients in scanning optical microscopy," *Journal of Microscopy*, **135**(3), pp. 275-286.

Hamilton, D.K. & Sheppard, C.J.R. (1986), "Interferometric measurements of the complex amplitude of the defocus signal V(z) in the confocal scanning optical microscope," *Journal of Applied Physics*, **60**(8), pp. 2708-2712.

Hell, S.W., Stelzer, E.H.K., Lindek, S. & Cremer, C. (1994), "Confocal microscopy with an increased detection aperture - type-B 4Pi confocal microscopy," *Optics Letters*, **19**(3), pp. 222-224.

Hiraoka, Y., Sedat, J.W. & Agard, D.A. (1990), "Determination of three-dimensional properties of a light microscope system," *Biophysical Journal*, **57**, pp. 325-333.

Iravani, M.V. (1988), "Linear and differential techniques in the scanning optical microscope," *Proceedings SPIE*, **897** Scanning Microscopy Technology and Applications, pp. 43-54.

Kimura, S. & Munakata, C. (1990), "Depth resolution of the fluorescent confocal scanning optical microscope," *Applied Optics*, **29**(4), pp. 489-494.

Kimura, S. & Wilson, T. (1993), "Effects of axial pinhole displacement in confocal microscopes," *Applied Optics*, **32**(13), pp. 2257-2261.

Magiera, A. & Magiera, L. (1985), "Remarks on point spread function in confocal scanning microscope with apodized pupil," *Optica Applicata*, **XV**(1), pp. 107-110.

Massig, J.H. & Hellmuth, T. (1993), "The longitudinal resolution and the light transmission of direct view confocal microscopes," *Optik*, **95**(2), pp. 86-90.

Mathews, H.J., Hamilton, D.K. & Sheppard, C.J.R. (1989), "Aberration measurement by confocal interferometry," *Journal of Modern Optics*, **36**(2), pp. 233-250.

Mendez, E.R. (1985), "Speckle statistics and depth discrimination in the confocal scanning optical microscope," *Optica Acta*, **32**(2), pp. 209-221.

Mendez, E.R. (1986), "Speckle contrast variation in the confocal scanning microscope - Hard edge apertures," *Optica Acta*, **33**(3), pp. 269-278.

Mills, J.P. & Thompson, B.J. (1986), "Effects of aberrations and apodization of the performance of coherent optical systems. I. The amplitude impulse response," *Journal of the Optical Society of America A*, **3**(5), pp. 694-703.

Mills, J.P. & Thompson, B.J. (1986), "Effects of aberrations and apodization of the performance of coherent optical systems. II. Imaging," *Journal of the Optical Society of America A*, **3**(5), pp. 704-716.

Noda, T. & Kawata, S. (1992), "Separation of phase and absorption images in phase-contrast microscopy," *Journal of the Optical Society of America A.*, **9**(6), pp. 924-930.

Reinholz, F. & Wilson, T. (1993). "The imaging of thick phase edges in confocal scanning microscopes," *Optik*, **95**(1), pp. 43-46.

Rosenbluth, A.E., Progler, C. & Fullenbaum, M. (1993). "Confocal filtering of the instantaneous image in scanned darkfield," *Journal of Vacuum Science & Technology B*, **11**(6), pp. 2183-2190.

Sandison, D.R. & Webb, W.W. (1994). "Background rejection and signal-to-noise optimization in confocal and alternative fluorescence microscopes," *Applied Optics*, **33**(4), pp. 603-615.

Sheppard, C.J.R. & Wilson, T. (1979). "Effects of spherical aberration on the imaging properties of scanning optical microscopes," *Applied Optics*, **18**(7), pp. 1058-1063.

Sheppard, C.J.R. & Wilson, T. (1981). "The theory of the direct-view confocal microscope," *Journal of Microscopy*, **124**(2), pp. 107-117.

Sheppard, C.J.R. (1986), "The spatial frequency cut-off in three dimensional imaging II," *Optik*, **74**(3), pp. 128-129.

Sheppard, C.J.R. & Wilson, T. (1986), "On the equivalence of scanning and conventional microscopes," *Optik*, **78**(1), pp. 39-43.

Sheppard, C.J.R. & Wilson, T. (1986), "Reciprocity and equivalence in scanning microscopes," *Journal of the Optical Society of America A*, **3**(5), pp. 755.

Sheppard, C.J.R. & Mathews, H.J. (1987), "Imaging in high-aperture optical systems," *Journal of the Optical Society of America A*, **4**(8), pp. 1354-1360.

Sheppard, C.J.R. & Gu, M. (1991), "Aberration compensation in confocal microscopy," *Applied Optics*, **30**(25), pp. 3563-3568.

Sheppard, C.J.R., Connolly, T.J. & Gu, M. (1993), "Scattering by a one-dimensional rough surface and surface profile reconstruction by confocal imaging," *Physical Review Letters*, **70**(10), pp. 1409-1412.

Sheppard, C.J.R. & Gu, M. (1993), "Imaging by a high aperture optical system," *Journal of Modern Optics*, **40**(8), pp. 1631-1651.

Sheppard, C.J.R., Connolly, T.J. & Gu, M. (1993), "Imaging and reconstruction for rough surface scattering in the Kirchhoff approximation by confocal microscopy," *Journal of Modern Optics*, **40**(12), pp. 2407-2421.

Sheppard, C.J.R., Gu, M., Brain, K., & Zhou, H. (1994), "Influence of spherical aberrations on axial imaging of confocal reflection microscopy," *Applied Optics*, **33**(4), pp. 616-624.

Sheppard, C.J.R. & Cox, I.J., "Resolution of scanned optical systems," *Unknown*, pp. 279-281.

Stokseth, P.A. (1969), "Properties of a Defocused Optical System," *Journal of the Optical Society of America*, **59**(10), pp. 1314-1321.

Streibl, N. (1991/92), "Three-dimensional image formation with optical imaging," *Zeiss Inform.*, **31**(103E), pp. 36-40.

van der Voort, H.T.M., Brakenhoff, G.J. & Janssen, G.C.A. (1988), "Determination of the 3-dimensional optical properties of a confocal scanning laser microscope," *Optik*, **78**(2), pp. 48-53.

van der Voort, H.T.M., Brakenhoff, G.J. & Janssen, G.C.A., Valkenburg, A.C. & Nanninga, N. (1987), "Confocal scanning laser fluorescence and reflection microscopy: measurements of the 3-D image formation and applications in biology," *Proceedings SPIE*, **809** Scanning Imaging Technology, pp. 138-143.

Wilson, T. & Sheppard, C.J.R. (1982), "Imaging with finite values of Fresnel number," *Journal of the Optical Society America*, **72**(12), pp. 1639-1641.

Wilson, T. & Hamilton, D.K. (1982), "Dynamic focusing in the confocal scanning microscope," *Journal of Microscopy*, **128** (2), pp. 139-143.

Wilson, T., Carlini, A.R. & Sheppard, C.J.R. (1985), "Phase contrast microscopy by nearly full illumination," *Optik*, **70**(4), pp. 166-169.

Wilson, T. & Carlini, A.R. (1986), "The images of thick step objects in the confocal scanning optical microscope," *Optik*, **72**(3), pp. 109-114.

Wilson, T., Carlini, A.R. & Hamilton, D.K. (1986), "Images of thick step objects in confocal scanning microscopes by axial scanning," *Optik*, **73**(3), pp. 123-126.

Wilson, T. & Hewlett, S.J. (1991), "Superesolution in confocal scanning laser microscopy," *Optics Letters*, 16 (14), pp. 1062-1064.

Wilson, T. (1993), "Confocal microscopy with detector offset," *Journal of Modern Optics*, **40**(3), pp. 401-412.

Wilson, T., Juskaitis, R. & Rea, N.P. (1994) "Scanning interference microscopy," *Proceedings SPIE*, **2184** Three-dimensional microscopy, p.199.

b3. Confocal Scanning Microscope setups

Black, J.F., Summers, C.J. & Sherman, B. (1972), "Scanned-laser microscope for photoluminescence studies," *Applied Optics*, **11**(7), pp. 1553-1562.

Brenan, C.J.H., Hunter, I.W. & Charette, P.G. (1992) "A reflection confocal scanning laser Raman microscope: design and preliminary results," in *Proceedings Scanning*, **14**, Suppl. II, pp. 66-68.

Brenan, C.J.H. & Hunter, I.W. (1993) "Chemical imaging with a confocal scanning laser Raman microscope and its biological applications," in *Proceedings of Canadian Medical and Biological Engineering Conference*, **19**, pp. 22-25.

Brenan, C.J.H. & Hunter, I.W. (1994) "Three-dimensional chemical imaging with a confocal scanning laser Raman microscope," in *Proceedings SPIE*, **2184** Electronic Imaging: Science and Technology, pp. 2-8.

Brenan, C.J.H. & Hunter, I.W. (1995) "Confocal Raman imaging with a confocal scanning laser FT-Raman microscope," *Applied Spectroscopy*, in press.

Brenan, C.J.H. & Hunter, I.W. (1995) "Design and characterization of a visible light FT-Raman spectrometer," *Applied Optics*, in press.

Butler, D.J., Horsfall, A., Hrynevych, M., Kearney, P.D. & Nugent, K.A. (1993), "Confocal profilometer with nanometric vertical resolution" *Optics Communications*, **100**(1-4), pp. 87-92.

Davinovits, P. & Egger, M.D. (1971), "Scanning laser microscope for biological investigations," *Applied Optics*, **10**(7), pp. 1615-1619.

Devaney, A.J. & Schatzberg, A. (1992), "The coherent optical tomographic microscope," *presented in SPIE 1992*, 10 pages (personal communication).

Dixon, A.E., Benham, G.S. (1987), "Confocal microscopes for 3-D imaging," *Photonics Spectra*, Oct., pp. 145-152.

Doukoglou, T.D., Hunter, I.W. & Brenan, C.J.H. (1992) "Confocal Scanning Laser Microscopy for Muscle Fiber Orientation Studies," in *Proceedings of Canadian Medical and Biological Engineering Conference*, **18**, pp. 106-107.

Doukoglou, T.D., Hunter, I.W. (1993), "Corneal studies using a spherical coordinate scanning confocal laser microscope (SCLM)," in *Proceedings of Canadian Medical and Biological Engineering Conference*, **19**, pp. 198-199.

Finzi, L. & Bustamante, C.J. (1988), "Design and application of a computer-controlled confocal scanning differential polarization microscope," *Review of Scientific Instruments*, **59**(11), pp. 2399-2408.

Franksson, O., Liljeborg, A., Carlsson, K. & Forgren, O. (1987), "Confocal laser microscope scanning applied to three-dimensional studies of biological specimens," *Proceedings SPIE*, **809** Scanning Imaging Technology, pp. 124-129.

Goldstein, S.R., Hubin, T., Rosenthal, S. & Washburn, C. (1990), "A confocal video-rate laser-beam scanning reflected-light microscope with no moving parts," *Journal of Microscopy*, **157**(1), pp. 29-38.

Gmitro, A.F. & Aziz, D. (1993), "Confocal microscopy through a fiber-optic imaging bundle," *Optics Letters*, **18**(8), pp. 565-567.

Hobbs, P.C.D., Jungerman, R.L. & Kino, G.S. (1985), "A phase sensitive scanning optical microscope," *Proceedings SPIE*, **565** Micron and Submicron Integrated Circuit Metrology, pp. 71-80.

Hunter, I.W., Lafontaine, S., Nielsen, P.M.F. & Hunter, P.J., (1989), "A micro-robot for performing optical and mechanical experiments on living microscopic objects," in *Proceedings of Canadian Medical and Biological Engineering Conference*, **15**, pp. 133-134.

Hunter, I.W., Lafontaine, S., Nielsen, P.M.F., Hunter, P.J. & Hollerbach, J.M. (1989), "Manipulation and dynamic testing of microscopic objects using a tele-micro-robot system," in *Proceedings IEEE Conference on Robotics and Automation*, Scottsdale AZ, pp. 1553-1558.

Hunter, I.W., Lafontaine, S., Nielsen, P.M.F., Hunter, P.J. & Hollerbach, J.M. (1989), "A tele-microrobot for manipulation and dynamic testing of single living cells," in *Proceedings IEEE Micro Electro Mechanical Systems Workshop*, Salt Lake City, UT, pp. 102-106.

Hunter, I.W., Lafontaine, S., Nielsen, P.M.F. & Hunter, P.J., (1988), "An apparatus for laser scanning microscopy and dynamic testing of muscle cells ," in *Proceedings SPIE*, **1028** Scanning Imaging Technology, pp. 152-159.

Hunter, I.W., Lafontaine, S., Nielsen, P.M.F. & Hunter, P.J., (1988), "An apparatus for muscle cell mechanical testing and laser scanning microscopy," in *Proceedings of Canadian Medical and Biological Engineering Conference*, **14**, pp. 109-110.

Hunter, I.W., Lafontaine, S., & Hunter, P., (1987), "A scanning laser microscope for muscle fiber studies," in *Proceedings SPIE*, **809** Scanning Imaging Technology, pp. 144-150.

Hunter, I.W. & Lafontaine, S., (1985), "A scanning laser microscope for muscle fiber studies," in *Proceedings of Canadian Medical and Biological Engineering Conference*, **11**, pp. 17-18.

Ichioka, Y., Kobayashi, T., Kitagawa, H. & Suzuki, T. (1985), "Digital scanning laser microscope," *Applied Optics*, **24**(5), pp. 691-696.

Koester, C.J. (1980), "Scanning mirror microscope with optical sectioning characteristics: applications in ophthalmology," *Applied Optics*, **19**, 1749-1757.

Phelan, R.J. Jr. & DeMeo, N.L. Jr. (1971), "Rapid scanning microscope for light probing and infrared mapping," *Applied Optics*, **10**(4), pp. 858-861.

Wang C.P. & Bow R.T. (1984), "Scanning laser video camera/microscope," *Optical Laser Technology*, pp. 247-250.

b4. Novel Confocal and Scanning Microscopy techniques

Bearden, A., O'Neil, M.P., Osborne, L.C. & Wong, T.L. (1993), "Imaging and vibrational analysis with laser-feedback interferometry," *Optics Letters*, **18**(3), pp.238-240.

Betzig, E., Lewis, A., Harootunian, A., Isaacson, M. & Kratschmer, E. (1986), "Near-field scanning optical microscopy (NSOM)," *Biophysical Journal*, **49**, pp. 269-279.

Betzig, E., Isaacson, M., Barshatzky, H., Lewis, A. & Lin, K. (1988), "Near-field scanning optical microscopy," *Proceedings SPIE*, **897** Scanning Microscopy Technology and Applications, pp. 91-99.

Cho, K., Mazzoni, D.I. & Davis, C.C. (1992), "Measurement of the local slope of a surface by vibrating-sample heterodyne interferometry: a new method in scanning microscopy," *Optics Letters*, **18**(3), pp. 232-234.

deFornel, F., Goudonnet, J.P., Salomon, L. & Lesniewska, E. (1989), "An evanescent field optical microscope," *Proceedings SPIE*, **1139** Optical Storage and Scanning Technology, pp. 77-84.

Dovichi, N.J. & Burgi, D.S. (1988), "Photothermal microscope," *Proceedings SPIE*, **897** Scanning Microscopy Techniques and Applications, pp. 70-74.

Juskaitis, R., Wilson, T. & Reinholz, F. (1993), "Spatial filtering by laser detection in confocal microscopy," *Optics Letters*, **18**(14), pp. 1135-1137.

Juskaitis, R., Rea, N.P. & Wilson, T. (1994), "Semiconductor laser confocal microscopy," *Applied Optics*, **33**(4), pp. 578-584.

Maher, E.F. (1985), "The SOMSEM - an SEM-based scanning optical microscope," *Scanning*, **7**(2), pp. 61-65.

Pohl, D.W., Fischer, U.Ch. & Durig U.T. (1988), "Scanning near-field optical microscopy (SNOM): basic principles and some recent developments," *Proceedings SPIE*, **897** Scanning Microscopy Technology and Applications, pp. 84-90.

b5. Confocal Microscopy Applications

Baker, L.R. (1989), "Precision measurement of micro-images," *Proceedings SPIE*, **1139** Optical Storage and Scanning Technology, pp. 27-31.

Bennett, S.D., Peltzer, E.A., McCall, J., DeRosa, R. & Smith, I.R. (1988), "Confocal optical metrology at 325 nm," *Proceedings SPIE*, **921** Integrated Circuit Metrology, Inspection and Process Control, pp. 85-91.

Cox., I.J., Hamilton, D.K. & Sheppard, C.J.R. (1982), "Observation of optical signatures of materials," *Applied Physics Letter*, **41**(7), pp. 604-606.

Davidson, M., Kaufman, K. & Mazor, I. (1988), "First results of a product utilizing coherence probe imaging for wafer inspection," *Proceedings SPIE*, **921** Integrated Circuit Metrology, Inspection and Process Control II, pp. 100-114.

Deitch, J.S., Smith, K.L., Lee, C.L., Swann, J.W. & Turner, J.N. (1990), "Confocal scanning laser microscope images of hippocampal neurons intracellularly labeled with biocytin," *Journal of Neuroscience Methods*, **33**, pp.61-76.

Devaney, A.J. (1992), "Diffraction tomographic reconstruction from intensity data," *IEEE Transactions on Image Processing*, **1**(2), pp. 221-228.

Dilly, P.N. (1988), "Tandem scanning reflected light microscopy of the cornea," *Scanning*, **10**, pp. 153-156.

Dixon, A.E., Doe, N. & Pang, T.-M. (1987), "Industrial applications of confocal scanning optical microscopy," *Proceedings SPIE*, **809** Scanning Imaging Technology, pp. 36-43.

Fay, F.S., Carrington, W., Lifshitz, L.M. & Fogarty, K. (1989), "Three-dimensional analysis of molecular distribution in single cells using digital imaging microscope," *Proceedings SPIE*, **1161** New Methods in Microscopy and Low Light Imaging, pp. 12-23.

Hamashima, M., Kato, K. & Ishizeki, T. (1988), "Optical measurement of half micron critical dimensions," *Proceedings SPIE*, **921** Integrated Circuit Metrology, Inspection and Process Control II, pp. 92-99.

Hamilton, D.K. & Wilson, T. (1982), "Surface profile measurement using the confocal microscope," *Journal of Applied Physics*, **53** (7), pp. 5320-5322.

Izat, J.A., Hee, M.R., Huang, D., Swanson, E.A., Lin, C.P., Shuman, J.S., Puliafito, C.A. & Fujimoto, J.G. (1993), "Micron-resolution biomedical imaging with optical coherence tomography," *Optics & Photonics news*, Oct., pp. 14-19.

Kino, G.S., Hobbs, C.D. & Corle, T.R. (1987), "Phase measurements with a Type 2 microscope," *Proceedings SPIE*, **749** Metrology: Figure and Finish, pp. 92-96.

Lange, D.A., Jennings, H.M. & Shah, S.P. (1993), "Analysis of surface roughness using confocal microscopy," *Journal of Material Science*, **28**(14), pp. 3879-3884.

Larrabee, R.D. (1987), "Submicrometer optical linewidth metrology," *Proceedings SPIE*, **775** Integrated Circuit Metrolofy, Inspection and Process Control, pp. 46-50.

Lemp, M.A., Dilly, P.N. & Boyde, A. (1985), "Tandem-scanning (confocal) microscopy of the full-thickness cornea," *Cornea*, 4, pp. 205-209.

Liang, K.K., Kino, G.S. & Khuri-Yakub, B.T. (1985), "Material characterization by inversion of V(z)," *IEEE Transactions on Sonics and Ultrasonics*, **SU-32** (2), pp. 213-223.

Massig, J.H., Preissler, M., Wegener, A.R. & Gaida, G. (1994), "Real-time confocal laser scan microscope for examination and diagnosis of the eye in vivo," *Applied Optics*, **33**(4), pp. 690-694.

Masters, B.R. & Paddock, S.W. (1989), "In vitro confocal imaging of the rabbit cornea," *Journal of Microscopy*, **157**, pp. 1-8.

Masters, B.R. & Farmer, M.A. (1993), "3-Dimensional confocal microscopy and visualization of the insitu cornea," *Computerized Medical Imaging & Graphics*, **17**(3), pp. 211-219.

Masters, B.R. & Thaer, A.A. (1994), "Real-time scanning slit confocal microscopy of the in vivo human cornea," *Applied Optics*, **33**(4), pp. 695-701.

Sandoz, P., & Tribillon, G. (1993), "Profilometry by zero-order interference fringe identification," *Journal of Modern Optics*, **40**(9), pp.1691-1700.

Sheppard, C.J.R., & Sheridan, J.T. (1989), "Micrometrology of thick structures," *Proceedings SPIE*, **1139** Optical Storage and Scanning Technology, pp. 32-39.

Stelzer, E.H.K. & Wijnaendts van Resandt, R.W. (1985), "Applications of fluorescence microscopy in the three dimensions / microtomoscopy," *Proceedings SPIE*, **602** Biostereometrics, pp. 63-70.

Takamatsu, T. & Fujita, S. (1988), "Microscopic tomography by laser scanning microscopy and its three dimensional reconstruction," *Journal of Microscopy*, **149**(3), pp. 167-174.

Tiaiani, H.J. & Uhde, H.-M. (1994), "Three-dimensional analysis by a microlens-array confocal arrangement," *Applied Optics*, **33**(4), pp. 567-572.

Tychinsky, V.P. (1989), "Lateral superdiffraction resolution of phase objects by means of computer microscope," *Proceedings SPIE*, **1139** Optical Storage and Scanning Technology, pp. 6-12.

Yoshida, H., Ito, K. & Ise, N. (1991), "Localized ordered structure in polymer latex suspensions as studied by a confocal laser scanning microscope," *Physics Reviews B*, **44**(1), pp. 435-438.

b6. Related topics

Bukys, A. (1991) "Considerations in the design of servo amplifiers for high performance scanning systems," *Proceedings SPIE*, **1454** Beam Deflection and Scanning Technology, pp. 186-195.

Liljeborg, A. (1988), "Digital position encoding of galvanometer scanner in a laser microscope," *Optical Engineering*, **27**(9), pp. 818-822.

Liu, K. & Yang, J.Y. (1989), "Reconstruction of 3-D refractive index fields from multi-frame interferometric data," *Proceedings SPIE*, **1161** New Methods in Microscopy and Low Light Imaging, pp. 42-46.

Yano, F. & Nomura, S. (1993), "Deconvolution of scanning electron microscopy images," *Scanning*, **15**, pp.19-24.